ROYAUME DU MAROC
Université Mohammed V - RABAT -
جامعة محمد الخامس – الرباط –
Faculté des sciences
كلية العلوم
CENTRE D'ÉTUDES DOCTORALES - SCIENCES ET TECHNOLOGIES

N° d'ordre : 3823

THÈSE

en vue de l'obtention du : **DOCTORAT**

Centre de Recherche : Centre des Sciences des Matériaux
Structure de Recherche : Laboratoire de Matériaux, Nanotechnologies et Environnement
Discipline : Sciences de la Matière Chimie
Spécialité : Chimie des matériaux et d'environnement

Présentée et Soutenue le : *22 / 07 / 2023*

par :

Yasmina ALAOUI

A comprehensive study on Potassium Calcium Alumina Phosphate glass systems: structural, thermal, optical, and anticorrosive properties analysis

Devant le JURY :

Abdelkbir BELLAOUCHOU	PES	Faculté des Sciences, Université Mohammed V -Rabat	Président
El Mostapha LOTFI	PES	PES, Ecole Nationale Supérieure d'Arts et Métiers, Université Mohammed -Rabat	Examinateur/Rapporteur
Lotfi RGHIOUI	PES	Faculté des Sciences, Université Mohammed V -Rabat	Examinateur/Rapporteur
Mohamed HARCHARRAS	PH	Faculté des Sciences, Université Ibn Tofail de Kénitra	Examinateur/Rapporteur
Ahmed GHANIMI	PH	Faculté des Sciences, Université Mohammed V -Rabat	Examinateur
Maria BOUDALIA	PH	Faculté des Sciences, Université Mohammed V -Rabat	Examinateur
Mouloud EL MOUDANE	PH	Faculté des Sciences, Université Mohammed V -Rabat	Directeur de thèse

Année Universitaire : 2022 - 23

Dedication

This thesis is dedicated to my beloved Mother, the unwavering source of love, strength, and inspiration in my life. Throughout my academic journey. You have been my guiding light, providing endless support and encouragement with your boundless belief in my abilities. Your sacrifices have not gone unnoticed. Words cannot adequately express the depth of my gratitude for all that you have done for me. Thank You for being my rock, my confidante, and my greatest cheerleader.

In the loving memory of my dear father, your absence is felt keenly, but your spirit lives on within me. I dedicate this thesis to you, as a tribute to the profound impact you had on my life. Through this work, I strive to honor your memory and make you proud.

To my little annoying brother, you challenged my patience, but also taught me the true meaning of resilience and unconditional love. Throughout our bond, I discovered the enduring strength of sibling love.

To my beautiful family, your unwavering love and endless support, a pillar that set me free. This work is a testament to your unwavering belief in me.

To my younger self, this thesis stands as a testament to the extraordinary journey we have embarked upon together. Reflecting upon our boundless dreams and unyielding determination, I am filled with profound gratitude for the lessons learned and the resilience gained. Little one, you were a force of curiosity and imagination, forever seeking knowledge with wide-eyed wonder. It is because of your insatiable thirst for understanding that I stand here today, armed with the strength to delve into the depths of intellectual pursuit. Though time has passed and we have grown, I carry your spirit within me, reminding me to approach each endeavor with an open mind and an unwavering belief in the power of knowledge. I dedicate this thesis to you, my younger

self, as a testament to our shared journey and as a tribute to the incredible potential that resides within us all.

With boundless gratitude and admiration.

Acknowledgments

My journey at Rabat's Faculty of Sciences commenced in 2011, marked by a fortuitous step into the realm of chemistry. Initially devoid of aspirations for a thesis, my passion for the discipline and the allure of scientific exploration gradually beckoned me toward this transformative odyssey. A thesis, I soon realized, is not just a scholarly endeavor but a profound voyage of personal growth. It is an intricate tapestry woven with threads of scientific inquiry, resilience, and self-discovery. Throughout this voyage, I navigated the labyrinth of time, work, and stress, honing the art of balance and perseverance amidst the demanding realms of Origin, Excel, and Word. It's a journey rife with challenges, yet each obstacle surmounted yields a profound sense of achievement. Engaging with a myriad of chemical intricacies, it opens gateways to international scientific forums, fostering encounters that enrich the tapestry of knowledge. As this manuscript stands testament to my journey, it bears witness to the invaluable contributions of those who supported and guided me along the way. In rewriting this narrative, I seek to transcend mere acknowledgment but to express heartfelt gratitude to all who illuminated my path.

This work was carried out in Morocco (Rabat) as part of the ***Laboratory of Materials, Nanotechnologies, and Environment (LMNE)*** of the faculty of Sciences, ***Mohammed V University in Rabat.***

First, I would like to express my deep sense of thanks and gratitude to my thesis supervisor **Pr**. **Mouloud EL MOUDANE,** Professor at the Faculty of Sciences, Mohammed V University of Rabat, for his guidance, precious advice, encouragement, patience, and the freedom he allowed me.

My warm gratitude goes to **Pr. Abdellah GUENBOUR**, Professor at the Faculty of Sciences, and former Director of ***LMNE*** at Mohammed V University of Rabat, for their invaluable support throughout my thesis journey.

I extend my sincere appreciation to **Pr. Abdelkbir BELLAOUCHOU,** Professor at the Faculty of Sciences, and current Director of ***LMNE*** at Mohammed V University of Rabat for accepting the presidency of the jury. Since day one on the research road, I wanted him to be the chairman of my thesis. Many thanks for his availability, and encouragement.

I am profoundly thankful to **Pr. Abdelkader ZARROUK**, Professor at the Faculty of Sciences, Mohammed V University of Rabat, for their exceptional guidance and support, which played a role in successfully submitting my article to respectable journals.

I would also like to thank **Pr. Mohammed HARCHARRAS** profusely, Professor at the Faculty of Sciences, University Ibn Tofail of Kenitra, for accepting to participate as a rapporteur in my thesis defense jury despite all his responsibilities and the distance that separates him from Rabat.

My profound thanks also go to **Pr. El Mostapha LOTFI**, Professor at the National School of Arts and Crafts (ENSAM), at the Mohammed V University of Rabat, for honoring me and accepting the task of the rapporteur of my thesis despite all his commitments.

My innermost gratitude to **Pr. Lotfi RGHIOUI,** Professor at the Faculty of Sciences, Mohammed V University of Rabat, for honoring me by agreeing to participate in this jury as rapporteur, and for reading my dissertation despite all his commitments.

My heartfelt note of gratitude to **Pr. Ahmed GHANIMI**, Professor at the Faculty of Sciences, Mohammed V University of Rabat, for agreeing to participate in this jury. Being an examinator of my thesis is such an honor and privilege.

My most special thanks to **Pr. Maria BOUDALIA**, Professor at the Faculty of Sciences, Mohammed V University of Rabat, for accepting to participate as an examinator of my thesis, and for her kind words, constructive advice, willingness to share knowledge, and encouragement.

I want to deeply thank **Pr. Mohamed TABYAOUI,** Professor at the Faculty of Sciences, Mohammed V University of Rabat, for his advice and wholehearted support throughout the growth of my thesis.

The special acknowledgment must also be extended to **Dr. Mohamed LAOURAYED** for all his technical support. Despite all his commitment, he has paid much attention to my needs during my thesis and a simple thanks is not enough to convey the depth of my gratitude.

Special thanks to **Asmae ER-RAFAI,** a holy person who brought kindness and goodness when it was much required. The feeling of someone 'listening' and understanding my struggles was most needed, and you've been able to calm my fears down. Thank you for your support, sense of humor, and all the great moments we have shared.

I would like to extend my sincere thanks to my dear **labmates** at ***LMNE***, especially those who are like family to me, for making the past years less stressful and truly unforgettable.

Finally, I am immensely grateful to **ALLAH** for his continuous blessings, which have enabled me to overcome challenges and persevere in my research.

Abstract

This thesis aims to study the thermal, structural, optical, and anticorrosive properties of ternary $CaO-K_2O-P_2O_5$ and quaternary $Al_2O_3-K_2O-CaO-P_2O_5$ glass systems.

The analysis by differential scanning calorimetry (DSC) showed that the thermal stability of our glasses increases with the increase of the contents of CaO and Al_2O_3 oxides. Measurements of density, molar volume, and chemical durability confirmed these results.

Furthermore, the structural evolution of the studied glasses was followed by IR and Raman vibrational spectroscopy. The study showed a strong cross-linking of the glassy network while incorporating CaO and a more powerful Al_2O_3.

Similarly, UV-Vis-NIR spectroscopy revealed that Al_2O_3 strengthens and enhances the semiconducting character of the glasses.

On the other hand, the study of the corrosion inhibition of mild steel by glasses of the $Al_2O_3-K_2O-CaO-P_2O_5$ system showed that this system has excellent anticorrosive activity in a 3.5% NaCl medium. The effect of composition and temperature on the anticorrosive activities was explored by gravimetry, polarization curves, and electrochemical impedance spectroscopy (EIS). The thermodynamic activation parameters were also calculated and discussed.

Keywords:

Phosphate glasses, IR and Raman spectroscopy, thermal and optical properties, chemical durability, inhibitor, corrosion.

Résumé

Cette investigation a pour but d'étudier les caractéristiques thermiques, structurelles, optiques et anticorrosives des systèmes de verre ternaires $CaO-K_2O-P_2O_5$ et des systèmes de verre quaternaires $Al_2O_3-K_2O-CaO-P_2O_5$.

La calorimétrie à balayage différentiel (DSC) a révélé que la stabilité thermique de nos verres augmente avec la teneur en oxydes CaO et Al_2O_3. Les mesures de densité, de volume molaire et de durabilité chimique ont toutes vérifié ces résultats.

De plus, la spectroscopie vibrationnelle IR et Raman a été utilisée pour suivre l'évolution structurelle des verres examinés. Cette investigation a dévoilé une réticulation du réseau vitreux tout en intégrant CaO et Al_2O_3. De même, la spectroscopie UV-Vis-PIR a permis de démontrer que Al_2O_3 renforce et améliore les propriétés semi-conductrices des verres.

La recherche relative à l'inhibition de la corrosion de l'acier doux par les verres du système $Al_2O_3-K_2O-CaO-P_2O_5$ a, quant à elle, indiqué que ce système présentait une activité anticorrosive remarquable dans un milieu à 3,5 % de NaCl. La gravimétrie, les courbes de polarisation et la spectroscopie d'impédance électrochimique ont été utilisées pour étudier l'effet de la composition et de la température sur les activités anticorrosives. Les paramètres d'activation thermodynamiques ont également été calculés et expliqués.

Mots clés :

Verres phosphatés, Spectroscopie IR et Raman, propriétés thermique et optiques, durabilité chimique, inhibiteur, corrosion.

Résumé général

Nos recherches actuelles visent à mieux comprendre les caractéristiques thermiques, structurales, optiques et anticorrosives des matériaux vitreux dans les systèmes $CaO-K_2O-P_2O_5$ et $Al_2O_3-CaO-K_2O-P_2O_5$. Avant d'être analysés, les échantillons de verre ont été fondus à des températures allant de 800 à 1000°C.

D'une part, nous avons confirmé la nature amorphe des matériaux synthétisés en utilisant la diffraction des rayons X (DRX) et la calorimétrie différentielle à balayage (DSC). Nos recherches ont révélé que la température de transition vitreuse Tg augmente avec la teneur en oxydes CaO et Al_2O_3. Ce résultat favorise la stabilisation thermique et la réticulation du réseau vitreux. Ces faits ont été confirmés par la mesure de la densité volumique (ρ), du volume molaire (V_m) et de la durabilité chimique dans trois solutions d'altération d'acidité variable. Nos résultats indiquent que l'ajout d'oxydes, Al_2O_3, rétrécit le réseau vitreux, créant plus de chaînes enchevêtrées et réticulées.

En outre, les résultats de l'étude suggèrent que l'ajout d'ions calcium et aluminium à la composition du verre entraîne la dépolymérisation des chaînes de phosphate constituées de métaphosphates et leur formation ultérieure en liaisons P-O-Ca et P-O-Al. Cette évolution structurale augmente la température de transition vitreuse, ce qui est cohérent avec la formation de liaisons P-O-Al. Le comportement du système quaternaire soutient également l'hypothèse selon laquelle Al_2O_3 entre partiellement dans le réseau en formant AlO_4.

D'autre part, la spectroscopie UV-Vis-PIR a révélé que l'ajout d'ions d'aluminium renforce la résistance de la matrice vitreuse et améliore les propriétés semi-conductrices des verres. En outre, le dernier axe de cette étude s'est concentré sur l'examen des caractéristiques anticorrosives du verre APCK. Plus précisément, les effets de la concentration, de la composition et de la température de l'inhibiteur sur le processus de corrosion ont été étudiés à l'aide de la gravimétrie, des courbes de polarisation et des techniques de spectroscopie d'impédance électrochimique, à la fois en présence et en absence de l'inhibiteur.

Les résultats montrent que tous les inhibiteurs étudiés sont des inhibiteurs mixtes (à prédominance anodique) dont l'efficacité augmente avec la concentration et la composition des inhibiteurs. Les valeurs maximales ont été obtenues pour l'inhibiteur $APCK_{15}$ à une concentration de 700 ppm. Les courbes de polarisation ont révélé que la densité de courant diminue avec l'augmentation de la concentration et de la composition des oxydes Al_2O_3.

Les diagrammes d'impédance de Nyquist et ceux de Bode ont montré que le processus électrochimique se produit par un transfert de charge sur une surface hétérogène, ce qui est le cas pour toutes les concentrations étudiées.

L'effet de la concentration sur l'activité inhibitrice de l'acier doux a été réalisé dans la gamme de 25-55°C. Les résultats montrent que le pouvoir inhibiteur des verres testés en milieu 3,5% NaCl pour une concentration de 700 ppm de l'inhibiteur $APCK_{15}$ diminue avec la température. Ce comportement peut être expliqué par le fait que les processus cathodiques et anodiques sont thermiquement activés (physisorption). Les paramètres thermodynamiques (Ea, ΔS_a^0, et ΔH_a^0) pour l'activation du processus de corrosion ont été calculés à différentes températures en absence et en présence de l'inhibiteur. Les signes positifs des enthalpies ΔH_a^0 reflètent la nature endothermique du processus de dissolution de l'acier. En même temps, les valeurs élevées et négatives de l'entropie ΔS_a^0 impliquent une diminution du désordre au cours de la transformation des réactifs en un complexe fer-verre activé.

Les isothermes d'adsorption de Langmuir, Temkin, Frumkin et El Awady ont été étudiées à partir des valeurs obtenues et des courbes de polarisation de l'inhibiteur $APCK_{15}$ à 298 K et pour les concentrations 100, 300, 500 et 700 ppm. L'adsorption des inhibiteurs sur la surface de l'acier obéit à l'isotherme de Langmuir. La valeur négative de l'énergie libre standard d'adsorption $\Delta G°_{ads}$ obtenue indique la spontanéité du processus d'adsorption de nos inhibiteurs sur la surface de l'acier et la stabilité de la double couche adsorbée sur la surface du métal. Le mécanisme d'inhibition est basé sur une forte physisorption et chimisorption du système de verre APCK.

List of publications

Y. Alaoui, M. El Moudane, A. Er-rafai, M. Khachani, A. Ghanimi, A. Sabbar, M. Tabyaoui, A. Guenbour, A. Bellaouchou, Structural study, thermal and physical properties of K_2O-CaO-P_2O_5 phosphate glasses. *Moroccan Journal of Chemistry*, (2021).
https://doi.org/10.48317/IMIST.PRSM/morjchem-v9i2.22505

Y. Alaoui, M. Laourayed, A. Er-rafai, M. Hammi, M. El Moudane, M. Boudalia, Z. Sekkat, I. Warad, A. Guenbour, A. Bellaouchou, A. Zarrouk, Effect of alumina insertion on structural properties, thermal stability, and chemical durability of potassium calcium based-phosphate glasses. *Inorganic Chemistry Communications*, (202).
https://doi.org/10.1016/j.inoche.2022.109632

M. Laourayed, **Y. Alaoui**, A. Er-rafai, , M. El Mouzahim, M. El Moudane, , M. Abid, , M. Beraich, , A. Guenbour, and A. Bellaouchou, , Structural, dielectric and optical properties of Ta_2O_5-Bi_2O_3-P_2O_5 phosphate glasses. *The European Physical Journal Applied Physics*, (2022).
https://doi.org/10.1051/epjap/2022220138

A. Er-Rafai, M. El Moudane, **Y. Alaoui**, M. Laourayed, M. Taibi, I. Warad, A. Guenbour, A. Bellaouchou, and A. Zarrouk. "Effect of Molybdenum Oxide on Structural Characteristics, Thermal Properties, and Chemical Dissolution of (50-x) K_2O-xMoO_3-50P_2O_5 Phosphate Glasses." *Biointerface Research in Applied Chemistry*, (2022).
https://doi.org/10.33263/BRIAC133.294

A. Er-Rafai, M. Laourayed, **Y. Alaoui**, M. El Moudane, N. Lazar, A. Benzaouak, A. Bellaouchou, The Effect of Li_2O/K_2O Ratio on the Electrical and Dielectric Properties of Li_2O-K_2O-MoO_3-P_2O_5 Glasses. *Biointerface Research in Applied Chemistry*, (2023)
https://doi.org/10.33263/BRIAC136.553

List of tables

Table IV. 1 Electrochemical parameters, inhibitory efficiency, and recovery rate obtained from polarization curves of mild steel in 3.5% NaCl solution before and after the addition of $APCK_{15}$ with different concentrations. 114

Table IV. 2 Electrochemical parameters, inhibitory efficiency, and recovery rate obtained from polarization curves of mild steel in 3.5% NaCl solution before and after the addition of $APCK_{15}$ with different concentrations……...…...116

Table IV. 3 Electrochemical parameters obtained by S.I.E. of mild steel in 3.5% NaCl medium without and with $APCK_{15}$ different concentrations……...…...…118

Table IV. 4 Electrochemical parameters obtained from polarization curves of mild steel in 3.5% NaCl solution before and after the addition of different compositions of $APCK_x$……..124

Table IV. 5 Electrochemical parameters obtained from Impedance diagrams of mild steel in 3.5% NaCl solution before and after the addition of different compositions of $APCK_x$……..126

Table IV. 6 Electrochemical parameters obtained from polarization diagrams of mild steel in 3.5% NaCl solution before and after the addition of $APCK_{15}$ (700ppm) at different temperatures……...…….……129

Table IV. 7 Activation parameters of the corrosion process of mild steel in 3.5% NaCl medium in the absence and presence of 700ppm of the inhibitor $APCK_{15}$…….....134

Table IV. 8 Adsorption Thermodynamic parameters for of $APCK_{15}$ inhibitor on steel at 298K…….…….137

List of figures

Chapter I:

Figure.I. 1 Obsidian (left) and fulgurite or lightning glass (right) images..... 7

Figure.I. 2 Thermogram of the heat capacity (C_p) as a function of the temperature of a glass sample. 9

Figure.I. 3 (a) Enthalpy plotted versus temperature diagram illustrating the different solidification paths of a standard glass [16] and (b) Gibbs free energy graph of a material's solid and liquid phases as a function of temperature [15]. 11

Figure.I. 4 Basic building block found in silica glasses is shown in (a). Pure silica glassy network as at (b). The network is broken up by adding modifiers, like Na_2O, interrupting the network as at (c). 14

Figure.I. 5 Diffractogram of a glassy structure (black curve) and the corresponding crystallized compound (red curve). 15

Figure.I. 6 Monosilicate structure $[SiO_4]^{4-}$. 16

Figure.I. 7 Phosphate tetrahedron unit $[PO_4]^{3-}$. 17

Figure.I. 8 PO_4 tetrahedra create the phosphate glass network. 20

Figure.I. 9 Q^n building blocks in phosphate glasses. 21

Figure.I. 10 Phosphate glasses' dissolution. (a) Hydration reaction (b) Network breakage. 22

Figure.I. 11 Glass degradation mechanism in an acidic environment: glass leaching... 27

Figure.I. 12 Attack mechanism of glass by sodium hydroxide. 28

Figure.I. 13 Corrosion in an aerated environment. 35

Figure.I. 14 Control of the electrochemical corrosion reaction through pure charge transfer..... 39

Figure.I. 15 Control of the electrochemical corrosion reaction through material transport processes (O_2 diffusion). 39

Figure.I. 16 Representation of the cathodic inhibition process (a) without inhibitor, (b) with inhibitor. 42

Figure.I. 17 Representation of the anodic inhibition process (a) without inhibitor, (b) with inhibitor. 43

Chapter II:

Figure. II. 1 Experimental device of the Archimedes method. 53

Figure. II. 2 The elements characteristic of a typical DSC system. 53

Figure. II. 3 A standard glass DSC thermogram. 54

Figure. II. 4 Diffraction of an X-ray beam fulfilling Bragg's condition.....56

Figure. II. 5 A block ray diagram of a typical mode powder diffractometer 56

Figure. II. 6 X-ray diffraction diagram of a vitreous glass system 57

Figure. II. 7 SIEMENS D5000 type XR diffractometer. 57

Figure. II. 8 Fourier Transform Infrared spectrophotometer's plan..... 59

Figure. II. 9 A JASCO 4600 FT/IR Fourier transform spectrometer type A..... 60

Figure. II. 10 Schematic diagrams of Raman Stokes (left) and anti-Stokes (right) effects 61

Figure. II. 11 A Renishaw RM1000 micro-Raman Spectrometer 62

Figure. II. 12 A JASCO V-670 spectrophotometer.....63

Figure. II. 13 . Scanning Electron Microscope (SEM) components. 65

Figure. II. 14 A JEOL JSM-IT 100 scanning electron spectrophotometer 65

Figure. II. 15 Manual polishing machine with variable speed from 100 to 500 rpm.... 68

Figure. II. 16 Diagrams of E(OCP) tracking as a function of time. 69

Figure. II. 17 Intensity-potential plot. 70

Figure. II. 18 Electrochemical parameters determination from Tafel's lines 71

Figure. II. 19 Proposed electrical equivalent circuit for the metal-electrolyte interface during inhibitor film adsorption..... 72

Figure. II. 20 Nyquist diagram 73

Chapter III:

Figure III. 1 Thermal treatment cycle adapted for the glasses' elaboration 76

Figure III. 2 X-ray diffraction patterns for the five compositions studied of $50P_2O_5$-$xCaO$-$(50-x)K_2O$ glass system, with: (a) x=0mol%, (b) x=10mol%, (c) x=20mol%, (d) x=30mol%, and (e) x=40mol%. 78

Figure III. 3 Diffractograms of the synthesized compositions of APCKx, where x = 2.5, 5, 7.5, 10, 12.5, and 15 mol%..... 78

Figure III. 4 SEM image and EDS of $50P_2O_5$-30CaO-$20K_2O$…….……....79

Figure III. 5 SEM-EDX analysis of $APCK_{2.5}$ glass sample..... 80

Figure III. 6 SEM-EDX analysis of $APCK_{15}$ glass sample. 81

Figure III. 7 FTIR spectra of $50P_2O_5$-xCaO-(50-x)K_2O glass system with: (a) x=0mol%, (b) x=10mol%, (c) x=20mol%, (d) x=30mol% ,and (e) x=40mol%..... 82

Figure III. 8 Raman spectra of $50P_2O_5$-xCaO-(50-x)K_2O glass system with: (a) x=0mol%, (b) x=10mol%, (c) x=20mol%, (d) x=30mol%, and (e) x=40mol%. 83

Figure III. 9 . IR spectra for the synthesized compositions of APCKx, where x = 2.5, 5, 7.5, 10, 12.5, and 15 mol %..... 86

Figure III. 10 Raman spectra for the synthesized compositions of APCKx, where x = 2.5, 5, 7.5, 10, 12.5, and 15 mol %..... 88

Figure III. 11 Variation of density and molar volume of Potassium Phosphate glasses with CaO content. 92

Figure III. 12 Densities and molar volumes in the function of Al_2O_3 content of APCKx glasses..... 92

Figure III. 13 Differential Scanning Calorimetry (DSC) curve of the synthesized glassy sample of the system $50P_2O_5$-xCaO-(50-x)K_2O whereas x= 20mol %.....94

Figure III. 14 DSC spectra for the synthesized compositions of APCKx, where x = 2.5, 5, 7.5, 10, 12.5, and 15 mol %..... 94

Figure III. 15 Variation of glass transition temperature (Tg) composition versus glass composition for the system $50P_2O_5$-xCaO-(50-x)K_2O (x= 0, 10, 20, 30, and 40mol %). 95

Figure III. 16 Variation of glass transition temperature (Tg) composition versus glass composition for the APCKx system where x = 2.5, 5, 7.5, 10, 12.5, and 15 mol %. 95

Figure III. 17 Weight loss (a) and variation of the pH solution (b) as a function of time spent submersing the APCK glass series in HCl solution. 97

Figure III. 18 Weight loss (a) and variation in the pH solution (b) as a function of time spent submersing the APCK glass series in NaOH solution. 98

Figure III. 19 Weight loss (a) and variation in the pH solution (b) as a function of time spent submersing the APCK glass series in deionized water. 98

Figure III. 20 Composition's dependency of DR for xAl_2O_3-(50-x)P_2O_5-10CaO-40K_2O glasses (APCK) (with x=2.5,5,7.5,10,12.5,15) after immersion in HCl solution (pH=3), in

deionized water (pH=7), and NaOH solution (pH=12) after 388 hours of immersion..101

Figure III. 21 Transmittance and absorbance spectra of $50P_2O_5$-xCaO-(50-x)K_2O glass system, (x=2.5,5,7.5,10,12.5,15 mol%)..... 103

Figure III. 22 Variation of the absorption and extinction coefficient as a function of the wavelength for glasses of composition $50P_2O_5$-xCaO-(50-x)K_2O..... 105

Figure III. 23 Determination of the direct optical gap energy of APCKx system..... 107

Figure III. 24 . Determination of the indirect optical gap energy of APCKx system. 107

Chapter IV:

Figure IV. 1 Evolution of corrosion rate and inhibitor efficiency for mild steel for different concentrations of APCK15 inhibitor in 3.5% NaCl solution at 25°C 111

Figure IV. 2 Evolution of the free potential as a function of time of mild steel in the absence and presence of 100, 300, 500, and 700 ppm of APCK15 at T=25 °C after 30 min of immersion..... 113

Figure IV. 3 Polarization curves of mild steel in 3.5% NaCl medium obtained at 25°C without and with the addition of different concentrations of the inhibitor $APCK_{15}$ ... 116

Figure IV. 4 Impedance diagram of mild steel obtained in 3.5% NaCl containing four different concentrations (100-300-500-700ppm) of $APCK_{15}$ glass composition 117

Figure IV. 5 Bode diagram for mild steel in 3.5% NaCl medium in the absence and presence of $APCK_{15}$ different concentrations..... 118

Figure IV. 6 Phase shift n observed at the spectrum reference point: (a) ideal case, in theory (uniformly accessible surface) and (b) spectrum obtained in most practical cases 119

Figure IV. 7 Inhomogeneities on the steel surface, observed after immersion of the electrode in the electrolyte..... 119

Figure IV. 8 Model of equivalent electrical circuit of the steel/NaCl interface and glassy inhibitors..... 120

Figure IV. 9 A simulated fitted spectra for the steel contact of 700 ppm of $APCK_{15}$ in a 3.5% NaCl solution via Z view program……...……120

Figure IV. 10 The free potential as a function of the immersion period in the absence and presence of APCKx different composition (x=0, 5, 10, 15mol%) at 25 °C after 1/2h of immersion……122

Figure IV. 11 The polarization curves of mild steel at 25 ˚C in 3.5% NaCl medium with and without different levels of APCKx…….123

Figure IV. 12 Impedance diagrams of mild steel at 25 ˚C in 3.5% NaCl medium with and without different levels of APCKx…….....125

Figure IV. 13 The OCP curves for mild steel in 3.5% NaCl solution at various temperatures without the $APCK_{15}$ (700ppm) inhibitor…….....127

Figure IV. 14 The OCP curves for mild steel in 3.5% NaCl solution at various temperatures with the $APCK_{15}$ (700ppm) inhibitor……...128

Figure IV. 15 The polarization curves for mild steel in 3.5% NaCl solution at various temperatures without the $APCK_{15}$ (700ppm) inhibitor…….....130

Figure IV. 16 The polarization curves for mild steel in 3.5% NaCl solution at various temperatures with the $APCK_{15}$ (700ppm) inhibitor……...130

Figure IV. 17 Arrhenius lines of corrosion current density of mild steel in 3.5% NaCl medium in the absence and presence of $APCK_{15}$ (700ppm)…….……..133

Figure IV. 18 The association between ln (icorr/T) and inverse temperature for C38 steel in a 3.5% NaCl solution is being studied with and without the addition of 700ppm of $APCK_{15}$……..…...134

Figure IV. 19 Langmuir (A), Temkin (B), Frumkin (C) and El Awady (D) adsorption isotherms of mild steel in 3.5% NaCl in the presence of $APCK_{15}$ at different concentrations at 298K……...136

Terms and symbol glossary

XRD: X-Ray Diffraction

DTA: Differential Thermal Analysis

DSC: Differential Scanning Calorimetry

C_p: Heat Capacity

T_g: Glass Transition Temperature

T_x: Crystallization Temperature

T_f: Fusion Temperature

FT-IR: Fourier Transform Infrared Spectroscopy

SEM: Scanning Electron Microscopy

EDX: Energy-Dispersive X-Ray Spectroscopy

UV-Vis-NIR : Ultra-Violet-Visible-Near Infrared spectroscopy

MAS-NMR: Magic Angle Spinning Nuclear Magnetic Resonance Spectroscopy

OM: Optical Microscopy

PCK: Phosphate-Calcium-Potassium glass system

APCK: Alumina- Phosphate-Calcium-Potassium glass system

NBO: Non-Bridging Oxygen

BO: Bridging Oxygen

ASTM: American Society for Testing Materials

EIS: Electrochemical Impedance Spectroscopy

CVD: Chemical Vapor Deposition

SCE: Saturated Calomel Reference Electrode

OCP: Open Circuit Potential

EEC: Electrical Equivalent Circuit

CPE: Constant Phase Element

Contents

Dedication ..... *ii*
Acknowledgement ..... *iv*
Abstract ..... *vii*
Résumé ..... *viii*
Résumé général ..... *ix*
List of publications ..... *xi*
List of tables ..... *xii*
List of figures ..... *xiii*
Terms and symbol glossary ..... *xviii*
Contents ..... *xix*

General introduction **1**
Thesis plan **4**

CHAPTER I: State of the literature **6**
I.1. Glass review of literature **7**
I.1.1. A brief history of Glass **7**
I.1.2. Definition of Glass **8**
I.1.3. Glass Transition Phenomenon **9**
I.1.4. Glass formation **10**
I.1.5. Classification of the preparation method of glasses **11**
I.1.5.1. Melt-quench technique. **11**
I.1.5.2. Glass by sol-gel method **12**
I.1.5.3. Glass by a chemical vapor deposition method **12**
I.1.6. The theories of glass structure **12**
I.1.7. Classification of glasses **15**
I.1.7.1. Natural glasses **15**
I.1.7.1.1. Mineral glasses **15**
I.1.7.1.2. Geological glasses **15**
I.1.7.1.3. Lunar glasses **15**
I.1.7.1.4. Biochemical glasses **16**
I.1.7.2. Artificial glasses **16**
I.1.7.2.1. Oxide glasses **16**
I.1.7.2.2. Fluoride glasses **18**
I.1.7.2.3. Chalcogenide glasses **18**
I.1.7.2.4. Amorphous metals **18**
I.1.8. Glass systems **18**
I.1.8.1. Silica glass system **19**
I.1.8.2. Borate glass system **19**

I.1.8.3. Phosphate glass system **19**
I.1.8.3.1. Phosphate glass structure **20**
I.1.8.3.2. Phosphate glass solubility **21**
I.1.8.3.3. Phosphate glasses applications **22**
I.1.9. Chemical durability of phosphate glasses **23**
I.1.9.1. Glass corrosion overviews **24**
I.1.9.1.1. Corrosion methods **24**
I.1.9.1.2. Corrosion kinetics **25**
I.1.9.1.3. Phosphate glasses corrosion mechanisms **27**
I.1.9.2. The factors affecting glasses' chemical durability **28**
I.1.9.2.1. Solution attack effect on glass-specific surface area/volume **28**
I.1.9.2.2. Glass composition influence **28**
I.1.9.2.3. Effect of the solution's pH **28**
I.1.9.2.4. Temperature effect **29**
I.1.10. Review several phosphate glass systems through literature analysis **29**
I.2. Corrosion Overview **32**
I.2.1. Definition of Corrosion **32**
I.2.2. Importance of Corrosion **32**
I.2.3. Prevention of Corrosion **33**
I.2.4. The origin of corrosion **33**
I.2.5. Different types of corrosion **33**
I.2.5.1. Chemical corrosion (Dry corrosion) **34**
I.2.5.2. Biochemical corrosion (Microbial corrosion) **34**
I.2.5.3. Electrochemical corrosion (Wet corrosion) **34**
I.2.6. Electrochemical corrosion mechanism **35**
I.2.7. Corrosion forms **36**
I.2.7.1. Uniform corrosion **36**
I.2.7.2. Localized corrosion **36**
I.2.7.3. Galvanic corrosion **36**
I.2.7.4. Pitting corrosion **36**
I.2.7.5. Selective corrosion **37**
I.2.7.6. Intergranular corrosion **37**
I.2.7.7. Stress corrosion cracking **37**
I.2.7.8. Erosion corrosion **37**
I.2.8. Thermodynamic aspect of corrosion **37**
I.2.9. Kinetic approach **38**
I.2.9.1. Control through charge transfer processes **38**
I.2.9.2. Control through material transfer processes **38**
I.2.9.3. Mixed control **40**
I.3. Corrosion inhibitors overview **40**
I.3.1. Definition **41**

I.3.2. Inhibitors' properties and classification **41**
I.3.3. Inhibitors' mechanism and the principle of action **43**
I.3.3.1. Type of adsorption **43**
I.3.3.1.1. Physisorption **43**
I.3.3.1.2. Chemisorption **43**
I.3.3.2. Concentration influence on the inhibitory effect **44**
I.3.3.3. Temperature influence on the inhibitory effect **46**
I.3.4. Corrosion inhibitors applications **47**
I.4. Conclusion **49**

CHAPTER II: Methods and Experimental parameters **51**
II.1. Introduction **52**
II.2. Phosphate based-glasses synthesis **52**
II.3. Thermo-Physical Characterization **52**
II.3.1. Density measurement **52**
II.3.2. Differential Scanning Calorimetry (DSC) **53**
II.4. Structural and optical Characterization **55**
II.4.1. X-Ray Diffraction analysis **55**
II.4.2. Fourier Transform InfraRed (FTIR) **58**
II.4.3. Raman spectroscopy **60**
II.4.4. Ultraviolet-Visible-Near Infrared spectroscopy (UV-Vis-NIR) **62**
II.5. Surface characterization **64**
II.5.1. Scanning Electron Microscopy (SEM) **64**
II.5.2. Energy dispersive spectroscopy (EDS) **65**
II.6. Durability investigations **65**
II.7. Analysis of the anticorrosive activity **66**
II.7.1. Material and sample preparation **66**
II.7.2. The Experimental media **66**
II.7.3. The evaluation process of corrosion inhibiting efficiency **66**
II.7.3.1. Gravimetric method **66**
II.7.3.2. Electrochemical measurements **68**
II.7.3.2.1. Experimental arrangement **69**
II.7.3.2.2. The evolution of Open Circuit Potential (OCP) **69**
II.7.3.2.3. Polarization plot **70**
II.7.3.2.4. Electrochemical Impedance Spectroscopy (EIS) **71**
II.8. Conclusion **73**

CHAPTER III: Preparation and structural, thermal, and optical characterization of CaO-K_2O-P_2O_5 and Al_2O_3-K_2O-CaO-P_2O_5 glass system **74**
III.1. Glass Preparation **75**
III.2. Structural properties of the studied glasses **77**

III.2.1. X-ray diffraction analysis **77**
III.2.2. SEM-EDX analysis **77**
III.2.3. FTIR and Raman spectroscopy analysis **82**
III.2.3.1. $50P_2O_5$-xCaO-(50-x)K_2O ternary glass system **82**
III.2.3.1.1. FTIR analysis **82**
III.2.3.1.2. Raman analysis **83**
III.2.3.2. xAl_2O_3-(50-x)P_2O_5-10CaO-40K_2O quaternary glass system **85**
III.2.3.2.1. FTIR analysis **84**
III.2.3.2.2. Raman analysis **85**
III.2.3.2. Results and discussion **89**
III.3. Thermo-physical characterization of the studied glasses **89**
III.3.1. Density (ρ) and molar volume (V_m) **89**
III.3.2. Thermal analysis by Differential Scanning Calorimetry (DSC) **91**
III.4. Chemical durability **95**
III.4.1. Weight loss (WL) and pH variation of APCK glass system **95**
III.4.1.1. In HCl solution **95**
III.4.1.2. In NaOH solution **96**
III.4.1.3. In deionized water **96**
III.4.2. Dissolution rate (DR) of APCK glass system **98**
III.5. Optical properties **100**
III.5.1. Absorbance and transmittance spectra **100**
III.5.2. Absorption (α) and extinction (K) coefficients **101**
III.5.3. Optical gap **104**
III.6. Conclusion **106**

CHAPTER IV: Corrosion inhibition analysis of mild steel in 3.5% sodium chloride medium by Al_2O_3-K_2O-CaO-P_2O_5 glass system **107**
IV.1. Introduction **108**
IV.2. Gravimetric study **108**
IV.3. Electrochemical process **110**
IV.3.1. The examination by the stationary electrochemical method **110**
IV.3.1.1. The effect of the inhibitor concentration addition **111**
IV.3.1.1.1. Open circuit potential evolution **111**
IV.3.1.1.2. Polarization curves **111**
IV.3.1.1.3. Electrochemical spectroscopy analysis **114**
IV.3.1.2. The effect of inhibitor's various compositions addition **119**
IV.3.1.2.1. Open circuit potential evolution **119**
IV.3.1.2.2. Polarization curves **120**
IV.3.1.2.3. Electrochemical spectroscopy analysis **122**
IV.3.2. The temperature effect **124**
IV.3.2.1. The temperature effect on OCP **125**

IV.3.2.2. Examining the Influence of Temperature on Polarization Curves 127
IV.3.3. Thermodynamic parameters estimation 130
IV.3.3.1. Determination of the activation parameters 130
IV.3.3.2 Thermodynamic adsorption isotherms 133
IV.4. Conclusion 136
Summary **..... 137**
References **..... .139**

General introduction

This thesis was conducted at the Materials, Nanotechnologies, and Environment laboratory in Mohammed V University in Rabat, where novel phosphate glasses were developed. The research focused on the industrial applications of these glasses in the materials sector. Glasses are commonly used in many aspects of daily life, from construction and transportation to food, multimedia, and nuclear energy. Advancements in technology have expanded their use in high-tech sectors like telecommunications and information transit. These glasses possess desirable properties such as mechanical strength, chemical resistance, and great thermal stability. As a result, the use of glass in various industries continues to grow in significance.

Phosphate glass materials are of keen interest in technological fields and are widely employed in various domains, including bioactive glass candidates [1–6], low temperature hermetic seals' materials [7–9], energy storage capacitors and optoelectronic devices [10–15], radioactive wastes' hosts , solid electrolytes [16,17], host glasses for solid-state lasers [18–21], etc. Moreover, a wide range of phosphate glasses were fabricated, via mixing network glass formers viz. SiO_2, P_2O_5, and intermediary/modifier oxides like Al_2O_3, K_2O, Na_2O, CaO, Fe_2O_3, MgO, TiO_2, ZnO, and others [22–24]. However, their susceptibility to alteration phenomena limits their effective utilization. Nevertheless, continuous efforts are being made to enhance their durability. According to the literature, the introduction of glass stabilizers has been commonly perceived to be the most appropriate mean [25]. The most prominent oxides that can improve the chemical durability of phosphate glasses are alkaline earths such as CaO, or alkali metal oxides such as K_2O, as well as intermediate oxides like Al_2O_3 [26,27].

Glasses carrying phosphorus and calcium in their composition form an interesting field of research based on the development of useful biomaterials for bone regeneration [28]. Numerous in vitro and in vivo studies revealed good biocompatibility of glasses when used in hard and soft tissue healing [29]. These glasses have valuable features explored as reinforcement phases for composite biomaterials and drug delivery systems. Their potential use was as fibers in tissue engineering, principally for any tissue with a medium to high anisotropy, such as muscles, and as dental restoratives, etc. [30,31].

However, the compositional variation that can be used for the binary glassy system CaO-P_2O_5 is limited. This system is hard to process due to high thermal expansion coefficients and exhibits excessive dissolution rates. Therefore, in order to develop more practical system, it is required to improve the complexity and use of ternary systems [32,33]. It was commonly perceived that CaO has a stabilizing impact on phosphate glasses because the divalent ions can generate ionic cross-links between the non-bridging oxygens of two distinct chains, so fortifying the glass network and adjusting material solubility [34,35]. While K_2O was extensively used as a glass flux

to diminish the working temperature, it also plays an essential part in setting the thermal expansion. Due to their network strengthening capabilities via their cross-linking action, Fe_2O_3 and TiO_2 has been claimed to have increased resistance to hydration [36]. To put it another way, TiO_2 affects the glass structure by forming Ti–O–P covalent link, which is thought to reinforce the glass structure while also narrowing water diffusion at the glass/ solution interface, limiting the pace of glass dissolution [37]. Also, joining Zinc, lead, and bismuth oxides with alkaline-earth elements can be utilized to give relatively good durability values. But they do not regularly match the specifications of phosphate glasses applications, so the most practical option is the synthesis of glasses with Al_2O_3 [38].

Indeed, Al_2O_3 was found to be considerably improving the physical and chemical properties of versatile glass systems by improving its aqueous durability [39,40], and chemical stability [39–42]. Bunker et al. [43]explained that through the substitution of alkali oxides by alkaline-earth oxides, the durability of (50-X)M_2O-XCaO-50P_2O_5 (M = Li, and Na) glasses is noticeably boosted. Peng et al. [44,45] looked at the favorable way to boost the chemical durability of the glass, also, the effects of Na_2O, K_2O, Al_2O_3… etc., in M_2O-MO-M_2O_3- P_2O_5 glasses (M_2O = Na_2O, K_2O, and Ag_2O; MO = BaO or PbO; M_2O_3 is either Fe_2O_3 or Al_2O_3), remarking that ionic cross-linking within non-bridging oxygen (NBOs) arranged by alkali and alkaline earth cations. So, improving the bond strength of this ionic cross-link is supposed to enhance chemical durability. While studying the properties of Al_2O_3 in phosphate glass. Researchers [39,40] discovered that the addition of Al_2O_3 in glass may significantly improve the chemical property of phosphate glass while also reinforcing the glass structure by forming P-O-Al [44]. They demonstrated that the modifier oxide affects the characteristics and structures of alumino-phosphate glasses through their research. They also observed that the enhancement of alumina concentration in alumino-phosphate glasses boosts durability [27].

In this study, we aim to investigate the structural, thermal, optical, and anticorrosive properties of novel glass systems with various compositions. So, we started by analyzing the 50P_2O_5-xCaO-(50-x)K_2O ternary glass system (with x= 0, 10, 20, 30, and 40 mol %). Then the upgraded quaternary glass system xAl_2O_3-(50-x)P_2O_5-10CaO-40K_2O (where x = 0, 10, 20, 30, and 40 mol%), where we kept the proportions of K_2O and CaO constant.

Thesis plan

This thesis is split into four chapters; ***The first chapter*** is devoted to a brief history and general concepts of glasses, structure, and physical properties, a bibliographic review of some Al_2O_3, CaO, and K_2O-based glass systems, and a synthetic reminder on corrosion and corrosion prevention methods, specifically corrosion inhibitors.

The second chapter discusses the experimental methods of preparation, spectroscopic techniques, physical measurements, characterization methods of the glassy phases, and all of the apparatus utilized in this study. The electrochemical methods utilized to examine the efficiency of the inhibitors and characterize the electrochemical behavior of the materials and surface analysis techniques are also highlighted.

The third chapter included investigations using X-ray diffraction, Differential Scanning Calorimetry (DSC), and Scanning Electron Microscopy (SEM) equipped with an EDX probe to control the glassy state and follow the compositions of the samples. As a result, we could identify the physical parameters of these glasses, such as the glass transition temperature, density, and molar volume. The leaching tests of the glasses were performed, the dissolution mechanisms were established, as well as the evolution of the chemical durability as a function of time and pH of the solution. In this chapter, we also explored the vibrational analysis of glassy materials using Fourier Transform Infrared Absorption Spectroscopy and Raman Scattering Spectroscopy. The findings help us better understand the effects of CaO and Al_2O_3 in the network of the examined glasses on the structural alterations caused by their integration. This research was required to assign vibration frequencies to the various structural entities and their linkages in the glass network. Optical measurements were likewise performed using Ultra-Violet-Visible-Proche Infrared spectroscopy (UV-Vis-PIR), and several optical characteristics were determined.

The fourth and last chapter will investigate the anticorrosive properties of glasses based on the Al_2O_3-CaO-K_2O-P_2O_5 system. The effect of inhibitor composition, concentration, and the temperature was investigated. Gravimetry, polarization curves, and electrochemical impedance spectroscopy were used to collect data. The inhibitor's adsorption phenomenon was investigated, and various adsorption isotherms (Langmuir, Temkin, and Frumkin...) were tried. SEM was used to examine the surface state, and the elemental analysis was performed by

combining it with a dispersive energy analysis (EDS) system.

Finally, a general conclusion gathers the most striking outcomes of this research endeavor, bringing this manuscript to a close while highlighting certain perspectives opened by this study.

CHAPTER I: State of the literature

I.1. Glass review of literature

I.1.1. A brief history of Glass

Glass is one of the many archaic materials known and operated by humankind. Before people comprehended making glasses, they had found naturally formed glasses, depicted in figure I.1, like obsidian, fulgurites, impactites, and tektites, and used these as arrowheads, knives, and primitive jewelry. The detailed history of the first synthetic Glass is not known. However, archaeologists found evidence confirming that around 3500 BC, ancient Egypt and Mesopotamia discovered glass formation [46]. Evidence indicates the presence of glass articles in coastal north Syria, Mesopotamia, and Ancient Egypt. Glass was first used in South Asia around 1730 BCE [47]. Also, they discovered glass evidence at Hastinapur and an archaeological site in Takshashila, both in ancient India. The Romanian Empire and the Anglo-Saxon period created glass artifacts for home, industrial, and religious settings usages. Glass development in China began late. Back then, glasses were constructed of barium oxide (BaO) and lead. Lead-barium glasses' use became obsolete after the end of the Han Dynasty. However, glass now plays a minor part in arts and crafts.

Figure I. 1. Obsidian (left) and fulgurite or lightning glass (right) images.

In the 14th century, the large-scale expansion of glass technology saw its beginning [48]. Architecture had proved the use of glass by the 15th century. All glass-related activity will be centered in Europe for the next 200 years. England had industrialized glass manufacturing by the end of the 17th century. Around the same period, Ravenscroft invented lead glass, a

mixture of silica, potash, and lead oxide. The development of this type of glass in the 18th century enabled the building of long-range telescopes, which are still commonly used today due to their radiation-shielding capabilities. In 1959 Pilkington Brothers pioneered glass sheets with consistent thickness and highly flat surfaces making a tremendous transformation in the architecture business. I. Angelini et al. gave a more detailed story about the evolution of vitreous materials throughout history [49].

Oxide glasses have caught the attention of academics and scientists in recent decades due to their remarkable features, which are particularly valuable in various fields. They are readily formed due to a lack of underlying crystalline structure. Glass is essential in multiple uses, including electronics [50]. This method also yields flat panel display glasses for television and computer screens. Thus, this archaic material plays a variety of roles in various fields, including photonics [51], biomedicine [52], radioactive waste storage [53], and many more, in addition to traditional ones such as windows, architecture, lenses, containers, and so on. Glass, formerly thought to be an optical, dielectric, or passivating material, is now being used to construct active devices such as switches, memory, sensors, solar cells, catalysts, etc. [54]. These extensive applications highlight glass's ever-increasing relevance in our current technology culture and industry.

Phosphate glasses have been used all around the world for over a century. They weren't found near volcanoes in streams like amorphous silica materials. The history of phosphate glasses is returned to the investigations of glass science's pioneer Otto Schotts (1851-1935) [55].

I.1.2. Definition of Glass

Over the years, various descriptions have been assumed and updated to highlight what glass is. According to Zachariasen, Tamann, and Greaves, a glass-like material corresponds to a non-crystallized solid state. Moreover, on the atomic scale, glasses are described by the lack of long-range periodicity in their crystal structures [56,57]. Also, the American Society for Testing Materials (ASTM) defined glass as an inorganic product of fusion that has cooled to a rigid condition without crystallization. Several materials, such as organic polymers and metal alloys, also have non-crystalline structures, but not all are glasses [58].

Nowadays, the most adopted definition is the one given by Zarzycki, which is that glass is a non-crystalline material that displays the glassy transition phenomenon [59]. Another explanation given by Haase, Scholze, and Simon is to create an amorphous solid. The liquid must be cooled quickly enough or have a too-high viscosity, preventing crystallization at the melting point and

allowing the liquid to remain in its liquid state. Consequently, a specific volume and enthalpy discontinuity is seen at a characteristic temperature known as glass transition temperature T_g.

I.1.3. Glass Transition Phenomenon

Due to the complexity of the glass transition process, numerous theories have been put forth based on different characteristics of the glasses. Since any glassy substance must have the glass transition as a necessary property, and it depends on numerous factors, including heat capacity, thermal conductivity, melting temperature, cooling pace, etc., these theories have largely fallen short of expectations. Depending on the technique utilized for its measurement, a sizable variance in the value of glass transition temperature (T_g) has also been noted. This is because distinct degrees of freedom are arrested when a melt is quenched to form a glass, but these degrees of freedom start to relax during heating. These degrees of freedom, which correlate to various attributes, are employed. As a result of the varied rates at which these multiple degrees of freedom are associated with the different characteristics used to calculate T_g relaxation, various values of T_g are measured [60].

Experimentally, we can use DTA or DSC (thermal differential analysis) to determine the glass transition temperature. The schematic thermogram of a glass sample's heat capacity C_p is shown in figure I.2 the temperature T_g (an endothermic phenomenon), we can also see the temperature at which crystallization begins (T_x), the temperature at which it reaches its maximum (T_p), and the temperature at which it fuses (T_f) (endothermic phenomenon) [60]. T_g is the intersection of the baseline with the inflection tangent of the glass transition domain. T_x is the baseline intersection with the crystallization peak's inflection tangent. Also, T_p is the crystallization peak's maximal point.

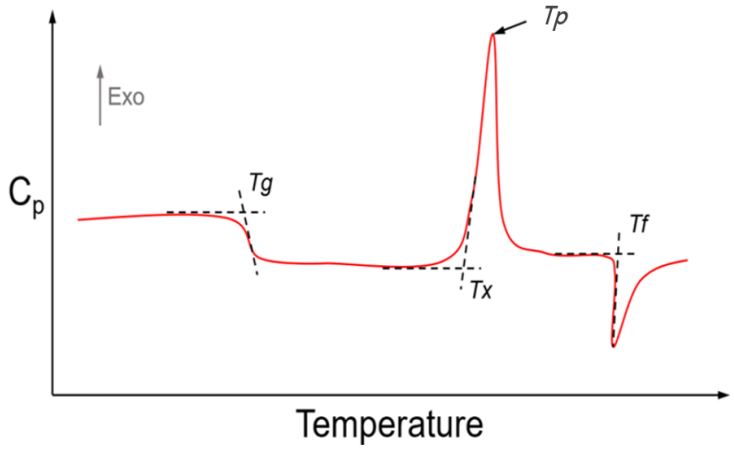

Figure I. 2. Thermogram of the heat capacity (Cp) as a function of the temperature of a glass sample.

I.1.4. Glass formation

While a long-range disordered atomic network is simple to understand, the idea of a material undergoing a time-dependent glass transformation is more challenging to grasp. Using an enthalpy (or volume) as a function of the temperature diagram, as displayed in figure I.3.a, the methodology of cooling a material from its molten condition takes a predictable course after the melting point is reached (T_m). Which is called the melting temperature, where the Gibbs free energy of the solid-state equals the Gibbs free energy of the liquid phase, as illustrated in figure I.3.b and mentioned in the following equation:

$$\Delta G = G^S - G^L = 0 \ ^{61}$$

The solidification process through a fantastic arrangement of atoms (or molecules) results in a crystal lattice with a dramatic drop in enthalpy because the new crystalline configuration has substantially lower internal energy than its liquid predecessor. Atoms align perfectly in an organized manner in quest of the material's lowest energy state. Lowering the temperature while exceeding the melting point creates the main driving force for solidification ($G>0$). The supercooled liquid phenomenon is when a liquid remains in its state at temperatures below the melting point when subjected to sufficient cooling rates. While dropping the temperature, the viscosity of the fluid rises fast until the atoms lack the requisite mobility to rearrange into their equilibrium condition (crystalline structure) and remain "frozen" in a metastable state, forming a glass [62]. Glasses are thus solid structures distant from their equilibrium configuration, whereas the molten state "freezes" into a reliable system rather than crystallizing.

Figure I.3.a depicts the time-dependent glass modification procedure as the temperature area where enthalpy gently drops from its liquid-state level to that appropriate to the solid state, rather than a sudden decrease, where the crystalline transformation would occur. With the cooling rate, the treated liquid determines (along with other elements) the viscosity variation and, thus, the frozen state instant is achievable. This process is time-dependent.

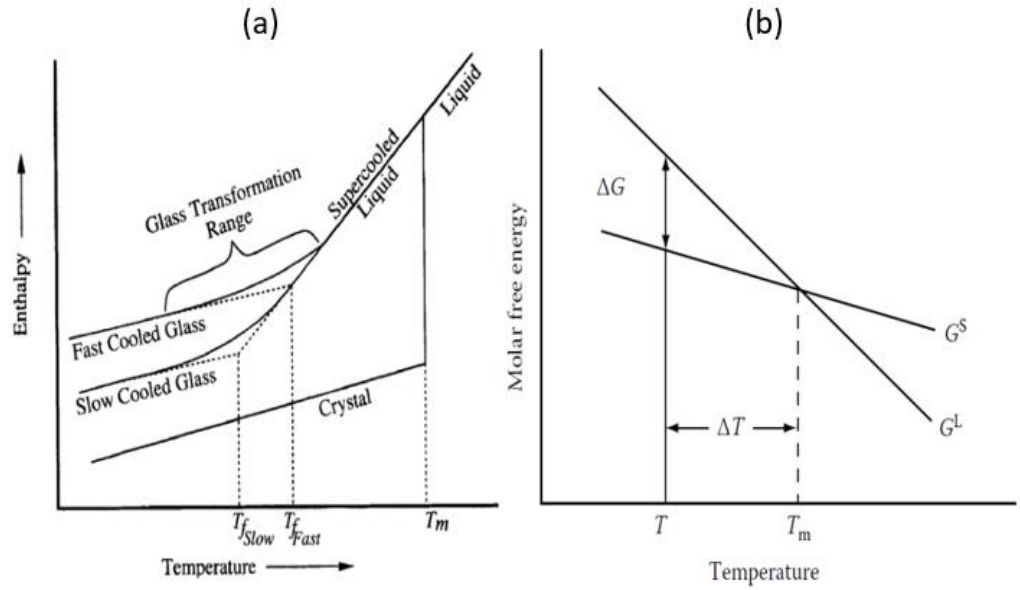

Figure I. 3. (a) Enthalpy plotted versus temperature diagram illustrating the different solidification paths of a standard glass [16] and (b) Gibbs free energy graph of a material's solid and liquid phases as a function of temperature [15].

Hruby [63] characterized the tendency of a material to assemble glass by establishing a parameter K_g, which includes the T_g, T_M, and crystallization temperature (T_c) as follows:

$$K_g = \frac{T_c - T_g}{T_m - T_c}$$

If (T_c-T_g) is tremendous and (T_m-T_c) comes up short, nucleation and crystallization are strongly inhibited, and the system's glass-forming tendency is high. T_g is described in terms of the experimental time scale as the temperature at which a liquid achieves stable viscosity.

I.1.5. Classification of the preparation method of glasses

The most common glass-creation methods are melt-quench, sol-gel, and chemical vapor deposition.

I.1.5.1. Melt-quenching technique.

The melt-quench technique was the first to be established for glass fabrication. The inorganic raw materials are precisely weighed as per composition in the melt-quench process.

The well-mixed and dried components are placed in a premium alumina or platinum crucible and melted in a temperature-controlled furnace. The raw components are then homogenized in a mortar with a pestle or ball mill in an acetone medium.

The homogenized molten is quenched in a mold. The melt-quench process is used to create the glass in this approach. By annealing, the synthesized glasses at comparatively low temperatures to the glass casting temperature, the residual internal tensions caused by the temperature gradient during forming and subsequent cooling are considered withdrawn [64]. The melt quench technique yields more extensive materials than single-crystal or polycrystalline ceramics. It also has the advantage of providing greater compositional flexibility than chemical vapor deposition or the sol-gel process. This strategy has certain drawbacks as well. This approach, for example, is inappropriate for creating ultra-pure glasses used in optical communication systems. This procedure adds certain impurities from the crucible or furnace materials to the glass. Due to the requirement for exceptionally high temperatures, glasses including refractory elements such as SiO_2, TiO_2, Al_2O_3, and ZrO_2 are hard to manufacture with this process.

I.1.5.2. Glass by sol-gel method

Using the sol-gel process, raw components' colloidal solution (sol) is transformed into a gelatinous product (gel). There is no need for melting or quenching in this process. Fine-grained gel bulks made up of diverse organic compounds are annealed at a specific temperature before being sintered at a higher temperature than the annealing temperature. Two processes are currently happening during this procedure: hydrolysis and condensation [65].

I.1.5.3. Glass by a chemical vapor deposition method

In the early 1940s, the chemical vapor deposition (CVD) process for creating glasses was invented. Following the production of the glass material, the original metal halide vapor is thermally activated via homogenous oxidation or hydrolysis. An oxy-hydrogen flame or oxygen plasma initiates the oxidation or hydrolysis reaction. The initial elements in this technique are liquid at ambient temperature. They have a shallow boiling temperature compared to alkaline halides, earth, transition metals, or rare-earth elements. Raw materials are purified by distilling them repeatedly under their melting points. This approach helps produce ultra-high purity glasses [65].

I.1.6. The theories of glass structure

Until the 20th century, Goldschmidt and Zachariasen revealed the conceptual underpinnings of the science connecting the glass structure to its formation. So, the main theories have been intensively revised and improved over time.

Starting with Goldschmidt, in 1926 [66], formed a hypothesis revealing that most oxides with a

radius ratio of R_c/R_o in the range of 0.2-0.4 will form a glass. (R_c is the radius of the cation, and R_o is the radius of the anion.). However, Goldschmidt's theory was quickly superseded by Zachariasen's more comprehensive approach in 1932 [56].

Zachariasen's outlined rules to create glass are [67]:

1. No more than two cations may be connected to an oxygen atom.
2. The number of cations coordinated is low: 3 or 4.
3. Oxygen polyhedral Share corners, no edges or faces.
4. At least three corners must be shared in 3D networks.

In general, all four rules should be satisfied for glass formation to occur. Low coordination numbers and corner-sharing rules imply that glass formation is more likely with open, low-density polyhedral structures. The Zachariasen-Warren network theory was created in 1933 to enrich Zachariasen's rules. According to the theory, it must first produce tiny polyhedral building blocks for an oxide or compound to transform into glass. There can only be one point (a corner, not a face or an edge) at which a polyhedral unit can be joined to another. The short-range order of glasses is interconnected to the idea of a 3-dimensional network made up of tiny polyhedral building blocks. This theory includes other elements serving as anions in a network, such as Fluorine and Sulphur, stating that they are the ones connecting neighboring polyhedral blocks and, as a result, binding to no more than two cations, even though Oxygen is the most prevalent anion in glasses (central atoms of the polyhedron).

According to the Zachariasen-Warren network theory, a polyhedron can have a maximum of six corners, at least three of which must be connected to other polyhedral units. The tetrahedron built-in silica glasses, as shown in figure I.4.a, illustrate a building block. In Figure I.4.b, the 3-dimensional network of units is represented in two dimensions: the silicon atom in the block's center and oxygen atoms at its corners [68]. Figure I.4.c disrupts the glassy matrix by adding network modifiers such as Na_2O [69].

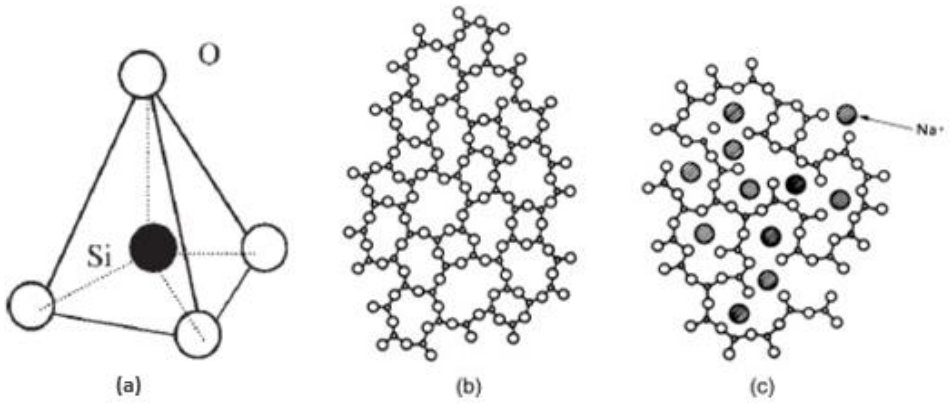

Figure I. 4. Basic building block found in silica glasses is shown in (a). Pure silica glassy network as at (b). The network is broken up by adding modifiers, like Na_2O, interrupting the network as at (c).

The theory of Zachariasen categories the significance of cations within the structure by:

- Network formers include Si, P, Ge, As, B, etc. They can create the glass network outlined building blocks with a coordination number of 3 or 4 (SiO_2, P_2O_5, GeO_2, As_2O_3, etc.).

- Network modifiers, instead of Network-formers, play a destructive role in the network by breaking the bridges connecting the unit blocks to generate oxides and diminishing the connection of the chains. Their coordination number is 6, e.g., Na_2O, K_2O, CaO, Li_2O, etc. For instance, the glass network shown in figure II.4.c is illustrated after adding Na atoms.

- Intermediates are characterized by their ability to connect with the fundamental glass matrix to maintain structural continuity. They cannot create glass independently, but they may be capable of substituting some Network-former cations in the system. When having a coordination number 4, these cations strengthen the network, even though they break it when their coordination number is ≥ 6, identically to the Network modifiers. E.g: Al_2O_3, ZrO_2, TiO_2, PbO, ZnO, etc. [69].

An X-ray diffraction pattern illustrates how a crystal and a glass differ structurally. Bragg peaks representing an organized distribution of atoms in the three directions of space will identify the crystal. We may "resolve the structure," that is, figure out where the atoms are about one another inside the elementary lattice—by looking at the location and intensity of these peaks. The unit cell, or the smallest organized structural entity holding all the atoms of a compound, is defined as the smallest region of space in which an integer number Z of crystal units is inscribed. The simple unit's infinite repetition introduces the concept of order at a long distance in the three spatial directions.

The basic meaning of a diffraction halo, which is the loss of order at long distances but the

existence of some order at short distances, is the loss of order at long distances in the case of a glass, where the imprint of X-ray diffraction is presented (figure I.5).

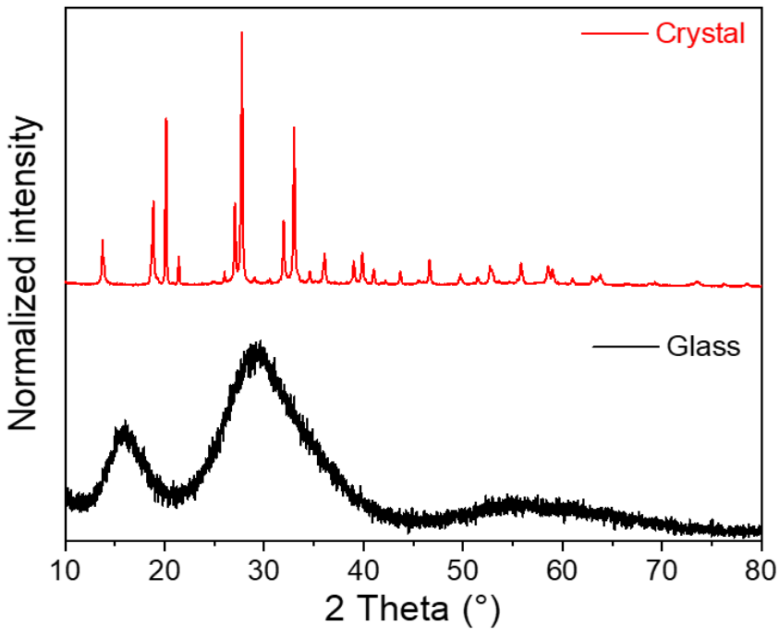

Figure I. 5. Diffractogram of a glassy structure (black curve) and the corresponding crystallized compound (red curve).

I.1.7. Classification of glasses

I.1.7.1. Natural glasses

Glass variants were already present in nature before man. There are two kinds of natural glass: glass with a mineral origin and glass from living things.

I.1.7.1.1. Mineral glasses

Since the Apollo missions, a new area of research devoted to the lunar ones has emerged in addition to the geological glasses, which were the focus of most research concerning the glasses of mineral origin.

I.1.7.1.2. Geological glasses

Geological glasses cover a wide composition range. The simplest is the almost pure SiO_2 of fulgurites and Libyan Desert glass, produced by the melting of quartz sand by lightning and the impact or explosion of extraterrestrial bodies, respectively. Tektites have also been produced by extraterrestrial sources but have compositions similar to those of their igneous rock source. By far, the most common glasses are produced by the cooling of magma. The best known are the SiO_2-rich obsidians, extensively used and traded over long distances in Prehistory because of their outstanding properties resulting from their fully amorphous nature [70].

I.1.7.1.3. Lunar glasses

Since there is no water on the Moon, the magmas are viscous, which encourages glass creation. Thus, many glassy rocks have evolved in the lunar soil from the primordial lunar rocks due to

multiple collisions from meteorites and volcanic ash [71]. This twofold metamorphosis could be highlighted thanks to the lunar glass fragments that the Apollo expeditions brought back, which were the subject of several laboratory studies.

I.1.7.1.4. Biochemical glasses

Glasses seen in nature are primarily made of silica. Diatomite shells and sponge and mollusk skeletons are two examples of the silica that is thought to be dumped on the ocean floor each year in quantities of several gigatons [72].

I.1.7.2. Artificial glasses

Even though a vast range of chemicals can form glasses, few have gained practical significance. We separate several large groups based on their application field.

I.1.7.2.1. Oxide glasses

Oxide glass family applications receive the most responses [59]. Nowadays, they count for more than 90% of the glasses made. Due to the inexpensive cost of raw materials and the moderate production temperature, this family naturally tends to dominate over time. Oxide glasses come in a variety of varieties.

a. Single oxide glass system

- SiO_2: Because of their ubiquity in nature, silicates have been extensively researched. They were viewed as a conventional network-forming oxide in both crystals and glasses on account of silicon's great affinity for Oxygen, and the fact that the structural unit of silica is tetrahedral, with silicon coordinated four times by Oxygen ($[SiO_4]^{4-}$ depicted in figure I.6). The tetrahedron serves as the fundamental unit. One mono silicate is cross-connected with its neighbors to form a network. Silica glass is scientifically relevant due to its outstanding resistance to chemical agents and low coefficient of expansion ($0.5x10^{-6}$), providing exceptional thermal shock resistance.

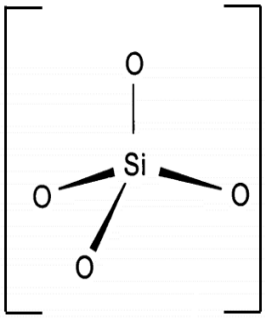

Figure I. 6. Monosilicate structure $[SiO_4]^{4-}$.

- B_2O_3: Boric anhydride is an easily vitrifiable oxide. Obtaining its crystallized form is very difficult. The glass structure of B_2O_3 is an incomplete stacking of boroxol rings with trichlorinated boron (BO_3). Due to its hygroscopic nature, B_2O_3 is never utilized alone in practice. It is part of the composition of many industrial glasses.

- P_2O_5: The $[PO_4]^{3-}$ tetrahedron in figure I.7 is the unit structure in all P_2O_5-based glasses, and it is coupled to form a three-dimensional network, like mica glasses. Chain structures are formed when alkali ions are incorporated into a three-dimensional network. Compared to SiO_2 in vitreous form, P_2O_5 in glassy form is extremely difficult to obtain because P_2O_5 is extraordinarily hygroscopic and volatile.

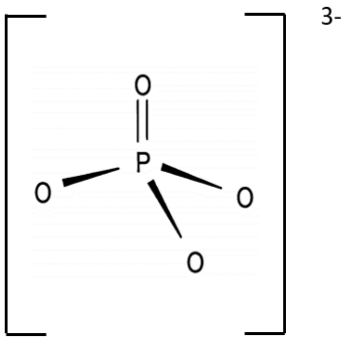

Figure I. 7. Phosphate tetrahedron unit $[PO_4]^{3-}$.

b. Multi-formers glasses

Binary glasses SiO_2-B_2O_3, SiO_2-GeO_2, and SiO_2-TiO_2 have been synthesized via direct fusing or vapor-phase hydrolysis [73]. These glasses were developed for optical conductors (photonics), where hyper-pure glasses with refractive indexes similar to vitreous silica are required. Because some glasses in the SiO_2-TiO_2 family have a coefficient of expansion near zero, they can be used to make rigid and thermally stable telescope mirrors. The structure of these glasses is still entirely unknown; in particular, it is not clear whether mixed chains of the type Si-O-Ti-O-Si form or micro-domains richer in one of the components form.

c. Glasses assembled from formers and other oxides

This category contains many visual oxide lenses. The addition of different oxides allows for significant modification of the characteristics of the various glasses. Phosphate glasses are one example [74–77].

I.1.7.2.2. Fluoride glasses

The network's highest natural frequency of molecular vibrations determines the spectral limit of glass transparency on the infrared spectrum. This natural frequency is reduced as the ions present get heavier and less charged. The field of glasses in which fluorine replaced Oxygen has been investigated to generate infrared transmission optical fibers. A series of fluorinated glasses with formers of zirconium fluoride ZrF_4, AlF_3, GaF_2, and InF_3 were produced and examined in 1975 [78].

I.1.7.2.3. Chalcogenide glasses

When group VI elements (S, Se, Te) are mixed with one or more group IV (Ge, Si) or V (Sb, As) elements or halogens, they produce glasses, the resulting glasses are called chalcogenides, in the 1960s, these glasses were very successful when a transition between two states of low and high electrical conduction was observed [79].

I.1.7.2.4. Amorphous metals

Amorphous metals or metallic glasses generated by ultra-rapid quenching of liquid alloys have long piqued scientific attention. Some of these are currently being made industrially, for example, Ni-Fe-P-Al-B. Their structure is fundamentally disordered compact. They have intriguing mechanical properties [80,81].

I.1.8. Glass systems

Throughout history, numerous types of glasses have been invented. The phrase glass system was coined to identify and arrange them. Oxide glasses are the most frequently investigated systems; they include several glass families, such as borate, silicate, germanate, and phosphate. The backbone comprises B_2O_5, SiO_2, GeO_2, P_2O_5, etc. The network formers in chalcogenide glasses are S, Se, and Te, which can be coupled with Ge, As, and Sb to produce amorphous materials with fascinating optical characteristics ideal for several applications, such as IR applications.

Fluoride glasses are popular among halide, and oxy-halide glasses have the most outstanding exponent. These materials have been researched for transoceanic optical fiber waveguides and many other things because of their transparency range, low optical losses, and durability [82]. The following section summarizes several oxide glasses' various structural characteristics and qualities.

I.1.8.1. Silica glass system

In recent years silica glass system has received incredible attention. Silica's applications span from lenses to optical glass fibers. By introducing levels of network modifiers, and intermediates and managing the number of impurities in the structure, the material qualities can be adjusted to demonstrate high thermal shock resistance, purity, and mechanical strength. Silica glass has outstanding optical transparency from ultraviolet to near-infrared areas and chemical and thermal resistance [62], [82]. On the other hand, notable downsides include its excessive melting point and poor rare-earth solubility, particularly in comparison to different oxide glasses, including the phosphate family [83].

Tetrahedral 6-coordinated 4 oxygen atoms constitute amorphous silicate. 6-coordinated silicon groups have likewise been identified in a handful of crystalline materials [84]. Silicate systems take the form of orthosilicate structural units, orthosilicate units, Si-O stretching vibrations of tetrahedral silicate units, symmetric stretching vibrations of silicate tetrahedra, inter-tetrahedral Si-O-Si bonds, and structural unit Q^n_{sin} (n = 0 to 4), where Q_{Si} symbolizes the tetrahedral unit and n is the number of bridging oxygens (BO) [85–87].

I.1.8.2. Borate glass system

Borate glasses are essential in various applications, including thin amorphous films for battery applications, bioactive glasses for tissue engineering, nuclear waste disposal, photonic applications, the invention of infinitely adjustable or shorter pulse lasers, optical fiber amplifiers, and fiber lasers [88–91].

Under ordinary circumstances, pure Borate glasses are challenging to create because they contain no moisture [92]. Water-free Borate glasses are made by melting orthoboric acid at a pressure of 1 mm Hg over many hours. Structural investigations on pure borate glasses indicated that the structure agrees perfectly with the Krogh-Moe description [93]. Following this, the significant component of B_2O_3 glasses is boroxol rings. Krogh-Moe's study suggested the existence of five distinct varieties of borate molecules in the glass structure.

The borate matrix includes the vibrations of isolated diborate ($B_4O_7^{2-}$) groups, breathing of O^- atoms, loose diborate vibrations, chain or ring type meta- and pentaborate ($B_5O_8^-$) groups, symmetric breathing vibrations of six-member borate rings with one or two BO_3 triangles replaced by a (BO_4^-) tetrahedral, symmetric breathing vibrations of boroxol rings, triborate ($B_3O_5^-$), tetra-borate ($B_8O_{13}^{2-}$), ortho-borate (BO_3^{3-}), pyroborate ($B_2O_5^{4-}$) groups and linked $[BO_3]^{3-}$ triangles with one free vertex [94,95].

I.1.8.3. Phosphate glass system

Even though P_2O_5 is one of the classic glass-producing oxides, along with the ones stated above, the nature of the glass, its applications, and research and development have been limited due to its hygroscopic nature. It was only when the addition of at least 30% metal oxides was discovered to considerably improve the durability of the glass that potential applications were aggressively pursued [96].

Phosphate glasses' properties are dictated by their structures, which are dictated mainly through the chemistry, concentration, and coordination environments of metal oxides introduced to the glasses and their impact on the ensuing phosphate chain length dispersion [97–99].

I.1.8.3.1. Phosphate glass structure

Phosphate-based glass relates to phosphorous glass former. The basic polyhedrons that make up the structure of phosphate glasses have been revealed as tetrahedron blocks that can connect to produce P_n units; phosphate anions containing n tetrahedra generate polymer-like chains or rings. As in silicate glasses, the former glass cation is encircled by four oxygens (PO_4) [100]. Because of phosphorous' pentavalent (P^{+5}), a tetrahedron with four bridging oxygens would generate a positively charged block, which is avoided if one of the anions (Oxygens) forms a double bond with the center atom, O = P [62,101]. As shown in figure I.8, the essential block constructing the network in phosphate glasses is linked to three nearby tetrahedra (3 bridging oxygens).

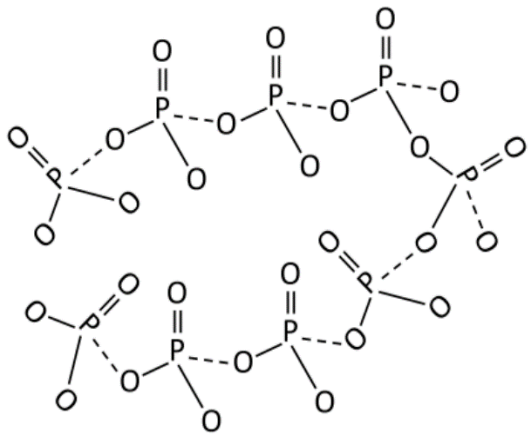

Figure I. 8. PO_4 tetrahedra creates the phosphate glass network.

Q^i notation is used to classify the phosphate glass tetrahedron. The phosphate atom is represented by "Q," and "i" reflects the number of bridging oxygen atoms sharing the corner of adjacent phosphate tetrahedra ranging from zero to three, as seen in figure I.9 [102], well with Q^3 unit with the highest predominant form of block in the amorphous P_2O_5.

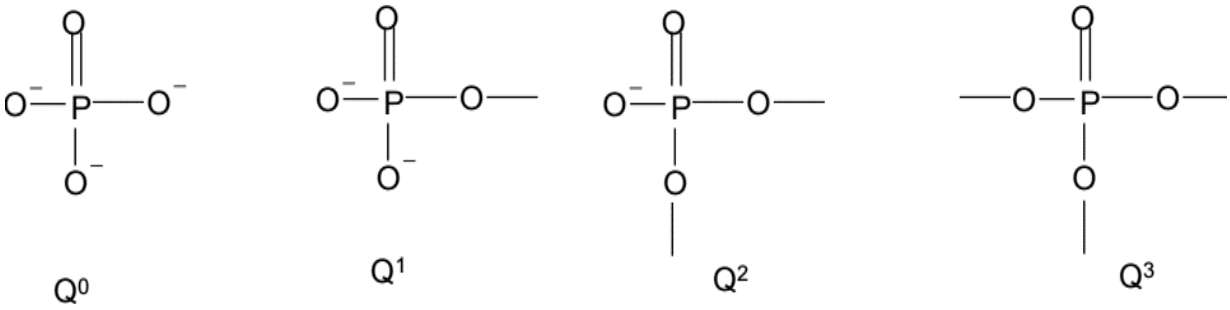

Figure I. 9. Q^n building blocks in phosphate glasses.

The glass composition's cation ratio determines the prevalence of any specific Q species. If a cation balances the charge on an oxygen atom, oxygen bridging cannot occur [103]. When phosphorus pentoxide is heated without cation inputs, the Q^3 molecule is the leading phosphate group, generating a strongly cross-linked phosphate system. The insertion of metal cations, such that $[M_2O] = [P_2O_5]$ where M is any monovalent cation, such as Na^+, K^+, or Li^+, results in non-branched phosphate chains of potentially limitless length [104]. Again, when the metaphosphate composition (O/P = 3) is attained, most building blocks will be in the Q^2 configuration, generating rather 2-dimensional chains or ring-shaped structures. Each extra M_2O (O/P >3) produces terminated Q^1 species. Reducing the technically feasible chain length [105]. Whenever the concentration of M_2O is double that of P_2O_5, the terminating Q^1 species predominates. Because this anion can only build one oxygen bridge, it is known as a chain terminator, creating either phosphate dimers or pyrophosphates when it is the only species involved [104]. Whenever the concentration of M_2O is at least three times greater than that of P_2O_5, the non-bridging Q^0 blocks, also known as orthophosphate, take over, obtaining greater depolymerization values till the glass can no longer be formed [102,106].

Polymerization of phosphates occurs in the absence of a low concentration of metallic cations. However, adding higher numbers of metal cations results in the inhibition of phosphate polymerization. This occurs as the number of bridging oxygens available per phosphate anion decreases [105]. Therefore, the system is called ultra-phosphate whenever the O/P ratio is <3. When O/P =3 metaphosphate, and at higher ratios O/P >3, the glass is named polyphosphate.

I.1.8.3.2. Phosphate glass solubility

It should be noted that contamination with water is a problem when making phosphate glasses. One of the most significant disadvantages of phosphate glasses is their propensity to hydrolyze and dissolve quickly in aqueous environments. Water is similar to alkali oxide as it reduces

polymerization by forming hydroxyl groups [107]. It should be noted that the inclusion of intermediate oxides like B_2O_3 and Al_2O_3 has been observed to lower the glass's water solubility [108]. The reaction of phosphate glasses with water molecules can take two forms:

- The first, known as the Hydration reaction, occurs when an ion exchange places with a hydrogen atom, producing a hydrated layer, as depicted in figure I.10. a.
- Next is network breakdown, in which the glass network is damaged, releasing phosphate chains from the structure to enter the media [109], as seen in figure I.10.b.

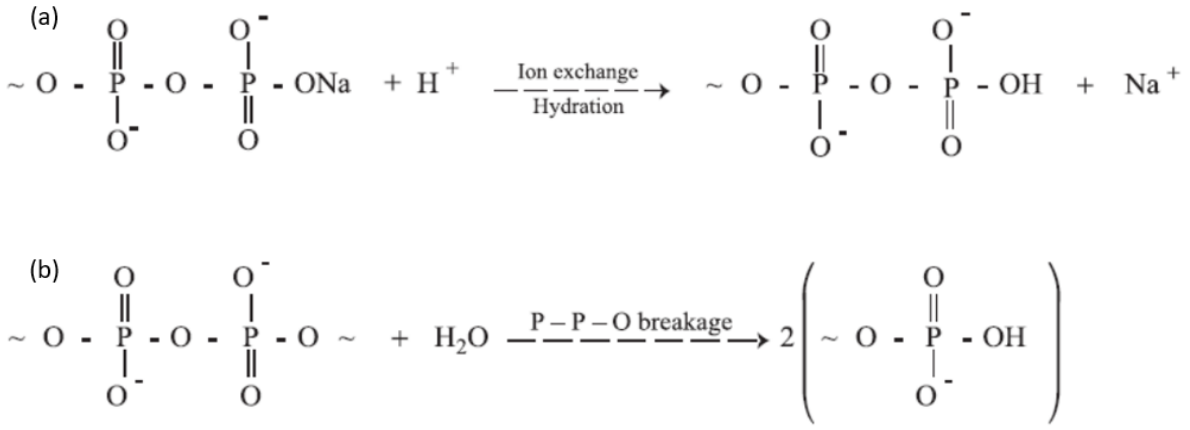

Figure I. 10. Phosphate glasses' dissolution. (a) Hydration reaction (b) Network breakage.

The addition of oxide modifiers to the glass composition results in non-bridging oxygens, each placed adjacent to an alkali ion, to maintain local charge neutrality. On the other hand, network modifiers typically diffuse in the interstitial space of network chains, reducing the glass's free volume [62].

According to Bunker et al. [43], the Na-H ion exchange reaction determines the phosphate glass dissolution kinetics, in which it dissolves evenly, and the composition of dissolution products in the solution is identical to the bulk glass. In contrast, Liu et al. [110] proposed that phosphate glass dissolving is controlled by phosphate glass network breakage, with the Na-H ion exchange mechanism restricted to hydrating the glass surface and establishing the mechanism of phosphate system fracture.

I.1.8.3.3. Phosphate glasses' applications

Because of its advantageous physical features, such as tunable chemical durability in aqueous environments, high thermal expansion coefficient, and moderate melting and handling

temperatures, phosphate glasses have been investigated and exploited for several applications [43,111]. The qualities and applications of phosphate glasses differ greatly depending on their composition.

Biodegradable phosphate glasses are operated for bone scaffold renewal, glass fibers for antibacterial or trace element delivery systems, and muscle rejuvenation for hard and soft tissue repair [112–114]. Phosphate glass fibers also strengthen biodegradable implants[115]. Copper and silver introduction to phosphate glasses has improved local infection treatment [116,117]. Phosphate glass fibers containing Al_2O_3 and Fe_2O_3 are employed as cell guides and reinforcing materials for skeletal muscle regeneration. They have been shown to create myotubes through which muscle fibers can grow [118,119].

Because of their low absorption at specific frequencies, phosphate glasses possessing fluoride and doped with rare earth ions have displayed considerable promise for optical and laser applications [120–124]. Due to their inadequate melting temperature, low viscosity, and high thermal expansion coefficients, phosphate glasses are also appealing as glass-metal seals [125]. The inability of some phosphate glasses to last was operated to generate a treatment for trace element deficits in cattle and sheep [126–128].

Amorphous alkali aluminophosphate with glass transition temperatures beneath 400 °C has been created for specialty hermetic seals because of their high thermal expansion coefficients [129]. Incorporating alkali ions (e.g., K^+, Li^+, and Na^+) in phosphate glass is impressive for ion conduction applications. The structural properties of lithium iron phosphate glasses with nano-crystalline phases make them appealing as cathode materials for rechargeable batteries [130,131]. Because of their low optical dispersion and relatively high refractive indices, phosphate glasses have good chemical endurance as host matrices for rare-earth ions and transition metal ions in optical devices [129,132,133].

Phosphate glasses containing transition metals or rare-earth ions also have fascinating semiconducting, magneto-optical, and magnetic transition features that can be applied to construct and implement spin glasses, optical isolators, and optical switches [134–137]. Phosphate glasses containing divalent iron cations exhibit an efficient transmittance in the visible range (400700 nm). Nevertheless, they also have a significant Faraday effect due to charge transfer transitions from O^{2-} to Fe^{2+} in the near-ultraviolet to the blue range, which is suitable for emission from blue laser diodes [137].

I.1.9. Chemical durability of phosphate glasses

Glass is an inert material analogized to other materials; specific varieties of glass exhibit good corrosion resistance.

Researchers have always concentrated on glasses' aqueous dissolving behavior when discussing the chemical durability of phosphate glasses. This has been a recurring theme while examining their characteristics. It is still a long-standing concern that must be addressed throughout the design of new compositions for any application. The origin of their dissolution ease is due to the hygroscopic character of the phosphate units constituting the glass network, particularly to protonated species. It is most likely related to the high stability of phosphate compounds in solution [138]. While most people seek the best chemical durability, there are some industries where the dissolving rate of the glasses must be strictly controlled.

Nevertheless, it is crucial to acknowledge that all glass products are chemically reactive in solution. Diverse reactions occur depending on the attack medium. Many researchers have examined glass reactivity in acidic [139–142], neutral [142–145], and basic media [146–148].

I.1.9.1. Glass corrosion overviews

I.1.9.1.1. Corrosion methods

Interaction between a solid and a changing solution causes dissolution, breaking down into several mechanical or chemical stages. Each process requires the same sequence of essential reaction stages, which are as follows [142,143]:

1- Reactive species transport from solution to the solid surface
2- Reagents adsorption on the surface
3- Chemical reaction on the surface between the reagents and the solid
4- Reaction product desorption
5- The evacuation of the products from the surface of the solid to the solution

Phases 1 and 5 represent species transport, and from 2 to 4 exhibit surface phenomena phases. The first group relates to Fick's law which is a regulated diffusion process, viz, inter-diffusion between protons in solution and ions in the glass. A $t^{1/2}$ law governs the evolution of the concentration of solubilized mobile ions from the surface as a function of time t [144]. The second category includes surface reaction processes that can be characterized using transition state theory or the Grambnow model [148]. It is worth noting that for most glasses, the kinetically limiting step affecting the process's speed corresponds to surface reactions.

Surface reactions during corrosion produce surface layers, the production of which is related to the nature of the dissolution [43]. When directly related to the composition, all glass elements flow through the solution simultaneously. It is said to be congruent. On the other hand, if there is a selective transit of constituents of the glass into the changing solution via an ionic exchange mechanism, this dissolution is widespread for silicate glasses (rigid network). Finally, it is non-

congruent if the element ratios in the solution deviate from those in the glass.

These factors are closely related to the dissolution reaction stoichiometry. Also, the fate of the corrosion products in the liquid phase (referred to as leachate) can lead to variations in saturation concentrations, inducing precipitations and re-deposition, thus potentially modifying the surface layer and, thus, the glass/solution interface. The media pH heads the modalities of dissolution [145]. Sodosilicate glass dissolving in an acidic solution occurs in two steps:

- Dealkalization by an alkali ion exchange from the glass with an H^+ proton from the solution
- Glass matrix dissolution of a broken bond, such as by the action of a hydroxyl ion generated during the dealkalization.

In a neutral or basic solution, hydrolysis occurs by the breakdown of network linkages caused by the action of the hydroxyl ion OH^-.

I.1.9.1.2. Corrosion kinetics

The kinetics of a dissolving procedure in a secured system, controlled by its limiting step, is represented as follows [142,143]:

$$\boldsymbol{V_i = \frac{dC_i}{dt} = k_{ri} \cdot \left(\frac{S}{V}\right) \cdot (C_{si} - C_i)\alpha_i}$$

Where:

$\boldsymbol{V_i}$**:** the dissolution rate of the considered glass oxide i;

$\boldsymbol{C_i}$ and $\boldsymbol{C_{si}}$: represent, respectively, the mass concentration and the saturation concentration of ***i***;

S: solid/liquid contact surface;

V: the solution volume;

$\boldsymbol{k_{ri}}$ and $\boldsymbol{\alpha_i}$: denote the constant and partial reaction order of i, respectively.

Throughout the surface reactions limitation case, k_{ri} and α_i can be zero, resulting in linear concentration fluctuations over time. This formulation can represent the species transport steps. However, the kinetic constants correspond to mass transfer coefficients with essentially unitary order, meaning transient exponential-like evolutions.

The previous relation integration, resulting in the variation of C_i as a function of time for a specific dissolution process:

$$\boldsymbol{C_i = k_{ci}.\ (S/V)\ .t^{ni}\ et\ (\Delta m_i/S) = k_{ci}\ .t^{ni}}$$

Where:

Δm : i weight loss in solution ;

k_{ci}: Partial kinetic constant;

n_i: Reaction order.

When we consider a congruent dissolution, we get:

$$(\Delta m/S) = \sum_i (\Delta m_i/S) \text{ et } K = \sum_i (kci \, . \, fi)$$

With:

Δm : Total mass loss of the material in solution ;

K: Overall kinetic constant;

f_i: Mass fraction of i in the glass.

When considering selective dissolution, all processes must be included, and the experimentally described normalized mass loss becomes:

$$(\Delta m/S) = k_1 \, . \, t^{1/2} + k_2 \, . \, t^1 + k_3 . \, T^x + \ldots + k_j \, . t^y$$

Most glasses' corrosion kinetics may be described using only the first two terms. The first represents a diffusional stage, whereas the second represents the disintegration of the glass network itself. The terms listed below are associated with the remaining processes. The constants ki are sensitive to the S/V ratio, namely the behavior of the concentrations of the glass constituents in solution, and are systematically affected by pH and dissolving temperature.

To analyze the dissolution processes of glass most successfully experimentally, one must do the following:

- The corrosion profiles correspond to the glass weight losses per unit area and the dissolved species in the weathering solution with time.
- The pH development of the weathering solution.
- The nature and content of the eroded glass surface, all at various altering solution temperatures.

This procedure provides access to the initial dissolution speed, the corrosion modes (congruent, non-congruent, or selective), the dissolving mechanisms (hydration, hydrolysis), and the kinetic processes involved (diffusion, activation of the dissolution E_a described by the relation:

$$\boldsymbol{LnV = \frac{E_a}{RT} + B}$$

Where: $\boldsymbol{V}$: initial dissolution rate; $\boldsymbol{E_a}$: activation energy; $\boldsymbol{R}$: ideal gas constant; $\boldsymbol{T}$: temperature; and $\boldsymbol{B}$: constant.

I.1.9.1.3. Phosphate glasses corrosion mechanisms

a. Corrosion in neutral medium

Phosphate glass corrosion in a neutral environment was well explained previously in the "I.1.9.3.2. Phosphate glass solubility" paragraph.

b. Corrosion in an acidic medium

Dissolution occurs faster in an acidic pH solution at a greater temperature than at room temperature. Indeed, in the case of an acidic solution, dissolution increases while remaining congruent. The increasing temperature of the changing solution promotes the dissolution of the glasses. Also, it triggers hydrolysis reactions of the metaphosphate chains, resulting in the precipitation of hydrogen phosphate groups on the glass's surface, akin to partial passivation [149].

The mechanism of glass degradation by an acid solution is the exchange of ions between the aqueous solution and the glass surface, which is the dealkalization of the surface or leaching. Figure I.11 depicts this action in the example of a hydrochloric acid (HCl) solution attacking glass [150]. When Na^+ and OH^- ions enter the solution, the POH group proton exchanges its surface site with that of an alkaline ion and diffuses into the glass. The interdiffusion between the glass cation and the proton thus controls the kinetics. The hydronium ion is the cation that diffuses through the glass at low temperatures.

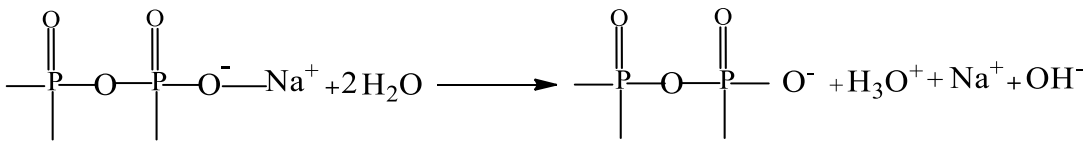

Figure I. 11. Glass degradation mechanism in an acidic environment: glass leaching [151].

c. Corrosion in basic medium

The degradation process governs the breakdown in this scenario. The glass is then totally

hydrated and dissolved by breaking the surface bridges. This mechanism is prominent for pH values greater than 10. Figure I.12 depicts the reaction mechanism for phosphate glasses:

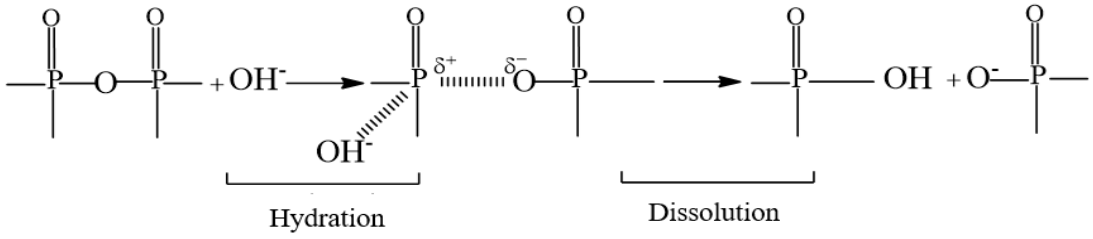

Figure I. 12. Attack mechanism of glass by sodium hydroxide [152].

The mechanism demonstrates that breaking the P-O-P bond (polarized bond: $P^{\delta+}$ -- $O^{\delta-}$) by the nucleophilic attack is critical in the depolymerization process. Hydroxide ions (OH^-) in the solution cause P-O-P bond breakage, allowing new P-O^- and P-OH bonds to form [137,149]. As a result, the species are wiped off one by one. Assuming no protective layer forms on the glass surface and no change in the solution, the reaction would be linear as a function of time.

I.1.9.2. The factors affecting glasses' chemical durability

I.1.9.2.1. Solution attack effect on glass-specific surface area/volume

Under certain conditions, the amounts of various constituents released from a glass are proportional to the surface area of the glass exposed [153]. $25K_2O$-$75SiO_2$ glass attack investigations in an aqueous medium with a pH= 6 and at a T= 40°C have revealed that dissolved SiO_2 amount increases with the S/V ratio as a function of time [144,153]. This parameter appears necessary for extended reaction periods because increasing this ratio from 0.5 to 1.5 enhances silica dissolution by a factor of three.

I.1.9.2.2. Glass composition influence

Glass' chemical durability is strongly reliant on its composition. If the solution pH in a glass containing no modifiers does not exceed 7, the network attack does not occur. Alkali inclusion in the glass's composition rapidly affects its chemical durability [154], not only due to mobile cations entrance but also due to the presence of non-bridging Oxygen, which generates a network that is more conducive to cation diffusion. Glass having a mixture of alkalis (Na_2O and K_2O) has been found to have a reduced corrosion rate than glass containing an equivalent amount of Na_2O or K_2O (mixed alkali effect) [148].

I.1.9.2.3. Effect of the solution's pH

As previously stated, the chemical durability of silicate glasses is incredibly reliant on the pH

and type of the attacking solution. Indeed, phosphate glasses are especially vulnerable to breakdown above pH 9 [151,155].

I.1.9.2.4. Temperature effect

According to Maclellan [156], the dissolved species number of glass in the solution increases by a factor of two for every 10°C increase. The Arrhenius equation can be used to express the corrosion rate of glass as a function of time:

$$\boldsymbol{A = B.e^{\frac{-E_a}{RT}}}$$

Where:

A: The reaction-specific rate;

B: A constant;

R: The ideal gas constant;

T: The absolute temperature.

The activation energy is denoted by the symbol Ea. It is defined as the minimum energy required for the reaction to occur. In the case of glasses of the K_2O-CaO-SiO_2 system at temperatures ranging from 10 to 250°C, this energy is 80 KJ/mol [156].

I.1.10. Review several phosphate glass systems through literature analysis.

Researchers have investigated the effects of varying the composition within the CaO-K_2O-P_2O_5 system to understand the influence of each component on the glass properties. By adjusting the ratios of CaO, K_2O, and P_2O_5, researchers can control properties such as glass transition temperature, thermal stability, mechanical strength, and degradation rate.

In addition to their bioactivity, CaO-K_2O-P_2O_5 glasses can also be tailored for specific applications by incorporating other elements or oxides into the glass composition such as Al_2O_3, which is so important in our investigations for its marvelous enhancing properties' effect.

CaO-K_2O-P_2O_5 glass system:

Here are a few researchers, who delivered interesting studies on this glass system:

1. F. Chen et al. focus on preparing and characterizing CaO-K_2O-P_2O_5 glasses with different compositions. The authors investigate the effects of varying the CaO, K_2O, and P_2O_5 content on the thermal and structural properties of the glasses.
2. C. Vitale-Brovarone et al. examine the in vitro bioactivity of CaO-K_2O-P_2O_5 glasses by evaluating their ability to form a hydroxyapatite-like layer when immersed in simulated

body fluid. The researchers investigate the influence of composition on the glass's bioactivity and discuss its potential for bone tissue engineering applications.

3. A. I. Sorour et al. investigate the structural and dissolution behavior of $CaO-K_2O-P_2O_5$ glasses with varying compositions. The authors analyze the effect of composition on the glass structure and discuss the relationship between the glass properties and their potential applications in tissue engineering.

$CaO-K_2O-P_2O_5$ glass system modified with Bi_2O_3 :

A study by Kaur et al. [157] examined the potential use of a calcium and potassium phosphate glass system, modified with bismuth, as a transparent window for shielding against gamma and neutron radiation in nuclear reactors. The researchers found that glasses containing 0.2 and 0.3 weight fractions of Bi_2O_3 provided better shielding against gamma and neutron radiation. These glass compositions are also cost-effective, requiring less thickness to prepare nuclear reactor shields. Adding Bi_2O_3 to $CaO-K_2O-P_2O_5$ glasses improves the glass structure and enhances its ability to protect against gamma rays and neutrons.

$CaO-K_2O-Na_2O-P_2O_5$ glass system:

According to research conducted by Sayyed et al. [158,159], glasses with lower P_2O_5 content are better at shielding against radiation. Thus, the combination of 20 CaO-10 K_2O-30 Na_2O-40P_2O_5 is the most effective radiation protection.

In addition, a study performed by Mariani et al. [160] has revealed the following:

1. Substituting Na_2O with K_2O leads to minor variations in density and microhardness values due to the heavier weight of K_2O.
2. The low T_g value indicates that P_2O5-CaO-Na_2O-K_2O glass samples are not thermally stable.
3. SEM micrographs of glass samples immersed in some solutions for 10 days indicate that P_2O_5-CaO-Na_2O-K_2O glass systems are bioactive materials.
4. Ultrasonic velocity measurements show that including K_2O results in non-bridging oxygen ions that weaken the glass structure, reducing its rigidity and ultrasonic velocity.

$K_2O-Na_2O-P_2O_5$ glass system:

Faivre et al. [1] researched the effects of adding CaO and Al_2O_3 to P_2O_5-Na_2O-K_2O glasses. They found that if CaO is substituted by (Na_2O + K_2O) or Al_2O_3 substitutes P_2O_5, it improves glass density, decreases the coefficient of thermal expansion, raises the glass transition temperature,

and decreases the water dissolution rate. These changes are due to the increasing modifier field strength and network cross-linking.

RO-Na_2O-Al_2O_3-P_2O_5 glass system (R = Mg, Ca, Sr, Ba):

In a study conducted by Byun et al. [161], the properties and structure of glasses containing (45-x) RO-xNa_2O-2.5Al_2O_3-52.5P_2O_5 (where R = Mg, Ca, Sr, Ba, and $0 \leqslant x \leqslant 31$ mol%) were examined. The molar volume of glasses in the MgO series varied due to the formation of end groups resulting from the substitution of Na^+ ions by Mg^{2+} ions, affecting the density and refractive index of the glasses. When Na_2O was substituted for CaO, the properties of CaO-containing glasses were mainly influenced by the low field strength of Na^+ ions, despite an increase in the end groups of the glasses. For SrO^- and BaO-containing glasses, differences in mass, field strength, and polarizability between Na^+ ions and alkaline earth ions explained the variation in properties, despite slight differences in the structure of the glasses due to Na_2O substitution.

Na_2O-Al_2O_3-P_2O_5 glass system:

Based on the Raman spectra analysis of ternary sodium aluminophosphate glasses, it is clear that glasses with $Al_2O_3/P_2O_5<0.63$ predominantly consist of $(PO_3)_n^{n-}$ chains and rings, and various types of phosphate groups and AlO_4 tetrahedra. On the other hand, for glasses with $Al_2O_3/P_2O_5 >0.63$, the glassy network primarily consists of $AlPO_4$ groups [162].

Ag_2O-Al_2O_3-P_2O_5 glass system:

Researchers El-Damrawi et al. [163] studied the composition of glasses of different Al_2O_3, Ag_2O, and P_2O_5 percentages using ^{27}Al, ^{31}P MAS-NMR, and FTIR spectroscopy. They compared complex ternary phosphate glasses' structure with a simple binary silver phosphate. The study revealed that aluminum is an intermediate ion, while silver is a powerful modifier. With a higher concentration of Al_2O_3, the average number of non-bridging oxygen atoms in the structure of silver aluminophosphate glasses (SAP) reduces. The SAP glass system comprises aluminum ions in the Al(6) and Al(4) coordination. The fraction of Al(6) increases with the concentration of Al_2O_3. In glasses containing more than 20 mol Al_2O_3, Al(6) is more significant than Al(4). The glass can be transformed into a glass ceramic by heat treatment at 600°C for 4 hours.

NiO-BaO-Al_2O_3-P_2O_5 glass system:

The BaO-Al_2O_3-P_2O_5 glasses studied by Prasad et al. [164] had varying concentrations of NiO, ranging from 0 to 1.0 mol%. The research found that the glasses' corrosion resistance was

higher, and their formability significantly improved as the NiO concentration increased to 0.6 mol%. The studies on optical absorption, magnetic susceptibility, and IR spectra revealed that nickel ions occupied tetrahedral and octahedral positions in the glass lattice. However, the latter became dominant when the glass matrix's NiO concentration exceeded 0.6 mol%. Additionally, dielectric property studies showed that the presence of nickel oxide in the glass network significantly improved the glasses' insulation capability when the NiO concentration was less than or equal to 0.6 mol%.

Li_2O-Al_2O_3-P_2O_5 glass system:

Pershina et al. [165] studied how the amount of alumina affects various properties of glass, such as the glass transition temperature (T_g), crystallization temperature, thermal stability, density, and ionic conductivity. They found that T_g increases in all glass compositions when Al_2O_3 is added instead of P_2O_5. The amount of alumina also affects the crystallization stability, with a maximum effect at 6.25 mol% Al_2O_3. The changes in ionic conductivity and density are non-linear and non-additive, reaching a maximum of 6.25 mol% Al_2O_3. IR spectroscopy showed the breakdown of the phosphate network. At the same time, ^{31}P NMR revealed significant changes in the glass structure at x > 6.25 mol%, leading to extreme changes in molar volume and maximum ionic conductivity.

I.2. Corrosion Overview

I.2.1. Definition of Corrosion

A metal's characteristics alter when it is exposed to corrosion because of an unintended yet harmful reaction to the environment. It is permanent and ongoing for corrosion to occur.

It often comprises a series of electrochemical redox processes [166]. This way, certain species are reduced at cathodic sites ($2H^+ + 2e^- \rightarrow H_2$) while the metal is oxidized to a corrosion product at anodic sites (like

$M \rightarrow M^{2+} + 2e^-$). Most corrosion processes have an electrochemical nature, making electrochemical approaches practical research tools in the field of corrosion. More specifically, electrochemical techniques can be used to evaluate the kinetics of electrochemical processes (such as corrosion rates) in specific environments. They can also detect or alter the environment's oxidizing power (or potential).

I.2.2. Importance of Corrosion

Metals and alloys are used widely in industry. The development of many new technologies employs some uncommon and expensive metals. Furthermore, the increasing pollution of the environment produces a more corrosive medium. Therefore, there is a much greater need for

corrosion protection techniques.

Corrosion results in a tremendous financial loss, both directly and indirectly. For example, there is added cost in using protection methods, replacing corroded equipment, using other more expensive resistant metals, as well as production and efficiency loss and industrial accidents due to corrosion. Research is needed to understand the detailed corrosion mechanisms better and, as a result, find more efficient corrosion control methods.

I.2.3. Prevention of Corrosion

Many methods can be applied to control and minimize a material's corrosion in a specific environment. First, selecting the appropriate metal or alloy for a particular corrosive system is the most common method. Judicious use of the proper materials for construction and good design practices can maintain corrosion rates within tolerable limits.

Second, altering environmental conditions can produce marked changes in corrosion properties. Typical changes in the medium that are often used are (1) lowering the temperature, (2) decreasing velocity, (3) removing Oxygen or oxidizers, and (4) changing concentration. Another method is the addition of substances called inhibitors to an environment. Further, a protective coating on the material surface and cathodic and anodic protection are also used to combat corrosion [167].

I.2.4. The origin of corrosion

Corrosion is caused by various chemical and physical interactions between the material and its surroundings. The following factors contribute to material corrosion:

- the chemical composition and microstructure of the metal,
- the chemical composition of the surroundings,
- physical parameters (temperature, convection, ...),
- mechanical stresses (stresses, shocks, friction, etc...).

Thus, corrosion phenomena depend on the material and the surrounding environment [168].

I.2.5. Different types of corrosion

The combination of material/environment in contact constitutes an elementary corrosion system, which evolves under well-defined physicochemical and mechanical conditions. As a result, corrosion processes are affected by the material and the surrounding environment (composition, bacteria, atmospheric pollution, climate, and current...). Corrosion can be classified into several categories.

I.2.5.1. Chemical corrosion (Dry corrosion)

Chemical corrosion can occur when a metal is attacked by another liquid metal (Hg), a molten salt, or a non-aqueous solution (Al in CCl_4). It is commonly found in companies that produce or use acids. This corrosion occurs in a non-electrolytic solution or because of gas action (O_2, H_2S, and CO_2). Dry or high-temperature corrosion is used when the reagent is gaseous or occurs at a high temperature [169].

I.2.5.2. Biochemical corrosion (Microbial corrosion)

This form of corrosion, also known as bio-corrosion, encompasses all corrosion events in which bacteria act directly or indirectly through their metabolism, either by accelerating an already established process or by establishing conditions favorable to its development (e.g., CO_2, H_2S, NH_3 H_2SO_4 production by specific species of bacteria) [169].

I.2.5.3. Electrochemical corrosion (Wet corrosion)

Corrosion in the aqueous phase involves at least four phenomena:

- metal oxidation at the anodic sites
- species reduction in solution at the cathodic sites
- ionic conduction via the electrolyte between the two sites for species transport
- electronic conduction within the metal for electron transfer between the two sites

Physical separation of the anodic and cathodic sites is possible. When a metal encounters an aqueous solution, the corrosion phenomena become crucial. Wet corrosion is primarily electrochemical. It is caused by an interfacial and irreversible redox interaction between the metal and the agents in its surroundings (water, Oxygen, acids). The reaction is written as follows:

$$zM + nOx^{z+} \rightarrow zM^{n+} + nRed$$

Where:

M: The metal; M^{n+}: The corresponding ion; Red: The reduced species; Ox^{z+}: The associated oxidant.

This redox reaction is made up of two halves, anodic and cathodic. The anodic reaction corresponds to metal dissolution:

$$M \rightarrow M^{n+} + ne^-$$

The type of oxidizing species present in the solution influences the cathodic reaction. The most prevalent cathodic phenomena are proton H^+ reduction in an acidic liquid and oxygen reduction

in an aerated medium (neutral or basic). In the electrochemical reaction, two complementary processes intervene :

- The electronic transfer that occurs at the electrode surface in the double layer (the zone from which the species is reactive towards the metal, with a thickness of a nanometer order)
- The material transport of the redox species within the solution to the electrode surface can occur via diffusion, convection, and migration [169].

Metal consumption can be lowered over time by managing one of the phenomena outlined above and adopting one of the following processes:

- The inclusion of molecules that trap oxidants and slow the cathodic process,
- the application of metal coatings that make ionic conduction more complex,
- the covering of metals with insulating coatings that slow electronic conduction.

I.2.6. Electrochemical corrosion mechanism

Metal corrosion, like iron, is created in an electrochemical cell, either in the form of a galvanic cell or a concentration cell, according to the following processes (figure I.13) :

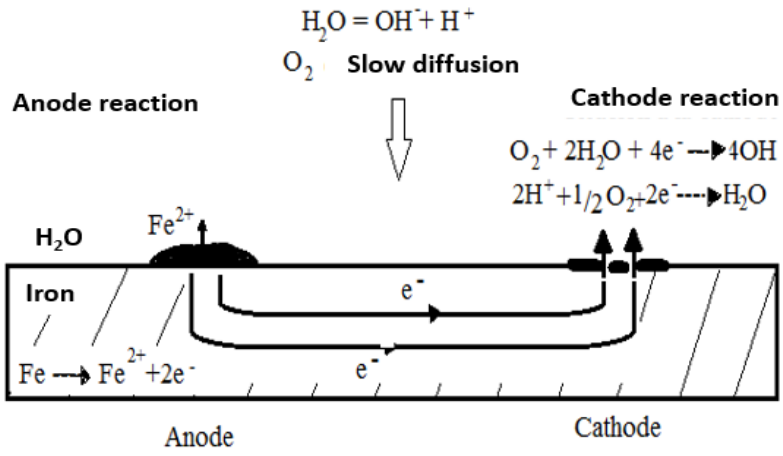

Figure I. 13. Corrosion in an aerated environment.

The oxidation process of iron occurs in the anodic behavior according to the following reaction:

$$Fe \rightarrow Fe^{2+} + 2e^{-}$$

Depending on the solution's composition, one of the following reactions happens in cathodic behavior:

- The reaction occurs in an acidic media with a pH < 5 that is friendly to O_2, such as sulfuric acid:

$$2H^+ + 2e^- \rightarrow H_2$$

- The predominant reaction in weak acid solutions and the presence of O_2 is:

$$O_2 + 4H^+ + 4e^- \rightarrow 2H^+ + 2OH^-$$

- However, in alkaline or neutral conditions (6.5 pH 8.5), including O_2, we will notice the following reaction:

$$2O_2 + 2H_2 + 4e^- \rightarrow 4OH^-$$

I.2.7. Corrosion forms

Metal corrosion can take numerous forms, defined primarily by the form that reveals itself on the corroded surface.

I.2.7.1. Uniform corrosion

When the entire surface of the metal in contact with the solution is attacked similarly, uniform corrosion develops. It causes the metal surface to dissolve uniformly in contact with the aggressive substance [170]. This type of corrosion occurs in acidic or alkaline settings**.**

I.2.7.2. Localized corrosion

This effect arises when the material is placed in an environment that exhibits a selective behavior toward it. This selectivity can have several origins both at the level of the material (heterophase alloy, presence of inclusions, locally insufficient surface protection, bimetallic material.) and the level of the environment (a local variation of the composition, pH, or temperature.

I.2.7.3. Galvanic corrosion

In an aqueous environment, it is one of the most prominent types of corrosion. It occurs due to the development of an electrochemical cell between two materials in which one of the electrodes (the anode) is consumed to benefit the other (the cathode), which stays intact. This reaction's selectivity is due to heterogeneity emanating from the material, the medium, or the physicochemical conditions at the interface [171]

I.2.7.4. Pitting corrosion

This is one of the types of corrosion caused by certain anions, particularly chloride ions, on "passivate" metals (aluminum, chromium, cobalt, copper, stainless steel, steel in concrete, etc...) that are covered by a passive oxide film.

This type of corrosion is particularly sneaky, as the attack is limited to pitting, is relatively

localized, and can develop very quickly in depth. At the same time, the rest of the surface is unaffected. The material can be pierced in a few days with no discernible weight loss to the structure.

I.2.7.5. Selective corrosion

This mode of corrosion, as the name implies, occurs in the selective dissolution of one of the alloy's elements if it is homogenous or one of the phases if the alloy is polyphase, resulting in the production of a porous metallic structure. The best-known example is dezincification (selective dissolving of zinc) in brass.

I.2.7.6. Intergranular corrosion

Intergranular corrosion is a selective attack on grain boundaries or their immediate surroundings, with the remaining material unaffected. The alloy disintegrates, and all mechanical qualities are lost. Impurities cause this type of corrosion in the joint, local enrichment (or depletion) of one of the constituents, or the precipitation of phases and chemical combinations during heat treatment (nitrides, carbides, etc.) [172].

I.2.7.7. Stress corrosion cracking

The corrosion is characterized by metal cracking caused by mechanical stress and an electrochemical reaction. It is defined as a process of fracture formation that can lead to the complete rupture of a part due to the combined action of mechanical stress and a corrosive environment.

Corrosion fatigue is a similar process to stress corrosion. The distinction is that the stress is cyclic (e.g., train wheels in service). Failure can occur even if the applied stress is significantly lower than the predicted mechanical strength of the steel.

I.2.7.8. Erosion corrosion

This corrosion is usually caused by small amounts of stagnant electrolyte solution in gaps, under deposits and joints, or in cavities or crevices, such as under nuts and rivet heads. Sand, dust, scale, and corrosion products are all solid substances that can form zones where the liquid can only be refreshed with effort. This phenomenon applies to all materials. This holds for joints constructed of flexible, porous, or fibrous materials (wood, plastic, rubber, cement, fabrics, etc.).

I.2.8. Thermodynamic aspect of corrosion

Any electrochemical contact is the site of oxidation and reduction reactions involving the

present reducing and oxidizing species. The following equilibrium describes the reversible reaction:

$$Ox + ne^- \rightarrow Red$$

Nernst's law governs the measurement of the electrode potential as well as the concentration of Ox and Red species, which is written as:

$$E_{eq} = E^o + \frac{RT}{nF} Log \frac{[Ox]}{[Red]}$$

Where $E°$ is the standard potential (V/ESH), R is the ideal gas constant (8.314 $J.K^{-1}.mol^{-1}$), T is the absolute temperature (in K), n is the number of electrons involved in the reaction, F is the Faraday constant (96 500 $C.mol^{-1}$), and **[Ox]** and **[Red]** are the activities of the Ox and Red species, respectively.

I.2.9. Kinetic approach

From a kinetic standpoint, the speed of an electrochemical reaction corresponds to the transfer of a particular number of electrons at the material/solution contact. Theoretically, the corrosion rate can be calculated directly by measuring the current density and understanding the kinetics of the anodic and cathodic reactions.

In practice, three major regimes can globally regulate the kinetics of the corrosion reaction.

I.2.9.1. Control through charge transfer processes

The case is confirmed when the interfacial reaction does not result in a significant change in the concentration of redox species in the electrolyte (figure I.15). The kinetics are unaffected by the medium's agitation.

The Bulter-Volmer relation applied to corrosion allows the system's behavior to be described using the equation.

$$I = I_a + I_c = I_0[exp\left(\frac{\propto nF}{RT}\mu\right) - exp\left(\frac{(1-\propto)nF}{RT}\mu\right)]$$

Where:

$\mu = E - E_{cor}$ is the overvoltage, α is the charge transfer coefficient.

I.2.9.2. Control through material transfer processes

This behavior is most noticeable in aerated solutions. In such a medium, the flow of dissolved Oxygen from the solution's heart does not entirely compensate for oxygen consumption at the metal/electrolyte interface, and the reaction is therefore limited by matter transport. In this procedure, the value of icorr is determined by the position of the diffusion "limit" bearing (figure I.14 and I.15).

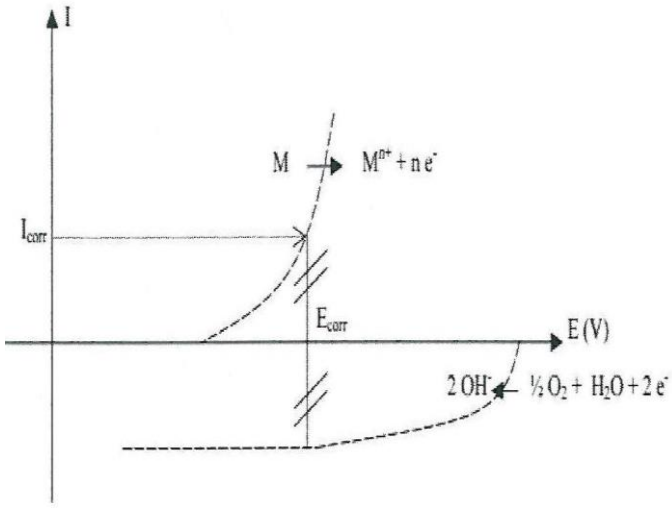

Figure I. 14. Control of the electrochemical corrosion reaction through pure charge transfer.

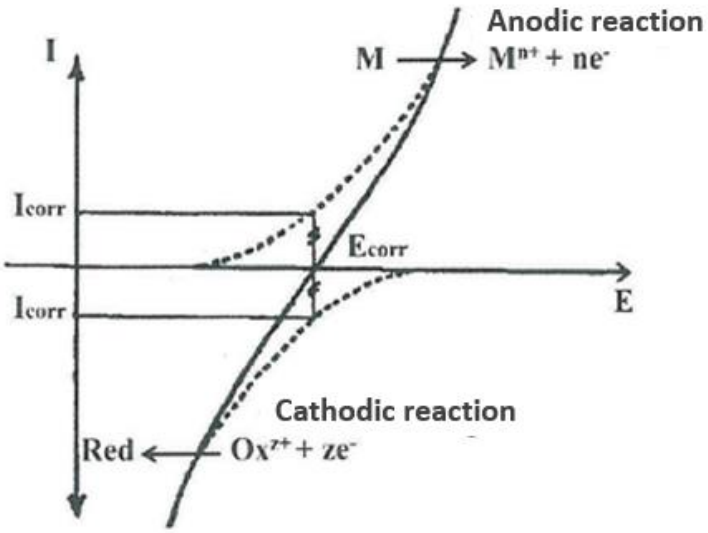

Figure I. 15. Control of the electrochemical corrosion reaction through material transport processes (O_2 diffusion).

The corrosion current is related to the oxygen amount dissolved in the solution:

$$\boldsymbol{I_{corr} = I_{lim} = \frac{nFC_{O_2}CD_{O_2}}{\delta . 10^{-3}}}$$

Where:

Do_2: Diffusion coefficient (cm^2/s);

δ: Epaisseur de la couche de diffusion (cm) ;

n : nombre d'électrons mis en jeu ;

F: Constante de Faraday (= 96500 $C.mol^{-1}$).

I.2.9.3. Mixed control

In contrast to the case where one step of an electrochemical reaction controls the overall kinetics and the system's response to the signal depends preferentially on the rate constant of this step, the response of the system to the signal depends on several rate constants, and the phenomena are much more complicated in the case of mixed Control. The corrosion current is obtained by the following relation thanks to a diffusion adjustment.

$$\frac{1}{I} = \frac{1}{I^*} + \frac{1}{I_i}$$

With:

I: The measured current corresponding to the mixed process;

I^*: The corrected diffusion current;

I_i: The diffusion steps current.

I.3. Corrosion inhibitors overview

Corrosion inhibitors have been used since the early nineteenth century. They were already being used to protect metals in procedures like sulfuric acid baths, protection against hostile water, acidified oil wells, and cooling systems at the time. Since the 1950s and 1960s, essential breakthroughs in corrosion technology have been made, such as using electrochemistry to evaluate inhibitors [173].

The use of chemical inhibitors to reduce the rate of corrosion processes is quite variable. They have been regarded as the primary protection against rusting. Most of what is known has come via trial-and-error research in the lab and the field. Even though the number of corrosion inhibitor studies has expanded dramatically, barely 5% of the literature produced in the previous decade discusses environment gentle inhibitors. In other words, the principles, equations, and ideas that guide the development and usage of inhibitors are quite limited [174].

Metals stand out from other materials due to various desirable features such as exceptional ductility, high tensile strength, resilience to high temperatures, good electrical conductivity,

ease of processing, etc. Their downside is that they are unstable when exposed to air and water, reducing their resistance to corrosion and wear. However, sufficient protection mechanisms are utilized against this phenomenon to serve their role during their projected lifetime. Corrosion inhibitors are required to control the deterioration of the material, its surface, or the aggressive environment with which it comes into contact [173].

I.3.1. Definition

According to the National Association of Corrosion Engineers (NACE), an inhibitor is a substance that stops corrosion when used at low concentrations [175,176] and according to ISO 8044, an inhibitor is a "chemical substance added to the corrosion system at a concentration chosen for its effectiveness, and which causes a decrease in the corrosion rate without significantly changing the concentration or significantly modifying the concentration of any corrosive agent contained in the aggressive. This is an innovative method of combating corrosion; the metal is not directly treated. Instead, the intervention is carried out through the medium [177].

An inhibitor is effective if it meets several criteria. For that, it must: Reduce a metal's corrosion rate without changing its physicochemical properties; Be stable at usage temperatures and in the presence of other environmental elements, particularly oxidants; Be effective at low concentrations; Yield with non-toxicity regulations; Be cost-effective [178].

I.3.2. Inhibitors' properties and classification

There are different categories of inhibitors based on their nature:

- Organic inhibitors have a wide range of applications and are presently the most utilized for environmental reasons [179–181]. These inhibitors are frequently obtained from petroleum sector compounds. They are all made up of at least one heteroatom with a high electron density and the ability to exchange electrons with metal, such as nitrogen, Oxygen, phosphorus, or sulfur. These inhibitors' remarkable efficiency, even at low concentrations, is their main feature.

- Inorganic inhibitors. Inhibitors that are inorganic or mineral and can be anions or cations. The essential mineral inhibitors are chromates, molybdates, silicates, and phosphates.

There are three possibilities depending on the electrochemical reaction to be inhibited:

- Cathodic, which slows down the reduction processes of Oxygen or the H^+ proton in water by reducing the diffusion or concentration of these species (figure I.16) [182].

Cations are the most likely to move to the cathode surface and precipitate as basic salts or hydroxides, forming adherent, compact films. Cathodic inhibitors include zinc, nickel, magnesium, alkaline phosphates, etc.

- Anodic inhibitors act on the anodic sites by decreasing the metal's oxidation reaction rate, decreasing the current dissolution density of the metal, and increasing the corrosion potential, forming a protective film based on insoluble corrosion products (figure I.17) [182]. Anodic inhibitors include orthophosphates, silicates, chromates, and others.
- Mixed, which simultaneously decreases the speed of both anodic and cathodic reactions [183,184]. Such an inhibitor consists of an oxidizing agent, like nitrates or chromates, and a non-oxidizing ingredient that precipitates as orthophosphates or silicates.

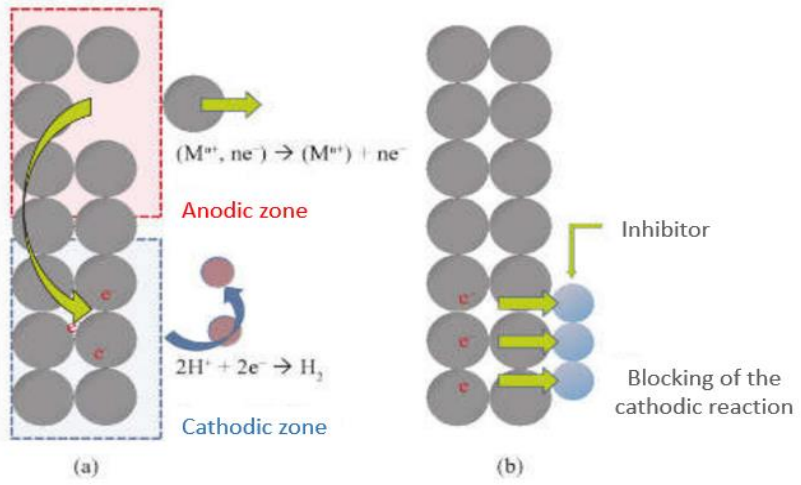

Figure I. 16. Representation of the cathodic inhibition process (a) without inhibitor, (b) with inhibitor.

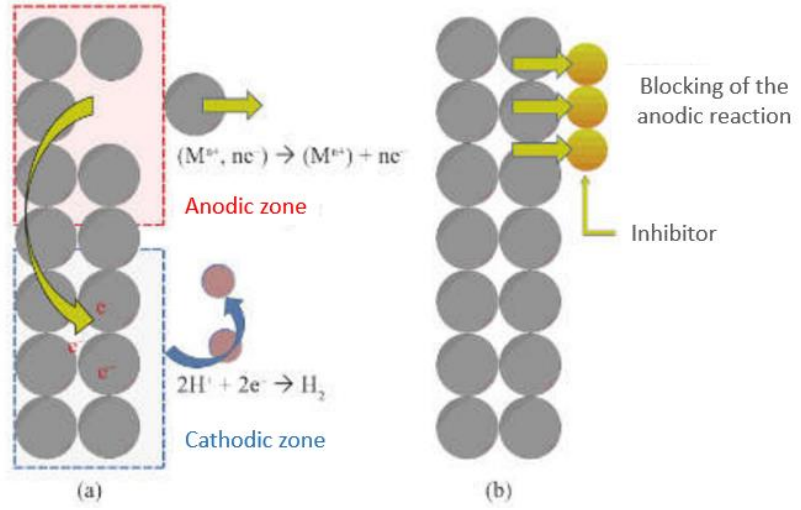

Figure I. 17. Representation of the anodic inhibition process (a) without inhibitor, (b) with inhibitor.

I.3.3. Inhibitors' mechanism and the principle of action

Corrosion inhibitors are linked to the corrosion system. They can function at the metal-corrosive media interface through adsorption and surface blockage. Depending on the mode of action, the inhibitor can either slow down the cathodic or anodic response or operate on both simultaneously (kinetic effect). Furthermore, the corrosion rate reduces over time in areas sensitive to corrosion by producing insoluble compounds that block the latter.

The adsorption of mineral compounds to the metal surface is the most common cause of corrosion inhibition. The following examples highlight the phenomenon:

- The study of adsorption isotherms: Langmuir, Temkin, Frumkin, and El Awady are the adsorption isotherms discovered to describe the adsorption of inhibitors on the metal surface.
- Scanning electron microscopy (SEM), photoelectron spectroscopy, and other techniques are used to examine the surface.

Understanding the factors influencing the inhibitors' adsorption phenomenon is crucial to apprehending these substances' inhibition mechanisms.

I.3.3.1. Type of adsorption

Adsorption is a fundamental surface phenomenon because any surface comprises atoms with incomplete chemical connections. This surface fills this void by trapping atoms or molecules in its proximity. Two types of adsorption processes can be identified based on the nature of the forces involved:

1) Physical adsorption or Physisorption (weak bonds)
2) Chemical adsorption, also known as chemisorption (more stable bonds)

The chemical structure of the organic product, the type of electrolyte, and the nature and charge of the metal all influence these two types of adsorptions [185].

I.3.3.1.1. Physisorption

Physical adsorption is reversible and preserves the identity of the adsorbed molecules. The electrostatic force between the molecules of the solute and the surface of the solid causes physisorption; three types of bonds are distinguished: Van der Waals bonds (always present), polar bonds (depending on surface charges and the inhibitor), and hydrogen bonds (established between a hydrogen bond donor and an acceptor, only N, O, P carrier of free doublet) [186]. The position of the metal's corrosion potential relative to its zero-charge potential defines its charge (E_0). Adsorption of cations is favored when the corrosion potential of the metal is less than E_0.

In contrast, the adsorption of anions is favored when the corrosion potential of the metal is more significant than E_0.

I.3.3.1.2. Chemisorption

Chemisorption is an irreversible and metal-specific process. It is a slow, temperature-dependent process with high activation energy. The merging of electrons between the polar region of the molecule and the metal surface results in significantly more stable chemical bonds (covalent, ionic, or metallic bonds) due to the high binding energies involved.

The inhibitor donates electrons to the metal atom on the surface. Most of the electrons come from unpaired duplicates of inhibitor molecules that are distinguishable from the rest by their high electronegativities, such as O, N, S, P, etc.

Chemical adsorption causes a significant shift in the electrical charge distribution of the adsorbed molecules. The metal nature being shielded influences the electron transfer binding. Indeed, electron transfer is standard in transition metals with unoccupied low-energy "d" orbitals. These metals are referred to as "Lewis's acids" or electron acceptors.

I.3.3.2. Concentration influence on the inhibitory effect

The laws of the adsorbed amount variation with inhibitor concentration are frequently represented by one of the classical isotherms described by Langmuir [187], Temkin [188], Frumkin [189], and El Awady [190]. These are utilized to learn more about the adsorption mechanisms. The relationship between an interface covering rate by the adsorbed species and the species concentration in solution is expressed by an adsorption isotherm.

- ***The Langmuir isotherm***

The Langmuir isotherm model posits that the surface has several energetically similar sites. Each of these sites can only adsorb one particle, and the adsorption energy is constant when the interactions between the adsorbed particles are ignored. Adsorption rate (V_{ads}) is proportional to C_{inh} inhibitor concentration and the fraction of unoccupied adsorption sites ($1-\theta$) and is expressed by equation [187]:

$$V_{ads} = K_{ads}\,(1-\theta)\,C_{inh}$$

$\boldsymbol{\theta}$: The fraction of sites occupied by the inhibitor ($0< \theta<1$); K_{ads}: equilibrium constant of the adsorption reaction.

The desorption rate V_{des}, on the other hand, is proportional to the fraction of sites occupied (θ) by adsorbed molecules and is described by the equation:

$$V_{des} = K_{des}.\theta$$

K_{des}: equilibrium constant of the desorption reaction

The two velocities are equivalent at equilibrium, resulting in the Langmuir isotherm equation [191]:

$$\frac{\theta}{1-\theta} = \frac{K_{ad}}{K_{des}} C_{inh} = bC_{inh}$$

The formula gives the fraction of the occupied sites, often known as the surface coverage rate:

$$\theta = \frac{bC_{inh}}{1 + bC_{inh}}$$

b: is the adsorption coefficient.

After a rearrangement, we obtain the relation :

$$\frac{C_{inh}}{\theta} = \frac{1}{b} + C_{inh}$$

The experimental plot of $\frac{C_{inh}}{\theta}$ Against C_{inh} is a straight line, showing that the inhibitor adsorption on the metal surface obeys the Langmuir isotherm.

- ***The Frumkin isotherm***

This kind of isotherm is determined statistically and considers interactions between adsorbed molecules. It is demonstrated by the subsequent equation:

$$lnC_{inh}\frac{(1-\theta)}{\theta} = -lnK_{ads} - 2\alpha\theta$$

Where:

K_{ads}**:** Adsorption-desorption Equilibrium constant;

α**:** A parameter related to the variation in free energy adsorption ;

θ**:** Surface coverage of the adsorbate (the fraction of the surface covered by adsorbed molecules) ;

C_{inh}**:** Inhibitor concentration in solution.

This type of isotherm depends on molecular interactions in the adsorption layer and the degree of surface heterogeneity. Generally speaking, the Frumkin isotherm can be considered as the general case of Langmuir (when $\alpha = 0$) and Temkin (when $\alpha >> 0$) [189].

➢ ***The Temkin isotherm***

The adsorption-free energy of the adsorbate is a linear function of θ: rate constants are functions of θ. There is attraction or repulsion between adsorbed species. The equation for this isotherm is as follows :

$$\boldsymbol{\theta = \frac{lnK_{ads}}{2a} + \frac{lnC_{inh}}{2a}}$$

Where:

$\boldsymbol{\theta}$ *:* Surface coverage of the adsorbate ;

$\boldsymbol{C_{inh}}$**:** Inhibitor concentration in solution;

a: The Temkin isotherm constant that describes the molecular interaction in the adsorbed layer and is a measure of the slope of the adsorption isotherm. Negative values of ***a*** indicate a repulsive interaction in the adsorbed layer [188].

➢ ***The El Awady isotherm***

The characteristic equation of this model is given by the formula:

$$\mathbf{\ln \frac{\theta}{(1-\theta)} = \ln K + y \ln C_{inh}}$$

Where:

$\boldsymbol{C_{inh}}$**:** Inhibitor concentration in solution;

$\boldsymbol{\theta}$ *:* Surface coverage of the adsorbate ;

$\boldsymbol{K_{ads}}$**:** Adsorption-desorption Equilibrium constant, $\mathbf{K_{ads} = K^{\frac{1}{y}}}$ **;**

y: is the number of water molecules replaced by the inhibitor molecule.

This model takes into account the number of active sites. There is multilayer adsorption if the value is 1/y or less than unity. On the other hand, if the value is greater than unity, the inhibitor occupies more than one active site [190].

I.3.3.3. Temperature influence on the inhibitory effect

Temperature significantly impacts corrosion phenomena; the electrochemical corrosion rate grows exponentially with temperature. The latter is one of the factors that can alter a material's behavior in a corrosive environment. Furthermore, it can alter the metal-inhibitor interaction in a given environment.

The rate of a chemical reaction often rises with temperature. The empirical law of Arrhenius is

frequently used to describe the fluctuation of the corrosion rate.

$$i_{corr} = Aexp\left(-\frac{E_a}{RT}\right)$$

Where: E_a is the activation energy, and A is a pre-exponential factor.

The activated complex theory leads to a more explicit manner of expressing the fluctuation of the corrosion rate with temperature, which leads to:

$$i_{corr} = \frac{RT}{Nh} exp\left(\frac{\Delta S_a^o}{R}\right) exp\left(-\frac{\Delta H_a^o}{RT}\right)$$

N is Avogadro's number, h is Planck's constant, R is the ideal gas constant, and $\Delta Ha°$ and $\Delta Sa°$ are the activation enthalpy and entropy, respectively.

However, in some circumstances, we can have the reverse effect since temperature impacts other corrosion elements. According to some writers, the rise in an inhibitor's protective effect with increasing temperature is related to a shift like adsorption. The inhibitor is physically adsorbed at low temperatures, whereas chemisorption is preferred at high temperatures.

Radovico [192] categorized inhibitors into three groups based on temperature action, based on a comparison of activation energies determined in their presence (E_a) or absence (E_a^0):

- For the inhibitors whose inhibition rate reduces as temperature rises. The activation energy E_a obtained is greater than the activation energy E_a^0 obtained in the absence of the inhibitor ($E_a > E_a^0$). Electrostatic bonds allow these inhibitors to adsorb on the substrate (physisorption). This form of temperature-sensitive bonding prevents efficient corrosion resistance when the temperature rises.

- Inhibitors have a constant inhibition rate with temperature for which $E_a=E_a^0$. This category's protective power does not alter with temperature; very few substances come into this group.

- Inhibitors retain an inhibition rate that increases with increasing temperature as the value of E_a decreases ($E_a < E_a^0$). Strong chemical connections bind the inhibitor's organic molecules to the metal surface (chemisorption). According to Gomma, inhibitors in this group are the most effective. The investigation of the influence of temperature is critical because it can provide information on the mode of action of the inhibitor (chemisorption or physisorption) as well as the apparent energies of activation and inhibition of the corrosion process.

I.3.4. Corrosion inhibitors applications

Inhibitors enclose various established applications; acidic media are typically employed in the industry. In these settings, the selection of an inhibitor or an inhibiting formulation will be determined by the corrosion system, namely the temperature, the flow rate, dissolved organic or inorganic components, and others.

Organic compounds are the most employed inhibitors in acidic conditions. These inhibitors initially work by adsorption on the surface of metals before interfering with the corrosion reaction pathways to slow them down. In the adsorption method, the inhibitor forms a mono- or multi-molecular layer with the metal that acts as an insulating barrier against the aggressive species in the solution.

A wide range of organic compounds, including aromatic molecules and macromolecules with linear or branched chains, are identified as inhibitors in an acidic solution; they adsorb on the active sites of the metal surface without affecting the mechanism of partial electrochemical reactions. They block the sites and reduce the pace of cathodic, anodic, or mixed corrosion in proportion to the fraction of active sites obstructing the corrosion. In an acidic environment, the suppression of corrosion of iron and its alloys by compounds has been intensively explored in recent years [193]. It is common to put corrosion inhibitors on metals and alloys that encounter a harsh environment. These investigations suggest that organic chemicals, particularly those containing N, S, and O, have high inhibitory effectiveness. Unfortunately, most of these substances are cheap and harmful to individuals and the environment. These inhibitors can cause temporary or permanent damage to the neurological system and disturb our body's biochemical processes and enzyme system [194]. Because of raised environmental awareness, more stringent environmental restrictions, and the need to develop environmentally friendly processes, attention is now focused on creating non-toxic alternatives to currently employed organic inhibitors. Natural plant products and several non-toxic inorganics and organic chemicals with polar functionalities with nitrogen, Oxygen, sulfur, and phosphate in conjugated system molecules [195] have been successfully used as corrosion inhibitors for numerous metals.

Efficient inhibitors in acid solutions have little or no effect in near-neutral solutions. This is due to differences in the mechanism of the corrosion processes. In acid solutions, the inhibitor action is caused by adsorption on oxide-free metal surfaces. In these media, the main cathodic process is hydrogen evolution. On the other hand, in neutral aqueous solutions, the corrosion processes result in the formation of insoluble surface products such as oxides, hydroxides, or salts. The cathodic reaction is oxygen reduction. The inhibitors influence the oxide-covered surface by increasing or maintaining the protective characteristics of the oxide or the surface compounds in the aggressive solutions [196]. In many cases, inorganic compounds are used as inhibitors in near-neutral solutions:

- Ca^{2+} and Mg^{2+} ions are usually present in industrial waters. They produce local alkalinity in the system and react with anions to form carbonate precipitates on the metal surface. Corrosion attack is thus prevented.

- Ni^{2+}, Co^{2+}, Zn^{2+}, and Fe^{2+} are intentionally added to water to modify surface film protective properties. They also tend to form insoluble hydroxides, especially in cathodic areas and are more alkaline due to the hydroxyl ions produced by the reduction of Oxygen. In the case of corrosion inhibition of zinc in 3% NaCl solution by the action of diluted cobalt chloride, Leidheiser and Suzuki [197] attributed the inhibiting efficiency to introducing Co atoms into the zinc surface oxide, which led to inhibition of cathodic oxygen reduction. On the other hand, the inhibiting efficiency of Fe^{2+} against corrosion of Cu-Ni alloys in water is attributed to the forming of a ϒ-FeOOH protective layer.

- Inorganic anions such as polyphosphates, phosphates, silicates, and borates contribute to the formation and maintenance of protective films according to various mechanisms. Their action limits the diffusion of dissolved Oxygen to the metal surface and therefore affects the cathodic reaction and, in some cases, even the anodic reaction. For example, polyphosphates in the presence of zinc or calcium can produce a thin amorphous salt film. This salt film restricts the diffusion of dissolved Oxygen to the metal surface. The film is a poor electronic conductor, so oxygen reduction does not occur on the film surface.

- Oxidizing inhibitors such as chromates and nitrites are commonly used to reduce the corrosion rate of metals and alloys with active-passive anodic behavior. They function by causing self-passivation of the metallic material because the oxide films on metals offer high resistance to the diffusion of metal ions, and the anodic reaction of metal dissolution is inhibited.

I.4. Conclusion

In order for a material to be regarded as glass, it has to fulfill two requirements, as opposed to crystalline materials. First, the arrangement of its atomic network must lack any long-range order or periodicity, and second, the material must experience a time-dependent glass transformation process under a specific temperature range, which is unique to each glass.
The glass allows for recycling and the development of new applications. The glass business has grown significantly. Depending on the application, the progress of technology varies substantially. Many factors must be considered, including glazing, containers, optical fibers, and coatings. Glass can be vitrified in various compositions, including ultraphosphates and orthophosphates. Furthermore, because they take practically all oxides in their glassy network,

they can provide the same potentialities as their crystalline counterparts but with simplified shaping.

Nevertheless, the efficiency with which P_2O_5 dissolves the oxides allows for producing glasses with more complex compositions involving the development of mixed networks. The latter acquires a cross-linking strengthened by the structural units of the oxides, significantly reducing the corrosion by the water of these vitreous materials and having properties equivalent to those of silicate glasses and a moderate melting temperature, distinguishing them from the latter, are doomed to an inevitable industrial development in the years to come.

Extensive research has recently been conducted on using phosphate glasses as corrosion inhibitors. The inhibitory efficiency of these glasses is determined by the glass's composition, the aggressive solution, and the action method of these inhibitors. However, physical and electrochemical characterization methods must be used to determine these inhibitors' effect, mode of action, and inhibitory efficiency.

CHAPTER II: Methods and Experimental Parameters

II.1. Introduction

This section will discuss the elaboration strategies and the many analytical and characterization methodologies employed in this thesis. We will discuss structural and microstructural characterization approaches, including X-ray diffraction (XRD), optical microscopy (OM), scanning electron microscopy (SEM), and energy-dispersive X-ray spectroscopy (EDS). The theory of thermal analysis using differential scanning calorimetry (DSC), the experimental methodology for density measurements, and chemical durability will next be presented. IR absorption and Raman scattering spectroscopies, as well as UV-VIS-NIR electronic spectroscopies, will be demonstrated. The gravimetric and electrochemical techniques used to investigate the anticorrosive characteristics of materials will be thoroughly presented.

II.2. Phosphate based-glasses synthesis

All raw materials had a purity greater than 99%. The synthesis of phosphate glass systems is carried out in a muffle furnace capable of reaching 1100°C. The reaction mixture is heated in a porcelain crucible to the desired temperature.

II.3. Thermo-Physical Characterization

II.3.1. Density measurement

The determination of the density is done through the Archimedes principle. Any material submerged in a fluid, whether wetted by it or crossing its free surface, experiences a vertical force directed from bottom to top and opposed to the weight of the volume of fluid displaced. Thus, the density can be estimated by measuring solid weight in the air and its mass immersed in a fluid and applying the following relationship:

$$\frac{\boldsymbol{\rho}}{\boldsymbol{\rho_{liquid}}} = \frac{\boldsymbol{m}}{\boldsymbol{m - m_{immersed}}}$$

Where $\boldsymbol{\rho}$ is the density of the sample, $\boldsymbol{\rho_{liquid}}$ the density of the liquid in which the bulk is placed (In our case Diethyl Phthalate (1.120 g/cm^3), $\boldsymbol{m}$ is the weight of the object measured in air and $\boldsymbol{m_{immersed}}$ the mass of the specimen once immersed.

The molar volume $\boldsymbol{V_M}$ of the glass samples can be calculated from the following relation:

$$\boldsymbol{V_M = \frac{M}{\rho}}$$

The density measurements were performed via a SHIMADZU AW220 balance depicted in figure II.1, which can measure densities at + 0,002 g/cm^3.

Figure II. 1. Experimental device of the Archimedes method.

II.3.2. Differential Scanning Calorimetry (DSC)

DSC is a technique used to determine the thermal properties of glassy materials. When heated, this instrument detects changes in heat flow between a sample and a reference material. The dual illustration and the reference are typically heated and cooled at a controlled linear pace. In other words, the device contains two crucibles, the reference, and the sample to be analyzed. These two crucibles are placed in a preheated oven to the desired temperature, usually at 10°C/min. These crucibles are linked to a thermocouple, which measures the temperature and sends it to a computer. As we heat, the computer calculates the difference in temperature between the sample crucible and the reference crucible and translates it into heat flux (figure II.2). Thus, we use DSC to calculate the amount of additional heat that must be applied to the reference crucible to achieve the same temperature as the sample crucible. This analysis is performed in an inert atmosphere to avoid sample interactions with oxygen in the air.

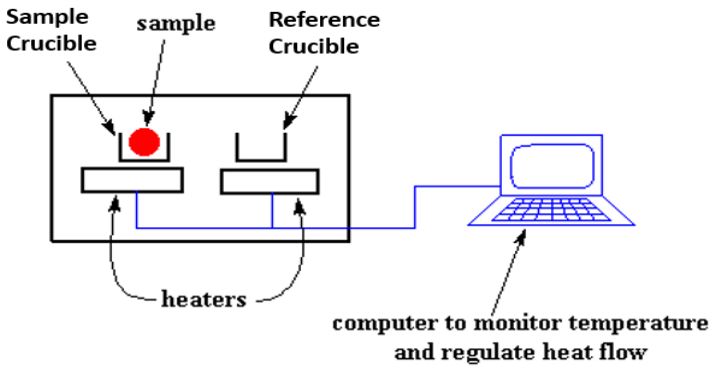

Figure II. 2. The elements characteristic of a typical DSC system.

After the DSC measurement, the heat flow as a function of temperature is shown (figure II.3). It is essential to select which side of the spectrum represents exothermic processes and which represents endothermic reactions.

The first endothermic peak shows the sample's glass transition behavior. The specimen evolves into a viscous state with increasing chain mobility in this temperature range, resembling the first steps of liquid-like behavior. Changes in the material's heat capacity characterize this shift from a solid to a viscous-like state. While it occurs across a wide temperature range, it is often referred to as occurring at a single mean temperature known as the "Glass transition temperature" (T_g) [60,62].

Glass crystallization happens at greater temperatures. This exothermic reaction can be observed as a highly energetic peak in the diffractogram. T_p, often known as the "crystallization temperature," is the temperature at which the vitreous network crystallizes. The commencement of crystallization is a third critical temperature that can be extrapolated from the DSC curve noted as T_x, which is significant since it pertains to the network's thermal stability. When T_x-T_g > 90 °C, the specimen is classified as an "excellent glass former," but when T_x-T_g < 90 °C, the specimen is classified as a "poor glass former" [198].

The samples' glass transition temperature (T_g) is identified at the endothermic inflection point of the curve. The crystallization point (T_p) is the temperature at which the exothermic peak reaches its highest. T_x is intended to be the start of the exothermic peak.

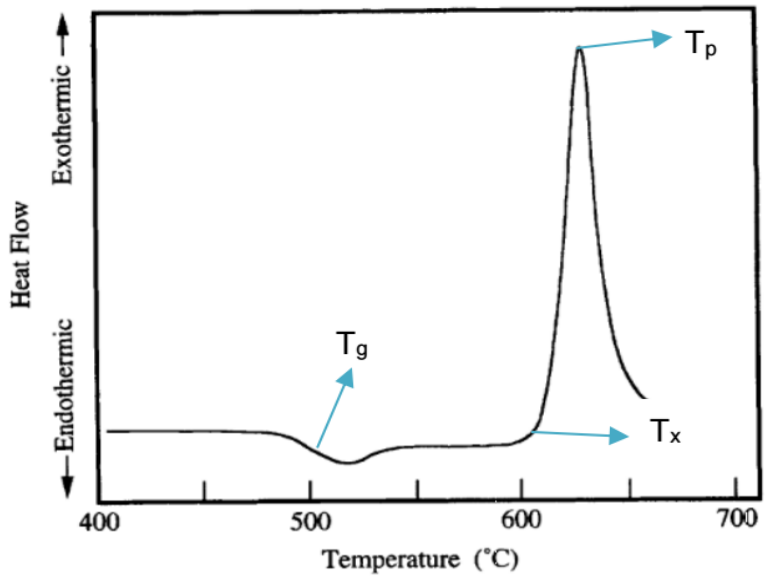

Figure II. 3. A standard glass DSC thermogram.

DSC thermograms were obtained in our studies using a SETRAM type 12 device. The measurements were carried out on large chunks of glass weighing about 20 mg and heated to 600°C at a rate of 10°C/min.

II.4. Structural and Optical Characterization

II.4.1. X-Ray Diffraction analysis

For materials characterization, XRD is a must-have tool. It is a non-destructive technology frequently utilized in phases' identification and structural characterization for various materials, from crystalline to amorphous. Generally, the method is employed to gather data during environmental temperature, but in-situ diffraction is a function of extrinsic restrictions like temperature, pressure, stress, electric field, and environment. XRD is also significant for interpreting solid-state transitions and material behavior. The principles of crystal XRD are given in multiple solid-state physics books [199,200].

The XRD technique principle operates on the dispersion of X-rays by a crystal composed of a reasonably defined pattern of atoms, ions, and molecules. Because the crystal matrix is made up of parallel arrays of atoms that correspond to the parallel lines of the diffraction grating, the inter-planar distance may be directly measured using the separations of the diffraction pattern's bright fringes. Since these inter-planar intervals are identical to the wavelength of X-rays, crystal planes act as diffraction gratings. Just at a specific angle does the interaction of X-rays reflected by a set of parallel surfaces matching Bragg's requirement result in constructive interference.

The condition for a diffraction peak to appear, first given analytically by W.L. Bragg, was presented as the fulfillment of a simple equation linking the matrix distance of a particular set of planes to the diffraction angle, recognized as the Bragg condition [201]. The Bragg equation [201] can be defined as follows:

$$2\,d\,\sin\theta = n\,\lambda$$

Where n is a natural number, λ the X-ray wavelength, d is the distance between two planes, and θ the diffraction angle.

Bragg condition is depicted in figure II.4, including the incident and diffracted beams, the diffraction angles, and the interplanar spacing.

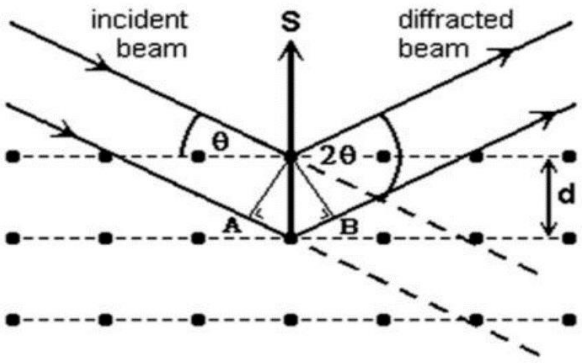

Figure II. 4. Diffraction of an X-ray beam fulfilling Bragg's condition.

XRD tests can be conducted, whether on single crystals or polycrystalline specimens. The Laue technique, Weissenberg photograph methods, or, most typically, an automated four-circle diffractometer are used to study the former type samples. The Debye-Scherrer photographic technique or the powder diffractometer is used to check specimens [202]. Powder diffraction is operated for qualitative and quantitative phase identification, refining crystalline material structure solutions, and assessing particle size and strain in materials. The powder can be an aggregate of tiny grains with a single structure; each fine grain is instructed unsystematically. Figure II.5 depicts a typical block ray diagram of a powder diffractometer. In this method, a powdered specimen is subjected to monochromatic X-ray radiation as a smeared layer, contact flat pack or capillary. The diffracted beam intensity is recorded at various angles. The intensity equivalent to constructive interference of the diffracted beam from the crystallographic plane is perceived as a peak matching the Bragg angle in a crystalline material.

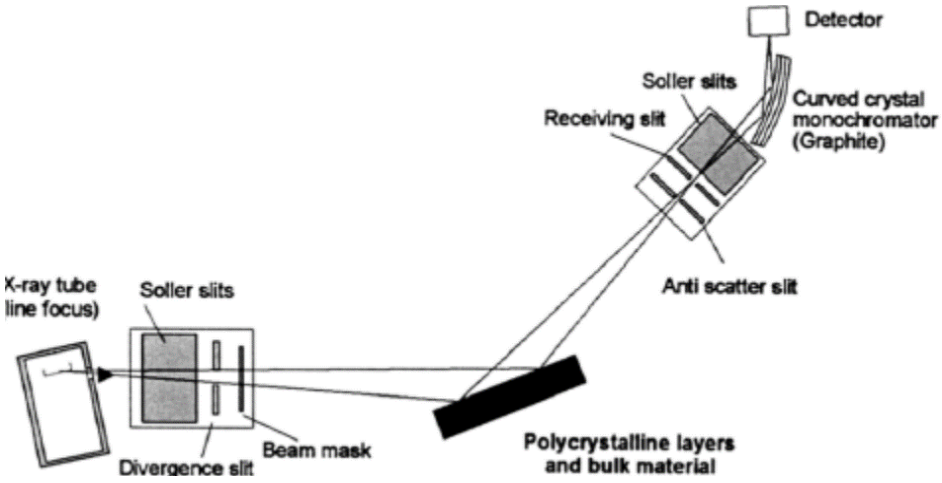

Figure II. 5. Diffraction of an X-ray beam fulfilling Bragg's condition.

While no firm peaks are seen in an X-ray study of a glassy structure, the amorphous phase exhibits only distinctive halos, as shown in figure II.6. Conversely, crystal phases in a glass

network produce sharp peaks (sometimes a combination of sharp peaks and a halo structure that becomes smaller as crystallization advances).

During our study, the X-ray spectra of the samples were collected at ambient temperature using a Siemens D5000 diffractometer (figure II.7). The copper $K\alpha_1$ line ($\lambda K\alpha_1$ = 1,5406 Å) was chosen as the wavelength for the XR diffractograms recorded.

XR diagrams were taken step-by-step in an angular domain 2θ (10^o-60^o) with a 20-minute maximum companion time. The experiments were carried out on a sieved powder of grain size <50μm spread on a glass sample holder to prevent any fluctuation in the intensity of the XRD peaks due to selecting the size or orientation phenomena.

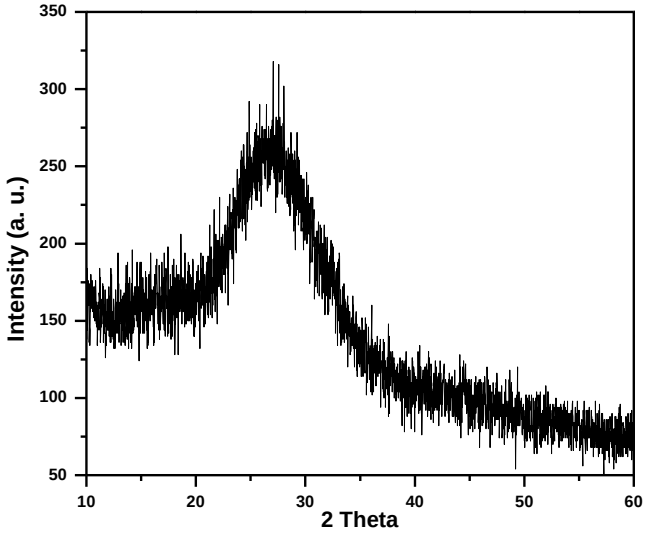

Figure II. 6. X-ray diffraction diagram of a vitreous glass system.

Figure II. 7. SIEMENS D5000 type XR diffractometer.

II.4.2. Fourier Transform InfraRed (FTIR)

The most frequent type of infrared spectroscopy is FTIR, which refers to "Fourier transform infrared." Infrared spectroscopies work on the idea that infrared (IR) radiation is absorbed when it traverses a sample. The radiation emitted by the specimen is determined. Because various molecules emit distinct spectra due to their unique structures, the diagram can be utilized to identify and classify between molecules. The spectra are individual and almost identical to people's fingerprints. For various purposes, FTIR is the favored technique of infrared spectroscopy.

First and foremost, it does not damage the sample. Second, it is much speedier than prior procedures. Third, it is far more sensitive and accurate. In an FTIR spectrometer (figure II.8), an infrared spectrum analyzes the radiation absorption caused by a molecule's bonds. Photons varying from 700 nm to nearly 1 mm make up infrared light. Even though the energy of these photons is insufficient to cause electronic transitions, they cause the molecules in the sample to vibrate. Because each bond has a distinct unique vibrational frequency, IR photons of characteristic energy are absorbed by a specific bond in the specimen. Not all vibrational molecular motions absorb infrared light; the molecule's dipole moment must shift to be IR active [203].

The beam splitter first divides the IR beam from the infrared source into two equal parts. One of the beams is focused on a fixed mirror, while the other targets a moving mirror. The beam splitter receives both reflected beams. The effect of the moving mirror causes constructive and destructive interferences among the beams, resulting in an interferogram. Once both beams have passed through the beam splitter, they are remerged and directed to the sample, where they interact with it. Following that, a detector generates the interferogram for each wavelength. The Fourier transform is performed on the interferogram to produce the sample's ultimate spectrum [204].

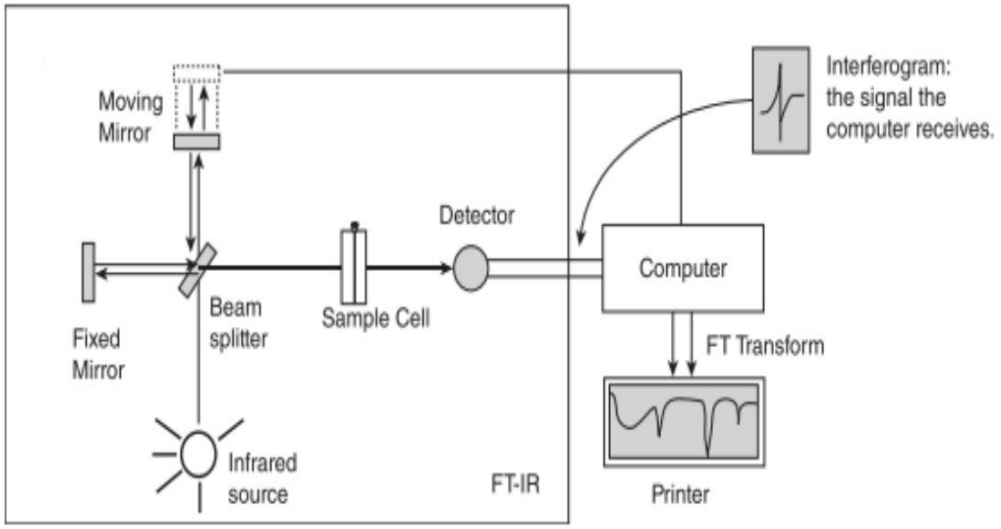

Figure II. 8. Fourier Transform Infrared spectrophotometer's plan.

The position of these absorption bands depends mainly on the mass of the atoms and their difference in electronegativity. Therefore, a given material has a group of characteristic absorption bands to identify it.

$$\vartheta_0 = \frac{1}{\pi}\left(\frac{k}{\mu}\right)^{1/2} \qquad \text{avec} \qquad \mu = \frac{mM}{(m+M)}$$

v_0 is the oscillator vibration frequency, μ identified as the oscillator reduced mass linking m to M, and K is the stiffness constant.

Therefore, the infrared spectra measure the absorbance A, quantity dependent on the ratio between the starting intensity I_o and the transmitted intensity I_t (Beer-Lambert law) according to the vibration frequency.

$$A = log\left(\frac{I_0}{I_t}\right)$$

The variation in absorption caused by the sample can be expressed as a ratio:

$$T = \frac{I_t}{I_0}$$

Where T is the transmittance.

In the present study, all infrared experiments were carried out using a JASCO 4600 FTIR Fourier transform spectrometer type A (figure II.9) with a frequency range of 400 to 4000 cm^{-1} (medium infrared) with a resolution of 4 cm^{-1}. The samples to be analyzed are in the form of powders or little bulks.

Figure II. 9. A JASCO 4600 FT/IR Fourier transform spectrometer type A.

II.4.3. Raman spectroscopy

Raman spectroscopy is a method for non-destructive chemical examination that delivers extensive data on a chemical's structure, phase, and polymorphic, crystallinity, and molecular interactions. It is dependent on light's interactions with chemical bonds in a material.

A monochromatic incoming frequency's radiation ν_0 (usually from a laser) is dispersed inelastically from various vibrational states of the specimen in Raman spectroscopy. Most of the incident light is scattered elastically (Rayleigh scattering), with only a minor percentage (1 in 10^7 photons) at frequency ν_0-$\Delta\nu_0$ (or ν_0+$\Delta\nu_0$). Raman shift refers to a bit of variation in the frequency of Raman or inelastically scattered light. This shift relates to the energy necessary to cause a molecule to vibrate. The new vibration frequencies are the result of polarity shifts caused by the excitatory wave's electric field, per the equation:

$$\boldsymbol{P_{induced} = \alpha\, E\ \nu}$$

With $\boldsymbol{E}$ oscillating at the frequency $\boldsymbol{\nu_i}$ in such a way that:

$$\boldsymbol{E = E_0 \cos(2\pi \nu_i t)}$$

Raman activity will occur when the derivative of polarity related to the normal Q coordinate is non-zero, i.e., only for movements that cause a change in the polarity of the molecule. In this instance, we have:

$$\left(\frac{\partial P}{\partial Q}\right) = \left(\frac{\partial \alpha}{\partial Q}\right)_{Q=0} . E$$

$$I_{Raman} \propto \left(\frac{\partial \alpha}{\partial Q}\right)^2$$

The Raman effect involves two scattering processes (figure II.10). The first is distinguished by scattering from a lower vibrational level to a higher level (Stokes effect). In contrast, the second is by spreading from a higher vibrational level to a lower one (anti-Stokes effect). The spectrum frequencies measured are expressed as a wavenumber shift or Raman shift, which is defined as the difference between the incident and scattered wavenumbers:

$$\Delta\omega = \omega_0 - (\omega_0 - \omega_i) = \omega_i$$

The frequency changes spectrum is unique to the sample and not to the source. As a result, the Raman shifts Δω is linked to the molecular characteristics of the examined substance and correlate to the molecule's vibration frequencies. The Boltzmann distribution describes the intensity ratio between the Stokes and anti-Stokes lines: the Stokes lines are more intense than the anti-Stokes lines because the low-energy vibrational modes are the most populated.

Raman spectroscopy is thus an extremely effective method for highlighting the several elementary groups that comprise the structure of glasses. This approach will produce a strong signal for strongly polarizable substances such as P-O bonds.

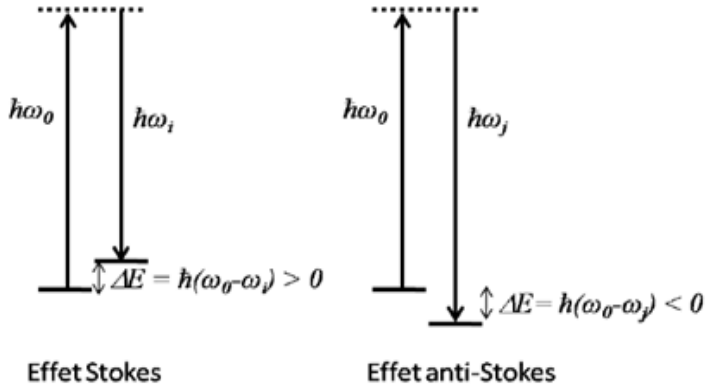

Figure II. 10. Schematic diagrams of Raman Stokes (left) and anti-Stokes (right) effects.

In the present study, the Raman spectra were recorded at room temperature using a Renishaw RM1000 micro-Raman Spectrometer (figure II.11) linked to a He-Ne laser (19mW) and the 632.8nm line. A 50x long working distance objective was utilized to focus the laser spot on the sample surface. Raman spectra were captured at numerous locations on the sample and recorded using a Peltier-cooled CCD camera. For all measurements, a grating of 1800 lines mm^{-1} was utilized, yielding a spectral resolution of 1 cm^{-1}. The spectra ranged from 200 to 1400 cm^{-1}.

Figure II. 11. A Renishaw RM1000 micro-Raman Spectrometer.

II.4.4. Ultraviolet-Visible-Near Infrared spectroscopy (UV-Vis-NIR)

UV-Visible spectroscopy provides qualitative information about the nature of the bonds in the sample and quantitative information about the concentration of species absorbing in this spectral region (via the Beer-Lambert law). This spectroscopy is extensively employed in practical chemistry (after creating a calibration line and transferring an experimental measurement) and chemical or biochemical analysis because it is non-destructive and rapid. The UV-Visible electronic transitions in a molecule involve the most critical chemical energies (about 13000 to 50000 cm^{-1} or 160 to 665 kJ. mol^{-1}). The energies involved are of the same order of magnitude as the molecules' binding energies, and these radiations can occasionally trigger bond breakage. They cause electronic transitions between different energy levels of molecules in general.

Ultraviolet-Visible-Near Infrared spectroscopy is a spectroscopic technique that uses photons with wavelengths in the ultraviolet (100 nm - 400 nm), visible (400 nm - 750 nm), or near-infrared (750 nm - 1400 nm) range. When exposed to this wavelength range of light, molecules, ions, or complexes will likely experience one or more electronic transitions.

UV-Vis-NIR spectroscopy and Raman spectroscopy are both based on the interaction of an electromagnetic wave with the vibrational modes of the matter under study. The energy differential, ΔE, of an electromagnetic beam of frequency ν absorbed and emitted by matter follows the Planck-Einstein relation:

$$\Delta E = h\nu$$

h is Planck constant (h = 6,63.10^{-34} J.s.). In a vacuum, frequency ***ν*** and wavelength ***λ*** are related by the speed of light (c=3.10^{8} m.s^{-1}), as follows:

$$\nu = c/\lambda$$

Where: $\Delta E = hc/\lambda$

According to this connection, the wavelength of absorbed radiation is typical of the energy difference between two electronic levels. By measuring this difference, we can learn about the electronic structure of the atomic structure and, thus, about the substance analyzed. The transmission limit in the UV-Vis-NIR range is caused by the glass matrix's electronic order transitions. The energy gap between the conduction band and the valence band of the glass matrix corresponds to the energy of the least wavelength the glass transmits. Because the energy of the radiation is more significant at shorter wavelengths, the glass is no longer transparent.

The optical spectra in our investigation were acquired using a JASCO V-670 spectrophotometer and an integrating sphere (figure II.12). This setup allows you to analyze absorption over a wide spectral range, from 250 nm (ultraviolet) to 1800 nm (red) (visible). The sample is a few millimeters thick polished glass.

Figure II. 12. A JASCO V-670 spectrophotometer.

II.5. Surface characterization

II.5.1. Scanning Electron Microscopy (SEM)

The scanning electron microscope (SEM) is a widespread piece of equipment for photographing and analyzing the composition of diverse substances. Due to the depth of focus of the SEM instruments, images have a three-dimensional effect up to a length scale of a few tens of nanometers. Because of the remarkably bass wavelength of accelerated electrons, electron microscopy delivers images of a sample at far better magnification, resolution, and depth of focus than optical microscopy, which uses visible light.

SEM function relies on a beam of very intense electrons scanning the surface of a sample, and the consequence of this interaction is displayed on a screen. Figure II.13 depicts the course of the electron beam from the source to the sample.

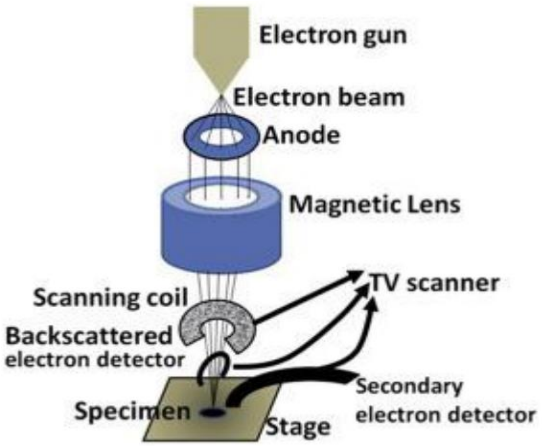

Figure II. 13. Scanning Electron Microscope (SEM) components.

In this technique, two interactions appear between the electron beam and the specimen. These interactions can be elastic if the electron beam hits the sample and switches direction without modifying energy (backscattered electrons) or inelastic if the electron beam strikes an orbiting shell electron of the specimen, inducing secondary electron ejection, typical photon radiation (x-ray and visible radiation), and different types of events from the specimen interaction volume. Because the scattering intensity is Z (atomic number) dependent, backscattered electrons allow element distribution investigation. On the other hand, secondary electrons are liberated from a relatively limited volume in the surface region and can thus be utilized to investigate the surface of objects. These interactions provide critical information about the specimen, allowing the material's surface features and chemical makeup to be determined. The equipment used for the thesis measurements is a JEOL JSM-IT 100 apparatus coupled to an X-ray energy dispersive spectrometer depicted in figure II.14.

Figure II. 14. A JEOL JSM-IT 100 scanning electron spectrophotometer.

II.5.2. Energy dispersive spectroscopy (EDS)

EDS (energy dispersive spectrometer) is an analytical technique that can be used with scanning electron microscopy (SEM). When operated with this imaging instrument, EDS can give elemental analysis in areas as small as a nanometer in diameter. The electron beam's interaction with the sample generates X-rays that are characteristic of the elements present in the sample. The analysis can determine the elemental composition of individual points or create an image of the scanned area's lateral distribution of elements.

The sensitivity of specific sensors to the flux and energy of photons emitted by the observed sample is operated in this technique. This technique requires the following components :

- an excitation source (the primary electron beam created by the SEM)
- an X-ray detector
- a processor that allows pulse recording
- a system for storing and interpreting the emitted data

Scanning electron microscopy was utilized to view and study the surface of the glasses (SEM). Carbon was exploited to metalize the materials under investigation. This metallization prevents a significant accumulation of charges on the surface of the samples (insulators) and reduces the penetration depth of the beam, improving image quality. The tests were performed using a JEOL JSM-IT 100 linked to an X-ray energy dispersive spectrometer (X-EDS) (figure II.14).

II.6. Durability investigations

Compared to silicate glasses, the modification of glasses in aqueous solution has received comparatively little attention until recently. The mechanisms leading to the dissolution of these phosphate glasses are still being debated in the literature [83,205,206].

In our study, we tracked the evolution of the solution's immersion time, mass loss, and pH based on the glass composition (the balance used for these measurements is a SHIMADZU AW220 and a pH meter IC3505). The measurements were taken on glassy samples cut into discs to make calculating the outer area of the specimens studied easier. The specimen was taken from the etching solution at the end of each experiment and wiped and cleaned three times with distilled water to remove the surface solution. Leaching tests were carried out at room temperature. To compute the dissolution rate, we utilized the following equation:

$$\boldsymbol{DR = \frac{\Delta W}{At}}$$

Where: ΔW: Weight loss (g); A: Sample surface (cm^2); and t: Immersion time (min).

II.7. Analysis of the anticorrosive activity

II.7.1. Material and sample preparation

This study's material is mild steel with the chemical composition shown in Table II.1. Before the trials, the steel samples were pre-treated with granulometry abrasive paper (220, 400, 600, 800, 1200, and 1500), rinsed with distilled water, acetone, and washed with bi-distilled water, and dried with a drier.

Table II. 1. Mild steel chemical composition:

Element	C	Si	Mn	Cu	S	Fe
Composition (Weight %)	0.179	0, 165	0.439	0,203	0.034	Balance

II.7.2. The Experimental media

The experimental medium used for anticorrosive tests is a 3,5% NaCl solution prepared by dissolving a stoichiometric amount of sodium chloride in distilled water. Before each test, the mild steel samples were polished with increasingly fine abrasive paper (grade 100-400-800-1200) on a rotating disc using a polishing machine (figure II.16), followed by rinsing with distilled water and drying under an air stream.

II.7.3. The evaluation process of corrosion inhibiting efficiency

II.7.3.1. Gravimetric method

This method is simple to adopt and does not require large equipment. Its basic premise is based on measuring the loss of weight (W) experienced by a sample (mild steel) of surface (S) during a time t of immersion in a corrosive solution kept at a constant temperature.

Weight loss measures were conducted during a 24-hour immersion at room temperature, with and without adding our inhibitors at various doses. The mild steel samples are rectangular (2 cm x 1 cm x 1 cm) and immersed in 50 ml of 3.5M NaCl solution without and with various tested inhibitors.

The following relationship gives the corrosion rate:

$$\boldsymbol{CR = \frac{W}{st}}$$

$\boldsymbol{CR}$ is the corrosion rate ($mg.cm^{-2}.h^{-1}$) of the coupon of sectional area (S, cm^2) over time and $\boldsymbol{W}$ is the weight loss.

The following formula is used to assess the inhibitory efficacy:

$$\boldsymbol{EI\% = \frac{CR_{corr} - CR_{corr}^{inh}}{CR_{corr}} \times 100}$$

$\boldsymbol{CR_{corr}}$: The corrosion rate in the absence of inhibition; $\boldsymbol{CR_{corr}^{inh}}$: The corrosion rate in the presence of inhibition.

The inhibitory effectiveness value reported is the average of three experiments conducted under identical conditions for each concentration.

Figure II. 15. Manual polishing machine with variable speed from 100 to 500 rpm.

II.7.3.2. Electrochemical measurements

The assessment of inhibitory efficiency, as indicated by weight loss, does not provide an understanding of corrosion mechanisms. On the other hand, Electrochemical measurements are a more comprehensive technique since they investigate the foundation of the corrosion phenomenon, the electrochemical process.

Electrochemical techniques allowed the study to be tackled from two perspectives. They are monitoring the open circuit potential over time, a characteristic of the alteration of the interface between a metal and its environment or using a high-speed cyclic voltameter. The quantitative aspect (polarization curves at moderate scanning speed, impedance spectroscopy.) allows us to access the reaction rate and the values of physical parameters representing the system's state (double-layer capacitance, transfer resistance, film capacitance, etc.).

Electrochemical approaches such as Stationary Methods and Transient Methods were used to evaluate the efficiency of corrosion inhibitors of materials.

II.7.3.2.1. Experimental arrangement

The electrochemical tests were performed via an Origalys potentiostat controlled by the Origamaster corrosion analysis software in static condition with a corrosion cell that consists of three electrodes. A saturated calomel reference electrode (SCE) will be a reference for all the potentials indicated in this study, the auxiliary electrode is a platinum electrode, and the working electrode is made of mild steel. A thermostat with water circulation allows for maintaining the electrolyte at the desired temperature. Before each curve is plotted, the surface of the working electrode is well-treated. The electrode is held before each measurement at its corrosion-free potential. Measurements are made at 303K in a 3.5 M sodium chloride solution.

II.7.3.2.2. The evolution of Open Circuit Potential (OCP)

The open circuit potential is also referred to as spontaneous potential, dropout potential, or free potential. It is the most immediately measurable electrochemical parameter. It is measured with a reference potential, in this case, a saturated calomel electrode. Monitoring the free potential as a time function helps understand a material's behavior in contact with a wet, corrosive environment. It gives information on the preliminary transformations of the processes in progress at the metal/electrolyte interface: corrosion passivation [207]. Curves of various types are typically discovered. Figure II.17 depicts numerous scenarios of potential evolution throughout time.

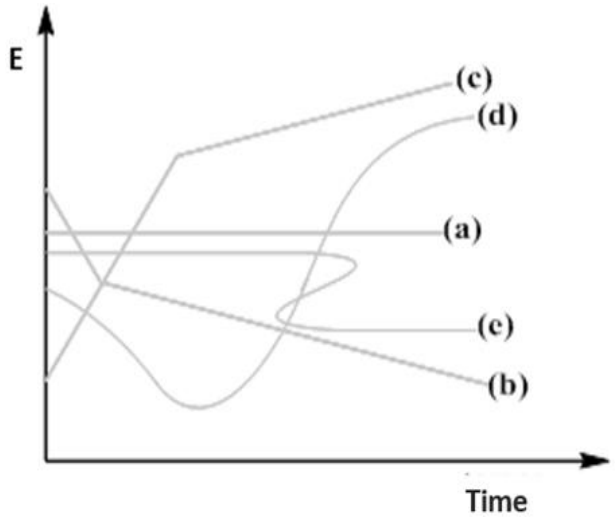

Figure II. 16. Diagrams of E(OCP) tracking as a function of time.

a) The potential is constant, and the interface does not change over time;

b) The potential only decreases, and the material becomes less and less noble by a continuous attack of the metal;

c) The potential increases over time; this is the case of passivation, i.e., the formation of a protective passivating layer;

d) The potential becomes more negative and then tends towards more positive values. This is the case of an attack followed by passivation;

e) The metal-medium interface, which is stable for a certain period, can change abruptly.

II.7.3.2.3. Polarization plot

The method entails applying a predetermined voltage to the sample for the reference electrode and measuring the resulting current density through the working electrode. The shape of the polarization curves is determined by the physicochemical processes that cause corrosion. The polarization curve at the corrosion potential can be thought of as a linear section. The curve's exploitation takes into account its shape as well as the scale used for the plot: linear i=f(E) (figure II.18) or logarithmic log(i)= f (E) [18].

The acquired curve also reveals the metal's sensitivity to localized corrosion. The appearance of pitting on the sample is reflected in the rising potential turn by a sudden increase in current. Stern et al. established the value of Icorr for the first time in their original publications [208].

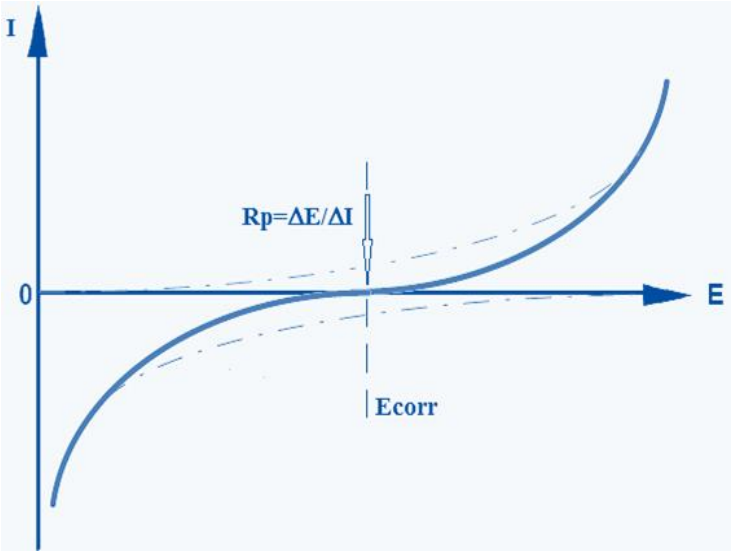

Figure II. 17. Intensity-potential plot.

Polarization measurements were performed to learn more about the kinetics of anodic and cathodic reactions. The approach entails applying a fixed voltage to the sample concerning the reference electrode and measuring the stationary current that forms after a set time in the electrical circuit between the reference electrode and the working electrode (figure II.14). Stern was the first to calculate the value of I_{corr} [209]. The point is reached by evaluating the anodic and cathodic branches, which are assimilated to Tafel lines on the curve log(I)=f(E) (I_{corr}, E_{corr}). Tafel's extrapolation approach and polarization curve diagrams depict the anodic-cathodic zones in determining the corrosion potential (E_{corr}) and corrosion current density (I_{corr}) [210].

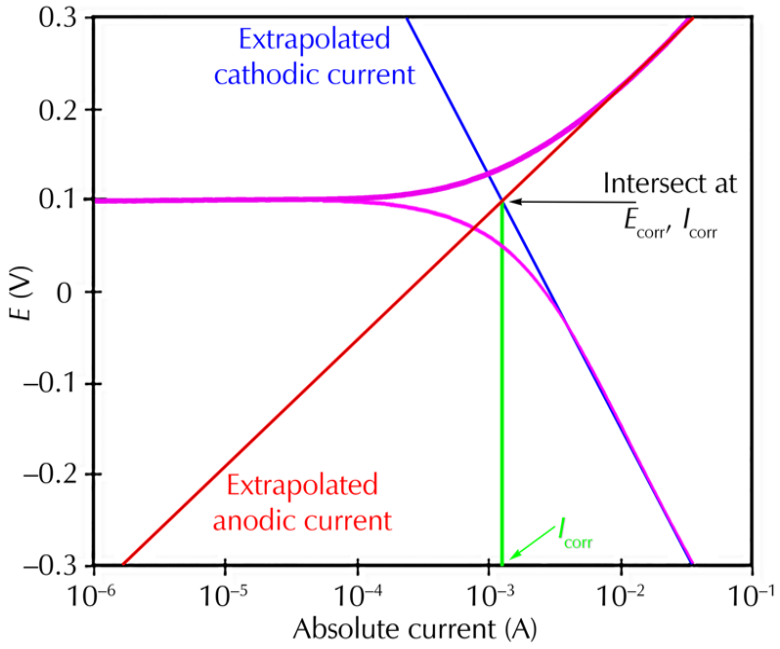

Figure II. 18. Electrochemical parameters determination from Tafel's lines.

The intensity-potential curves are acquired using a scanning speed of 1mV/S in kinetic-potential mode. Because of this speed, we were able to place ourselves in quasi-stationary settings and achieve good reproducibility of results. These curves are recorded in a potential interval between must define the Tafel mV/ECS interval. The efficiency of an inhibitor can be determined by knowing the corrosion current of the metal in a corrosive solution without an inhibitor (i_{corr0}) and with a known inhibitor's quantity (i_{corr}). The following equation then defines it:

$$\boldsymbol{E_I}\ (\%) = \frac{\boldsymbol{i_{corr} - i_{corr}(inh)}}{\boldsymbol{i_{corr}}} \times \mathbf{100}$$

$\boldsymbol{i_{corr}}$ and $\boldsymbol{i_{corr}}$ ***(inh)*** represent the corrosion currents in the absence and presence of an inhibitor, respectively.

II.7.3.2.4. Electrochemical Impedance Spectroscopy (EIS)

The electrochemical impedance is measured by evaluating the system's electrochemical response to a disturbance, which is usually a low-amplitude alternative signal. An impedance spectrum analysis aims to assign actual quantities to each stage detected on the Nyquist and Bode diagrams. This can be approached by modeling the spectrum with an Electrical Equivalent Circuit (EEC), which is made up of a few simple elements: The following are the most frequently utilized elements:

- The impedance resistance R is exclusively modeled by its fundamental part ;
- The impedance capacitance ;
- The impedance inductance Z_i=jLω

The interpretation of the diagrams using EEC must respect two essential conditions:

- All the elements of the circuit must have a precise physical meaning associated with the physical properties of the system;
- The simulated spectrum from the EEC must be as close to the experimental spectrum as possible, and the inaccuracy must not be systematic as a function of frequency.

In the framework of corrosion inhibitor research, impedance spectroscopy determines the product's mode of action [211]. In the case of inhibitor adsorption, the impedance spectrum in the Nyquist plane is represented by a more or less flattened capacitive semi-loop, which may exhibit a phase shift for the real axis. The inhomogeneity of the electrode surface causes this phase shift. Variations in the content or thickness of the layer that forms on the electrode surface are attributed to this phase shift by other studies [212]. The coefficient n accounts for surface

inhomogeneities using a Constant Phase Element (CPE). The following equation represents such an element:

$$\boldsymbol{Z_{CPE} = Q^{-1}(i\omega)^{-n}}$$

With $\boldsymbol{Q}$, an interfacial capacitance. In the ideal case, the coefficient ($\boldsymbol{n}$=1) and the physical model result in a planar capacitor.

Figure II.20 depicts the illustration of EEC of the adsorption mechanism.

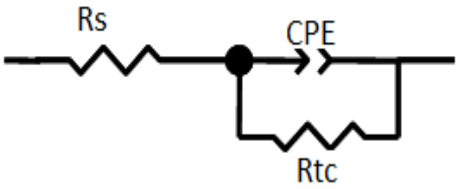

Figure II. 19. Proposed electrical equivalent circuit for the metal-electrolyte interface during inhibitor film adsorption.

This circuit is made up of a constant phase element ($\boldsymbol{Q_{dc}}$), which is utilized to account for the previously specified inhomogeneities, an electrolyte resistance (R_s), and a charge transfer resistance (R_{ct}). The equation yields the value of the double-layer capacitance:

$$\boldsymbol{C_{dc}=Q_{dc}\ (\omega_{max})}$$

With $\boldsymbol{\omega=2\pi f}$ ($\boldsymbol{f}$ represents the frequency at which the imaginary value reaches a maximum on the Nyquist diagram).

On the impedance diagram, the gradual adsorption of the inhibiting entities onto the substrate is represented by an increase in the capacitive loop. In other words, an increase in R_{ct} and a decrease in C_{dc}. Impedance measurements are often presented in the complex Nyquist plane. The abscissa corresponds to the genuine part of the impedance and the ordinate to the imaginary part (figure II.21).

Impedance spectroscopy is utilized in corrosion inhibitor investigations to determine the method of action of these inhibitors. The following equation is used to compute the corrosion inhibition efficiency of mild steel using the charge transfer resistance:

$$\boldsymbol{E_I}\ (\%) = \frac{\boldsymbol{R_{tc}^i - R_{tc}^0}}{\boldsymbol{R_{tc}^i}} \times \mathbf{100}$$

Where: $\boldsymbol{R_{tc}^i}$and $\boldsymbol{R_{tc}^0}$ are the charge transfer resistance values with and without an inhibitor,

respectively.

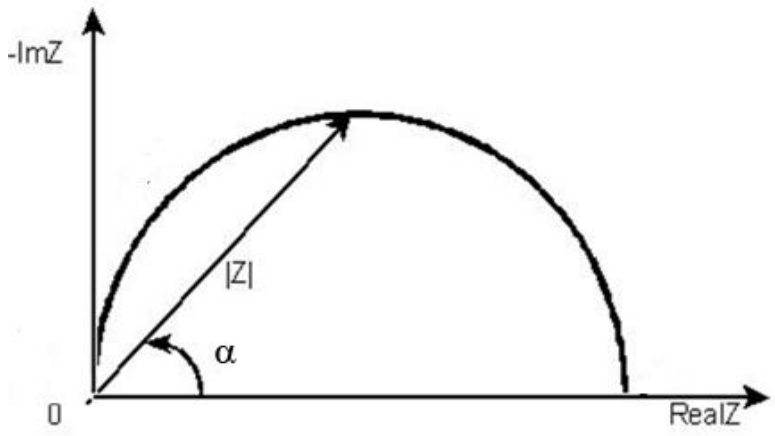

Figure II. 20. Nyquist diagram.

II.8. Conclusion

This chapter thoroughly analyzes how different analytical tools were used to understand the glass system in this thesis. A multidimensional understanding of glass properties, structure, and behavior was achieved by combining various techniques like surface analysis, crystallography investigations, thermal analysis, spectroscopic methods, optical investigation, and anticorrosive properties analysis. This comprehensive analysis provides a strong basis for further research in glass science and technology applications.

Chapter III: Preparation and structural, thermal, and optical characterization of $CaO-K_2O-P_2O_5$ and $Al_2O_3-K_2O-CaO-P_2O_5$ glass systems

III.1. Glass Preparation

The $50P_2O_5$-xCaO-(50-x)K_2O and xAl_2O_3-(50-x)P_2O_5-10CaO-40K_2O glass systems were synthesized at room temperature using appropriate proportions of precursors, ammonium dihydrogen phosphate ($NH_4H_2PO_4$), calcium carbonate ($CaCO_3$), potassium carbonate (K_2CO_3), and aluminum oxide anhydrous extra pure (Al_2O_3) according to the following reaction schemes:

$$x\,K_2CO_3 + y\,CaCO_3 + 2z\,NH_4H_2PO_4 \rightarrow [x\,K_2O, y\,CaO, z\,P_2O_5] + 2z\,NH_3 + 3z\,H_2O + (x+y)\,CO_2$$

$$x\,K_2CO_3 + y\,CaCO_3 + 2z\,NH_4H_2PO_4 + t\,Al_2O_3 \rightarrow [x\,K_2O, y\,CaO, z\,P_2O_5, t\,Al_2O_3] + 2z\,NH_3 + 3z\,H_2O + (x+y)\,CO_2$$

The precursors were first weighed and mixed in a quartz mortar before being transferred to a porcelain crucible to preheat overnight at 120°C. The combination was then annealed at 200 to 500°C to discharge NH_3, H_2O, and CO_2. The temperature was then steadily increased to the melting point of about 800-1000°C (figure III.1). Finally, amorphous specimens were obtained by quenching the molten product to room temperature in the air.

The resulting phosphate glasses of $50P_2O_5$-xCaO-(50-x)K_2O, where x=0, 10, 20, 30, and 40 mol% were labeled as PCK_0, PCK_{10}, PCK_{20}, PCK_{30}, and PCK_{40} respectively. While $APCK_{2.5}$, $APCK_5$, $APCK_{7.5}$, $APCK_{10}$, $APCK_{12.5}$, and $APCK_{15}$, for the compositions of xAl_2O_3-(50-x)P_2O_5-10CaO-40K_2O glass system, where = 2.5, 5, 7.5, 10, 12.5, and 15 mol%. Table III.1 details the synthesized specimens' glass composition and codes.

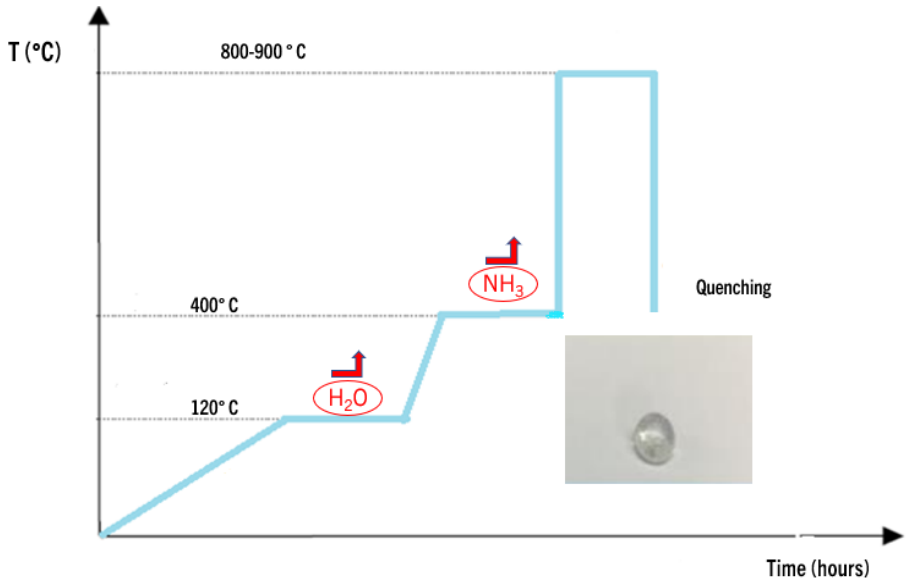

Figure III. 1. Thermal treatment cycle adapted for the glasses' elaboration

Table III. 1. Glass compositions and notations used.

Glass notation	Batch composition (%)			
	Al_2O_3	P_2O_5	CaO	K_2O
PCK_0	0	50	0	50
PCK_{10}	0	50	10	40
PCK_{20}	0	50	20	30
PCK_{30}	0	50	30	20
PCK_{40}	0	50	40	10
$APCK_{2.5}$	2.5	47.5	10	40
$APCK_5$	5	45	10	40
$APCK_{7.5}$	7.5	42.5	10	40
$APCK_{10}$	10	40	10	40
$APCK_{12.5}$	12.5	37.5	10	40
$APCK_{15}$	15	35	10	40

III.2. Structural properties of the studied glasses

III.2.1. X-ray diffraction analysis

The X-ray diffractograms of the synthesized compositions of xAl_2O_3-(50-x)P_2O_5-10CaO-40K_2O (where = 2.5, 5, 7.5, 10, 12.5, and 15) and 50P_2O_5-xCaO-(50-x)K_2O (where x=0, 10, 20, 30, and 40 mol%) are depicted in figures III.2 and III.3. They presented a broad hump between 20° and 40° (2θ) without sharp peaks, showing an amorphous structural character for all te glassy phosphate samples.

III.2.2. SEM-EDX analysis

Figures III.4, III.5, and III.6 illustrate SEM images of PCK_{30}, $APCK_{2.5}$, and $APCK_{15}$ systems. The presence of a homogeneous amorphous surface can be seen. The registered EDX elemental mapping scanned from two locations on the surface of d and in three separate sites on $APCK_{2.5}$ and $APCK_{15}$ show the fundamental composition similarities in the different regions of the samples, demonstrating the continuous distribution of the elements.

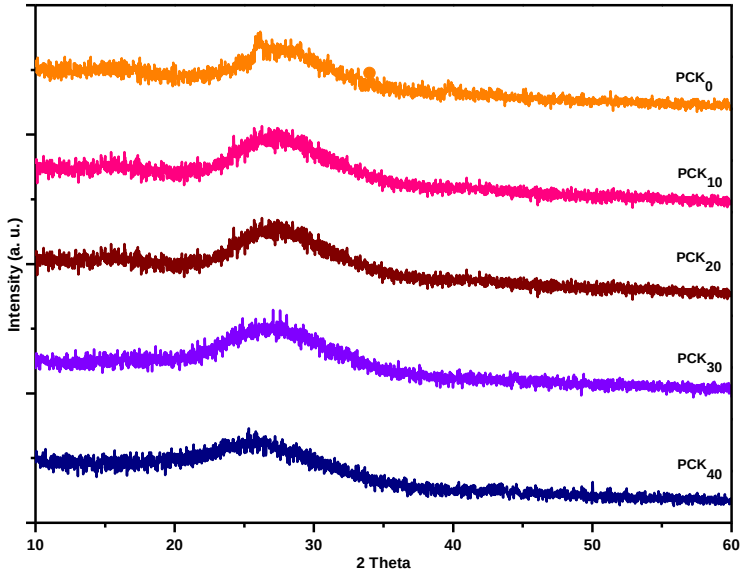

Figure III. 2. X-ray diffraction patterns for the five compositions studied of $50P_2O_5$-xCaO-(50-x)K_2O glass system, with: (PCK_0) x=0mol%, (PCK_{10}) x=10mol%, (PCK_{20}) x=20mol%, (PCK_{30}) x=30mol%, and (PCK_{40}) x=40mol%.

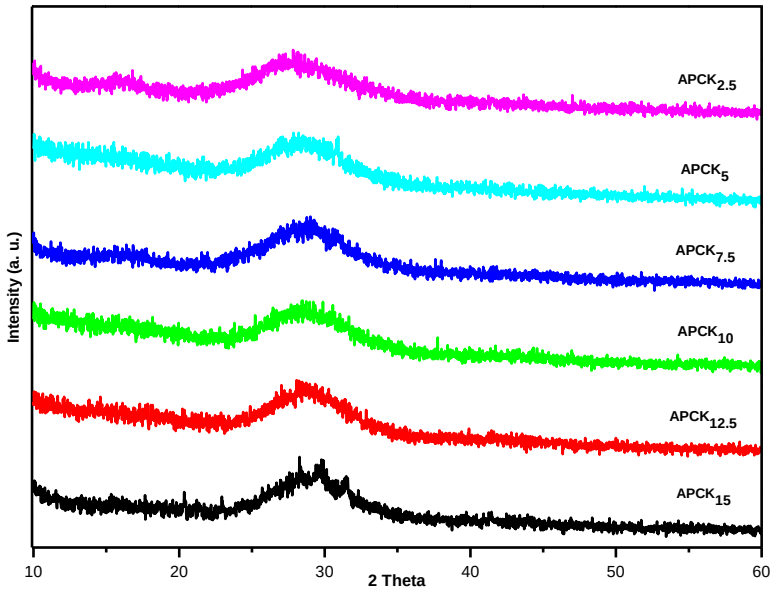

Figure III. 3. Diffractograms of the synthesized compositions of $APCK_x$, where x = 2.5, 5, 7.5, 10, 12.5, and 15 mol%.

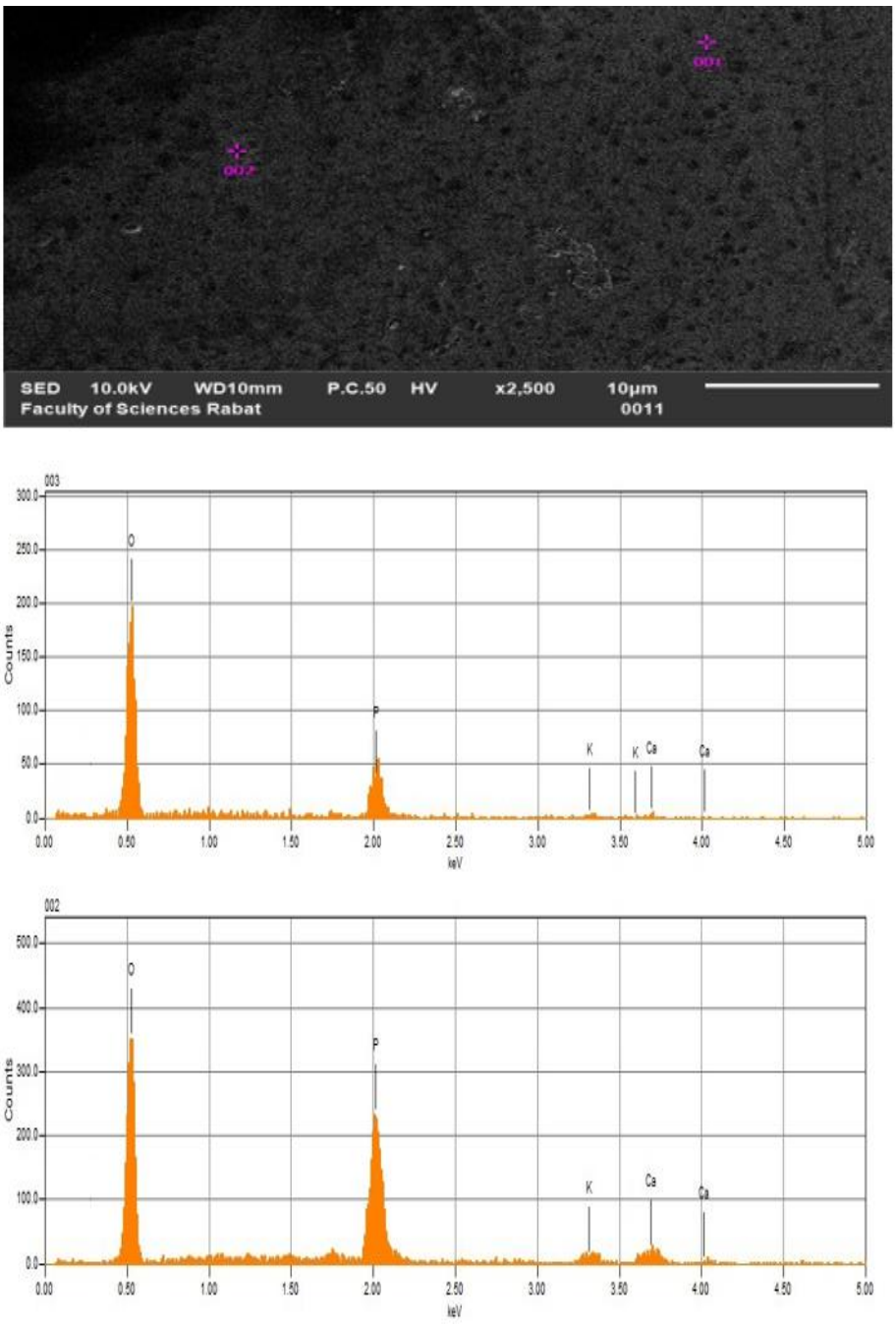

Figure III. 4. SEM image and EDS of $50P_2O_5$-30CaO-$20K_2O$.

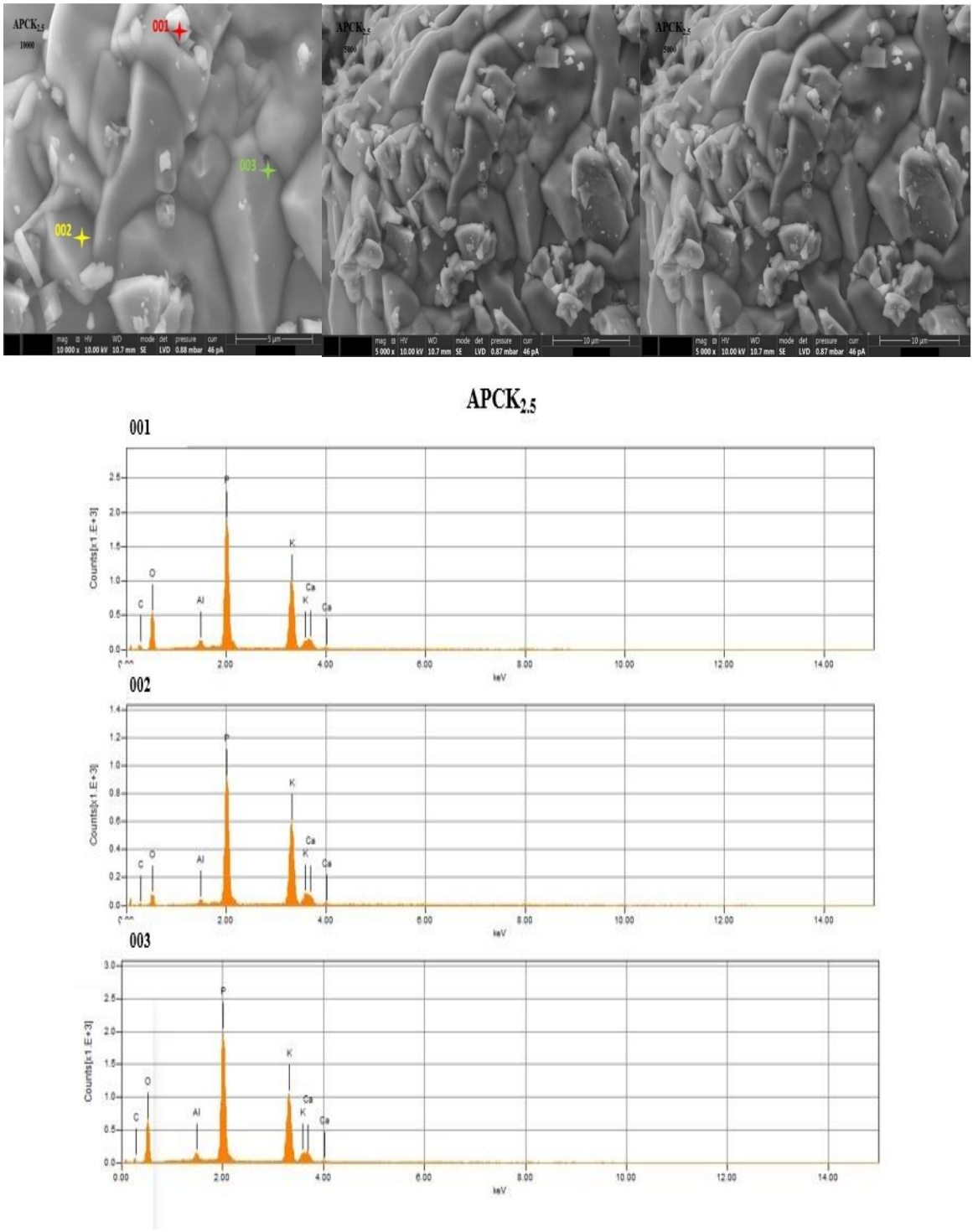

Figure III. 5. SEM-EDX analysis of $APCK_{2.5}$ glass sample.

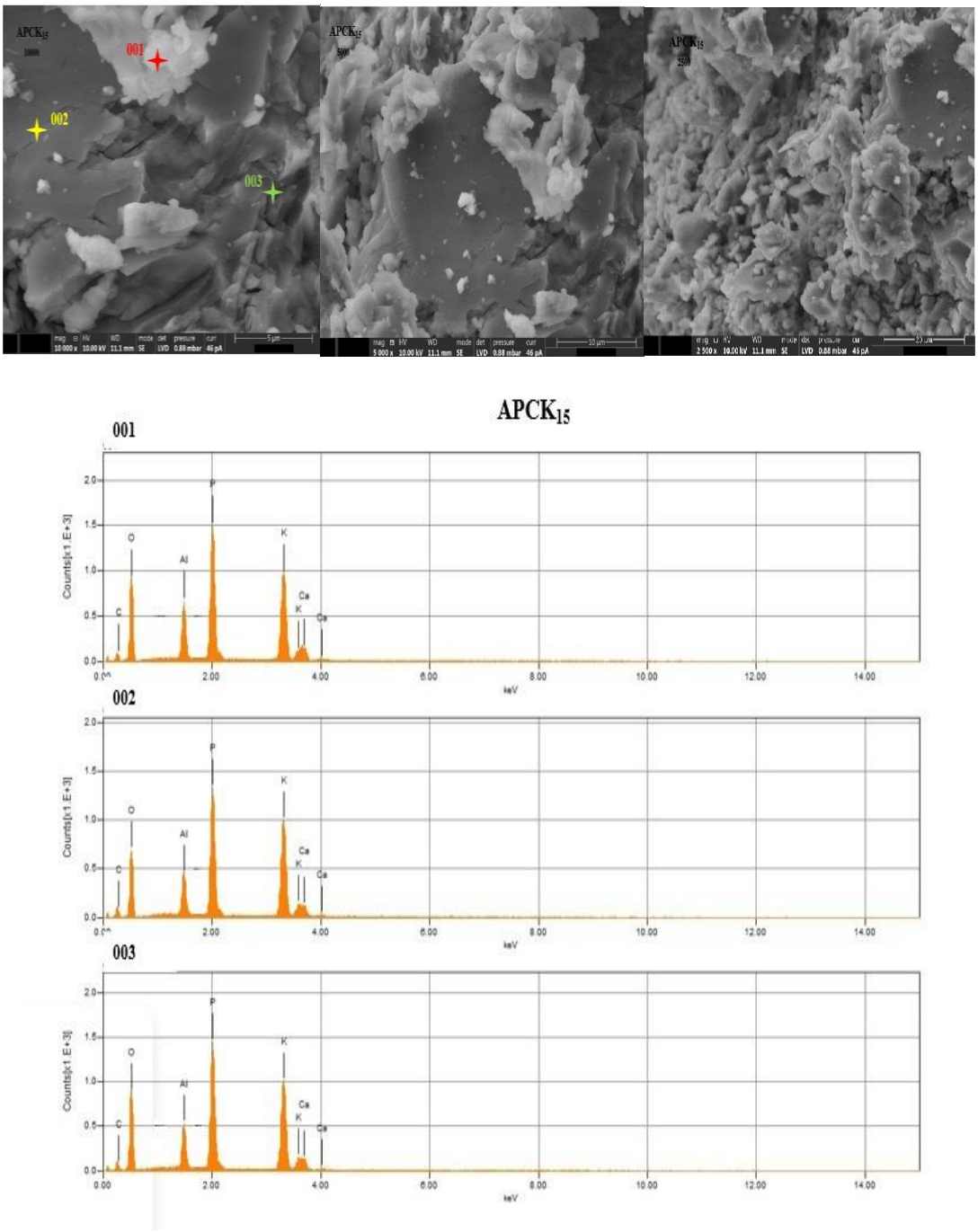

Figure III. 6. SEM-EDX analysis of $APCK_{15}$ glass sample.

III.2.3. FTIR and Raman spectroscopy analysis

III.2.3.1. $50P_2O_5$-xCaO-(50-x)K_2O ternary glass system

III.2.3.1.1. FTIR analysis

The FT-IR spectra of the glass samples are shown in figure III.7. The diverse vibration bands are identified based on the literature and listed in table III.2 [213–215].

The remarked bands at 1260 cm^{-1} are associated with the asymmetric stretching vibration $\nu_{as}(PO_2)$ of the bonds linking atoms of non-bridging oxygen (NBO) with phosphorus [45,216,217]. At the same time, the bands around 1180 cm^{-1} are ascribed to the symmetric stretching vibration $\nu_s(PO_2)$ [28,218]. The presence of bands near 1090 cm^{-1} is assigned to the asymmetric stretching vibration $\nu_{as}(PO_3)$. However, those near 1000 and 990 cm^{-1} are attributed to chain end groups [29]. The lines associated with asymmetric and symmetric stretching vibrations of P-O-P bridges are observed at around 880 cm^{-1} and 800-760 cm^{-1} [29,30,117,219,220]. The bands located at 530 cm^{-1} correspond to the deformational modes of P-O- (PO_4^{3-}) groups.

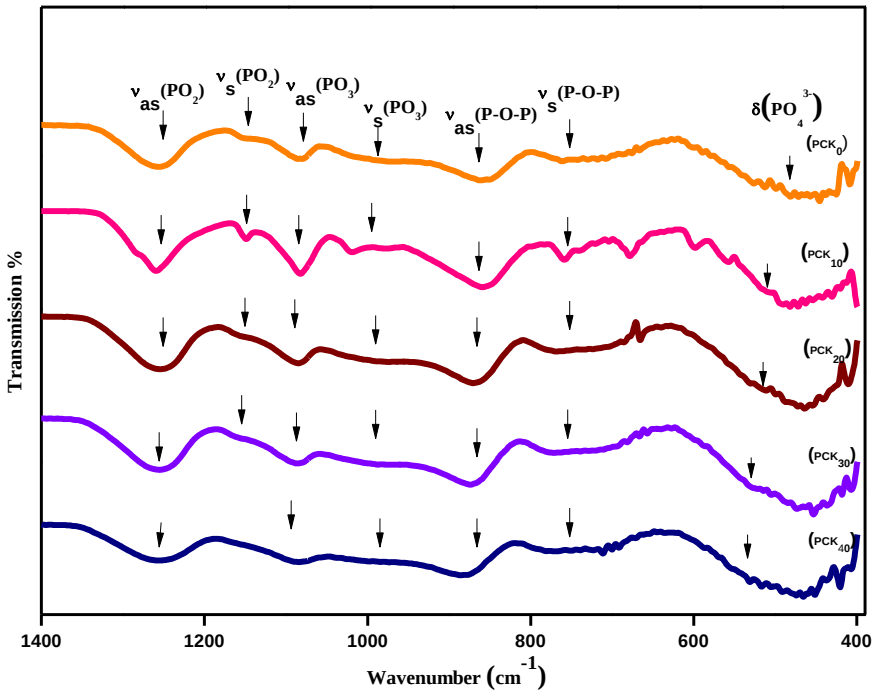

Figure III. 7. FTIR spectra of $50P_2O_5$-xCaO-(50-x)K_2O glass system with: (PCK_0) x=0mol%, (PCK_{10}) x=10mol%, (PCK_{20}) x=20mol%, (PCK_{30}) x=30mol%, and (PCK_{40}) x=40mol%.

III.2.3.1.2. Raman analysis

The Raman spectra of $50P_2O_5$-xCaO-(50-x)K_2O glasses (where x = 0, 10, 20, 30, and 40mol%) are shown in figure III.8. Seven peaks are visible in the spectra and listed in table III.2: 1258, 1175, 1098, 990, 780, 680, and 555 cm^{-1}.

The bands located at 1258 and 11175 cm^{-1} is attributed to the asymmetric and symmetric vibration νas ((PO_2) and νs(PO_2)) of the non-bridging oxygen atoms (NBO), which are linked to the phosphorus atoms (O-P-O) in metaphosphate chains (Q^2) [77,221–224]. While the bands observed at 1098 cm^{-1} and 990 cm^{-1} are characteristic of the asymmetric $\nu_{as}(PO_3)$ and the symmetric vibrations $\nu_s(PO_3)$ of NBO on Q^1 tetrahedral [225]. The bands sited at 780 and 680 cm^{-1} are associated with the asymmetric and symmetric stretching modes of oxygen bridged and related to phosphorus atoms (P-O-P), where two tetrahedral are connected in the phosphate chains [226–228]. However, the band situated at 555 cm^{-1} is correlated to the deformation modes of $P\text{-}O^-$ (PO_4^{3-}) groups [229].

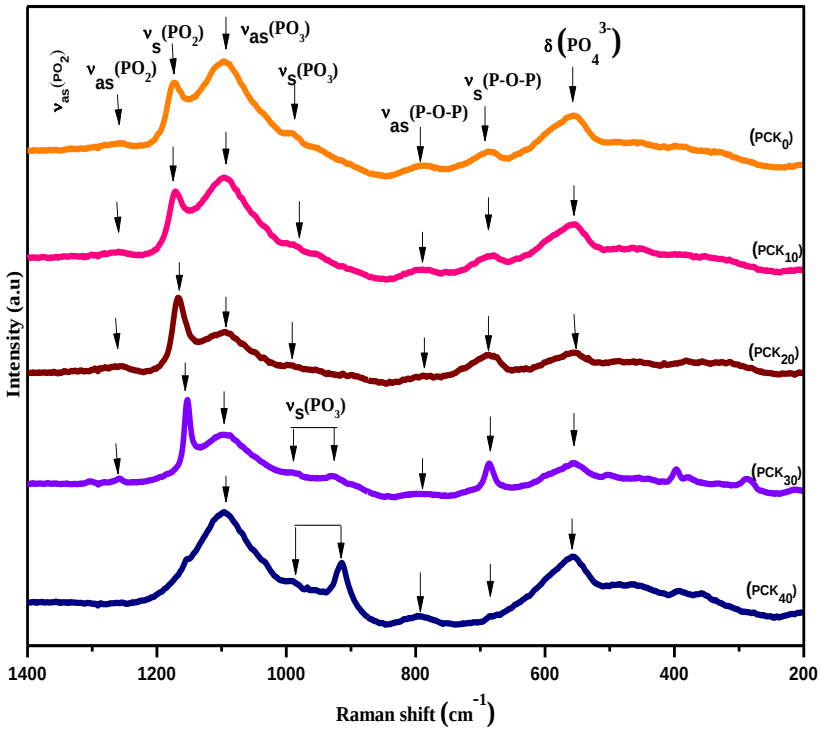

Figure III. 8. Raman spectra of $50P_2O_5$-xCaO-(50-x)K_2O glass system with: (PCK_0) x=0mol%, (PCK_{10}) x=10mol%, (PCK_{20}) x=20mol%, (PCK_{30}) x=30mol%, and (PCK_{40}) x=40mol%.

Table III. 2. Frequencies and attributions of IR and Raman bands of PCK_0, PCK_{10}, PCK_{20}, PCK_{30}, and PCK_{40} compositions of $50P_2O_5$-xCaO-(50-x)K_2O glass system.

Samples	**PCK_0**		**PCK_{10}**		**PCK_{20}**		**PCK_{30}**		**PCK_{40}**		**Attributions**
Frequencies in cm^{-1}	**IR**	**Raman**	**IR**	**Raman**	**IR**	**Raman**	**IR**	**Raman**	**IR**	**Raman**	
	1260	1258	1260	1258	1260	1258	1260	1258	1265	---	$\nu_{as}(PO_2)$
	1180	1175	1180	1175	1180	1175	1180	1175	1180	1175	$\nu_{s}(PO_2)$
	1095	1098	1095	1098	1095	1098	1095	1098	1095	1098	$\nu_{as}(PO_3)$
	1000	990	1000	990	1000	990	1000	990	1000	990	$\nu_{s}(PO_3)$
	880	780	880	780	880	780	880	780	880	780	$(POP)_{as}$
	800	680	800	680	800	680	800	680	800	680	$(POP)_{s}$
	530	550	530	550	530	550	530	550	530	550	$\delta(PO_4^{3-})$

III.2.3.2. xAl_2O_3-$(50-x)P_2O_5$-10CaO-$40K_2O$ quaternary glass system

III.2.3.2.1. FTIR analysis

The FTIR spectra of the synthesized $APCK_x$ (x = 2.5, 5, 7.5, 10, 12.5, and 15 mol %) glasses with various compositions of alumina are presented in figure III.9. Characteristic bands associated with the addition of Al_2O_3 are shown, which are consistent with designations for phosphate materials [34,36,230]. In figure III.9, the $APCK_x$ glasses exhibited six IR bands (listed in table III.3). The peak at ~ 1259 cm^{-1} is ascribed to the vibration of P=O and the asymmetric stretching vibration of PO_2' υas (PO_2)'. This peak no longer appears in the spectra where the compositions of Al_2O_3 exceed 10 mol %. The peak at ~ 1186 cm^{-1} is owing to the symmetric stretching of PO_2' υ_s (PO_2)'. The band's intensity reduces with increasing Al_2O_3 content. The band at 1079 cm^{-1} is identified as the asymmetric stretching of PO_3' υas (PO_3)'. The band that appears at ~ 1026 cm^{-1} is due to the symmetric vibration of PO_3 υ_s(PO_3). However, the tiny band at ~ 1042 cm^{-1}, when alumina content reaches 5%, is due to the PO_4 vibration. When the Al_2O_3 proportion rises, the concentration of PO_4 increases, which fortifies the glass structure. The band at ~ 865 cm^{-1} is assigned to the asymmetric stretching of POP' υ_{as} (POP)'. The peak at ~ 740 cm^{-1} is associated with POP' υ_s (POP)' symmetric stretching. The peak at ~ 520 cm^{-1} is associated with the P-O-P vibration in [PO_4]. Moreover, within the range of 400-500 cm^{-1} and 700- 800 cm^{-1}, bending vibrations of P-O-P units [38] overlapped with the vibrations of [AlO_6] and [AlO_4] structural units, respectively [39–41,43]. Making their distinction concerning the vibrations given to the phosphate groups is difficult to discern.

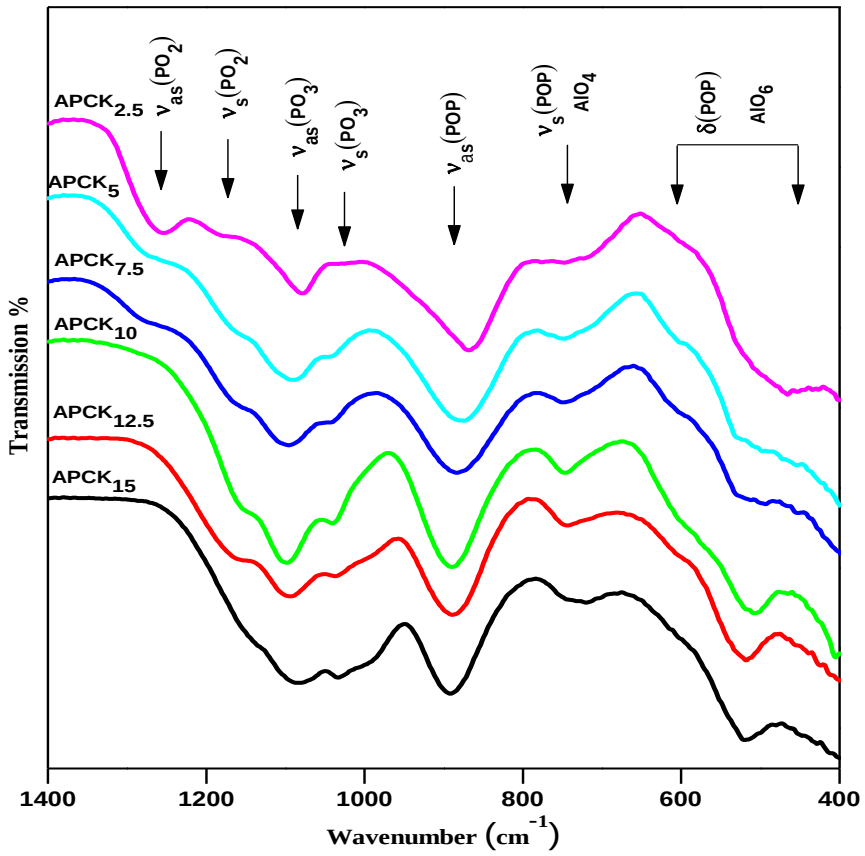

Figure III. 9. IR spectra for the synthesized compositions of APCKx, where x = 2.5, 5, 7.5, 10, 12.5, and 15 mol %.

III.2.3.2.2. Raman analysis

The Raman spectrum of $APCK_x$ (x = 2.5, 5, 7.5, 10, 12.5, and 15 mol %) glass system illustrated in figure III.10, were recorded in the frequency range from 200-1400 cm^{-1}. Raman peaks occur at ~1277 cm^{-1}, ~1158 cm^{-1}, ~1059 cm^{-1}, ~896 cm^{-1}, ~715 cm^{-1}, ~533 cm^{-1}, ~469 cm^{-1}, and ~338 cm^{-1} (listed in table III.3). We have made the following band assignments for our spectra:

- ~1277 cm^{-1} attributed to PO_2 asymmetric stretching of non-bridging oxygen, in Q^2 units (υ_{as} (PO_2), (Q^2));
- ~1158 cm^{-1} assigned to PO_2 symmetric stretching of non-bridging oxygen, in Q^2 units (υ_s (PO_2), (Q^2));
- ~1060 cm^{-1} identified as the symmetric vibration PO_3 groups of non-bridging oxygen on Q^1 (υ_{as} (PO_3), (Q^1));
- ~1023 cm^{-1} identified as symmetric vibration PO_3 groups of nonbridging oxygen on Q^1 (υ_s (PO_3), (Q^1));

- ~896 cm^{-1} attributed to the asymmetric stretching vibration P-O-P of bridging oxygen in PO_4 tetrahedron in Q^1 groups (υ_{as} (P-O-P), (Q^1)) [35,44,45];
- ~715 cm^{-1} attributed to the symmetric stretching of the bridging oxygen in Q^2 units (υ_s (P-O-P), (Q^2)), overlapped with the vibrations of the AlO_4 structural units[231];
- ~533 cm^{-1} identified as POP vibrations in PO_4 and v(Al–O), the vibrations involving the Al-O bonds [232–234].
- ~469 cm^{-1} bending vibration of PO_2^- units, overlapped with the vibrations of AlO_6 structural units [234].
- ~338 cm^{-1} O–P–O bending motions [235].

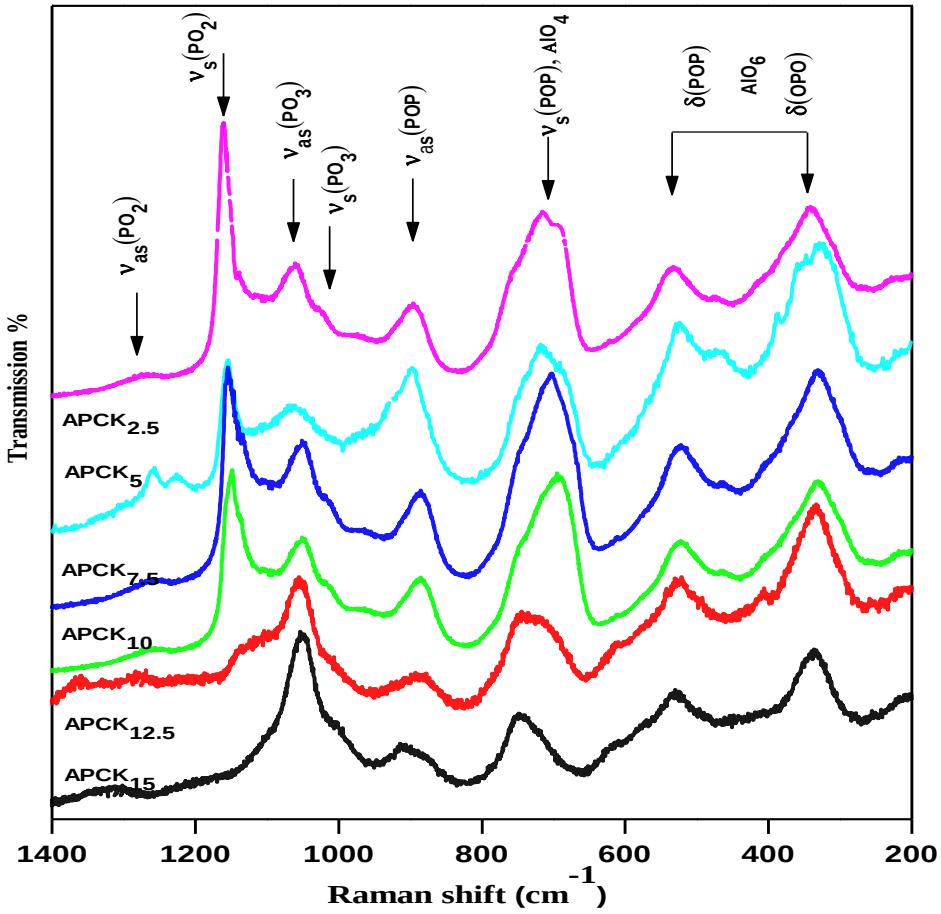

Figure III. 10. Raman spectra for the synthesized compositions of APCKx, where x = 2.5, 5, 7.5, 10, 12.5, and 15 mol %.

Table III. 3. Frequencies and attributions of IR and Raman bands of APCKx glass system, where x = 2.5, 5, 7.5, 10, 12.5, and 15 mol%.

Samples	$APCK_{2.5}$		$APCK_5$		$APCK_{7.5}$		$APCK_{10}$		$APCK_{12.5}$		$APCK_{15}$		Attributions
	IR	Raman	IR	Raman	IR	Raman	IR	Raman	IR	Raman	IR	Raman	
Wavenumber in cm^{-1}	1259	1277	1259	1277	1259	1277	---	---	---	---	---	---	P=O, $\upsilon_{as}(PO_2)$
	1186	1158	1186	1158	1186	1158	1186	1158	1186	1158	1186	1158	$\upsilon_s(PO_2)$
	1079	1060	1079	1060	1079	1060	1079	1060	1079	1060	1079	1060	$\upsilon_{as}(PO_3)$
	1026	1023	1026	1023	1026	1023	1026	1023	1026	1023	1026	1023	$\upsilon_s(PO_3)$
	865	896	865	896	865	896	865	896	865	896	865	896	υ_{as} (POP)
	740	715	740	715	740	715	740	715	740	715	740	715	υ_s (POP) AlO_4
	520	~533-~338	520	~533-~338	520	~533-~338	520	~533-~338	520	~533-~338	520	~533-~338	δ(POP) δ(OPO) AlO_6 ν(Al–O)

III.2.3.2. Results and discussion

CaO inclusion into K_2O-P_2O_5 generates almost the disappearance of $\nu_s(PO_2)$ $\nu_{as}(PO_3)$ and the reduction in the intensity of $\nu_s(PO_3)$. This phenomenon is because PO_3 is considered a phosphate chain ending group. Besides, the apparition of P-O-Ca bonds in the glass network, when CaO substitutes K_2O, causes the shrinkage of the NBO and the growth in the cross-linking. The depolymerization of P-O-P bonds in the analyzed glassy samples is mainly due to the rise of CaO content, causing a slight change in the spectra [236,237]. Furthermore, the existence of pyrophosphate groups could be explained by the presence of two specific bands related to the symmetric and asymmetric vibrations of the P-O-P Bridge [237].

As Al_2O_3 content increases, the vibration of P=O, υ_{as} (PO_2), and υ_s (PO_2) reduce drastically and shifted towards lower frequencies before they vanished and no longer appeared for x=15% Al_2O_3, the principal peaks of phosphate have been diminished as alumina content grows. The latter band may be connected to the bridging of Al with oxygen atoms to form AlO_4 [238], which plays a former role [239–241]. So, some AlO_4 structural units penetrate the phosphate network as formers, and the characteristic bands of phosphate glasses will be modified by the quantity of these oxygens [242]. The growth of Al_2O_3 rather than P_2O_5 increases the polymerization degree of the P-O-P in $APCK_x$ glass system by creating stronger P-O-Al bonds. Which delivers a more reticulated and stiff glass network.

III.3. Thermo-physical characterization of the studied glasses

III.3.1. Density (ρ) and molar volume (V_m)

The density is a useful tool for investigating changes in the structure of phosphate glasses. It is, nevertheless, influenced by the compactness of the glassy structure. Glass network density (ρ) and molar volume (V_m) is affected by a variety of parameters, including structure, coordination number, cross-link density, and interstitial space dimensionality [243]. The determination of density values was at room temperature using Archimedes' principle.

The molar volume V_m of the investigated glasses was calculated using their density and molar mass M: $V_m=M/\rho$

The density and molar volume values obtained are summarized in Table III.4 and shown as a function of composition in figures III.11 and III.12.

Table III.4 and figures III.11 and III.12 show that the density of the glasses of both synthesized systems increases continuously both when potassium is replaced by calcium ($50P_2O_5$-xCaO-(50-x)K_2O) or P_2O_5 is substituted by Al_2O_3 (xAl_2O_3-(50-x)P_2O_5-10CaO-40K_2O) while the

molar volume decreases continuously.

Figure III.11 graphically depicts the plots of V_m values. The latter increases as the CaO level increases. This finding could be explained by replacing K_2O, which has a low density (2.35 g/cm^3), with CaO, which has a high density (3.34 g/cm^3). Similarly, this behavior may be explained by differences in the atomic masses of Ca^{2+} and K^+. Also, in figure III.12, the density has increased with the incremental expansion of alumina content; this growth in density is owing to the substitution of P_2O_5 (2.39 g/cm^3) by Al_2O_3 (2.95 g/cm^3), having a higher density. Nevertheless, the molar volume delivered a delinquent behavior of dropping for both glass systems. Whereas the cation exchange, the chain length is reduced.

Introducing CaO or Al_2O_3 to the glass system cross-links the glass network and contracts the stacking of oxygen ions, creating new Ca-O-P and Al-O-P bonds that replace the old P-O-P bounds. Consequently, this substitution reduces the molar volume, shrinks the glass network, and increases the density [1,35].

Table III. 4. Glass composition (mol %), density ρ (g/cm³), molar volume Vm (cm³/mol), glass transition temperature T_g (°C), crystallization temperature T_x (°C), and thermal stability T_x-T_g (°C) of $50P_2O_5$-xCaO-(50-x)K_2O and xAl_2O_3-(50-x)P_2O_5-10CaO-40K_2O glass system.

Glass notation	Batch composition (%)				ρ (g/cm^3)	V_m (cm^3/mol)	T_g (°C)	T_x (°C)	T_x-T_g (°C)
	Al_2O_3	P_2O_5	CaO	K_2O					
PCK_0	0	50	0	50	2.30	52.34	254	----	----
PCK_{10}	0	50	10	40	2.43	50.54	300	----	----
PCK_{20}	0	50	20	30	2.48	47.98	341	----	----
PCK_{30}	0	50	30	20	2.49	46.26	386	----	----
PCK_{40}	0	50	40	10	2.57	43.17	471	----	----
$APCK_{2.5}$	2.5	47.5	10	40	2.490	45.486	342.84	437.46	94.62
$APCK_5$	5	45	10	40	2.526	44.442	375.42	445.97	70.55
$APCK_{7.5}$	7.5	42.5	10	40	2.533	43.925	377.98	446.89	68.91
$APCK_{10}$	10	40	10	40	2.549	43.257	418.72	----	----
$APCK_{12.5}$	12.5	37.5	10	40	2.551	42.831	426.3	542	115.7
$APCK_{15}$	15	35	10	40	2.593	41.752	443.48	546.68	103.2

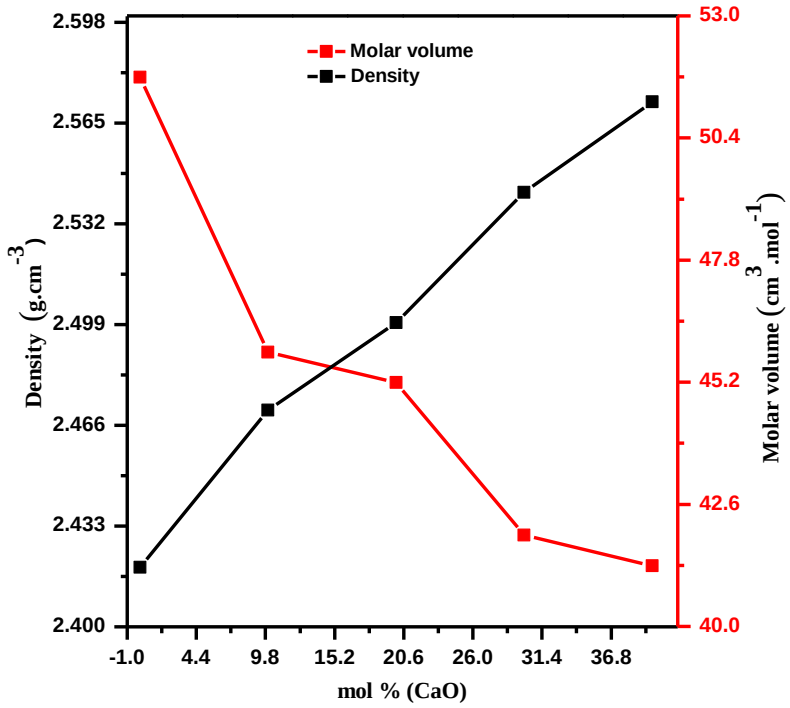

Figure III. 11. Variation of density and molar volume of Potassium Phosphate glasses with CaO content.

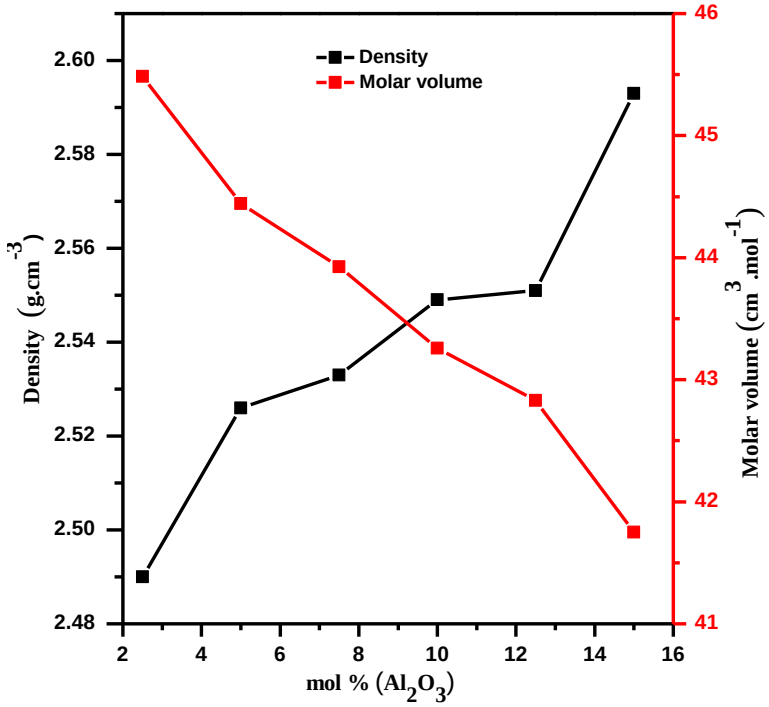

Figure III. 12. Densities and molar volumes in the function of Al_2O_3 content of APCKx glasses.

III.3.2. Thermal analysis by Differential Scanning Calorimetry (DSC)

The glass transition temperature measures the temperature at which the system's viscosity reaches a value of 10^{13} poise. Its value is correlated to the rigidity of the network. It depends on

its degree of interconnectivity and the organization of atoms within the glassy network. It is strongly linked to the density of covalent bonds to the length and number of bonds between cations and anions (oxygen). It then depicts the free volume between the structural entities [244]. The values of T_g have a direct relationship with the strength and density of the bonds. A high value of T_g corresponds to high connectivity of the glass network.

Figures III.13 and III.14 display the DSC thermal analysis curves of the $50P_2O_5$-xCaO-(50-x)K_2O and xAl_2O_3-(50-x)P_2O_5-10CaO-40K_2O glass systems. Table III.4 contains the values of the glass transition temperatures T_g and the onset crystallization temperature T_x. Figures III.15 and III.16 illustrate the differences in T_g as a function of CaO and Al_2O_3 content.

In figure III.13, T_g values vary from 254°C (x=0%) for potassium phosphate to 471°C (x=40%). The substitution of K_2O by CaO resulted in a significant increase in T_g. In figure III.14 T_g and T_x values show an improved trend. A steady ascent of 101°C is registered amongst extreme compositions (x=2.5 and 15%). The line graphs show that T_g values increase dramatically with CaO and Al_2O_3 composition, and, as a result, a significant change in the glass structure.

In $50P_2O_5$-xCaO-(50-x)K_2O glass system, replacing Potassium with Calcium that has a higher electronegativity (1eV), leads to create P-Ca-O new bonds with a better covalent character. While replacing P_2O_5 with Al_2O_3 in xAl_2O_3-(50-x)P_2O_5-10CaO-40K_2O glassy system, Al^{3+} delivered by alumina will contribute to the glass structure and improve its compactness [219]. Besides, the glass structure can be broken by Al_2O_3, creating a new, more stable bond P-O-Al as an alternative of P-O-P [43,245], making the glass more rigid (this result agrees with the evolution of density). Hence, the glass network evolves additional compactness as Al_2O_3 proportions grow, which conducts T_g and T_x higher values.

The thermal stability of the network is associated with T_x -T_g. We can classify the investigated specimens into two categories; good glass former if T_x-T_g > 90 °C and poor glass former if T_x-T_g < 90 °C [234]. From table III.4, we can notice that the synthesized glasses containing 2.5, 12.5, and 15% of Al_2O_3 have a greater T_x-T_g value. This represents a more stable glass-forming power. Nevertheless, samples with 5 and 7.5% Al_2O_3 have lower thermal stability. In other words, the different rearrangement of the glass entities when they are above T_g and heading to lower crystallization temperatures causes a drop in the thermal stability factor.

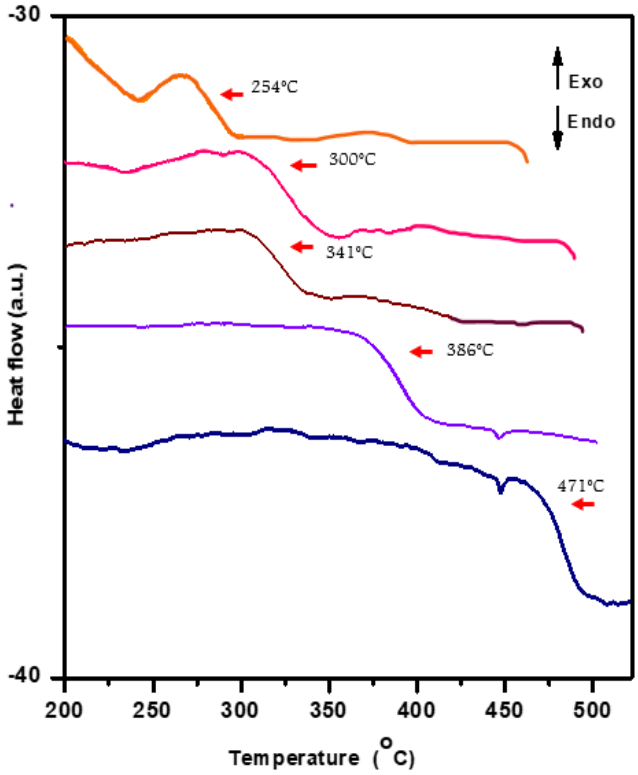

Figure III. 13. Differential Scanning Calorimetry (DSC) curve of the synthesized glassy sample of the system $50P_2O_5$-$xCaO$-$(50-x)K_2O$ whereas x= 0, 10, 20, 30, 40mol %.

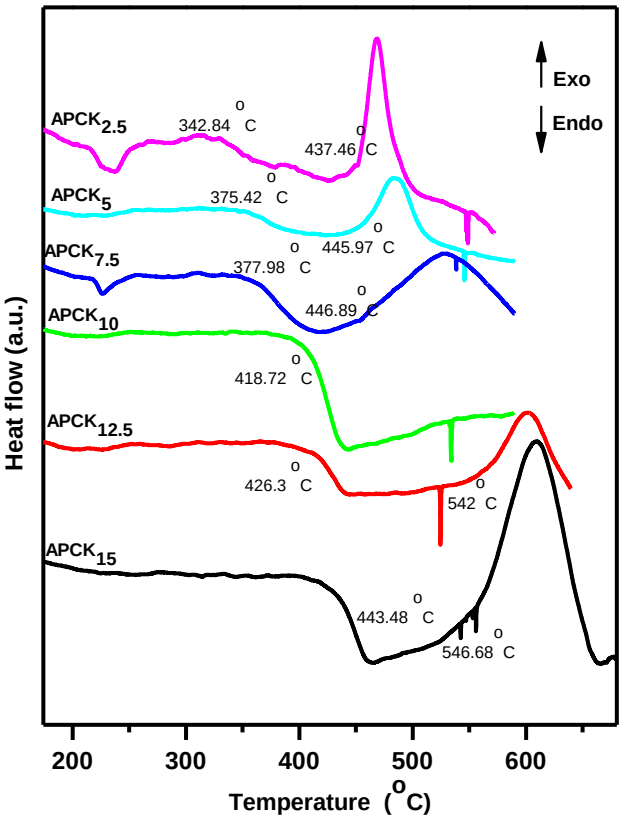

Figure III. 14. DSC spectra for the synthesized compositions of APCKx, where x = 2.5, 5, 7.5, 10, 12.5, and 15 mol %.

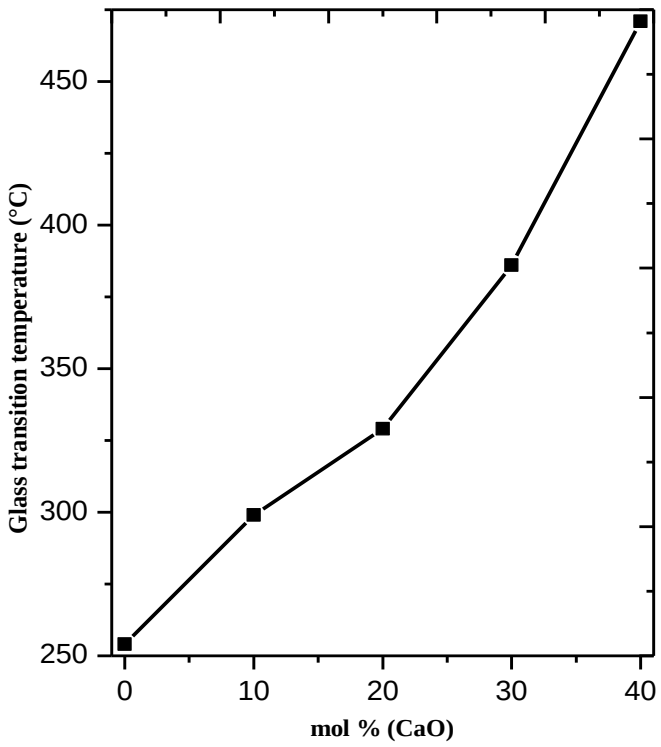

Figure III. 15. Variation of glass transition temperature (Tg) composition versus glass composition for the system $50P_2O_5$-$xCaO$-$(50-x)K_2O$ (x= 0, 10, 20, 30, and 40mol %).

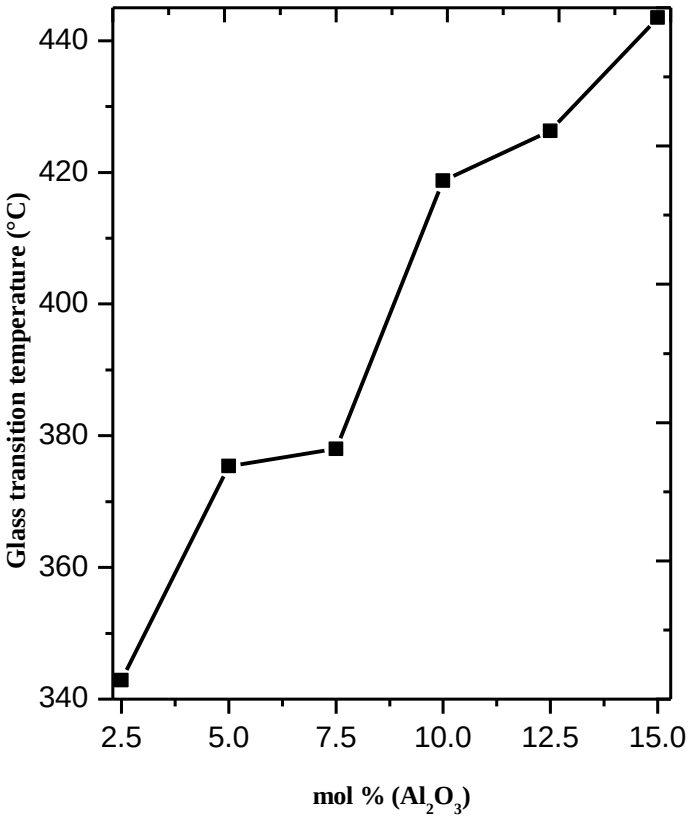

Figure III. 16. Variation of glass transition temperature (Tg) composition versus glass composition for the APCKx system where x = 2.5, 5, 7.5, 10, 12.5, and 15 mol %.

III.4. Chemical durability

Phosphate glasses have low chemical durability, limiting their use. However, it has been demonstrated that adding oxides considerably enhances their corrosion resistance and chemical durability, making them analogous to silicate glasses like ZnO, Al_2O_3, and TiO_2, these oxides generate M-O-P bonds that are relatively stable [22–24].

We once investigated the chemical durability of a PCK glassy system. However, the samples spalled and dissociated after only 24 hours of immersion in the solutions. So, with the insertion of Al_2O_3, the glass was upgraded to a quaternary system to enhance its efficiency.

In this section, we exhibit the dissolution of our boosted APCK quaternary glassy system under diverse conditions in a closed and non-renewed environment. All leaching studies were carried out in a sealed, unstirred setting. We immersed glass blocks in an aggressive solution so that all specimen surfaces were in touch. Our trials were all carried out at room temperature.

III.4.1. Weight loss (WL) and pH variation of APCK glass system

The total weight loss is expressed by the following formula:

$$\textbf{Weight loss} = \frac{\Delta m}{S}$$

Where ***m :*** mass loss of the glass sample (mg)

S : surface of the sample (cm^2)

The chemical durability of the system APCK was determined by weight loss (WL) measurements versus leaching time in deionized water, HCl, and NaOH solutions, as shown in figures III.17.a, III.18.a, and III.19.a, respectively. We have also investigated pH variations as a function of immersion time for the system APCK; results are exhibited in the III.17.b, III.18.b, and III.19.b figures.

III.4.1.1. In HCl solution

During the vitreous samples' immersion in HCl solution, we remarked a dramatic increase in WL after the first 48 hours for the samples with alumina content (5mol%), while the sample containing 7.5% Al_2O_3 grew drastically after 200 hours of immersion. Moreover, the sample with 2.5% Al_2O_3 tended to crack and spall in the solution after approximately 75 hours.

However, specimens with an Al_2O_3 content of 10 mol% faced a weak WL throughout the experiment in an acidic solution. The pH grew during the first immersion time (less than 144h), then stabilized towards a maximum value of pH=6 (figure III.17).

III.4.1.2. In NaOH solution

Samples with Al_2O_3 content ≤7.5% express a continuous increase of WL throughout the entire 360 hours of immersion in NaOH solution (pH=12), while samples containing a percentage of alumina ≥10% showed light WL during the experiment reaching a minimum value for the specimen rich in Al_2O_3 (15 mol%). The values of pH decrease drastically for the samples as the immersion time increases toward a minimum pH=9 (figure III.18).

III.4.1.3. In bi-distilled water

WL for the samples with alumina ≤7.5% rose significantly for the first 70 hours, while $APCK_{2.5}$ cracked and spalled in the solution after 75 hours of immersion. The samples containing ≥10mol% of Al_2O_3 faced a diminutive WL throughout the 350 hours of immersion in a neutral solution. The dissolution of the six samples started with an increase in the pH in the first 50 hours, then a progressive decrease during the rest of the experiment (figure III.19).

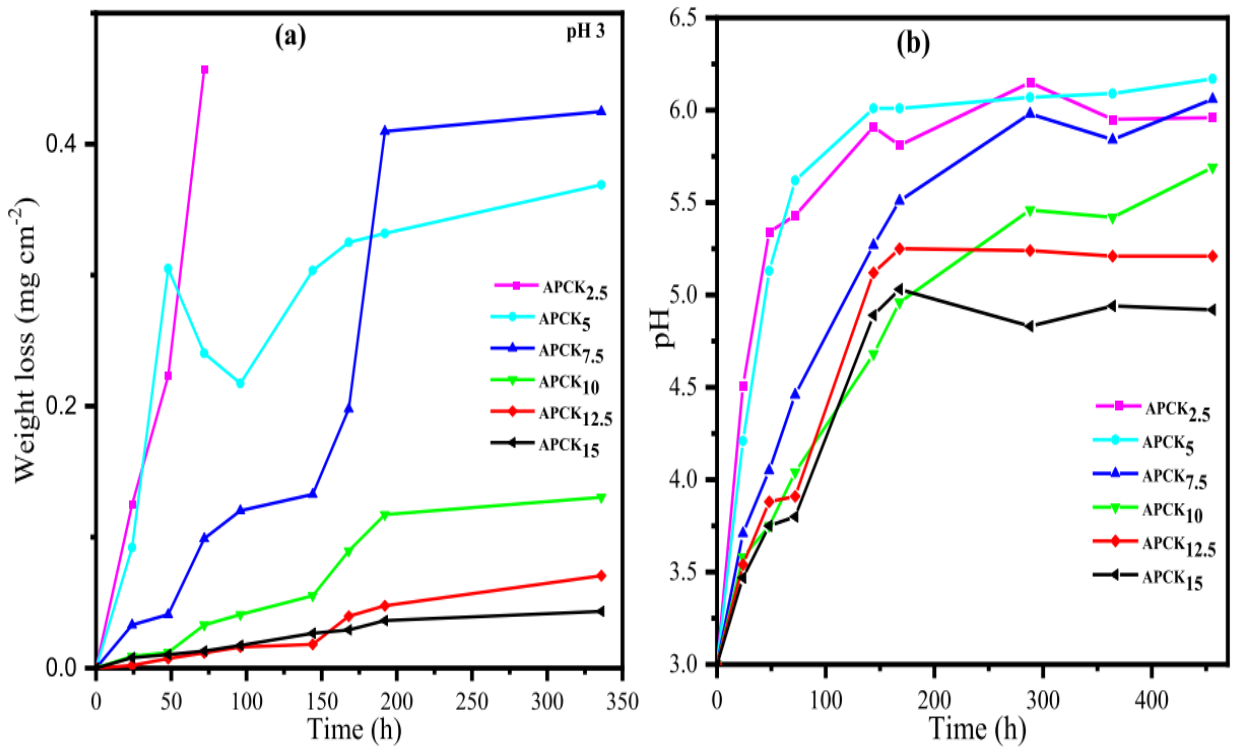

Figure III. 17. Weight loss (a) and variation of the pH solution (b) as a function of time spent submersing the APCK glass series in HCl solution.

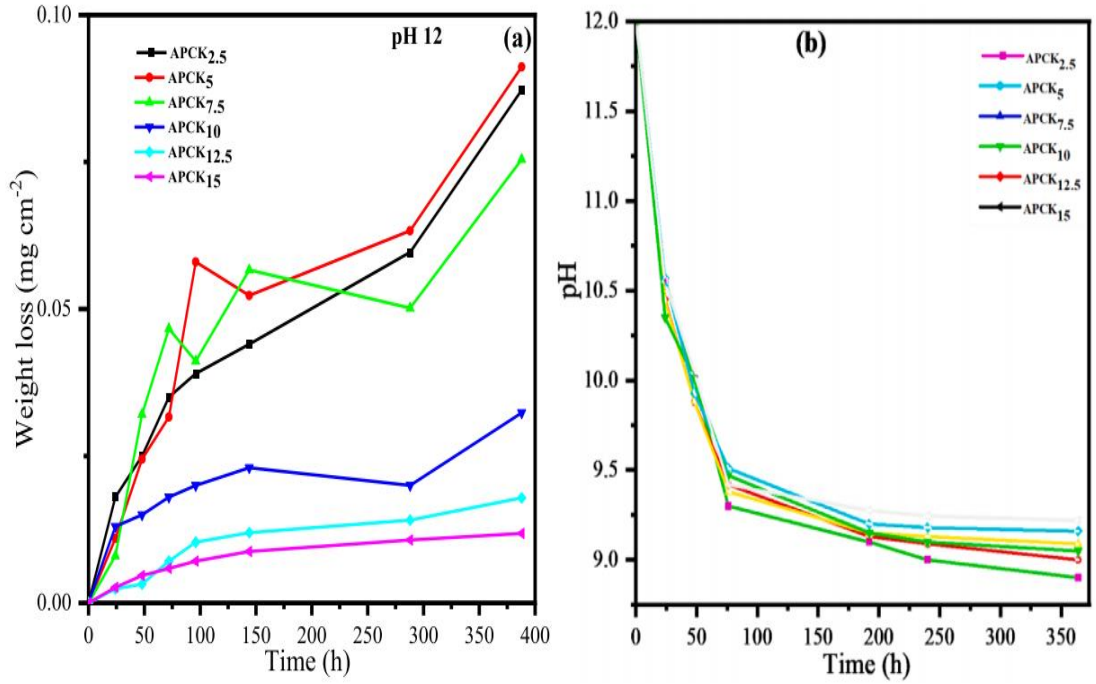

Figure III. 18. Weight loss (a) and variation in the pH solution (b) as a function of time spent submersing the APCK glass series in NaOH solution.

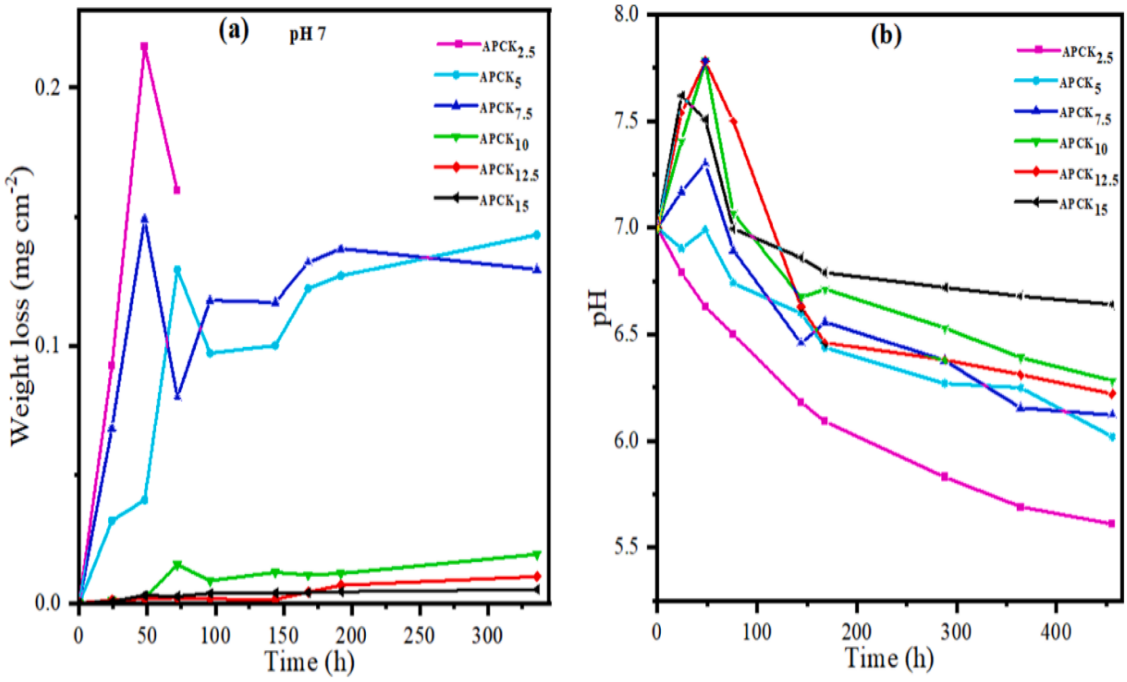

Figure III. 19. Weight loss (a) and variation in the pH solution (b) as a function of time spent submersing the APCK glass series in deionized water.

III.4.2. Dissolution rate (DR) of APCK glass system

The dissolution rate is calculated by the following equation:

$$DR = \frac{\Delta m}{St}$$

Where ***t*** is the immersion time (min).

Figure III.20 illustrates the investigations gathered on the effect of alumina proportions on the log of dissolution rate (DR) values of glasses immersed in various solutions: deionized water (pH=7), HCl solution (pH=3), and NaOH solution (pH=12).

The DR values continue to diminish steadily in neutral and acidic solutions. Still, $APCK_{2.5}$ samples spalled in water and dissociated after 72 hours of immersion. Moreover, the DR values of the other specimens shrink progressively throughout the experiment. On the other hand, in the basic solution, the DR of the six vitreous samples decreases progressively to a minimum value after 336 hours of immersion.

The vast field of dissolution rates studied for phosphate glasses can be described based on the glass composition. The addition of modifier ions to phosphate glasses, such as K_2O, Na_2O, MgO, BaO, (…), is known to affect their chemical durability strongly [246]. Thus, Minami and Mackenzi [247] were the first to study the effect of alumina on glasses generally, discovering that the association of Al_2O_3 presented to serve slight water durability, extensive acid durability, and indistinguishably basic durability. Moreover, the work by Bunker et al. [167] described the tiniest details of the effect of aqueous solution on phosphate glasses. They informed that while exposing phosphate glasses to water, there is a propensity for a hydration operation to occur at the glass's surface, dominating the beginning of the dissolution reactions, While Liu et al. [110] suggested that the hydration reaction only initiates the network breakage, which is to say that the hydrolysis reaction is the effective dominant reaction. So, in figure III.19, the dissolution process is initiated by a growth of pH, which can be hydration of the surface of the glass. A decrease in pH values due to the water molecule's diffusion in the glass system causes the OH^- ions to be consumed and phosphoric acid to be generated [113,248,249]. In figure III.18, the rise of pH in an acidic solution was associated with the extraction of cations by ionic exchange mechanisms, between hydrogen and mobile ions of the glass network, at the start of the glass corrosion, leading to the accumulation of OH^- ions in the solution. Besides, the experiment intensifies the entrance of H_2O into the samples and, thereby, the corrosion by hydrolysis [249]. In a NaOH solution, in figure 9, we assume that depletion of OH^- ions during glass dissolution

improves the chain hydrolysis, while discharging the proton H^+ toward the solution, chain hydrolysis stimulates the decrease of the pH [167].

Introducing Al_2O_3 into the xAl_2O_3-(50-x)P_2O_5-10CaO-40K_2O system interrupts P-O-P links and creates a novel P-O-Al system. This increases the glass density (ρ) (figure III.11) while turning the glass structure more compact and improving the aqueous durability as well as the chemical stability of the glasses. Trivalent cations such as Al^{3+} are effective cross-linking agent that makes glasses' structure durable to aqueous attack and then resistant to hydrolysis [250]. Generally, the shrinkage in WL with the expansion of Al_2O_3 content is allotted to the replacement of P-O-P bonds easily hydrolyzable by P-O-Al bonds that are more hydration resistant.

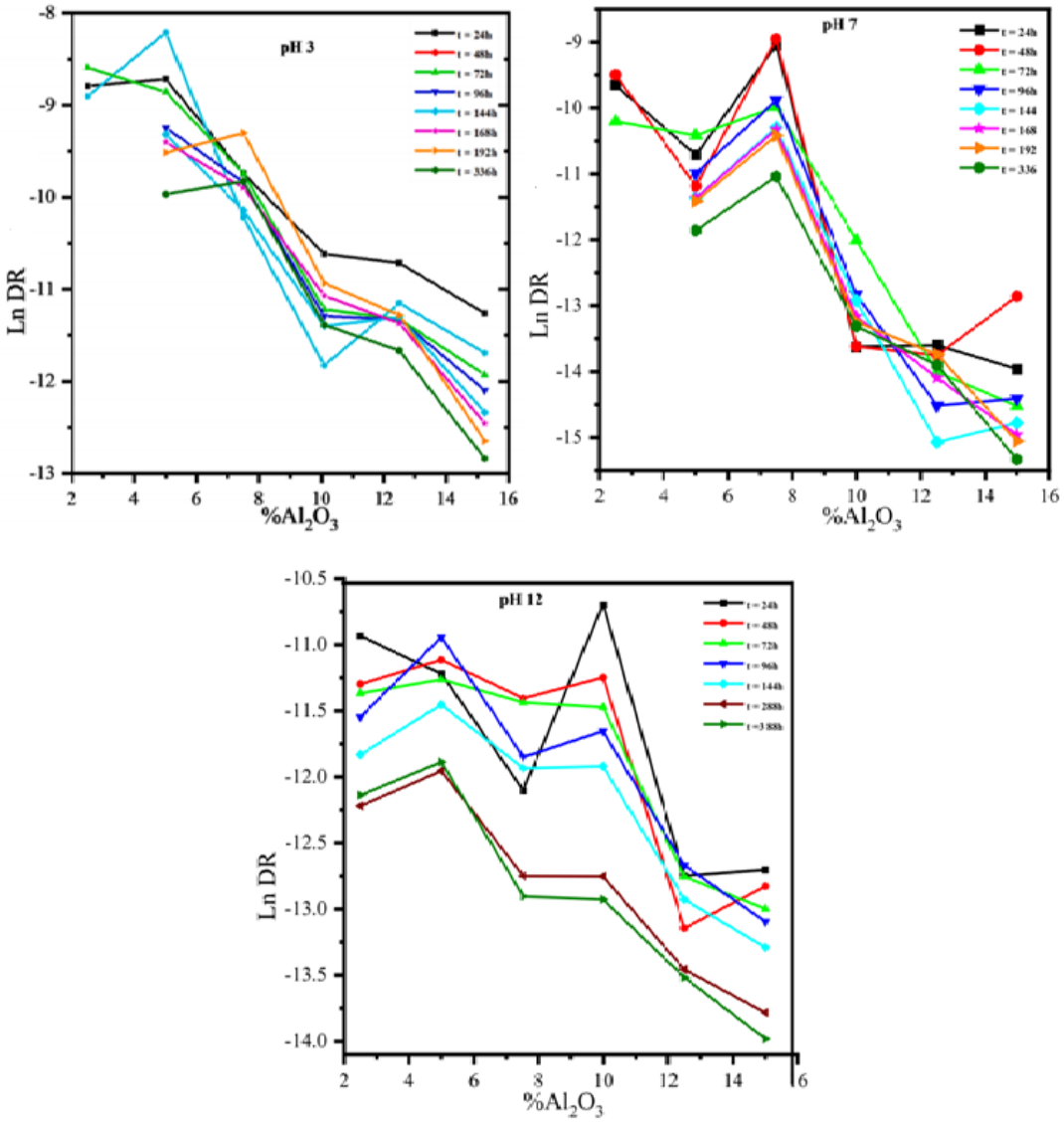

Figure III. 20. Composition's dependency of DR for xAl_2O_3-(50-x)P_2O_5-10CaO-40K_2O glasses (APCK) (with x=2.5,5,7.5,10,12.5,15) after immersion in HCl solution (pH=3), in deionized water (pH=7), and NaOH solution (pH=12) after 388 hours of immersion.

III.5. Optical properties

The UV-visible spectral region is of particular importance in this section. It aims to calculate the optical constants, extinction coefficient, absorption coefficient, and gap energy.
The interaction of photons with glass is globally translated by an important material property: the absorption coefficient, which reflects the ratio of optical power absorbed per unit thickness of the material. The absorption coefficient varies with wavelength.
Optical spectra were recorded with a Jasco V covering the UV-Visible and IR range operating between 200 and 2000 nm at room temperature.

III.5.1. Absorbance and transmittance spectra

Generally, the xAl_2O_3-(50-x)P_2O_5-10Cao-40K_2O glass system, where x=2.5,5,7.5,10,12.5,15 mol% is characterized by its transparency. Figures III.21 exhibit the UV transmittance and absorbance spectra of our investigated glass samples in the wavelength range 190-800 nm.

The UV–visible absorption showed one band around 248-260 nm whose intensity increases with the increase of the Al_2O_3 content, shifting towards higher wavelengths. This band could be due to a charge transfer between the oxygen and the aluminum ion. Also, this type of band could be characteristic of amorphous materials containing impurities of transition metals.

Furthermore, changes in the glass structures might underlie the bands displacement. In other words, as the amount of Al_2O_3 increases, so does the stiffness of the glass system.

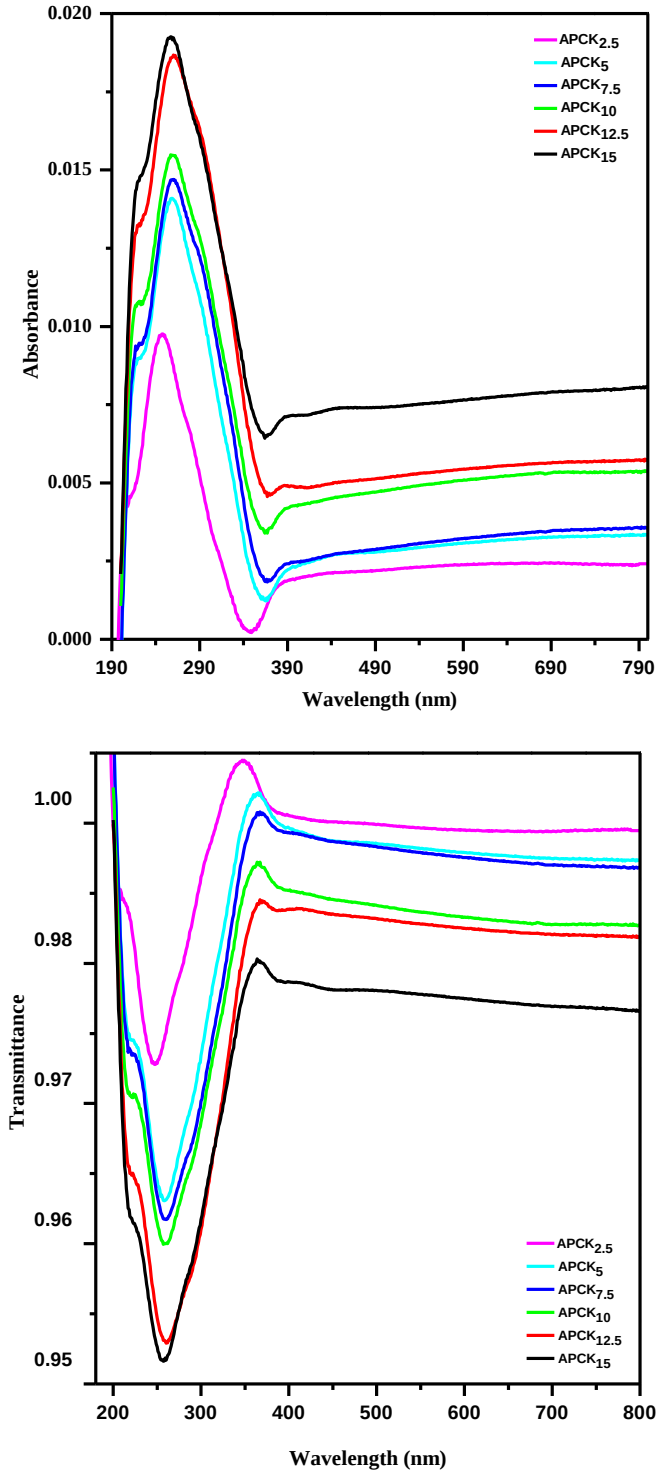

Figure III. 21. Transmittance and absorbance spectra of $50P_2O_5$-xCaO-(50-x)K_2O glass system, (x=2.5,5,7.5,10,12.5,15 mol%).

III.5.2. Absorption (α) and extinction (K) coefficients

Using the absorbance values obtained experimentally, we calculated the absorption coefficients and extinction k of the glasses studied employing the following relations :

$$\alpha = \frac{1}{d} ln\left(\frac{100}{T}\right); A = -log\ (T)\ ; \quad K = \frac{\alpha\lambda}{4\pi}$$

With ***d:*** the thickness of the sample; ***T:*** transmittance; ***A:*** absorbance.

Figures III.22 show the absorption and extinction coefficients variation with wavelength for the samples investigated. The absorption and extinction coefficients increase as the wavelength grows. This research demonstrates that the glassy network becomes mildly absorbing, particularly at long wavelengths (UV-visible). Furthermore, the extinction coefficient demonstrates that long-wavelength rays lose a tiny amount of energy when it passes through the glasses. The energy loss, however, becomes minimal when the concentration of Al_2O_3 increases.

We noticed that as the aluminum content increases in our synthesized system, the absorption and extinction factors increase, making our glasses more light absorbent.

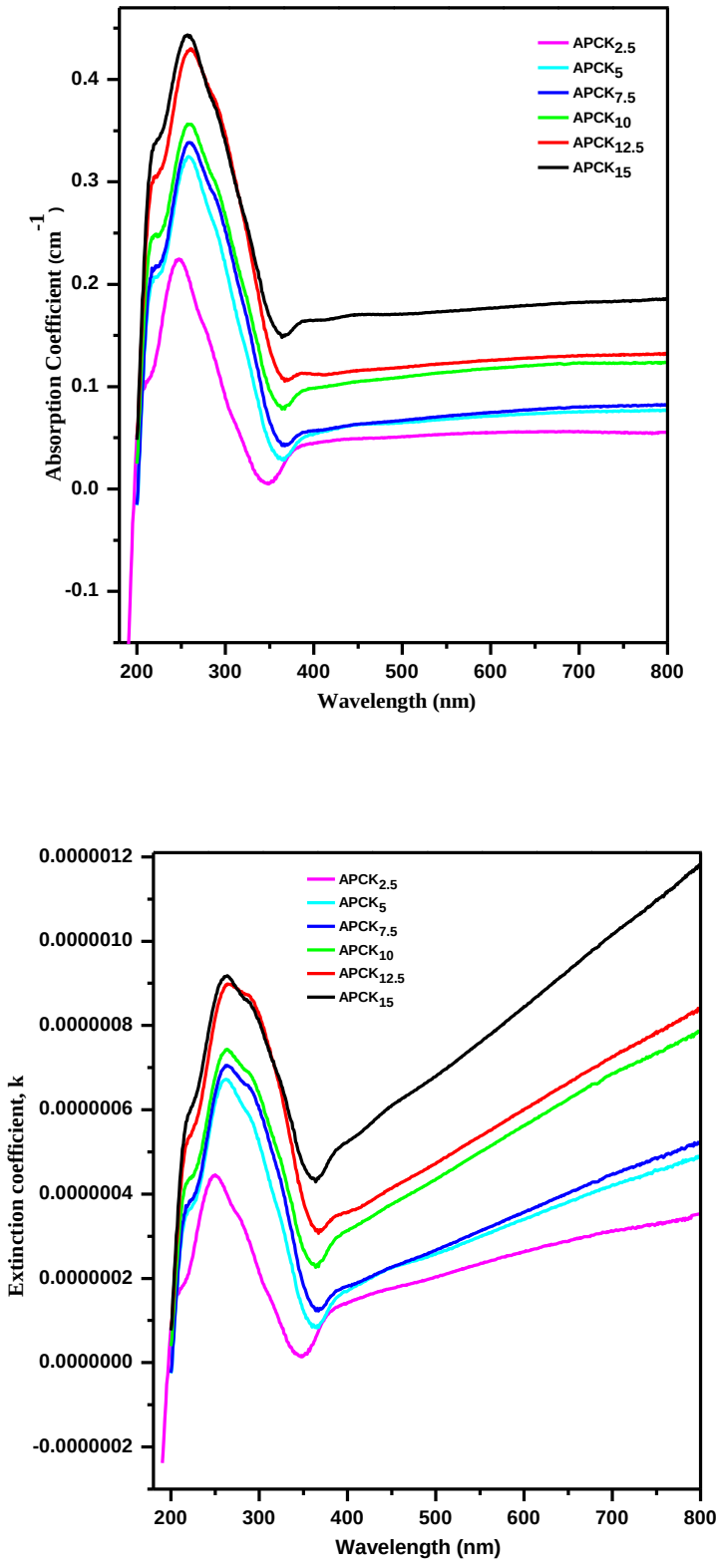

Figure III. 22. Variation of the absorption and extinction coefficient as a function of the wavelength for glasses of composition $50P_2O_5$-xCaO-(50-x)K_2O.

III.5.3. Optical gap

Using the law of Tauc [251], the absorption coefficient has enabled calculating the optical gap energy of various glassy materials. This law is expressed in several ways depending on whether the electronic transitions are done directly or indirectly.

$$(\alpha h\vartheta)^{1/2} = A(h\vartheta - E_g) \quad \textbf{indirect gap}$$

$$(\alpha h\vartheta)^{2} = A(h\vartheta - E_g) \quad \textbf{direct gap}$$

As shown in figures III.23 and III.24, the indirect and direct optical gap values of the studied samples, were obtained by extrapolating the linear part of the curves $(\alpha h\vartheta)^{1/2}$ and $(\alpha h\vartheta)^{2}$ versus $(h\vartheta)$ for zero absorption. Table III.5 groups the direct and indirect optical gap values of the different vitreous samples.

The analysis of these figures shows that the optical gap energy decreases as the aluminum concentration increases. This indicates an improvement of the semiconductor character of our glasses.

Table III. 5. The indirect and direct E_g values of the APCKx studied glasses.

Samples	$APCK_{2.5}$	$APCK_5$	$APCK_{7.5}$	$APCK_{10}$	$APCK_{12.5}$	$APCK_{15}$
E_g indirect	3.73	3.44	3.37	3.27	3.20	3.13
E_g direct	3.93	3.76	3.67	3.62	3.50	3.41

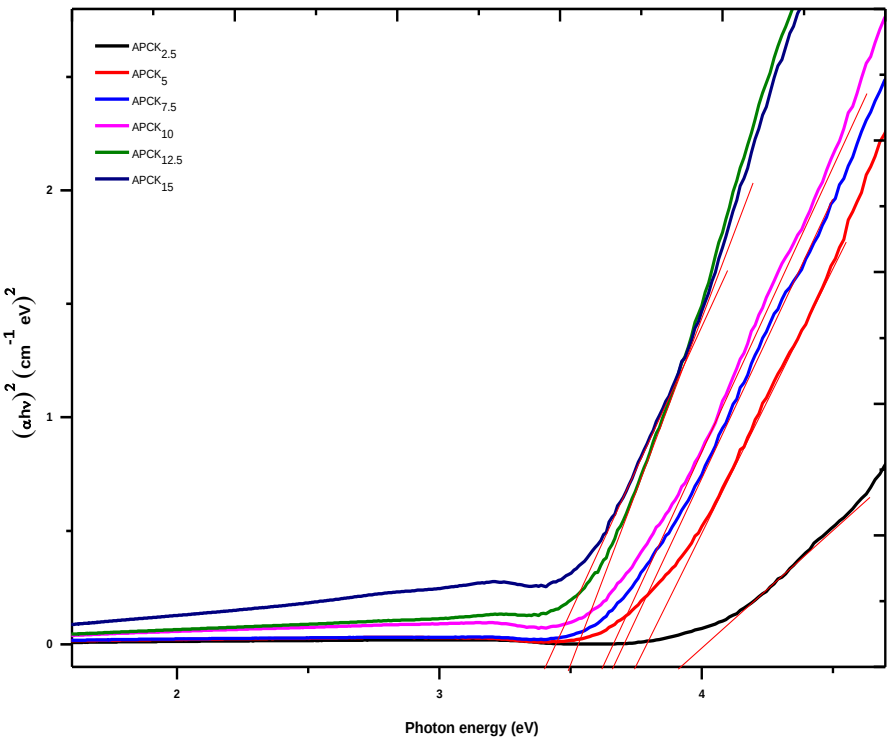

Figure III. 23. Determination of the direct optical gap energy of APCKx system.

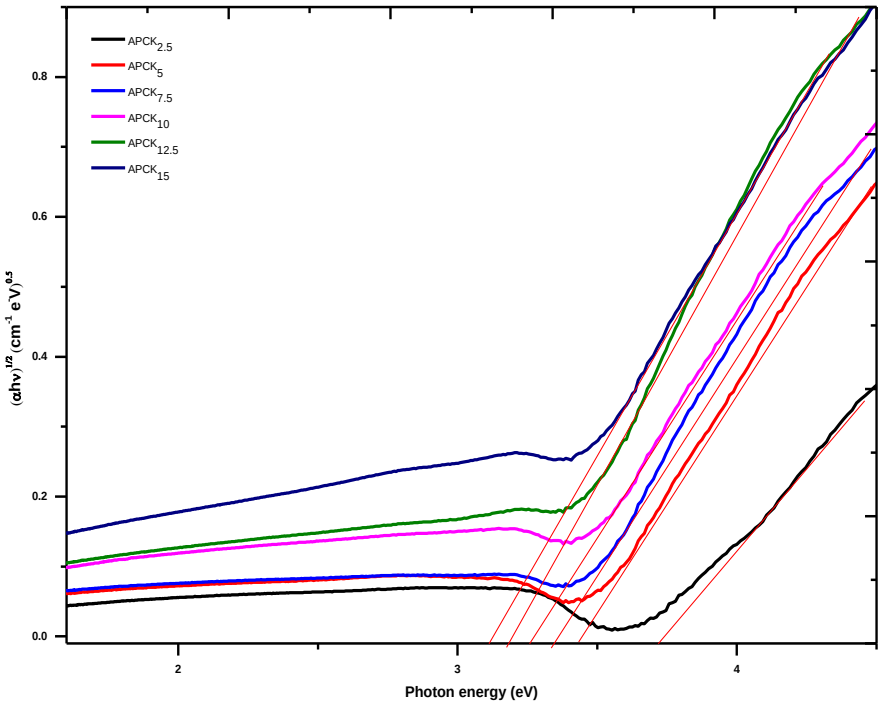

Figure III. 24. Determination of the indirect optical gap energy of APCKx system.

III.6. Conclusion

The preparation parameters for the glasses were given in this chapter, as well as the thermos-physical, chemical, and the vibrational and optical spectroscopic investigation of the two systems of glasses analyzed was presented.

The effect of composition on spectra evolution was thoroughly investigated to determine the structural role of the CaO and Al_2O_3 oxides. When calcium oxide displaces potassium oxide, phosphate chains are depolymerized by the association of CaO into P-O-Ca bonds. However, integrating Al_2O_3 content in APCK glasses systems breaks the PO bond and forms fresh P-O-Al links. This increases the strength of the glass structure. Chemical durability is also connected with an increase in Al_2O_3 content in the APCK system, which replaces easily hydrolyzable P-O-P bonds with more hydration-resistant P-O-Al bonds. A similar result was obtained using optical spectroscopy. Consequently, the results of the experiments on transmittance, reflectance, and the evolution of the various optical constants reveal that the Al^{3+} cations reinforce the glassy matrix and increase the semiconductor character by generating stronger bonds.

Thermophysical studies demonstrate that the glass transition temperature T_g rises with increasing CaO and Al_2O_3 content due to the cross-linking of the glass matrix by the generation of Ca-O-P and Al-O-P bonds. Increased CaO and Al_2O_3 content increased density and decreased molar volume, confirming that the glass matrix becomes more compact. Additionally, investigations of the dissolution phenomena of glasses as a function of immersion time in three different acidity media indicated that the decrease in dissolution rate DR with increasing Al_2O_3 content is due to the replacement of easily hydrolyzable P-O-P bonds with more resistant P-O-Al bonds.

The results acquired in this chapter will be compared to those of the anticorrosive characteristics we shall investigate in the subsequent Chapter.

Chapter IV: Corrosion inhibition analysis of mild steel in 3.5% sodium chloride medium by Al_2O_3-K_2O-CaO-P_2O_5 glass system

IV.1. Introduction

Materials science includes a required field of study known as corrosion inhibition. This field aims to develop methods and techniques to mitigate or lessen the negative effect of corrosion on various metallic components and structures. One such material that is commonly affected by corrosion in harsh environments, such as those rich in chloride, is mild steel.

Phosphate glass has gained significant attention in corrosion research due to its potential to inhibit the corrosion of mild steel in a 3.5% NaCl solution. This inorganic material possesses several properties, making it a promising corrosion inhibitor for mild steel. This research study investigates the effectiveness of APCK phosphate glass as a corrosion inhibitor when applied to mild steel surfaces submerged in a 3.5% NaCl solution.

IV.2. Gravimetric study

Gravimetric tests were performed in 50 ml beakers. A thermostat bath was used to maintain the desired temperature. The mild steel samples are rectangular. Before each test, they undergo surface polishing with abrasive paper, rinsing with distilled water, degreasing with ethanol, rinsing with distilled water, and finally, drying. The mild steel samples were immersed vertically for 24h in 3.5% NaCl solution in the absence and presence of the inhibitors analyzed. We studied the inhibitory efficiency of the glassy composition $APCK_{15}$ of the $50P_2O_5$-xCaO-$(50-x)K_2O$ at different inhibitor concentrations for an immersion time of 24h. The following are the experimental conditions :

- The concentration range of the inhibitor varies from 100, 300, 500, and 700 ppm.
- 3.5% sodium chloride solution is the corrosive medium.
- The temperature is 25°C.

Table IV.1 summarizes the corrosion rate (W), inhibition efficiency (IE%), and recovery rate (θ) calculated by gravimetric analysis for various concentrations of $APCK_{15}$ in 3.5% NaCl medium at 25°C.

Table IV. 1. Corrosion rate and inhibitory efficiency obtained for mild steel by gravimetry for $15Al_2O_3$-$35P_2O_5$-$10CaO$-$40K_2O$ glasses in 3.5% NaCl medium at 25°C.

	C (ppm)	CR ($mg.cm^{-2}.h^{-1}$)	IE (%)	θ
Blank	0	0.523	0	0
$APCK_{15}$	100	0.313	40.15	0.4015
	300	0.229	56.21	0,5621
	500	0.135	74.19	0.7419
	700	0.092	82.41	0.8241

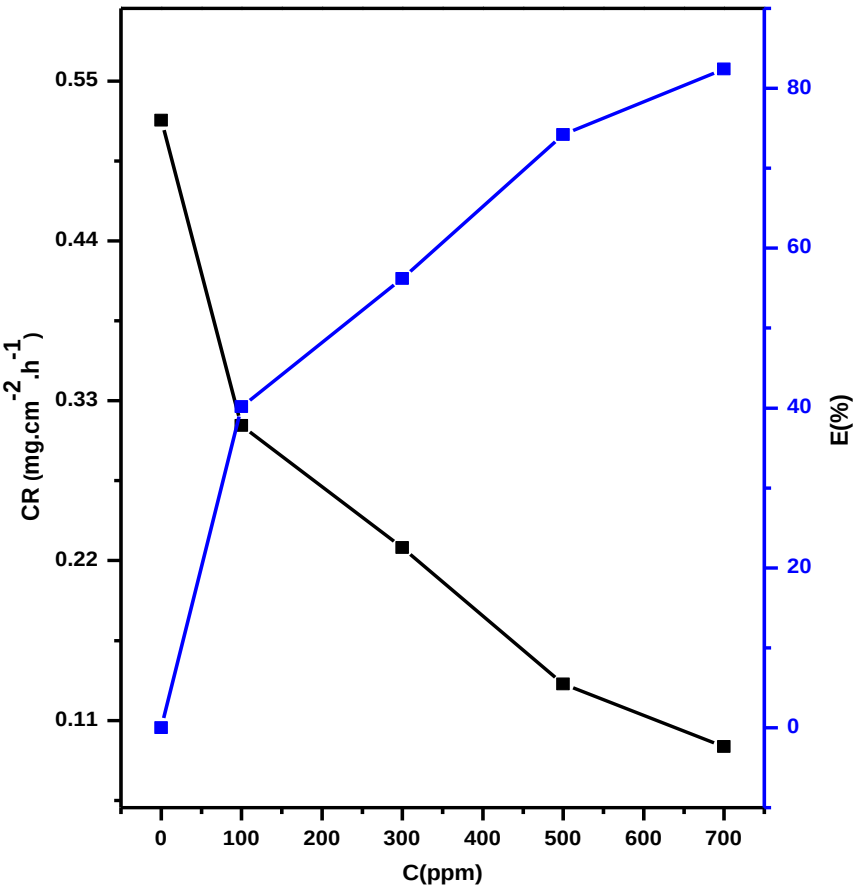

Figure IV. 1. Evolution of corrosion rate and inhibitor efficiency for mild steel for different concentrations of $APCK_{15}$ inhibitor in 3.5% NaCl solution at 25°C

The examination of the results of table IV.1 and figure IV.1 show that the studied glass composition presents satisfactory anticorrosive properties of the mild steel in 3.5% NaCl medium. It is documented that the corrosion rate (CR) drops with the expansion in the inhibitor concentration and reaches a maximum value of about 82.41 % for the 700ppm concentration. When the concentration of the inhibitor increases, the recovery rate also increases and, therefore, the inhibitor's efficiency.

The overall gravimetric measurements indicate that the increase in the inhibitory efficiency of the $APCK_{15}$ glassy sample with concentration results from the strong interaction of this inhibitor with the metal surface. Clearly, the inhibitor adsorbs more on the metal surface. It shields the active sites on the surface, which generates the formation of a barrier layer between the mild steel and the corrosive medium that diminishes the reactivity of the metal. We hypothesize that the constituents of our glasses can adsorb to the steel surface in NaCl medium via electrostatic interaction between the cations of the glassy network and the chloride ions adsorbed on the surface [252,253]. Furthermore, chemical bond formation between the glassy phase and the metallic surface is caused by the electron donor effect of free doublets of inhibitory molecules such as O and P doublets.

Gravimetric determination of inhibitory efficiency has the benefit of being simple to implement, but it needs to provide knowledge of the mechanisms involved in the corrosion process. Electrochemical techniques (polarization curves, electrochemical impedance spectroscopy, etc.) remain an important tool because they allow for a better understanding of corrosion phenomena.

IV.3. Electrochemical process

Before examining the behavior of mild steel immersed in an inhibited medium, the electrochemical behavior of the metal/medium contact must be understood. Electrochemical tests were carried out in the presence and absence of inhibitor at various concentrations. The applied voltage varies continuously in the potentiostatic approach. Before beginning the measurements, the potential of the working electrode is maintained for 30 minutes i=f (E).

IV.3.1. The examination by the stationary electrochemical method

The electrochemical method operated to characterize the metal/electrolyte interface is established by plotting logarithmic polarization curves, which allows us to calculate the corrosion current density from the experimentally acquired curve Log i = f(E).

IV.3.1.1. The effect of the inhibitor concentration addition

IV.3.1.1.1. Open circuit potential (OCP) evolution

Open circuit potential values, while not providing direct information on corrosion kinetics, do provide qualitative thermodynamic information. Tracking the variation of the working electrode's free potential as a function of time is essential for delineating corrosion domains and inhibition processes and identifying optimal inhibition concentrations.

The electrochemical tests were performed on a mild steel plate. The evolution of the free potential as a function of the immersion period in the absence and presence of different 4 concentrations of $APCK_{15}$ at 25 ^{o}C after 1/2h of immersion (when the potential reaches its stabilization) is presented in figure IV.2.

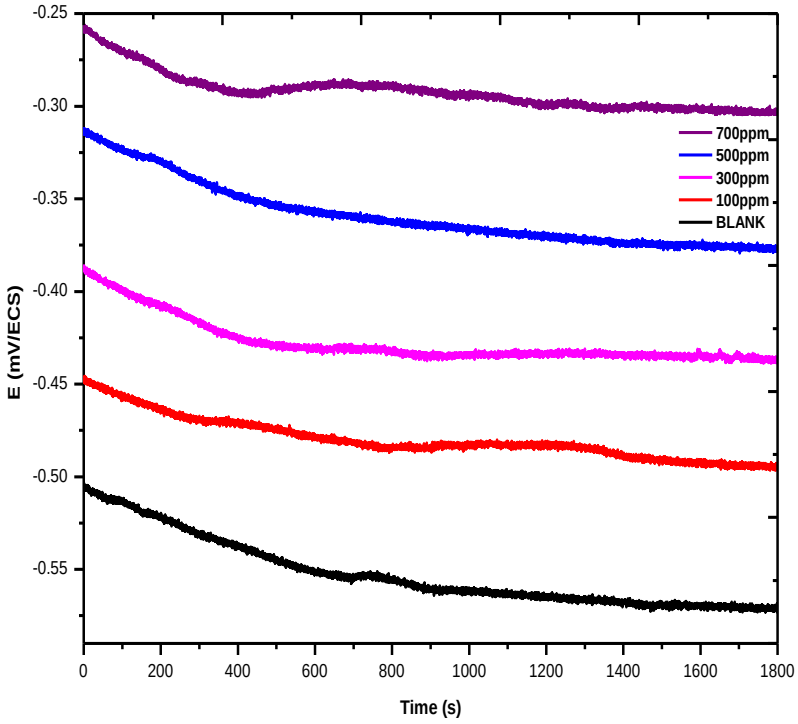

Figure IV. 2. Evolution of the free potential as a function of time of mild steel in the absence and presence of 100, 300, 500, and 700 ppm of $APCK_{15}$ at T=25 ^{o}C after 30 min of immersion.

As shown in figure IV.2, we state that the values of the E potential in all cases (in the absence or presence of $APCK_{15}$) start to decrease in the first few minutes. This potential stabilizes after 30 minutes of immersion. The addition of different concentrations of $APCK_{15}$ shifts the free potential to less negative values compared to the blank and without changing the shape of the E= f (t) curve. These results suggest that the addition of the glass provides an inhibition effect of the mild steel in a 3.5% NaCl solution.

IV.3.1.1.2. Polarization curves

The applied potential in the potentiostatic technique varies continuously from -800 mV/ECS to 0 mV/ECS. The working electrode's potential is stabilized for 30 min before proceeding with the measurements of the corrosion current as a function of the potential I_{corr}=f (E). Figure IV.3 and Table IV.2 shows the polarization data of mild steel in 3,5% NaCl medium in the absence and presence of the glassy inhibitor at different concentrations at 25°C. The shape of the curves is Log i= f(E) as a function of the concentrations of $APCK_{15}$.

Figure IV.3 displays two parts in the polarization curves observed:

- a cathodic activation region in which the oxygen reduction reaction controls the cathodic process.
- an anodic activation domain, almost presumably owing to steel dissolution.

In our findings, the anodic activation domain therefore comprises two potential domains. A first active range corresponds to steel dissolution according to the reaction:

$$\boldsymbol{Fe \rightarrow Fe^{2+} + 2e^{-}}$$

The electrons produced by the active dissolution of steel are consumed to maintain electron balance by the oxygen dissolved in the medium according to cathodic reactions. Depending on the active dissolution reaction of the steel, the hydrated Fe^{2+} ions are formed and released into solution. Anodic polarization increases the rate of active dissolution to a potential of -245 mV, which marks the start of the transpassivation potential. Beyond this point, the anodic current density increases steadily.

In the second transpassive dissolution range, occurring at potentials equal to or greater than E_T, there is a notable increase in current, indicative of transpassive dissolution of the steel. This phenomenon signifies the onset of pitting corrosion, characterizing the corrosion mode within this range as pitting. The potential marking the beginning of transpassivation serves as a critical parameter in understanding a probable transition to pitting corrosion [254].

However, with 100ppm of the inhibitor in the corrosive solution, an abrupt change of the slope of the polarization curve is observed in -500 mV/ECS. Such anodic slope change would be related to changes in the metal dissolution mechanism, in which the formation of iron intermediary species with the oxygen or with the ions of the medium would play a main role.

In the other hand, the cathodic curves show a wide range of linearity, corresponds to the limiting current density of the oxygen reduction on the surface of the mild steel occurs according to pure activation kinetics, indicating that the reaction is under Tafelian electron transfer control.

Anodic reaction and cathodic reaction are given in the following equations [255–258] :

$$2H_2O + O_2 + 4e^- \rightarrow 4\ OH^-$$

$$2H_2O + 2e^- \rightarrow 2OH^- + H_2$$

According to the literature [259,260], the classification of inhibitors is based on the difference in the corrosion potential (ΔEcorr = Ecorr with inhibitor - Ecorr without inhibitor). If this difference exceeds 85 mV, the inhibitor is classified as either cathodic or anodic. Conversely, if the difference is less than 85 mV, the inhibitor is classified as a mixture inhibitor.

In our study, variations in ΔEcorr were observed in the 3.5% NaCl solution. For instances where ΔEcorr exceeded 85 mV, a slight shift in the corrosion potential ranging from 91.1-113.7 mV occurred at inhibitor concentrations of 500 and 700 ppm, respectively. Conversely, when ΔEcorr was less than 85 mV, a minor shift in the corrosion potential ranging from 33.4-80.5 mV was observed at inhibitor concentrations of 100 and 300 ppm, respectively.

Furthermore, each additional concentration delineates the type of inhibitor at play. The addition of 500 and 700 ppm indicates that $APCK_{15}$ glass functions as an anodic inhibitor, as evidenced by the curve shifting towards the positive side (anodic). Similarly, the inclusion of 100 and 300 ppm suggests our glass acts as a mixed inhibitor with dominant anodic effectiveness, supported by the polarization curve's shift towards the positive side (anodic). Moreover, the greater change in the anodic Tafel slope compared to the cathodic Tafel slope indicates that the inhibitor's effect is more pronounced in controlling the anodic reaction.

Table IV.2 presents intriguing observations regarding the behavior of βa and βc values as the concentration of $APCK_{15}$ increases from 100 to 700 ppm. Initially, both βa and βc values decrease with rising inhibitor concentration, indicative of the inhibitor's effectiveness in reducing corrosion rates. However, at a concentration of 700 ppm, a reversal occurs, with βa and βc values increasing. This unexpected shift may be attributed to the rapid breakdown of the protective layer formed during the cathodic reaction [261,262].

In the absence of the inhibitor, the current density is recorded at 219 $\mu A/cm^2$. Upon the addition of the inhibitor, a significant reduction in current density is observed. Specifically, with the introduction of 100 ppm of $APCK_{15}$, the current density decreases to 538.7 $\mu A/cm^2$, highlighting the inhibitor's efficacy. This reduction in current density becomes even more pronounced with higher inhibitor concentrations, plummeting to 32 $\mu A/cm^2$ at 700 ppm. These phenomena underscore the inhibitory effect of $APCK_{15}$, primarily attributed to its adsorption onto the metal surfaces [260].

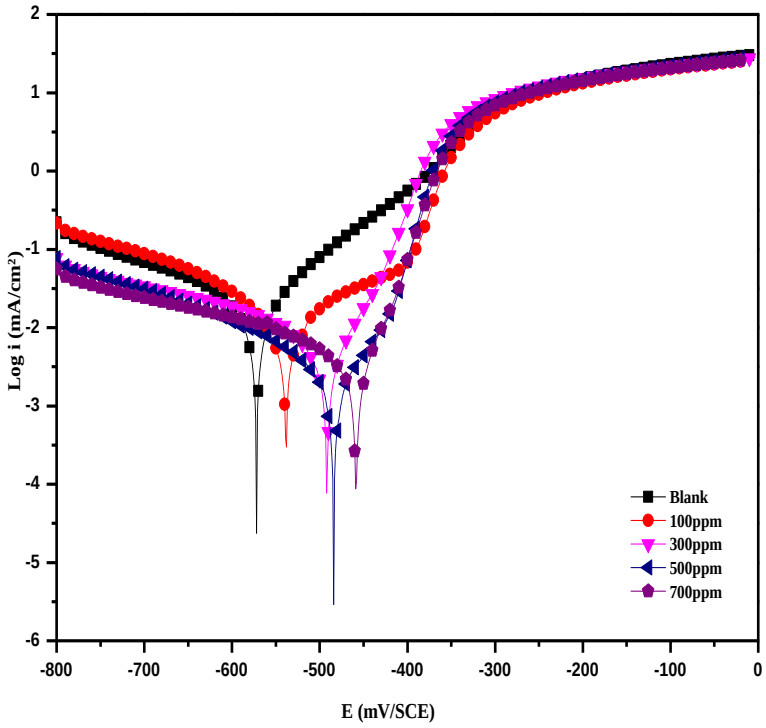

Figure IV. 3. Polarization curves of mild steel in 3.5% NaCl medium obtained at 25°C without and with the addition of different concentrations of the inhibitor APCK$_{15}$.

Table IV. 2. Electrochemical parameters, inhibitory efficiency, and recovery rate obtained from polarization curves of mild steel in 3.5% NaCl solution before and after the addition of APCK$_{15}$ with different concentrations.

Concentrations (ppm)	-Ecorr (mV/SCE)	i_{corr} (µA/cm^2)	-βc (mV/dec)	βa (mV/dec)	E(%)
Blank	572.1	219	263.2	122.9	---
100	538.7	126	77.6	95.9	42.47
300	491.6	100	40.2	60.6	54.34
500	484.0	60	30.8	55.2	72.6
700	458.4	42	50.1	65.3	80.82

IV.3.1.1.3. Electrochemical spectroscopy analysis

Electrochemical impedance spectroscopy assesses an electrode's response to a sinusoidal modulation of potential with minimal amplitude across various frequencies. This method, when combined with stationary l=f(E) curves, offers a more thorough exploration of inhibitor mechanisms.

In Figure IV.4 and Table IV.3, Nyquist diagrams and electrochemical impedance parameters, respectively, depict observations from mild steel immersed in 3.5% NaCl solution at 25°C, both in the absence and presence of 100, 300, 500, and 700 ppm of the APCK$_{15}$ glassy inhibitor.

These analyses were conducted after 30 minutes of immersion at the natural corrosion potential. Figure IV.4 reveals impedance diagrams with non-ideal semicircles, attributed to frequency dispersion of interfacial impedance arising from electrode surface heterogeneity [263,264]. Such heterogeneity, stemming from factors like roughness, contaminants, dislocations, inhibitor adsorption, and porous layer formation, can lead to deviations from perfect semicircular behavior [265,266].

In the absence and presence of the inhibitor, graphs in 3.5% NaCl solution exhibit single capacitive loops notably distorted from the real axis. This distortion often indicates a charge transport mechanism on an inhomogeneous surface.

Upon introducing inhibitors into the corrosive solution, the size of distorted half-circles alters. These impedance diagrams feature loops whose size (R_{ct} diameter) increases with inhibitor concentration, suggesting enhanced protective properties. This observation underscores the influence of phosphate glasses on processes at the steel/NaCl corrosive media interface.

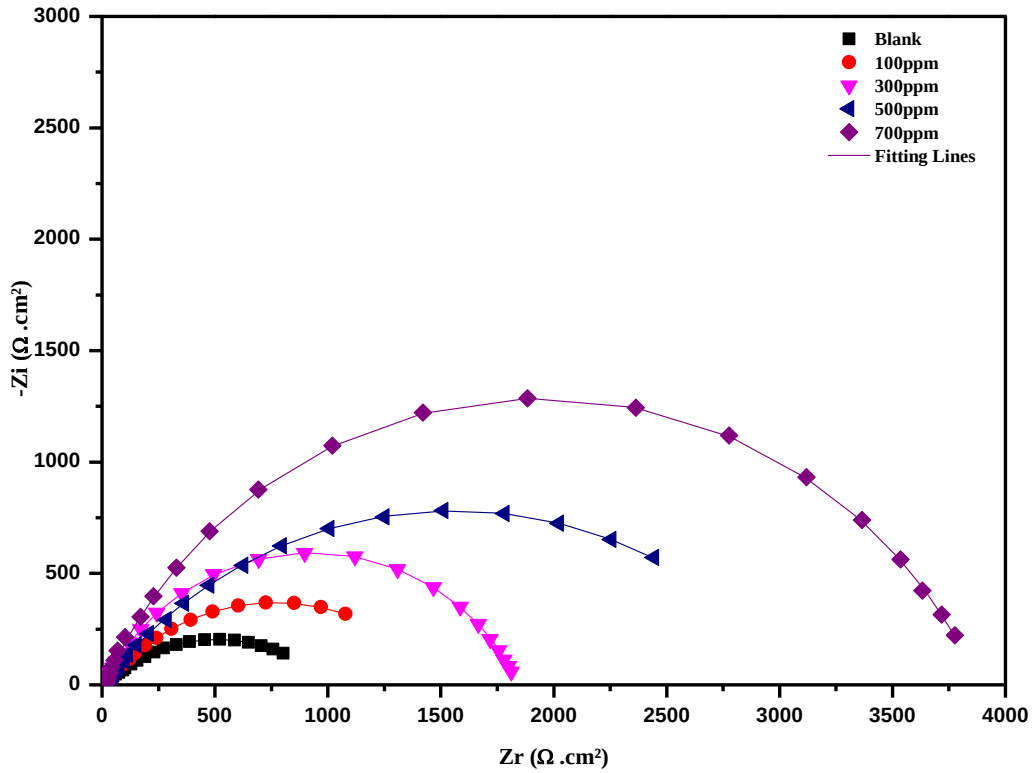

Figure IV. 4. Impedance diagram of mild steel obtained in 3.5% NaCl containing four different concentrations (100-300-500-700ppm) of $APCK_{15}$ glass composition.

Table IV. 3. Electrochemical parameters obtained by S.I.E. of mild steel in 3.5% NaCl medium without and with $APCK_{15}$ different concentrations.

Concentrations (ppm)	R_s ($\Omega.cm^2$)	R_{tc} ($\Omega.cm^2$)	10^6 Q ($\Omega^{-1} s^n cm^{-2}$)	n	C_{dl} ($\mu F\ cm^{-2}$)	E_{SIE} (%)
Blank	10.56	985.4	1199	0.7	1420	---
100	12.26	1512	1613	0.8	1088	34
300	12.35	1834	149.1	0.7	625.9	46
500	7.78	3104	586.9	0.8	484.2	68
700	12.09	3869	136.2	0.8	109.7	75

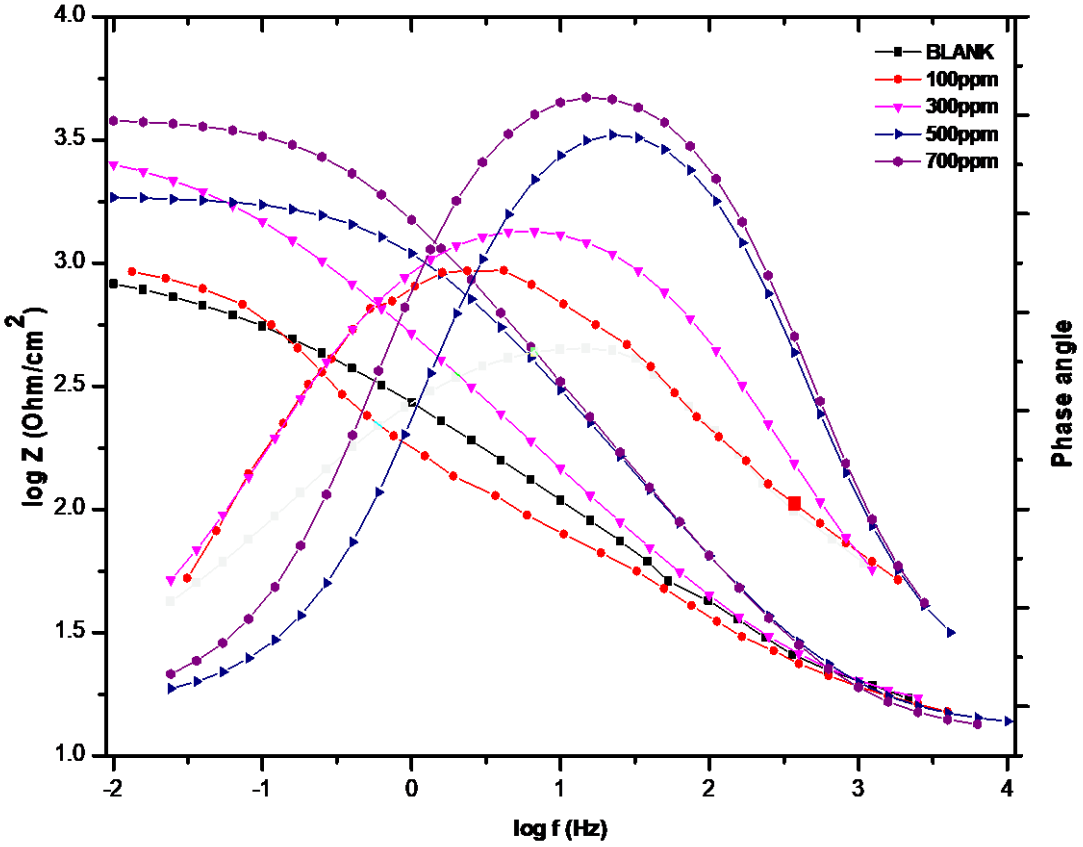

Figure IV. 5. Bode diagram for mild steel in 3.5% NaCl medium in the absence and presence of $APCK_{15}$ different concentrations.

In the Bode diagram (Figure IV.5), a single time constant is evident. This observation suggests a unified response in the system. The phase shift (n) depicted in Figure IV.6 is frequently attributed in literature to surface inhomogeneities on the electrode. These irregularities arise from processes such as corrosion product formation or metal oxidation, leading to alterations

in the active electrode surface, as illustrated in Figure IV.7.

Various publications offer alternative explanations for this phase shift, attributing it to factors such as impurities or dislocations [267,268], inhibitor adsorption, development of porous layers, and changes in the thickness or composition of surface films or coatings on the electrode. These diverse perspectives highlight the complexity of factors influencing electrochemical behavior [269–271].

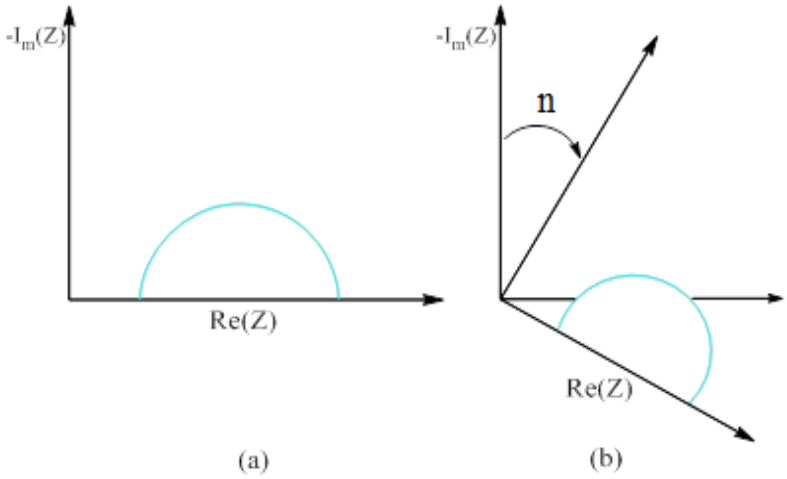

Figure IV. 6. Phase shift n observed at the spectrum reference point: (a) ideal case, in theory (uniformly accessible surface) and (b) spectrum obtained in most practical cases.

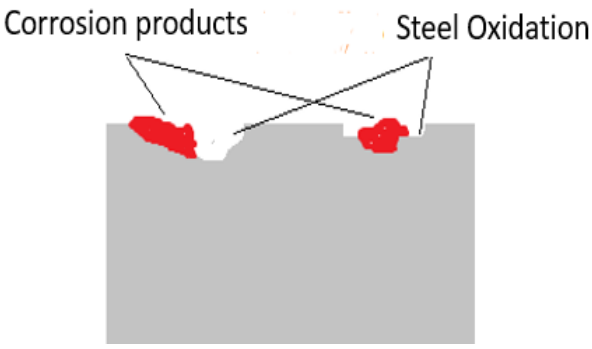

Figure IV. 7.Inhomogeneities on the steel surface, observed after immersion of the electrode in the electrolyte.

The surface inhomogeneities are accounted for by a constant phase element (CPE) through the coefficient n. Such an element is described by the following equation [267]:

$$\mathbf{Z_{CPE}} = \boldsymbol{Q^{-1}(i\omega)^{-n}}$$

Where $\boldsymbol{Q}$ is a proportionality coefficient, $\boldsymbol{\omega}$ is the angular frequency (in rad s/1) and $i^2 = -1$ is an imaginary number and n is related to the phase shift [267,271]. For integers of n = 1, 0, -1 the CPE is reduced to a planar capacitor (C), a resistance (R), and an inductor (L), respectively.

The impedance data were fitted using the equivalent circuit shown in figure IV.8, where R_s characterizes the solution resistance and R_{ct} is the charge transfer resistance (R_{ct} values are determined from the difference at the minimum and maximum frequencies on the real axis (diameter of the semicircle) [272].

The CPE and Q elements were converted to a pure capacitance (C) using the following equation [272]:

$$\boldsymbol{C = (QR_{ct}^{1-n})^{1/n}}$$

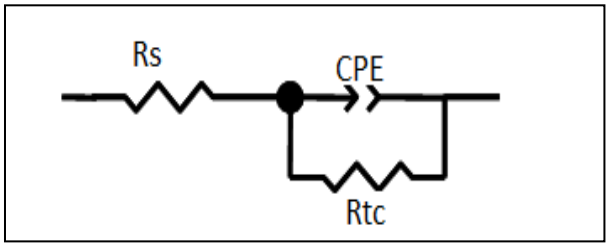

Figure IV. 8. Model of equivalent electrical circuit of the steel/NaCl interface and glassy inhibitors.

The model in figure IV.8 provided an excellent parametric match to the experimental impedance spectra for all samples. Figure IV.9 displays the actual and simulated fitted spectra for the steel contact of 700 ppm of $APCK_{15}$ in a 3.5% NaCl solution via Z view program. Similar curves were generated for the remaining samples.

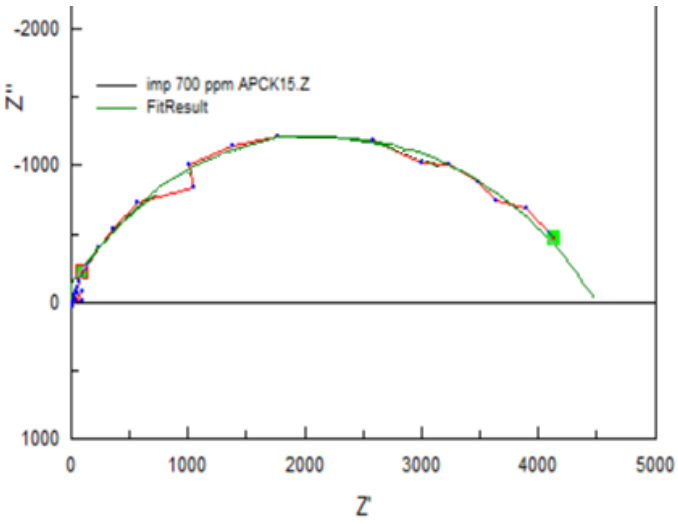

Figure IV. 9. A simulated fitted spectra for the steel contact of 700 ppm of $APCK_{15}$ in a 3.5% NaCl solution via Z view program.

The impedance spectra contain a single capacitive loop, indicating that the inhibitor is absorbed by creating a protective film on the surface.

Table IV.4 summarizes the values of the various parameters obtained by S.I.E. and from the parametric fitting using CPE utilizing Z-view application. The corrosion-inhibiting efficiency of the steel is computed from R_{ct} using the following formula:

$$\boldsymbol{IE}(\%) = \frac{\left(\boldsymbol{R_{ct}^{inh}} - \boldsymbol{R_{ct}}\right)}{\boldsymbol{R_{ct}^{inh}}}$$

Where $\boldsymbol{R_{ct}}$ and $\boldsymbol{R_{ct}^{inh}}$ are respectively the values of the charge transfer resistances of the steel after immersion without and with addition of the inhibitor.

Table IV.3 shows that the increased concentration of the inhibitor to a solution of the value of the charge transfer resistance (R_{ct}) and inhibitor efficiency (IE%) will remarkably increase and the value of the capacity will decrease.

R_{ct} value without inhibitor is 985.7 Ω.cm^2 whereas, maximum value occurs when adding the $APCK_{15}$ concentration of 700ppm, which is 3869 Ω.cm^2 and the inhibitor efficiency increased to 75%. Also, table IV.3 shows that the addition of the inhibitor concentration decreased capacity double layer, indicating that the relationship between R_{ct} and C_{dl} is inversely proportional. This is a phenomenon that occurs due to a decrease in local dielectric constant or increasing the density of electric double layer.

The addition at a concentration of 700 ppm is an effective concentration of $APCK_{15}$ adsorbed on the surface of the mild steel in a 3.5% NaCl solution. This follows the potentiodynamic polarization test, which states that adding the 700ppm of the glassy inhibitor resulted in the highest inhibition efficiency.

IV.3.1.2. The effect of inhibitor's various compositions addition

IV.3.1.2.1. Open circuit potential evolution

Figure IV.10 depicts the evolution of the free potential over the immersion period, both in the absence and presence of $APCK_x$ with different compositions (x=0, 5, 10, 15 mol%), at 25°C, after 30 minutes of immersion. Notably, the E_{corr} potential shows a declining trend in all scenarios within the initial minutes, eventually stabilizing after the 30-minute mark.

Interestingly, the introduction of varying compositions of our synthesized glass causes a slight shift in the free potential towards negative values compared to the blank scenario. However, this alteration doesn't affect the overall shape of the E= f (t) curve. These observations suggest

that the inclusion of glass inhibits the corrosion of mild steel in a 3.5% NaCl solution.

This shift in free potential indicates a protective effect on the metal surface, likely due to the presence of inhibitor chemicals or compounds. Such protection serves to retard the corrosion rate by delaying the dissolution reaction of iron.

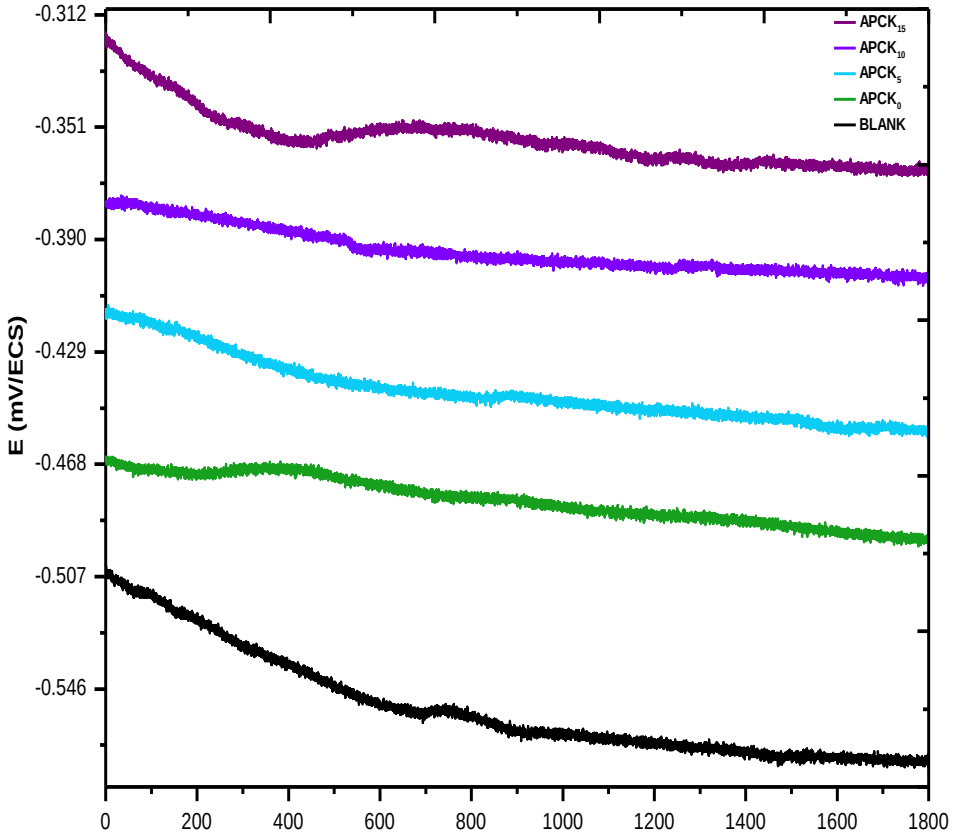

Figure IV. 10. The free potential as a function of the immersion period in the absence and presence of APCKx different composition (x=0, 5, 10, 15mol%) at 25 oC after 1/2h of immersion.

IV.3.1.2.2. Polarization curves

Under consistent operating conditions as previously outlined, polarization curves were generated for various compositions of $APCK_x$ (x=0, 5, 10, 15mol%) in a 3.5% NaCl medium, as depicted in Figure IV.11. Analysis of the obtained polarization curves reveals a striking similarity in the shape of the log i= f(E) curves across all APCK inhibitors, indicating uniform inhibitory activity within the NaCl medium. Moreover, the inclusion of vitreous APCK compounds leads to a noticeable reduction in corrosion current densities, with higher inhibitor levels exacerbating this decline.

Further examination of Table IV.4 demonstrates the significant impact of adding various inhibitors on polarization curves, manifesting in reduced corrosion current densities (i_{corr}) as the concentration of the inhibitors increases. Notably, the inhibitory effectiveness of the materials correlates positively with the molar fraction of alumina, with the $APCK_{15}$ sample exhibiting the highest efficiency at 75%.

Analysis of the variation in corrosion potential (E_{corr}) values across the series reveals a mixed inhibitory behavior, with additional shifts observed in corrosion potential for $APCK_{10}$ and $APCK_{15}$ compositions, indicative of their anodic inhibitory action. This is corroborated by a more pronounced modification in the anodic Tafel slope compared to the cathodic area, underscoring the inhibitors' efficiency in controlling the anodic reaction.

The inhibitory mechanism exhibited by the utilized glasses primarily involves the adsorption of polyphosphate compounds onto the steel surface, facilitating the formation of a robust protective layer. Comprising potassium, calcium, aluminum, phosphorus, and oxygen, these phosphate chains play a crucial role in adsorption, effectively shielding the metal surface. By impeding active anodic and cathodic sites and reducing heat transfer, they expedite the growth of a protective layer. This physical barrier impedes the diffusion of corrosive species, accelerating the coverage rate of the metal surface and bolstering its corrosion resistance [273,274]

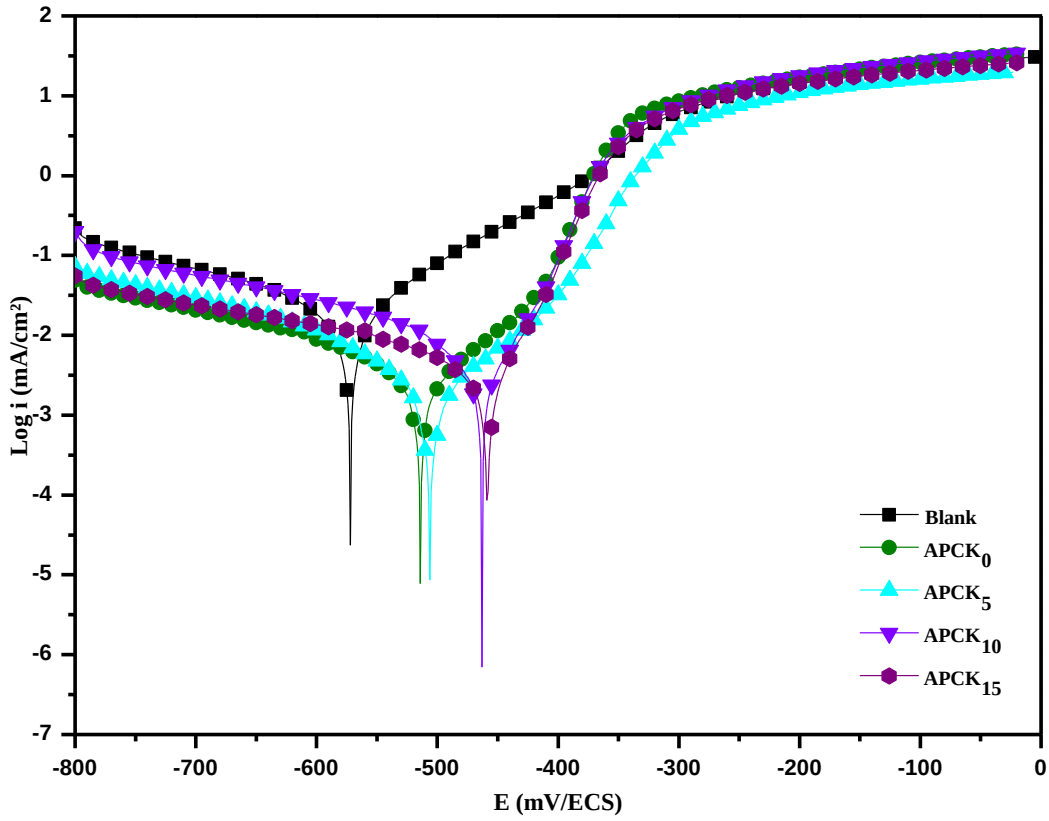

Figure IV. 11. The polarization curves of mild steel at 25 °C in 3.5% NaCl medium with and without different levels of APCKx.

Table IV. 4. Electrochemical parameters obtained from polarization curves of mild steel in 3.5% NaCl solution before and after the addition of different compositions of APCKx.

Compositions (mol%)	-Ecorr (mV/SCE)	i_{corr} ($\mu A/cm^2$)	E(%)	θ
BLANK	572.1	219	---	---
$APCK_0$ = PCK_{10}	514.2	160	26.95	0.27
$APCK_5$	506.2	127	42.01	0.42
$APCK_{10}$	463	50	77.17	0.77
$APCK_{15}$	458.4	42	80.82	0.81

IV.3.1.2.3. Electrochemical spectroscopy analysis

Figure IV.12 and Table IV.5 present Nyquist diagrams and electrochemical impedance parameters, respectively, obtained from mild steel immersed in a 3.5% NaCl solution at 25°C. These measurements were conducted in the absence and presence of different compositions of

$APCK_x$ glassy inhibitor ($APCK_0$, $APCK_5$, $APCK_{10}$, and $APCK_{15}$) at a concentration of 700 ppm, following a 30-minute immersion period at the natural corrosion potential.

The Nyquist diagrams in Figure IV.12 show unideal semicircles indicating frequency dispersion of interfacial impedance due to electrode surface heterogeneity caused by roughness and contaminants [263–265]. This results in a single capacitive loop that is notably deformed, suggesting inhibitor adsorption and surface protection.

Table IV.5 summarizes the electrochemical impedance parameters obtained through S.I.E. and parametric fitting using CPE via the Z-view application. The corrosion-inhibiting efficiency of the steel is assessed through the charge transfer resistance (R_{ct}). The table illustrates that increasing the inhibitor concentration leads to a significant increase in R_{ct} and inhibitor efficiency (IE%) while decreasing the capacity of the double layer (C_{dl}). Specifically, the addition of $APCK_{15}$ (700 ppm) results in a maximum R_{ct} value of 3869 $\Omega.cm^2$, corresponding to an inhibitor efficiency of 75%. Concurrently, C_{dl} decreases, indicating an inverse relationship between R_{ct} and C_{dl} attributed to changes in local dielectric constant or electric double-layer density.

The presence of $APCK_x$ compositions alters the structure of the electric double layer through inhibitor adsorption at the metal-solution interface. This is evidenced by the increase in R_{ct} values and decrease in C_{dl} values with increasing inhibitor concentration. Notably, the maximum C_{dl} value of 109.7 $\mu F/cm^2$ is observed with $APCK_{15}$ (700 ppm), indicating its effectiveness in adsorbing onto the mild steel surface in a 3.5% NaCl solution.

These findings align with potentiodynamic polarization tests, highlighting $APCK_{15}$ (700 ppm) as the most effective composition of the glassy inhibitor in inhibiting corrosion of mild steel.

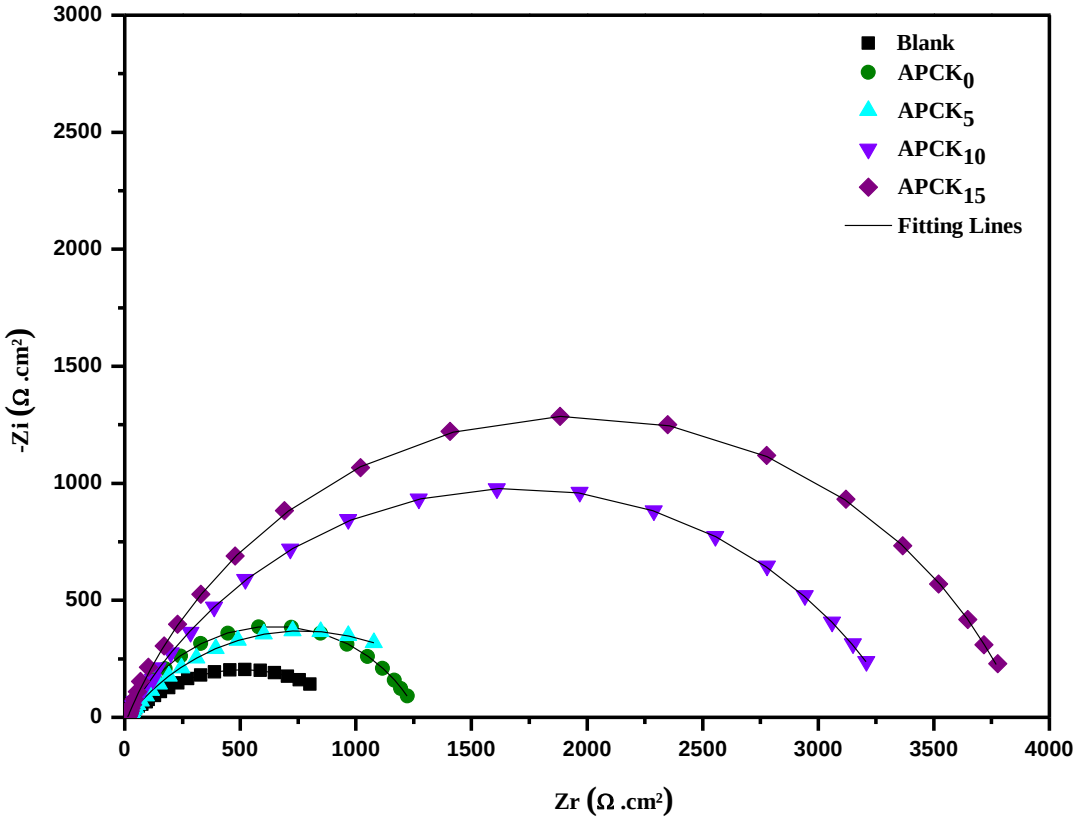

Figure IV. 12. Impedance diagrams of mild steel at 25 °C in 3.5% NaCl medium with and without different levels of APCKx.

Table IV. 5. Electrochemical parameters obtained from Impedance diagrams of mild steel in 3.5% NaCl solution before and after the addition of different compositions of APCKx.

Compositions (mol%)	R_s ($\Omega.cm^2$)	R_{tc} ($\Omega.cm^2$)	10^6 Q (Ω^{-1} s^n cm^{-2})	n	C_{dl} ($\mu F\ cm^{-2}$)	E_{SIE} (%)
Blank	10.56	985.4	1199	0.6	1420	---
$APCK_0$	13.92	1263	484.4	0.6	1393.8	22
$APCK_5$	12.01	1512	286.9	0.6	808.8	35
$APCK_{10}$	11.11	3339	166.19	0.7	348.13	71
$APCK_{15}$	12.18	3869	136.2	0.8	109.7	75

IV.3.2. The temperature effect

The stability of a corrosion inhibitor within harsh environments hinges greatly on its capacity to endure operating temperatures. Temperature stands as a pivotal factor, exerting significant influence on material behavior amidst corrosive surroundings. As temperatures elevate, the

performance of inhibitors can undergo alterations, thereby affecting substrate behavior within aggressive environments [275,276]. The corrosion resistance of steel may diminish as inhibitors desorb, leading to the rapid dissolution of inorganic compounds or complexes with temperature escalation. While extensive research has delved into corrosion inhibition in acidic mediums, investigations into chloride solutions remain limited, fostering a keen interest in exploring the potential of phosphate glasses as inhibitors for mild steel in 3.5% NaCl solutions.

Our comprehensive study has successfully examined the $APCK_{15}$ glass system (700 ppm), aiming to deepen our understanding of its corrosion-inhibiting properties. Focusing on the impact of temperature on corrosion rate and inhibition efficiency, particularly following a 30-minute immersion within a temperature range of 30 to 60°C, our research has yielded pivotal insights. We have established a robust correlation between temperature and corrosion inhibition, allowing us to discern the type of adsorption the inhibitor exhibits on the metal surface—whether chemisorption or physisorption—and to elucidate the thermodynamic activation parameters, including activation energy E_a, activation enthalpy ΔH_a^o, and activation entropy ΔS_a^o of the corrosion process.

These findings not only shed light on the efficacy of the $APCK_{15}$ glass system as a corrosion inhibitor but also hold promise for informing the development of more efficient and sustainable corrosion prevention methodologies.

IV.3.2.1. The temperature effect on OCP

The OCP curves for mild steel in 3.5% NaCl solution at various temperatures with and without the $APCK_{15}$ (700ppm) inhibitor are present in figures IV.13 and IV.14. The response of OCPs in immersion tests reflects the characteristics of the naturally formed oxides [277]. The mild steel's corrosion potential (E_{corr}) gradually shifts to a negative direction with prolonged immersion time under each temperature condition due to the corrosion layer's instability, reaching stability around 1800 seconds.

This phenomenon indicates that the corrosion of mild steel in 3.5% NaCl solution is controlled by activation reaction [278]. With the increase in temperature, the OCP of mild steel shifted negatively, indicating the initiation of corrosion processes [279] and the gradual degradation of corrosion resistance. The corrosion rate is determined by the diffusion of oxygen to the corroding surface, and the definitive factor is the concentration of dissolved oxygen in the electrolyte.

The OCP curves for mild steel in 3.5% NaCl solution at various temperatures with the $APCK_{15}$ (700ppm) inhibitor.

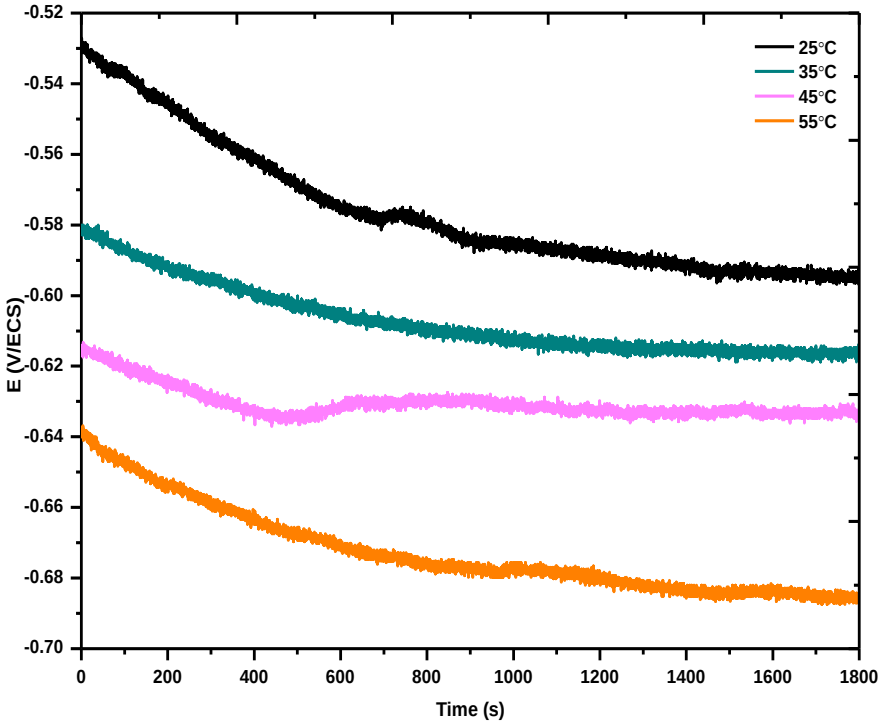

Figure IV. 13. The OCP curves for mild steel in 3.5% NaCl solution at various temperatures without the $APCK_{15}$ (700ppm) inhibitor.

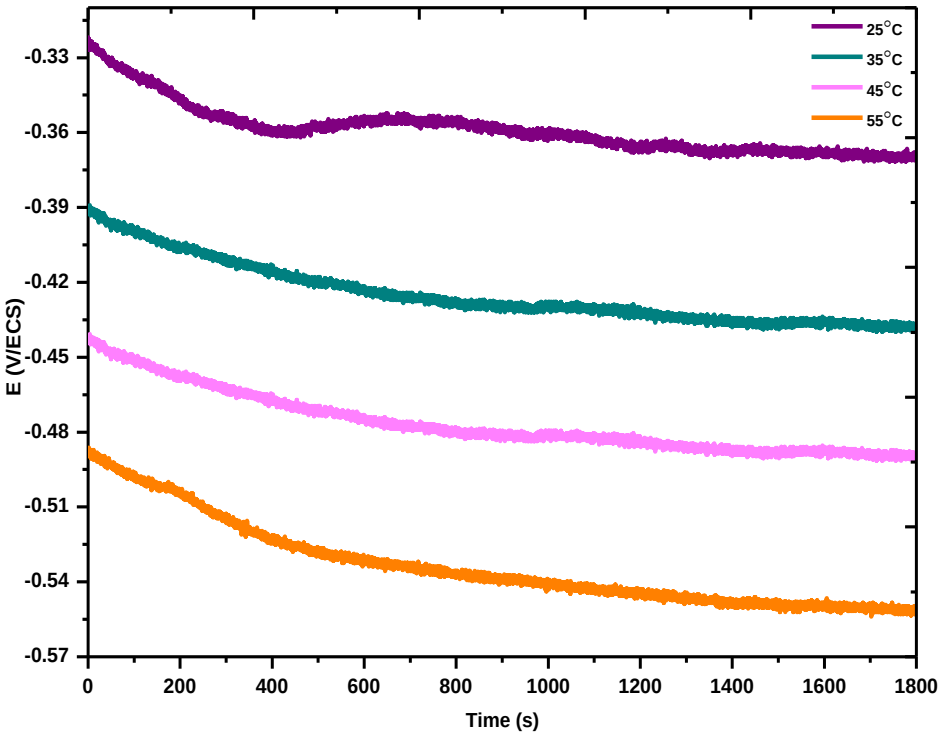

Figure IV. 14. The OCP curves for mild steel in 3.5% NaCl solution at various temperatures with the $APCK_{15}$ (700ppm) inhibitor.

IV.3.2.2. Examining the Influence of Temperature on Polarization Curves

The impact of temperature on the polarization curves of mild steel in a 3.5% NaCl solution was thoroughly analyzed in this study. The analysis was conducted in two parts, first without any additives and then with the optimal concentration of 700 ppm of the $APCK_{15}$ glass system (figures IV.15 and IV.16). For the remaining samples, the polarization curves had similar shapes for all concentrations.

The results of the inhibitory efficiencies (IE%) and electrochemical parameters of the corrosion of mild steel in 3.5% NaCl before and after adding 700 ppm of $APCK_{15}$ at different temperatures were presented in Table IV.6.

As depicted in Figure 5, both anodic and cathodic reactions exhibit enhancement with the rise in temperature from 25 to 55°C. This observation suggests a heightened corrosion rate for mild steel under elevated temperatures. Analyzing the data presented in Table 3 reveals a notable shift in the E_{corr} of steel towards negative values, from −572.1 to −662.77 mV/SCE for blank solutions and from −458.4 to −538.24 mV/SCE for solutions containing the inhibitor. Correspondingly, i_{corr} experiences an increase from 219 to 452 µA/cm^2 for blank solutions and from 42 to 208 µA/cm^2 for inhibitor-containing solutions, indicating a direct correlation between temperature and mild steel corrosion rate [280].

Furthermore, both β_a and β_c demonstrate a decrease with rising temperature, albeit with a more pronounced effect on β_c compared to β_a. This suggests that the cathode reaction predominantly governs the corrosion process. Specifically, the corrosion rate is influenced by the oxygen absorption reaction at the cathode and the active dissolution of the anode. These trends may be attributed to specific interactions between the inhibitor and the iron surface. As temperature increases, inorganic inhibitors tend to desorb, supporting the notion that the $APCK_{15}$ inhibitor is indeed adsorbed onto the mild steel surface.

These findings resonate with previous studies by Zhou et al. [25,281,282], wherein it was observed that the corrosion rate of steel increased with rising temperatures, reinforcing the impact of temperature on corrosion kinetics.

Table IV. 6. Electrochemical parameters obtained from polarization diagrams of mild steel in 3.5% NaCl solution before and after the addition of $APCK_{15}$ (700ppm) at different temperatures.

Temperature (°C)	Inhibitor	-Ecorr (mV/SCE)	i_{corr} ($\mu A/cm^2$)	βa (mV/dec)	-βc (mV/dec)	E(%)	θ
25	Blank	572.1	219	122.9	263.2	---	---
	In	458.4	42	60.73	41.36	80.82	81
35	Blank	591	225	119.9	208	---	---
	In	469.2	69.01	60.6	39.6	69.33	0.69
45	Blank	637.03	236	98.6	186	---	---
	In	488.92	89.02	36.8	25.2	62.28	0.62
55	Blank	662.77	452	88.4	139.8	---	---
	In	538.24	207.92	24.1	20.83	54	0.54

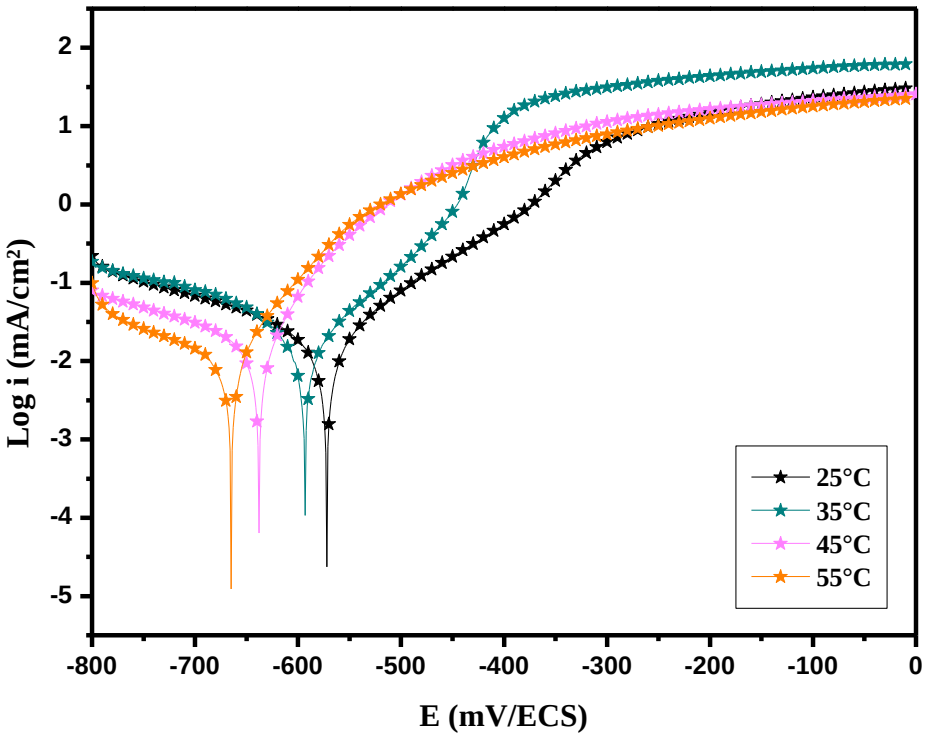

Figure IV. 15. The polarization curves for mild steel in 3.5% NaCl solution at various temperatures without the $APCK_{15}$ (700ppm) inhibitor.

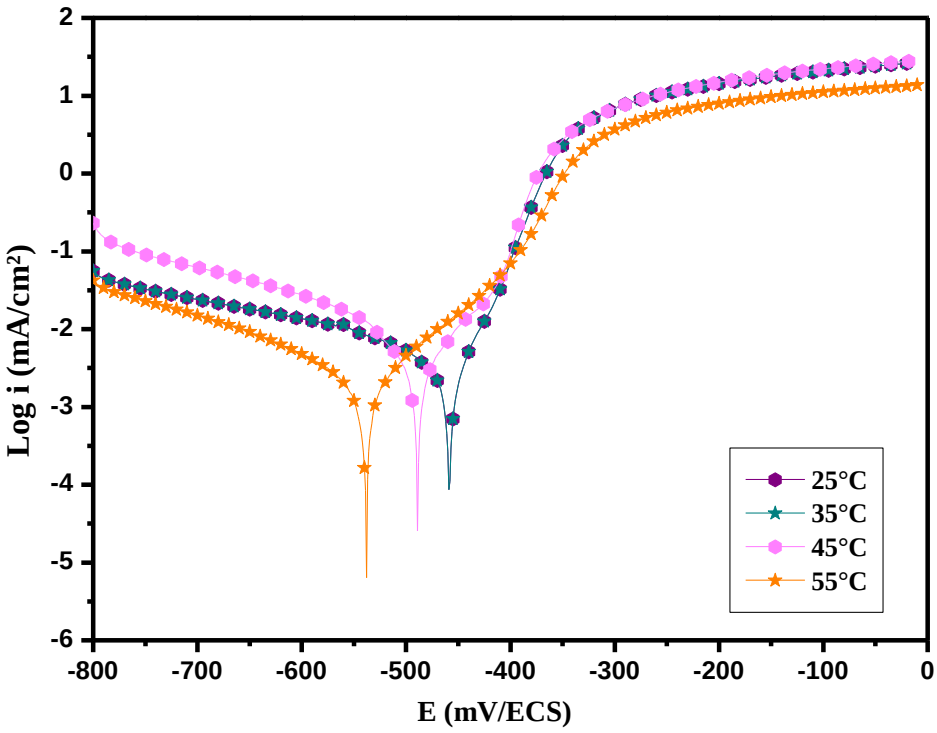

Figure IV. 16. The polarization curves for mild steel in 3.5% NaCl solution at various temperatures with the $APCK_{15}$ (700ppm) inhibitor.

At 25°C, $APCK_{15}$ at a concentration of 700 ppm demonstrates remarkable inhibitory efficiency, reaching an impressive 81%. However, as the temperature rises, the efficacy of the inhibitor diminishes due to desorption, indicating that the studied inhibitor primarily operates through physical adsorption onto the metal surface. Temperature exerts a significant influence on corrosion phenomena, with corrosion rates typically escalating alongside temperature increments. These temperature-induced changes affect inhibitor action [283], as noted by Putilova et al. [284], who propose that the protective power of inhibitors increases with rising temperatures, potentially due to shifts in adsorption mechanisms. Specifically, they suggest that at lower temperatures, inhibitors are primarily physically adsorbed, while at higher temperatures, chemisorption becomes favored. Our findings, in line with Radovici's classification, suggest that the inhibitor studied adheres to the surface through electrostatic bonds, indicative of physisorption onto the electrode surface [171].

IV.3.3. Thermodynamic parameters estimation

IV.3.3.1. Determination of the activation parameters

Thermodynamics can aid in comprehending how inhibitors interact with steel surfaces. This also enables the analysis of the stability of the glass film present on mild steel surfaces and determination of activation parameters for corrosion processes.

The activation parameters of the corrosion process were calculated at different temperatures in the absence and presence of inhibitors. Corrosion reactions are usually regarded as Arrhenius processes and the rate i_{corr} can be expressed by the relation:

$$i_{corr} = Aexp\left(-\frac{E_a}{RT}\right)$$

$$\text{Log } i_{corr} = LogA - \frac{E_a}{2.303\,RT}$$

Where:

i_{corr}**:** Corrosion current density,

A: Arrhenius constant,

E_a**.:** Activation energy,

R: Molar gas constant,

T: Absolute temperature (K).

The regression between log i_{corr} and $\frac{1}{T}$ was calculated by computer, and the parameters were calculated and given in table IV.7 Arrhenius plots of log i_{corr} and $\frac{1}{T}$ for the blank and different concentrations of $APCK_{15}$ in chloride medium are shown in figure IV.17. The slope of the line is $\frac{-E_a}{2.303\,R}$ and the intercept of the line extrapolated ($\frac{1}{T}$ =0) gives log A.

The regression analysis, conducted computationally between the logarithm of the corrosion current density (log i_{corr}) and the inverse of the absolute temperature yielded parameters detailed in Table IV.7. Arrhenius plots depicted in Figure IV.17 unmistakably illustrate the direct relationship between these variables, irrespective of $APCK_{15}$ concentration. The linear equation ln i_{corr} = f (1000/T) accurately captures this relationship.

Table IV.7 showcases the activation energies (E_a) obtained with and without the presence of 700 ppm $APCK_{15}$ inhibitor. It's observed that in the inhibitor's presence, E_a values are notably

higher compared to its absence. This elevation in activation energy stems from the alteration in the corrosion process mechanism induced by phosphate glass molecules, which effectively curtail steel dissolution in the corrosive milieu. Additionally, the presence of $APCK_{15}$ intensifies the energy barrier for the corrosion reaction, consequently lowering the corrosion rate [285–287].

The heightened activation energy often signals the formation of an adsorption-protecting layer via a physical mechanism. This layer, facilitated by the inhibitor, serves as evidence of its inhibitory action, further corroborating the role of $APCK_{15}$ in mitigating corrosion effects on steel surfaces.

An additional formula exists for the Arrhenius equation, which permits the calculation of both the enthalpy of activation (ΔH_a^0) and the entropy of activation (ΔS_a^0) through this equation:

$$i_{corr} = \frac{RT}{Nh} exp\left(\frac{\Delta S_a^o}{R}\right) exp\left(\frac{\Delta H_a^o}{RT}\right)$$

h is Planck constant, and N is Avogadro's number.

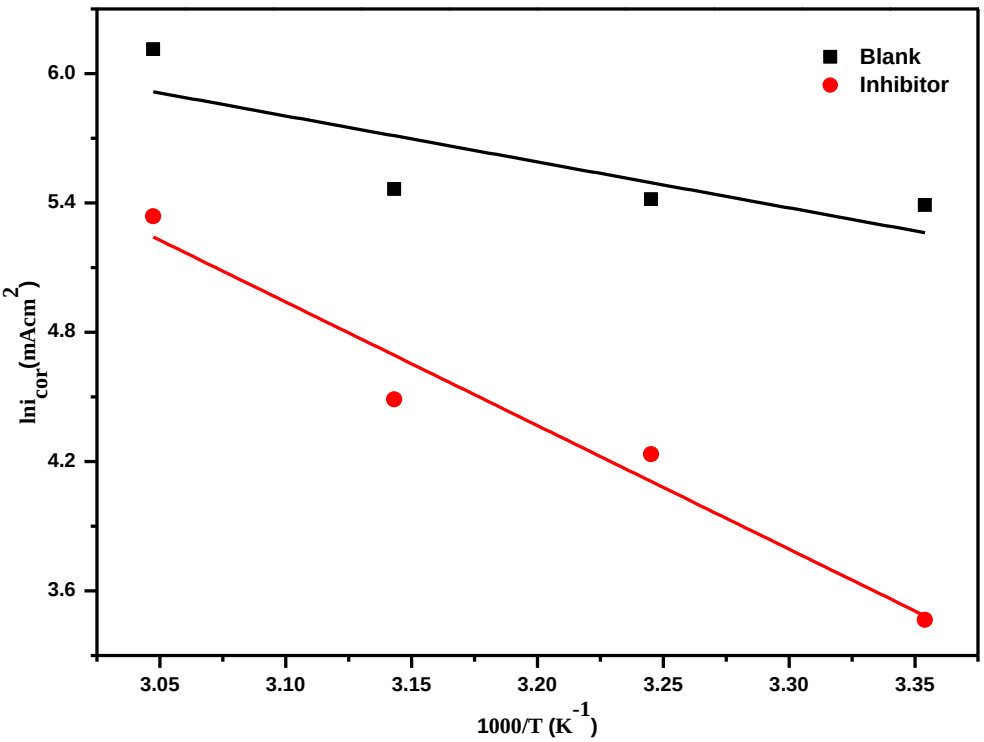

Figure IV. 17. Arrhenius lines of corrosion current density of mild steel in 3.5% NaCl medium in the absence and presence of $APCK_{15}$ (700ppm).

Analyzing the graph depicted as ln(i_{corr}/T) versus (1000/T) in Figure IV.18 enables the determination of ΔH_a^0 from the slope ($-\Delta H_a^0$ /R) and ΔS_a^0 from the intercept [ln(R/Nh) + (ΔS_a^0/R)]. The presence of the APCK inhibitor manifests in superior enthalpy values, indicative of heightened protective effects. Notably, the positive values of ΔH_a^0 suggest the endothermic nature of iron dissolution, indicating a deceleration of iron dissolution in the inhibitor's presence. The elevated values of both Ea and ΔH_a^0 imply the formation of a stable APCK layer. Furthermore, the parallel variations observed in activation energy and enthalpy validate the thermodynamic correlation between E_a and ΔH_a^0 [288]. This alignment underscores the thermodynamic stability conferred by the inhibitor, reinforcing its effectiveness in retarding corrosion processes on iron surfaces.

$$\boldsymbol{E_a - \Delta H_a^0 = RT}$$

The negative and high entropy ΔS_a^0 values imply that the activated complex in the rate-determining step signifies association, not dissociation. Therefore, it can be concluded that there is a decrease in disorder when the reactants transform into the activated iron-glass compound complex [289,290].

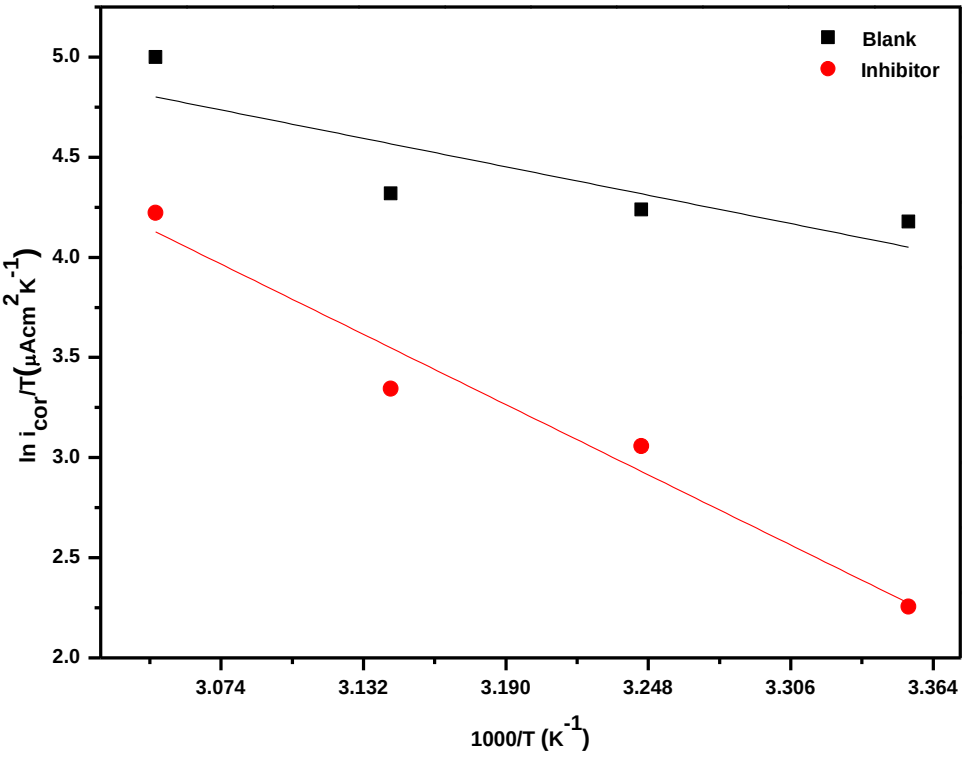

Figure IV. 18. The association between ln (icorr/T) and inverse temperature for mild steel in a 3.5% NaCl solution is being studied with and without the addition of 700ppm of APCK$_{15}$.

Table IV. 7. Activation parameters of the corrosion process of mild steel in 3.5% NaCl medium in the absence and presence of 700ppm of the inhibitor $APCK_{15}$.

	E_a (KJ.mol^{-1})	ΔS_a^0 (J.mol^{-1}.K^{-1})	ΔH_a^0 (KJ.mol^{-1})
Blanc	40.85	-95.65	17.73
$APCK_{15}$	109.81	-10.0030	47.68

IV.3.3.2 Thermodynamic adsorption isotherms

Understanding the behavior of inhibitor molecules and their interaction with the metal surface is crucial, and adsorption isotherms provide invaluable insights into this process. These isotherms, derived from data obtained through polarization measurements, offer essential information for characterizing inhibitor adsorption [291].

Adsorption isotherms illustrate the amount of substance adsorbed onto a surface as the inhibitor concentration in a solution increases. To discern the type of isotherm, the coverage rate of the inhibitor, $APCK_{15}$, on the metal surface is calculated using data from polarization measurements. This calculation allows for a comprehensive understanding of the adsorption process and provides insights into the effectiveness of the inhibitor in protecting the metal surface from corrosion. The specific equation is as follow:

$$\boldsymbol{\theta = \frac{i_{corr} - i_{inh}}{i_{corr}}}$$

Our experimental data analysis involved using three adsorption isotherms: Langmuir, Frumkin, Temkin, and the El-Awady thermodynamic/kinetic model [189,292,293]. Through this, we could determine the most suitable isotherm for describing the adsorption process of phosphate glass.

Langmuir isotherm: $\boldsymbol{\frac{C_{inh}}{\theta} = \frac{1}{b} + C_{inh}}$

Temkin isotherm : $\boldsymbol{\theta = \frac{\ln K_{ads}}{2a} + \frac{\ln C_{inh}}{2a}}$

Frumkin isotherm : $\boldsymbol{\ln\left(C_{inh}\frac{(1-\theta)}{\theta}\right) = -\ln K_{ads} - 2\alpha\theta}$

El Awady isotherm: $\boldsymbol{\ln\frac{\theta}{(1-\theta)} = \ln K + y \ln C_{inh}}$, where $\boldsymbol{K_{ads} = K^{\frac{1}{y}}}$

Where:

b: Adsorption coefficient ;

a : Interaction constant between adsorbed particles ;

K_{ads}**:** Adsorption-desorption Equilibrium constant;

α**:** A parameter related to the variation in free anergy adsorption ;

C_{inh}**:** Inhibitor concentration in solution.

Figures IV.19 show the plots of Langmuir, Frumkin, Temkin, and El Awady isotherms. Additionally, table IV.8 includes the adsorption parameters that were retrieved from polarization data of $APCK_{15}$ for 100, 300, 500, and 700ppm concentrations.

In order to determine the adsorption nature and strength of glass on steel surface, we calculated Gibbs free energy $\Delta G°_{ads}$ from K_{ads} by the following equation:

$$K_{ads} = \frac{1}{55,5} exp(\frac{\Delta G^0_{ads}}{RT})$$

where ***R*** is gas constant and ***T*** is absolute temperature and the constant value of 55.5 is the concentration of water in solution in mol. L^{-1}.

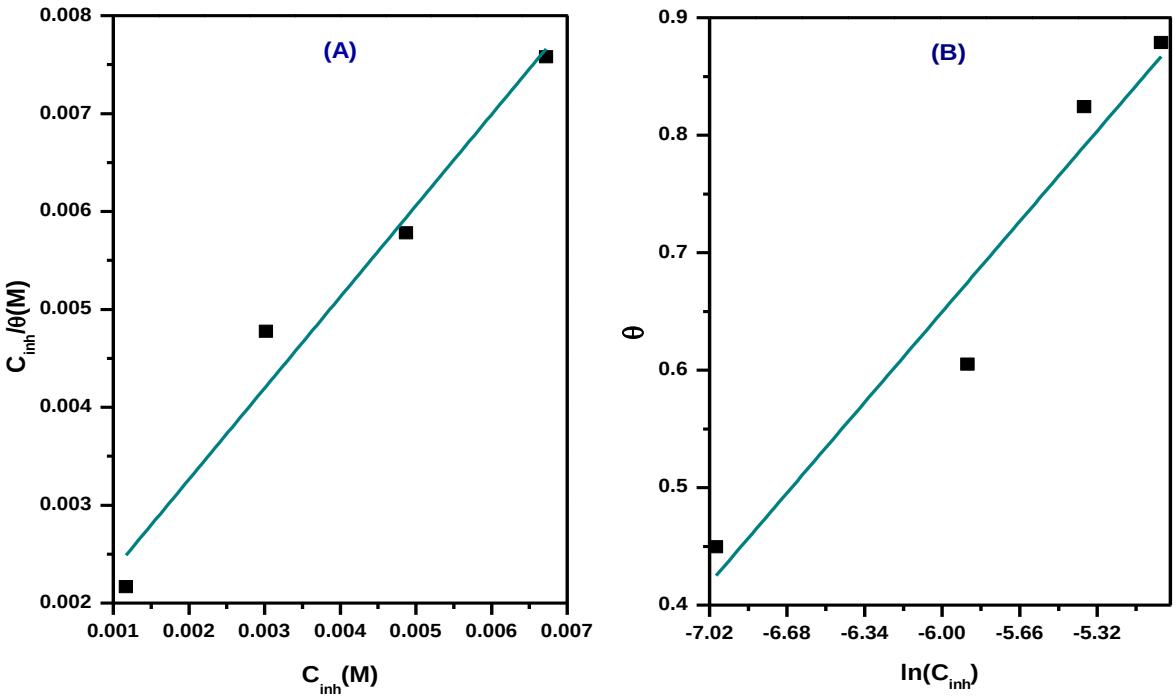

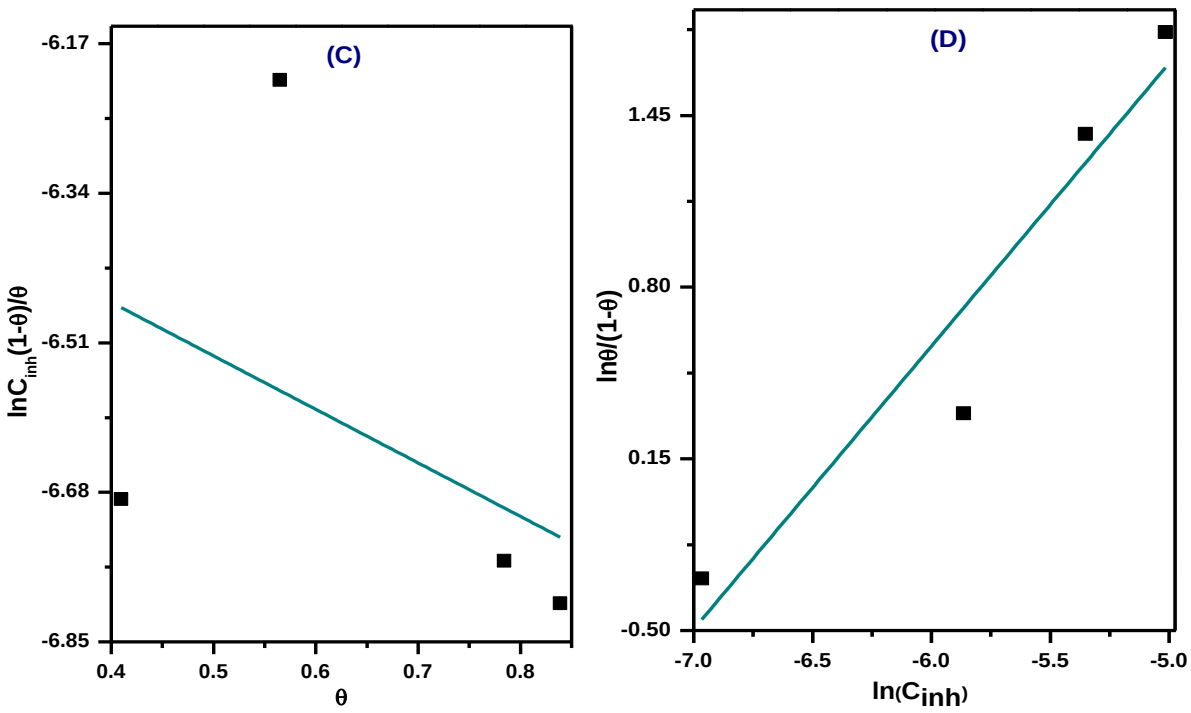

Figure IV. 19. Langmuir (A), Temkin (B), Frumkin (C) and El Awady (D) adsorption isotherms of mild steel in 3.5% NaCl in the presence of $APCK_{15}$ at different concentrations at 298 K.

Table IV. 8. Thermodynamic parameters for adsorption of $APCK_{15}$ inhibitor on steel at 298 K.

Isotherms	R^2	Log K_{ads}	ΔG_a^0(KJ/mol)	α	a	1/y
Langmiur	0.9556	9.79	-25.87	---	---	---
Temkin	0.9147	3.80	-31.66	---	2.21	---
El Awady	0.8816	2.85	-26.22	---	---	0.93
Frumkin	0.2075	2.70	-25.35	0.30	---	---

Upon analyzing the fitting processes of the data, it was discerned that one of the four models effectively described the adsorption process. The model exhibiting the highest R^2 value was deemed the most suitable. From the results presented in Table IV.19, it was concluded that the Langmuir isotherm model best represented the adsorption of $APCK_{15}$ on iron under the given conditions. The obtained slope while connecting $\frac{C_{inh}}{\theta}$ versus C_{inh} yielded a nearly linear correlation coefficient ($R^2 > 0.9$), indicating a strong fit with the Langmuir model ($R^2 = 0.9556$). The higher K_{ads} value signifies the robust adsorption ability of $APCK_{15}$ glass, thereby enhancing inhibition efficiency. Moreover, the negative values of $\Delta G°_{ads}$ indicate the substantial adsorption of the inhibitor onto the steel surface, indicative of superior performance. Typically,

$\Delta G°_{ads}$ values around -20 kJ/mol or less negative are associated with physical adsorption (electrostatic interaction), while values around -40 kJ/mol or more negative are linked to chemisorption [294]. The obtained value of $\Delta G°_{ads} \approx$ -32 kJ/mol suggests that $APCK_{15}$ adsorption on the iron surface is of a mixed type, encompassing both physisorption and chemisorption [255].

IV.4. Conclusion

To sum up, the Al_2O_3-K_2O-CaO-P_2O_5 quaternary system glasses have displayed highly promising results in preventing corrosion on mild steel in a 3.5% NaCl medium. By analyzing various glass compositions, we have observed that the inhibitory properties were impacted by concentration and temperature. To explore these effects, this investigation utilized gravimetry, polarization curves, and electrochemical impedance spectroscopy (EIS). These findings open up exciting possibilities for further research and development of these glasses for potential industrial application.

Summary

Our current research seeks to enhance the understanding of the thermal, structural, optical, and anticorrosive characteristics of vitreous materials in the $CaO-K_2O-P_2O_5$ and $Al_2O_3-CaO-K_2O-P_2O_5$ systems. To prepare the glass samples for analysis, they were melted at temperatures ranging from 800 to 1000°C.

On the one hand, we confirmed the amorphous nature of the synthesized materials using X-ray Diffraction (XRD) and Differential Scanning Calorimetry (DSC). Our research revealed that the glass transition temperature T_g increases as the oxides CaO and Al_2O_3 content increase. This result promotes thermal stabilization and cross-linking of the glass network. The facts were backed by measuring the volume density (ρ), the molar volume (V_m), and the chemical durability in three alteration solutions with varying acidity. Our findings indicate that adding the oxides, Al_2O_3 narrows the vitreous network, creating more entangled and cross-linked chains.

Furthermore, the study's findings suggest that adding calcium and aluminum ions to the vitreous composition leads to the depolymerization of phosphate chains made from metaphosphates and their subsequent formation into P-O-Ca and P-O-Al bonds. This structural evolution increases the glass transition temperature, which is consistent with the formation of P-O-Al bonds. The behavior of the quaternary system also supports the hypothesis that Al_2O_3 partially enters the forming network in AlO_4.

On the other hand, UV-Vis-NIR spectroscopy has revealed that adding aluminum ions enhances the vitreous matrix's strength and improves the glasses' semiconductor properties. Additionally, the final axis of this investigation focused on examining the anticorrosive characteristics of APCK glass. Specifically, the effects of inhibitor concentration, composition, and temperature on the corrosion process were explored using gravimetry, polarization curves, and electrochemical impedance spectroscopy techniques, both in the presence and absence of the inhibitor.

The results show that all the inhibitors studied are mixed inhibitors (with anodic predominance) whose effectiveness increases with the concentration and composition of the inhibitors. The maximum values were obtained for the inhibitor $APCK_{15}$ concentration at 700 ppm. The polarization curves revealed that the current density decreases with increasing concentration

and composition of the oxides Al_2O_3. The Nyquist impedance diagrams and those of Bode have shown that the electrochemical process occurs by a charge transfer on a heterogeneous surface, which is for all the concentrations studied.

The effect of the concentration on the inhibitory activity of the mild steel was carried out in the range of 25-55°C. The results show that the inhibitory power of the glasses tested in 3.5% NaCl medium for a concentration of 700 ppm of the $APCK_{15}$ inhibitor decreases with temperature. This behavior can be explained by the fact that the cathode and anode processes are thermally activated (physisorption). The thermodynamic parameters (E_a, ΔS_a^0, and ΔH_a^0 for activating the corrosion process were calculated at different temperatures in the absence and the presence of an inhibitor. The positive signs of the enthalpies ΔH_a^0 reflect the endothermic nature of the dissolution process of the steel. At the same time, the high and negative values of the entropy ΔS_a^0 imply a decrease in the disorder during the transformation of the reactants into an activated iron-vitreous compound-complex.

The adsorption isotherms of Langmuir, Temkin, Frumkin, and El Awady were studied from the values obtained from the polarization curves for the $APCK_{15}$ inhibitor at 298 K and for the concentrations 100, 300, 500, and 700 ppm. The inhibitors' adsorption on the steel surface obeys the isotherm of Langmuir. The negative value of the standard free adsorption energy $\Delta G°_{ads}$ obtained indicates the spontaneity of our inhibitors' adsorption process on the steel surface and the stability of the adsorbed double layer on the metal surface. The mechanism of inhibition is based on strong physisorption and chemisorption of the APCK glass system.

References

1. Faivre A, Despetis F, Duffours L, Colombel P. Effect of CaO and Al2O3 addition on the properties of K2O–Na2O–P2O5 glass system. *Int J Appl Glas Sci*. 2019;10(2):162-171. doi:10.1111/IJAG.13066
2. Oosterbeek RN, Margaronis KI, Zhang XC, Best SM, Cameron RE. Non-linear dissolution mechanisms of sodium calcium phosphate glasses as a function of pH in various aqueous media. *J Eur Ceram Soc*. 2021;41(1):901-911. doi:10.1016/J.JEURCERAMSOC.2020.08.076
3. Brauer DS, Karpukhina N, Law R V., Hill RG. Effect of TiO2 addition on structure, solubility and crystallisation of phosphate invert glasses for biomedical applications. *J Non Cryst Solids*. 2010;356(44-49):2626-2633. doi:10.1016/J.JNONCRYSOL.2010.03.022
4. Punj S, Singh J, Singh K. Ceramic biomaterials: Properties, state of the art and future prospectives. *Ceram Int*. 2021;47(20):28059-28074. doi:10.1016/J.CERAMINT.2021.06.238
5. Gharbi A, Ayadi S, Jouini N, et al. Original implementation of low-temperature SPS for bioactive glass used as a bone biomaterial. *J Mech Behav Biomed Mater*. 2022;126:104988. doi:10.1016/J.JMBBM.2021.104988
6. Hyunh NB, Palma CSD, Rahikainen R, et al. Surface Modification of Bioresorbable Phosphate Glasses for Controlled Protein Adsorption. *ACS Biomater Sci Eng*. 2021;7(9):4483-4493. doi:10.1021/ACSBIOMATERIALS.1C00735/SUPPL_FILE/AB1C00735_SI_001.PDF
7. Shi Y, Xi X, Zhao G, et al. Sealing performance of tempered vacuum glazing with silver oxide system low melting solder. *Mater Chem Phys*. 2022;275. doi:10.1016/j.matchemphys.2021.125202
8. Morena R. Phosphate glasses as alternatives to Pb-based sealing frits. *J Non Cryst Solids*. 2000;263-264:382-387. doi:10.1016/S0022-3093(99)00678-X
9. Kim S, Han K, Kim S, Kadathala L, Kim J, Choi J. Strengthening Thermal Stability in V 2 O 5-ZnO-BaO-B 2 O 3-M(PO 3) n Glass System (M = Al, Mg) for Laser Sealing Applications. Published online 2021. doi:10.3390/app11104603
10. Rivera FLF, Velazquez DYM, Martínez GVA, et al. Luminescent Properties of the Mn²⁺ Ion in Zinc Phosphate Glass. *Open J Appl Sci*. 2021;11(11):1212-1217. doi:10.4236/ojapps.2021.1111091
11. Mahamuda S, Syed F, Annapurna Devi CB, et al. Spectral characterization of Dy3+ ions doped phosphate glasses for yellow laser applications. *J Non Cryst Solids*. 2021;555:120538. doi:10.1016/J.JNONCRYSOL.2020.120538
12. Kiwsakunkran N, Chaiphaksa W, Chanthima N, et al. Fabrication of K2O–Al2O3–Gd2O3–

P2O5 glasses for photonic and scintillation materials applications. *Radiat Phys Chem*. 2021;188:109639. doi:10.1016/J.RADPHYSCHEM.2021.109639

13. Elbashar YH, Ibrahim AM, Elshaikh HA, El-Din Mostafa AG. Influence of CuO and Al2O3 addition on the optical properties of sodium zinc phosphate glass absorption filters. *Optik (Stuttg)*. 2016;127(18):7041-7053. doi:10.1016/J.IJLEO.2016.05.008

14. Elbashar YH, Badr AM, Elshaikh HA, Mostafa AG, Ibrahim AM. Dielectric and optical properties of CuO containing sodium zinc phosphate glasses. *Process Appl Ceram*. 2016;10(4):277-286. doi:10.2298/PAC1604277E

15. Ibrahim AM, Elbashar YH, Badr AM, Elshaikh HA, Mostafa AG. Mixed ionic–polaronic conduction in copper sodium phosphate glasses containing aluminium oxide. *J Microw Power Electromagn Energy*. 2017;51(1):71-89. doi:10.1080/08327823.2017.1291069

16. Ishiyama T, Suzuki S, Nishii J, Yamashita T, Kawazoe H, Omata T. Proton conducting tungsten phosphate glass and its application in intermediate temperature fuel cells. *Solid State Ionics*. 2014;262:856-859. doi:10.1016/J.SSI.2013.10.055

17. Muñoz F. The chemistry of melting oxynitride phosphate glasses. *Pure Appl Chem*. 2022;94(2):189-195. doi:10.1515/PAC-2021-0704/MACHINEREADABLECITATION/RIS

18. Yin Q, Kang S, Wang X, Li S, He D, Hu L. Effect of PbO on the spectral and thermo-optical properties of Nd3+-doped phosphate laser glass. *Opt Mater (Amst)*. 2017;66:23-28. doi:10.1016/J.OPTMAT.2017.01.036

19. Linganna K, Kumar KU, Jayasankar CK. Spectroscopy and 1.47 μm emission properties of Tm3+-doped metaphosphate laser glasses. *Mater Express*. 2013;3(1):71-78. doi:10.1166/MEX.2013.1099

20. Gonçalves TS, dos Santos JFM, Sciuti LF, Catunda T, de Camargo ASS. Thermo-optical spectroscopic investigation of new Nd3+-doped fluoro-aluminophosphate glasses. *J Alloys Compd*. 2018;732:887-893. doi:10.1016/J.JALLCOM.2017.10.152

21. Filho JC, Lourenço SA, Ferreira PZ, et al. Thermal window of constant luminescence quantum efficiency of Nd3+-doped phosphate glass. *J Lumin*. 2016;180:81-87. doi:10.1016/J.JLUMIN.2016.08.018

22. Ramakrishna P, Sitakanta Panda, Vinod Kumar P, Mohapatra DK, Jena H, Panigrahi BS. Structural and optical properties of Ce-doped strontium borophosphate glasses. *Indian J Phys*. 2021;95(11):2471-2478. doi:10.1007/s12648-020-01910-4

23. De Melo N, Murrell L, Islam MT, et al. Tailoring Pyro- and Orthophosphate Species to Enhance Stem Cell Adhesion to Phosphate Glasses. *Int J Mol Sci 2021, Vol 22, Page 837*. 2021;22(2):837. doi:10.3390/IJMS22020837

24. Moguš-Milanković A, Gajović A, Šantić A, Day DE. Structure of sodium phosphate glasses containing Al2O3 and/or Fe2O3. Part I. *J Non Cryst Solids*. 2001;289(1-3):204-213.

doi:10.1016/S0022-3093(01)00701-3

25. Zhou Y, Zhang J, Liao C, et al. Pb Stabilization by a New Chemically Durable Orthophosphate Phase: Insights into the Molecular Mechanism with X-ray Structural Analysis. *Environ Sci Technol*. 2020;54(11):6937-6946. doi:10.1021/ACS.EST.0C00643/SUPPL_FILE/ES0C00643_SI_001.PDF

26. Moreau F, Durán A, Muñoz F. Structure and properties of high Li2O-containing aluminophosphate glasses. *J Eur Ceram Soc*. 2009;29(10):1895-1902. doi:10.1016/J.JEURCERAMSOC.2008.12.016

27. Metwalli E, Brow RK. Modifier effects on the properties and structures of aluminophosphate glasses. *J Non Cryst Solids*. 2001;289(1-3):113-122. doi:10.1016/S0022-3093(01)00704-9

28. Matamoros-Veloza A, Hossain KMZ, Scammell BE, Ahmed I, Hall R, Kapur N. Formulating injectable pastes of porous calcium phosphate glass microspheres for bone regeneration applications. *J Mech Behav Biomed Mater*. 2020;102:103489. doi:10.1016/J.JMBBM.2019.103489

29. Mokhtari S, Skelly KD, Krull EA, et al. Copper-containing glass polyalkenoate cements based on SiO2–ZnO–CaO–SrO–P2O5 glasses: glass characterization, physical and antibacterial properties. *J Mater Sci*. 2017;52(15):8886-8903. doi:10.1007/S10853-017-0945-5/METRICS

30. Canillas M, Pena P, De Aza AH, Rodríguez MA. Calcium phosphates for biomedical applications. *Boletín la Soc Española Cerámica y Vidr*. 2017;56(3):91-112. doi:10.1016/J.BSECV.2017.05.001

31. Knowles JC. Phosphate based glasses for biomedical applications. *J Mater Chem*. 2003;13(10):2395-2401. doi:10.1039/B307119G

32. Hutmacher DW, Schantz JT, Lam CXF, Tan KC, Lim TC. State of the art and future directions of scaffold-based bone engineering from a biomaterials perspective. *J Tissue Eng Regen Med*. 2007;1(4):245-260. doi:10.1002/TERM.24

33. Lee S, Nagata F, Kato K, Nakano T, Kasuga T. materials Structures and Dissolution Behaviors of Quaternary CaO-SrO-P 2 O 5-TiO 2 Glasses. Published online 2021. doi:10.3390/ma14071736

34. Vitale-Brovarone C, Novajra G, Milanese D, Lousteau J, Knowles JC. Novel phosphate glasses with different amounts of TiO2 for biomedical applications: Dissolution tests and proof of concept of fibre drawing. *Mater Sci Eng C*. 2011;31(2):434-442. doi:10.1016/J.MSEC.2010.11.001

35. Alaoui Y, El Moudane M, Er-rafai A, et al. Structural study, thermal and physical properties of K2O-CaO-P2O5 phosphate glasses. *Moroccan J Chem*. 2021;9(3):454-463.

36. Es-soufi H, Bih L. Effect of TiO2 on the chemical durability and optical properties of Mo-based phosphate glasses. *J Non Cryst Solids*. 2021;558:120655.

doi:10.1016/J.JNONCRYSOL.2021.120655

37. Chialanza MR, Keuchkerian R, Gonçalves TS, de Camargo ASS, Fornaro L. The effect of cation modifier on improving the luminescent properties of borate glasses doped with Yb3 + and Er3 +. *J Non Cryst Solids*. 2018;483:79-85. doi:10.1016/j.jnoncrysol.2018.01.002

38. Frieser RG. A Review of Solder Glasses. *Electrocompon Sci Technol*. 1975;2(3):163-199. doi:10.1155/APEC.2.163

39. Brow RK. Nature of Alumina in Phosphate Glass: I, Properties of Sodium Aluminophosphate Glass. *J Am Ceram Soc*. 1993;76(4):913-918. doi:10.1111/J.1151-2916.1993.TB05315.X

40. Brow RK, Kirkpatrick RJ, Turner GL. Nature of Alumina in Phosphate Glass: II, Structure of Sodium Alurninophosphate Glass. *J Am Ceram Soc*. 1993;76(4):919-928. doi:10.1111/J.1151-2916.1993.TB05316.X

41. Filho JC, Zilio SC, Messias DN, et al. Effects of aluminum substitution by potassium in the P2O5–Al2O3–Na2O–K2O phosphate glasses. *J Alloys Compd*. 2020;815. doi:10.1016/j.jallcom.2019.152359

42. Alaoui Y, Moudane M El, Laourayed M, Boudalia M, Guenbour A. Effect of the Al 2 O 3 on the thermal and chemical durability of some aliminium calcium potassium phosphate glasses. :12.

43. Bunker BC, Arnold GW, Wilder JA. Phosphate glass dissolution in aqueous solutions. *J Non Cryst Solids*. 1984;64(3):291-316. doi:10.1016/0022-3093(84)90184-4

44. Peng Y, Day D. High Thermal Expansion Phosphate Glasses. Part 1. *Glas Technol*. 1991;32(5). Accessed March 21, 2022. https://scholarsmine.mst.edu/matsci_eng_facwork/1869

45. Peng Y, Day D. High Thermal Expansion Phosphate Glasses. Part 2. *Glas Technol*. 1991;32(6). Accessed March 26, 2022. https://scholarsmine.mst.edu/matsci_eng_facwork/1870

46. J.E. Hammesfahr and C.L. Strong, ―Creative Glass... - Google Scholar. Accessed October 29, 2022. https://scholar.google.com/scholar?hl=en&as_sdt=0%2C5&q=J.E.+Hammesfahr+and+C.L.+Strong%2C+―Creative+Glass+Blowing‖%2C+W.H.+Freeman+and++Co.+Ltd.%2C+San+Francisco+%281968%29.+&btnG=

47. Dussubieux L, … BG-J of A, 2010 undefined. Mineral soda alumina glass: occurence and meaning. *Elsevier*. Accessed October 29, 2022. https://www.sciencedirect.com/science/article/pii/S0305440310000300?casa_token=V4SbJTCXYGAAAAAA:yghbdUyliq91ojF7ZQ43fCBBQQfqFRbZIs12KkuX28rQKbNECyUekbWtHkM3Z7yE1iFE2g2ELHI

48. Brow RK, Schmitt ML. A survey of energy and environmental applications of glass. *J Eur Ceram Soc*. 2009;29(7):1193-1201. doi:10.1016/J.JEURCERAMSOC.2008.08.011

49. Angelini I, Gratuze B, Artioli G. Glass and other vitreous materials through history. *Eur Mineral Union Notes Mineral*. 2019;20:87-150. doi:10.1180/EMU-NOTES.20.3

50. Boolchand P. Insulating and Semiconducting Glasses. 2000;17. doi:10.1142/3959

51. Richardson K, Krol D, Hirao K. Glasses for Photonic Applications. *Int J Appl Glas Sci*. 2010;1(1):74-86. doi:10.1111/J.2041-1294.2010.00008.X

52. Stroganova EE, Mikhailenko NY, Moroz OA. Glass-Based Biomaterials: Present and Future (A Review). *Glas Ceram 2003 609*. 2003;60(9):315-319. doi:10.1023/B:GLAC.0000008235.49161.32

53. National Research Council (1995), ―Technical Bases... - Google Scholar. Accessed October 30, 2022. https://scholar.google.com/scholar?hl=en&as_sdt=0%2C5&q=National+Research+Council+%281995%29%2C+―Technical+Bases+for+Yucca+Mountain++Standards‖%2C+Washington%2C+D.C.%2C+National+Academy+Press&btnG=

54. Fritzsche H, Schwartz B. Stanford R. Ovshinsky: The science and technology of an American genius. *Stanford R Ovshinsky Sci Technol an Am Genius*. Published online January 1, 2008:1-382. doi:10.1142/6877

55. STEINER J. Otto Schott (1851 to 1935) : Founder of modern glass science and glass technology. *Glas Sci Technol*. 2001;74(10):292-302.

56. Zachariasen WH. The atomic arrangement in glass. *J Am Chem Soc*. 1932;54(10):3841-3851. doi:10.1021/JA01349A006/ASSET/JA01349A006.FP.PNG_V03

57. Greaves GN. EXAFS and the structure of glass. *J Non Cryst Solids*. 1985;71(1-3):203-217. doi:10.1016/0022-3093(85)90289-3

58. Tulyaganov D, Baino F. Silicate Glasses and Glass–Ceramics: Types, Role of Composition and Processing Methods. *PoliTO Springer Ser*. Published online 2021:119-152. doi:10.1007/978-3-030-85776-9_4/COVER

59. Zarzycki J. Les Verres et l'État Vitreux. Published online 1982:404.

60. Guerineau T. Synthèse et caractérisation de verres pour l'impression 3D par laser : verres phosphates et d'oxydes lourds à l'argent. Published online July 8, 2020. Accessed November 3, 2022. https://tel.archives-ouvertes.fr/tel-03311678

61. Porter DA, Easterling KE, Sherif MY. Phase Transformations in Metals and Alloys, Fourth Edition. *Phase Transform Met Alloy Fourth Ed*. Published online January 1, 2021:1-556. doi:10.1201/9781003011804/PHASE-TRANSFORMATIONS-METALS-ALLOYS-DAVID-PORTER-KENNETH-EASTERLING-MOHAMED-SHERIF

62. Shelby JE. Principles of glass formation. *Introd to Glas Sci Technol*. Published online January 12, 2005:7-25. doi:10.1039/9781847551160-00007

63. Hrubý A. Glass-forming tendency in the GeSx system. *Czechoslov J Phys*. 1973;23(11):1263-1272. doi:10.1007/BF01591209/METRICS

64. Yadav AK, Gautam CR. Synthesis, Structural and Optical Studies of Barium Strontium Titanate Borosilicate Glasses Doped with Ferric Oxide. *http://dx.doi.org/101080/00387010201492088*6. 2015;48(7):514-520. doi:10.1080/00387010.2014.920886

65. Yadav AK, Gautam CR. A review on crystallisation behaviour of perovskite glass ceramics. *http://dx.doi.org/101179/1743676113Y0000000134*. 2014;113(4):193-207. doi:10.1179/1743676113Y.0000000134

66. Beskow G. V. M. Goldschmidt: Geochemische Verteilungsgesetze der Elemente. *http://dx.doi.org/101080/11035892409454037*. 2010;46(6-7):738-743. doi:10.1080/11035892409454037

67. mmi. LECTURE 2 : STRUCTURE AND EXPERIMENTAL CHARACTERIZATION-Order in glasses-Zachariasen random network theory-Glass families and glass forming ability-Experimental tools for structural characterization Atomic modeling of glass-LECTURE 2 STRUCTURE.

68. Axinte E. Glasses as engineering materials: A review. *Mater Des*. 2011;32(4):1717-1732. doi:10.1016/J.MATDES.2010.11.057

69. Vogel W. Historical Development of Glass Chemistry. *Glas Chem*. Published online 1994:1-21. doi:10.1007/978-3-642-78723-2_1

70. Campos CP De, Hess K-U. Geological Glasses. *Encycl Glas Sci Technol Hist Cult*. Published online February 2021:815-829. doi:10.1002/9781118801017.CH7.2

71. Shaar R, Tauxe L, Ben-Yosef E, et al. Cooling rate correction of paleointensity determination for volcanic glasses by relaxation geospeedometry. *Earth Planet Sci Lett*. 2006;243(1-2):282-292. doi:10.1002/2014GC005455

72. Volcani BE. Cell Wall Formation in Diatoms: Morphogenesis and Biochemistry. *Silicon Siliceous Struct Biol Syst*. Published online 1981:157-200. doi:10.1007/978-1-4612-5944-2_7

73. Schultz PC. Vapor Phase Materials and Processes for Glass Optical Waveguides. *Fiber Opt*. Published online 1979:3-31. doi:10.1007/978-1-4684-3492-7_1

74. Oueslati Omrani R, Kaoutar A, El Jazouli A, et al. Structural and thermochemical properties of sodium magnesium phosphate glasses. *J Alloys Compd*. 2015;632:766-771. doi:10.1016/J.JALLCOM.2015.01.297

75. Tricot G, Revel B, Wegner S. Thermal stability of a low Tg phosphate glass investigated by DSC, XRD and solid state NMR. *J Non Cryst Solids*. 2011;357(14):2708-2712. doi:10.1016/J.JNONCRYSOL.2011.02.020

76. Pascuta P, Borodi G, Popa A, Dan V, Culea E. Influence of iron ions on the structural and magnetic properties of some zinc-phosphate glasses. *Mater Chem Phys*. 2010;123(2-3):767-771. doi:10.1016/J.MATCHEMPHYS.2010.05.056

77. El Hezzat M, Et-tabirou M, Montagne L, Palavit G, Mazzah A, Dhamelincourt P. Spectroscopic studies of the structure of Na2O-CdO-PbO-P2O5 metaphosphate glasses.

78. Poulain M, Poulain M, Lucas J. Verres fluores au tetrafluorure de zirconium proprietes optiques d'un verre dope au Nd3+. *Mater Res Bull*. 1975;10(4):243-246. doi:10.1016/0025-5408(75)90106-3

79. Ovshinsky SR. Reversible Electrical Switching Phenomena in Disordered Structures. *Phys Rev Lett*. 1968;21(20):1450. doi:10.1103/PhysRevLett.21.1450

80. Miracle DB. A structural model for metallic glasses. *Nat Mater 2004 310*. 2004;3(10):697-702. doi:10.1038/nmat1219

81. Chang C-C, Lin C-F, Chiou J-M. ARTICLES YOU MAY BE INTERESTED IN. *Appl Phys Lett*. 2010;97:49901. doi:10.1063/1.3473732

82. Yamane M, Asahara Y, Yamane M, Asahara Y. Glasses for Photonics. *glph*. Published online 2005:281. Accessed November 13, 2022. https://ui.adsabs.harvard.edu/abs/2005glph.book.....Y/abstract

83. Novajra G, Boetti NG, Ambrosone A, et al. Novel biocompatible and resorbable UV-transparent phosphate glass based optical fiber. *Opt Mater Express, Vol 6, Issue 6, pp 2040-2051*. 2016;6(6):2040-2051. doi:10.1364/OME.6.002040

84. Dupree R, Holland D, Mortuza MG. Six-coordinated silicon in glasses. *Nat 1987 3286129*. 1987;328(6129):416-417. doi:10.1038/328416a0

85. Cormier L, Calas G, Beuneu B. Structural changes between soda-lime silicate glass and melt. *J Non Cryst Solids*. 2011;357(3):926-931. doi:10.1016/J.JNONCRYSOL.2010.10.014

86. Claireaux CC, Chopinet M-H, Burov E, et al. Atomic mobility in calcium and sodium aluminosilicate melts at 1200 °C Atomic mobility in calcium and sodium aluminosilicate melts at 1200 • C. doi:10.1016/j.gca.2016.07.032ï

87. Rabinovich EM. Lead in glasses. *J Mater Sci 1976 115*. 1976;11(5):925-948. doi:10.1007/BF00542311

88. Zhou A, Wang W, Liu Q, et al. Stable, fast and high-energy-density LiCoO2 cathode at high operation voltage enabled by glassy B2O3 modification. *J Power Sources*. 2017;362:131-139. doi:10.1016/J.JPOWSOUR.2017.06.050

89. Baccaro S, Catallo N, Cemmi A, Sharma G. Radiation damage of alkali borate glasses for application in safe nuclear waste disposal. *Nucl Instruments Methods Phys Res Sect B Beam Interact with Mater Atoms*. 2011;269(2):167-173. doi:10.1016/J.NIMB.2010.10.019

90. Shaaban MH, Ali AA. Density, Electrical and Optical Properties of Yttrium-Containing Tellurium Bismuth Borate Glasses. *J Electron Mater 2014 4311*. 2014;43(11):4023-4032. doi:10.1007/S11664-014-3331-Y

91. Goyal P, Kumar Sharma Y, Pal S, Bind UC, Huang SC, Chung SL. Radiative Properties of Er3+ Doped Borosilicate Glasses for Fibre Optics Applications. *Mater Today Proc*. 2018;5(1):344-350. doi:10.1016/J.MATPR.2017.11.091

92. Sokolov IA, Murin I V., Kriit VE, Pronkin AA. Structure and electrical conductivity of Li2O-B2O3 glasses. *Glas Phys Chem 2013 391*. 2013;39(1):19-31. doi:10.1134/S1087659613010112

93. Krogh-Moe J. The structure of vitreous and liquid boron oxide. *J Non Cryst Solids*. 1969;1(4):269-284. doi:10.1016/0022-3093(69)90025-8

94. Gautam C, Yadav AK, Singh AK. A Review on Infrared Spectroscopy of Borate Glasses with Effects of Different Additives. *ISRN Ceram*. 2012;2012:1-17. doi:10.5402/2012/428497

95. Gayathri Pavani P, Sadhana K, Chandra Mouli V. Optical, physical and structural studies of boro-zinc tellurite glasses. *Phys B Condens Matter*. 2011;406(6-7):1242-1247. doi:10.1016/J.PHYSB.2011.01.006

96. Flory PJ. Random Reorganization of Molecular Weight Distribution in Linear Condensation Polymers. *J Am Chem Soc*. 1942;64(9):2205-2212. doi:10.1021/JA01261A049/ASSET/JA01261A049.FP.PNG_V03

97. Brow RK, Click CA, Alam TM. Modifier coordination and phosphate glass networks. *J Non Cryst Solids*. 2000;274(1-3):9-16. doi:10.1016/S0022-3093(00)00178-2

98. Zhang L, Brow RK. A Raman Study of Iron–Phosphate Crystalline Compounds and Glasses. *J Am Ceram Soc*. 2011;94(9):3123-3130. doi:10.1111/J.1551-2916.2011.04486.X

99. Sales BC, Boatner LA, Ramey JO. Chromatographic studies of the structures of amorphous phosphates: a review. *J Non Cryst Solids*. 2000;263-264:155-166. doi:10.1016/S0022-3093(99)00644-4

100. Biscoe J, Pincus AG, Smith CS, Warren BE. X-RAY STUDY OF LIME-PHOSPHATE AND LIME-BORATE GLASS*. *J Am Ceram Soc*. 1941;24(4):116-119. doi:10.1111/J.1151-2916.1941.TB14833.X

101. Bhat MH, Kandavel M, Ganguli M, Rao KJ. Li+ ion conductivities in boro-tellurite glasses. *Bull Mater Sci 2004 272*. 2004;27(2):189-198. doi:10.1007/BF02708504

102. Muñoz F, Rocherullé J, Ahmed I, Hu L. Phosphate Glasses. *Springer Handbooks*. Published online 2019:553-594. doi:10.1007/978-3-319-93728-1_16/COVER

103. MARTIN SW. Review of the structures of phosphate glasses. *Eur J solid state Inorg Chem*. 1991;28(1):163-205.

104. Van Wazer JR. Nomenclature of Phosphorus Compounds. *J Chem Doc*. 1964;4(2):84-90. doi:10.1021/C160013A005/ASSET/C160013A005.FP.PNG_V03

105. Van Wazer JR. Structure and properties of the condensed phosphates. II. A theory of the molecular structure of sodium phosphate glasses. *J Am Chem Soc*. 1950;72(2):644-647. doi:10.1021/JA01158A002/ASSET/JA01158A002.FP.PNG_V03

106. Hoppe U. A structural model for phosphate glasses. *J Non Cryst Solids*. 1996;195(1-2):138-147. doi:10.1016/0022-3093(95)00524-2

107. Brow RK, Kirkpatrick RJ, Turner GL. The short range structure of sodium phosphate glasses I. MAS NMR studies. *J Non Cryst Solids*. 1990;116(1):39-45. doi:10.1016/0022-3093(90)91043-Q

108. Yang X, Zhang L, Chen X, et al. Incorporation of B2O3 in CaO-SiO2-P2O5 bioactive glass system for improving strength of low-temperature co-fired porous glass ceramics. *J Non Cryst Solids*. 2012;358(9):1171-1179. doi:10.1016/J.JNONCRYSOL.2012.02.005

109. Gao H, Tan T, Wang D. Dissolution mechanism and release kinetics of phosphate controlled release glasses in aqueous medium. *J Control Release*. 2004;96(1):29-36. doi:10.1016/J.JCONREL.2003.12.031

110. Liu QX, Chen XM, Li X. Study on the hydrolysis of Na2O-CaO-SiO2-P2O5 bio glasses. *China Glas*. 1993;18:26-29.

111. Brow RK, Tallant DR. Structural design of sealing glasses. *J Non Cryst Solids*. 1997;222:396-406. doi:10.1016/S0022-3093(97)90142-3

112. Rahaman MN, Day DE, Sonny Bal B, et al. Bioactive glass in tissue engineering. *Acta Biomater*. 2011;7(6):2355-2373. doi:10.1016/J.ACTBIO.2011.03.016

113. Abou Neel EA, Ahmed I, Blaker JJ, et al. Effect of iron on the surface, degradation and ion release properties of phosphate-based glass fibres. *Acta Biomater*. 2005;1(5):553-563. doi:10.1016/J.ACTBIO.2005.05.001

114. Abou Neel EA, Ahmed I, Pratten J, Nazhat SN, Knowles JC. Characterisation of antibacterial copper releasing degradable phosphate glass fibres. *Biomaterials*. 2005;26(15):2247-2254. doi:10.1016/J.BIOMATERIALS.2004.07.024

115. Choueka J, Charvet JL, Alexander H, et al. Effect of annealing temperature on the degradation of reinforcing fibers for absorbable implants. *J Biomed Mater Res*. 1995;29(11):1309-1315. doi:10.1002/JBM.820291102

116. Mulligan AM, Wilson M, Knowles JC. Effect of increasing silver content in phosphate-based glasses on biofilms of Streptococcus sanguis. *J Biomed Mater Res Part A*. 2003;67A(2):401-412. doi:10.1002/JBM.A.10052

117. Mulligan AM, Wilson M, Knowles JC. The effect of increasing copper content in phosphate-

based glasses on biofilms of Streptococcus sanguis. *Biomaterials*. 2003;24(10):1797-1807. doi:10.1016/S0142-9612(02)00577-X

118. Shah R, Sinanan ACM, Knowles JC, Hunt NP, Lewis MP. Craniofacial muscle engineering using a 3-dimensional phosphate glass fibre construct. *Biomaterials*. 2005;26(13):1497-1505. doi:10.1016/J.BIOMATERIALS.2004.04.049

119. Ahmed I, Collins CA, Lewis MP, Olsen I, Knowles JC. Processing, characterisation and biocompatibility of iron-phosphate glass fibres for tissue engineering. *Biomaterials*. 2004;25(16):3223-3232. doi:10.1016/J.BIOMATERIALS.2003.10.013

120. Ebendorff-Heidepriem H, Ehrt D. Formation and UV absorption of cerium, europium and terbium ions in different valencies in glasses. *Opt Mater (Amst)*. 2000;15(1):7-25. doi:10.1016/S0925-3467(00)00018-5

121. Ebendorff-Heidepriem H, Ehrt D. Effect of Tb3+ ions on X-ray-induced defect formation in phosphate containing glasses. *Opt Mater (Amst)*. 2002;18(4):419-430. doi:10.1016/S0925-3467(01)00182-3

122. Ebendorff-Heidepriem H, Riziotis C, Taylor ER. Novel photosensitive glasses. Published online 2002.

123. Philipps JF, Töpfer T, Ebendorff-Heidepriem H, Ehrt D, Sauerbrey R. Energy transfer and upconversion in erbium–ytterbium-doped fluoride phosphate glasses. *Appl Phys B 2002 743*. 2014;74(3):233-236. doi:10.1007/S003400200804

124. Philipps JF, Töpfer T, Ebendorff-Heidepriem H, Ehrt D, Sauerbrey R. Spectroscopic and lasing properties of Er3+:Yb3+-doped fluoride phosphate glasses. *Appl Phys B 2001 724*. 2001;72(4):399-405. doi:10.1007/S003400100515

125. Wei TY, Hu Y, Hwa LG. Structure and elastic properties of low-temperature sealing phosphate glasses. *J Non Cryst Solids*. 2001;288(1-3):140-147. doi:10.1016/S0022-3093(01)00612-3

126. Allen WM, Sansom BF, Drake CF, Davies DC. A new method for the prevention of trace element deficiencies. *Vet Sci Commun 1978 21*. 1978;2(1):73-75. doi:10.1007/BF02291434

127. Allen WM, Sansom BF, Gleed PT, Mallinson CB, Drake CF. Boluses of controlled release glass for supplementing ruminants with copper. *Vet Rec*. 1984;115(3):55-57. doi:10.1136/VR.115.3.55

128. Allen WM, Sansom BF, Mallinson CB, Stebbings RJ, Drake CF. Boluses of controlled release glass for supplementing ruminants with cobalt. *Vet Rec*. 1985;116(7):175-177. doi:10.1136/VR.116.7.175

129. Brow RK. Review: the structure of simple phosphate glasses. *J Non Cryst Solids*. 2000;263-264:1-28. doi:10.1016/S0022-3093(99)00620-1

130. Garbarczyk JE, Wasiucionek M, Mauger A, et al. The thermal stability, local structure and

electrical properties of lithium-iron phosphate glasses Ionic conduction View project Polyanionic materials View project The thermal stability, local structure and electrical properties of lithium-iron phosphate glasses. *Mater Sci*. 2009;27(1). Accessed November 20, 2022. https://www.researchgate.net/publication/267717112

131. Yang S, Zavalij PY, Whittingham MS. Hydrothermal synthesis of lithium iron phosphate cathodes. *Electrochem commun*. 2001;3(9):505-508. doi:10.1016/S1388-2481(01)00200-4

132. Marino AE, Arrasmith SR, Gregg LL, Jacobs SD, Chen G, Duc Y. Durable phosphate glasses with lower transition temperatures. *J Non Cryst Solids*. 2001;289(1-3):37-41. doi:10.1016/S0022-3093(01)00706-2

133. Peyghambarian N, Schülzgen A. Fiber Lasers: High-Power Devices in Compact Packages. *Opt Photonics News, Vol 16, Issue 6, pp 36-41*. 2005;16(6):36-41. doi:10.1364/OPN.16.6.000036

134. Wedgwood FA, Wright AC. Short range antiferromagnetic ordering in vitreous Fe2O3 P2O5. *J Non Cryst Solids*. 1976;21(1):95-105. doi:10.1016/0022-3093(76)90095-8

135. Shaw JL, Wright AC, Sinclair RN, et al. Spin glass-like antiferromagnetic interactions in iron phosphate glasses. *J Non Cryst Solids*. 2004;345-346:245-250. doi:10.1016/J.JNONCRYSOL.2004.08.090

136. Akamatsu H, Fujita K, Murai S, Tanaka K. Magneto-optical properties of transparent divalent iron phosphate glasses. *Appl Phys Lett*. 2008;92(25):251908. doi:10.1063/1.2952460

137. Abbas L, Bih L, Nadiri A, El Amraoui Y, Mezzane D, Elouadi B. Properties of mixed Li2O and Na2O molybdenum phosphate glasses. *J Mol Struct*. 2008;876(1-3):194-198. doi:10.1016/J.MOLSTRUC.2007.06.018

138. Smets BMJ, Lommen TPA. The structure of germanosilicate glasses, studied by X-ray photoelectron spectroscopy. *J Non Cryst Solids*. 1981;46(1):21-32. doi:10.1016/0022-3093(81)90071-5

139. Niibori Y, Chida T, Tochiyama O. Dissolution Rates of Amorphous Silica in Highly Alkaline Solution. *http://dx.doi.org/101080/18811248200009714905*. 2012;37(4):349-357. doi:10.1080/18811248.2000.9714905

140. Mori H, Müller AHE. New polymeric architectures with (meth)acrylic acid segments. *Prog Polym Sci*. 2003;28(10):1403-1439. doi:10.1016/S0079-6700(03)00076-5

141. Paul A. Chemical Durability of Glass. *Chem Glas*. Published online 1982:108-147. doi:10.1007/978-94-009-5918-7_4

142. Crovisier JL, Honnorez J, Eberhart JP. Dissolution of basaltic glass in seawater: Mechanism and rate. *Geochim Cosmochim Acta*. 1987;51(11):2977-2990. doi:10.1016/0016-7037(87)90371-1

143. Matthew Asmussen R, Neeway JJ, Kaspar TC, Crum J V. Corrosion of glass, ceramics and

ceramic superconductors: Principles, testing, characterization and applications. *Corrosion*. 1992;73(11):1306-1319. doi:10.5006/2449

144. DOUGLAS RW, EL-SHAMY TMM. Reactions of Glasses with Aqueous Solutions. *J Am Ceram Soc*. 1967;50(1):1-8. doi:10.1111/J.1151-2916.1967.TB14960.X

145. Videau J-J, Le Flem G, Le G, Les F. Les verres phosphates : de la spécificité de l'atome de phosphore à la formation, la structure et la durabilité chimique de phosphates vitreux. Published online November 2, 2009:66. Accessed March 1, 2023. https://cel.hal.science/cel-00530128

146. EL-SHAMY TM, MORSI SE, TAKI-ELDIN HD, AHMED AA. CHEMICAL DURABILITY OF Na2O–CaO–SiO2 GLASSES IN ACID SOLUTIONS. *Glas Surfaces*. Published online January 1, 1975:241-250. doi:10.1016/B978-0-7204-0419-7.50026-3

147. Koudelka L, Pospíšil J, Mošner P, Montagne L, Delevoye L. Structure and properties of potassium niobato-borophosphate glasses. *J Non Cryst Solids*. 2008;354(2-9):129-133. doi:10.1016/J.JNONCRYSOL.2007.07.030

148. SEN S, TOOLEY F V. Effect of Na2O/K2O Ratio on Chemical Durability of Alkali-Lime-Silica Glasses. *J Am Ceram Soc*. 1955;38(5):175-177. doi:10.1111/J.1151-2916.1955.TB14924.X

149. Delahaye F, Montagne L, Palavit G, Touray JC, Baillif P. Acid dissolution of sodium–calcium metaphosphate glasses. *J Non Cryst Solids*. 1998;242(1):25-32. doi:10.1016/S0022-3093(98)00784-4

150. Karmakar B. Fundamentals of Glass and Glass Nanocomposites. *Glas Nanocomposites Synth Prop Appl*. Published online January 1, 2016:3-53. doi:10.1016/B978-0-323-39309-6.00001-8

151. El Hadrami A, Mesnaoui M, Maazaz M, Videau JJ. Kinetic dissolution of phosphate glasses containing toxic heavy metals. *J Non Cryst Solids*. 2003;331(1-3):228-239. doi:10.1016/J.JNONCRYSOL.2003.08.066

152. Rüssel C. Introduction to Glass Science and Technology. *Zeitschrift für Phys Chemie*. 1999;208(1-2):292-293. doi:10.1524/ZPCH.1999.208.PART_1_2.292

153. Flory PJ. Random Reorganization of Molecular Weight Distribution in Linear Condensation Polymers. *J Am Chem Soc*. 1942;64(9):2205-2212. doi:10.1021/JA01261A049/ASSET/JA01261A049.FP.PNG_V03

154. Barton J, Guillemet C (Claude). Le verre, science et technologie. Published online 2005:440. Accessed December 26, 2022. https://docplayer.fr/16645643-Le-verre-science-et-technologie-james-barton-et-claude-guillemet-chimie-i-materiaux.html

155. Im SH, Na YH, Kim NJ, Kim DH, Hwang CW, Ryu BK. Structure and properties of zinc bismuth phosphate glass. *Thin Solid Films*. 2010;518(24):e46-e49. doi:10.1016/J.TSF.2010.03.128

156. Cooper GI, Cox GA. The aqueous corrosion of potash-lime-silica glass in the range 10–250°C. *Appl Geochemistry*. 1996;11(4):511-521. doi:10.1016/0883-2927(96)00004-2

157. Kaur P, Singh KJ, Kurudirek M, Thakur S. Gamma-ray and neutron shielding behaviour of CaO-K2O-P2O5 glass system modified with Bi2O3. In: *AIP Conference Proceedings*. Vol 2115. AIP Publishing LLC; 2019:30251.

158. Sayyed MI, Albarzan B, Almuqrin AH, et al. Experimental and theoretical study of radiation shielding features of CaO-K2O-Na2O-P2O5 glass systems. *Materials (Basel)*. 2021;14(14):3772.

159. Aloraini DA, Sayyed MI, Kumar A, Kurtulus R, Almuqrin AH, Kavas T. Synthesis, structural investigation, mechanical calculations and photon shielding properties of CaO–K2O–Na2O–P2O5 glass system. *Opt Mater (Amst)*. 2021;117:111178.

160. Marikani A, Maheswaran A, Premanathan M, Amalraj L. Synthesis and characterization of calcium phosphate based bioactive quaternary P2O5–CaO–Na2O–K2O glasses. *J Non Cryst Solids*. 2008;354(33):3929-3934.

161. Byun J-O, Kim B-H, Hong K-S, Jung H-J, Lee S-W, Izyneev AA. Properties and structure of RO□ Na2O□ Al2O3□ P2O5 (R= Mg, Ca, Sr, Ba) glasses. *J Non Cryst Solids*. 1995;190(3):288-295.

162. Yifen J, Dehua J, Xiangsheng C, Beiya B, Xihuai H. Raman spectrum studies of the glasses in the system Na2O□ Al2O3□ P2O5. *J Non Cryst Solids*. 1986;80(1-3):147-151.

163. El-Damrawi G, Hassan AK, Shahboub A. Characteristic studies on Ag2O-Al2O3-P2O5 glasses and glass ceramics. *Mater Sci Eng B.* 2021;264:114957.

164. Prasad S, Reddy MS, Veeraiah N. Nickel ion—A structural probe in BaO–Al2O3–P2O5 glass system by means of dielectric, spectroscopic and magnetic studies. *J Phys Chem Solids*. 2006;67(12):2478-2488.

165. Pershina S V., Raskovalov AA, Antonov BD, et al. Extreme behavior of Li-ion conductivity in the Li2O–Al2O3–P2O5 glass system. *J Non Cryst Solids*. 2015;430:64-72. doi:10.1016/J.JNONCRYSOL.2015.10.003

166. Antonijevic MM, Petrovic MB. Copper Corrosion Inhibitors. A review. *Int J Electrochem Sci*. 2008;3:1-28. Accessed March 2, 2023. www.electrochemsci.org

167. BUNKER BC, ARNOLD GW, RAJARAM M, DAY DE. Corrosion of Phosphorus Oxynitride Glasses in Water and Humid Air. *J Am Ceram Soc*. 1987;70(6):425-430. doi:10.1111/J.1151-2916.1987.TB05663.X

168. Favre M, Landolt D. The influence of gallic acid on the reduction of rust on painted steel surfaces. *Corros Sci*. 1993;34(9):1481-1494. doi:10.1016/0010-938X(93)90243-A

169. Cramer SD, Covino BS, Scott WW, et al. ASM Handbook Volume 13A Corrosion:

Fundamentals, Testing, and Protection Prepared under the direction of the ASM International Handbook Committee. Published online 2003. Accessed March 2, 2023. www.asminternational.orgwww.asminternational.org

170. Jaubert L. Etude de la corrosion uniforme d'aciers non alliés et inoxydables : utilisation conjointe de l'émission acoustique et des techniques électrochimiques. *http://www.theses.fr*. Published online January 1, 2004. Accessed March 2, 2023. http://www.theses.fr/2004ISAL0044

171. Boudalia M, Fernández-Domene RM, Guo L, et al. Experimental and Theoretical Tests on the Corrosion Protection of Mild Steel in Hydrochloric Acid Environment by the Use of Pyrazole Derivative. *Materials (Basel)*. 2023;16(2):678. doi:10.3390/MA16020678/S1

172. Boudalia M, Guenbour A, Bellaouchou A, et al. Corrosion Inhibition of Organic Oil Extract of Leaves Of Lanvandula Stoekas on Stainless Steel in Concentrated Phosphoric Acid Solution. *Int J Electrochem Sci*. 2013;8:7414-7424. Accessed March 2, 2023. www.electrochemsci.org

173. Constantin F. Etude de l'efficacité d'inhibiteurs de corrosion utilisés dans les liquides de refroidissement. Published online November 15, 2011. Accessed June 7, 2023. https://theses.hal.science/tel-00690792

174. Li X, Deng S, Fu H. Inhibition of the corrosion of steel in HCl, H2SO4 solutions by bamboo leaf extract. *Corros Sci*. 2012;62:163-175. doi:10.1016/J.CORSCI.2012.05.008

175. Coburn SK. Corrosion source book. Published online January 1, 1984.

176. NACE Glossary of Corrosion Terms. In: *Materials Protection*. (1). ; 1965.

177. Papavinasam S. Corrosion Inhibitors. *Uhlig's Corros Handb Third Ed*. Published online April 19, 2011:1021-1032. doi:10.1002/9780470872864.CH71

178. Corrosion Inhibitors: Principles and Applications. *Anti-Corrosion Methods Mater*. 2002;49(3). doi:10.1108/ACMM.2002.12849CAE.001

179. Zarrouk A, Hammouti B, Lakhlifi T, Traisnel M, Vezin H, Bentiss F. New 1H-pyrrole-2,5-dione derivatives as efficient organic inhibitors of carbon steel corrosion in hydrochloric acid medium: Electrochemical, XPS and DFT studies. *Corros Sci*. 2015;90:572-584. doi:10.1016/J.CORSCI.2014.10.052

180. Özcan M, Dehri I, Erbil M. Organic sulphur-containing compounds as corrosion inhibitors for mild steel in acidic media: correlation between inhibition efficiency and chemical structure. *Appl Surf Sci*. 2004;236(1-4):155-164. doi:10.1016/J.APSUSC.2004.04.017

181. Aramaki K. Effects of organic inhibitors on corrosion of zinc in an aerated 0.5 M NaCl solution. *Corros Sci*. 2001;43(10):1985-2000. doi:10.1016/S0010-938X(00)00174-8

182. Yadav M, Kumar S, Sinha RR, Bahadur I, Ebenso EE. New pyrimidine derivatives as efficient organic inhibitors on mild steel corrosion in acidic medium: Electrochemical, SEM, EDX,

AFM and DFT studies. *J Mol Liq*. 2015;211:135-145. doi:10.1016/J.MOLLIQ.2015.06.063

183. Foad El Sherbini EE, Abd El Rehim SS. Pitting corrosion of zinc in Na2SO4 solutions and the effect of some inorganic inhibitors. *Corros Sci*. 2000;42(5):785-798. doi:10.1016/S0010-938X(99)00081-5

184. Aramaki K, Hagiwara M, Nishihara H. Impedance Study on Inhibition and Stimulation of Iron Corrosion in Acid Solution by Various Inorganic Anions and Tetra-alkylammonium Cation. *J Electrochem Soc*. 1988;135(6):1364-1369. doi:10.1149/1.2095988/XML

185. Bohm S, McMurray H, … DW-M and, 2001 undefined. Novel environment friendly corrosion inhibitor pigments based on naturally occurring clay minerals. *Wiley Online Libr*. Accessed June 7, 2023. https://onlinelibrary.wiley.com/doi/abs/10.1002/1521-4176(200112)52:12%3C896::AID-MACO896%3E3.0.CO;2-8

186. Koudelka M, Sanchez J, Augustyński J. On the Nature of Surface Films Formed on Iron in Aggressive and Inhibiting Polyphosphate Solutions. *J Electrochem Soc*. 1982;129(6):1186-1191. doi:10.1149/1.2124084/META

187. Langmuir I. The adsorption of gases on plane surfaces of glass, mica and platinum. *J Am Chem Soc*. 1918;40(9):1361-1403. doi:10.1021/JA02242A004/ASSET/JA02242A004.FP.PNG_V03

188. Orubite KO, Oforka NC. Inhibition of the corrosion of mild steel in hydrochloric acid solutions by the extracts of leaves of Nypa fruticans Wurmb. *Mater Lett*. 2004;58(11):1768-1772. doi:10.1016/J.MATLET.2003.11.030

189. Bilgiç S, Çaliskan N. Investigation of some Schiff bases as corrosion inhibitors for austenitic chromium-nickel steel in H2SO4. *J Appl Electrochem*. 2001;31(1):79-83. doi:10.1023/A:1004182329826/METRICS

190. Obot IB, Obi-Egbedi NO, Umoren SA. Adsorption Characteristics and Corrosion Inhibitive Properties of Clotrimazole for Aluminium Corrosion in Hydrochloric Acid. *Int J Electrochem Sci*. 2009;4:863-877. Accessed June 7, 2023. www.electrochemsci.org

191. Abiola OK, Otaigbe JOE, Kio OJ. Gossipium hirsutum L. extracts as green corrosion inhibitor for aluminum in NaOH solution. *Corros Sci*. 2009;51(8):1879-1881. doi:10.1016/J.CORSCI.2009.04.016

192. Radovico O. CORROSION INHIBITORS. Proceedings of the 3rd European Symposium, Ferrara, Italy, September 14--17, 1970. Published online January 1, 1990:330.

193. Onal AN, Aksut AA. Corrosion inhibition of aluminium alloys by tolyltriazole in chloride solutions. *Anti-Corrosion Methods Mater*. 2000;47(6):339-348. doi:10.1108/00035590010354177/FULL/XML

194. Raja PB, Sethuraman MG. Natural products as corrosion inhibitor for metals in corrosive media — A review. *Mater Lett*. 2008;62(1):113-116. doi:10.1016/J.MATLET.2007.04.079

195. Rani BEA, Basu BBJ. Green inhibitors for corrosion protection of metals and alloys: An overview. *Int J Corros*. 2012;2012. doi:10.1155/2012/380217

196. Ghailane T, Balkhmima RA, Ghailane R, et al. Experimental and theoretical studies for mild steel corrosion inhibition in 1 M HCl by two new benzothiazine derivatives. *Corros Sci*. 2013;76:317-324. doi:10.1016/J.CORSCI.2013.06.052

197. Khedr MGA, Lashien AMS. The role of metal cations in the corrosion and corrosion inhibition of aluminium in aqueous solutions. *Corros Sci*. 1992;33(1):137-151. doi:10.1016/0010-938X(92)90023-V

198. Claudy P. Analyse calorimétrique différentielle : théorie et application de la d.s.c. Published online 2005:390. Accessed December 8, 2022. http://www.sudoc.fr/084177136

199. Whiston C, Prichard FE. X-ray methods. Published online January 1, 1987.

200. Klug HP, Alexander LE. X-Ray Diffraction Procedures: For Polycrystalline and Amorphous Materials, 2nd Edition. *xdpf*. Published online 1974:992. Accessed November 29, 2022. https://ui.adsabs.harvard.edu/abs/1974xdpf.book.....K/abstract

201. Waseda Y, Matsubara E, Shinoda K. Scattering and Diffraction. *X-Ray Diffr Crystallogr*. Published online 2011:67-106. doi:10.1007/978-3-642-16635-8_3

202. Doweidar H, Moustafa YM, El-Egili K, Abbas I. Infrared spectra of Fe2O3–PbO–P2O5 glasses. *Vib Spectrosc*. 2005;37(1):91-96. doi:10.1016/J.VIBSPEC.2004.07.002

203. Khan SA, Khan SB, Khan LU, Farooq A, Akhtar K, Asiri AM. Fourier transform infrared spectroscopy: Fundamentals and application in functional groups and nanomaterials characterization. *Handb Mater Charact*. Published online September 18, 2018:317-344. doi:10.1007/978-3-319-92955-2_9/COVER

204. Pike ER. Introduction to Soft X-Ray Spectroscopy. *Am J Phys*. 2005;28(3):235. doi:10.1119/1.1935107

205. Sooiety TP, 関数な, 形などやはり基礎的な事柄を扱っているの, 価既約表現を表にしたもので本書の中心部分である. この表は92コの抽象群の既約表現表を参照するコンパクトな形式で与え二, Altmann の教えをうけた若手の学者大学）はともに. R. J. Bell: Introductory Fourier Transform Spectroscopy, Academic Press, 1972, 398 ページ, 24×16cm, $ 19.50. 日本物理学会誌. 1972;27(12):1020-1021. doi:10.11316/BUTSURI1946.27.12.1020

206. Takebe H, Baba Y, Kuwabara M. Dissolution behavior of ZnO–P2O5 glasses in water. *J Non Cryst Solids*. 2006;352(28-29):3088-3094. doi:10.1016/J.JNONCRYSOL.2006.04.002

207. Bommersbach P. c. Alemany-Dumont, JP Millet, B. Normand. *Electrochim acta*. 2005;51:1076-1084.

208. Béranger G, Mazille H. Corrosion des métaux et alliages: mécanismes et phénomènes. *Hermes*

(éd), Trait MIM. Published online 2002:365.

209. Stern M, Geary AL. A theoretical analysis of the shape of polarization curves. *J Electrochem Soc*. 1957;104(1):56-63.

210. Kelly RG, Scully JR, Shoesmith DW, Buchheit RG. Techniques in Corrosion Science and Engineering. Published online 2003.

211. Normand B. *Prévention et Lutte Contre La Corrosion: Une Approche Scientifique et Technique*. PPUR presses polytechniques; 2004.

212. Vogelsang J, Strunz W. The evaluation of experimental dielectric data of barrier coatings by means of different models. *Electrochim Acta*. 2001;46(24-25):3619-3625. doi:10.1016/S0013-4686(01)00644-2

213. Reidmeyer MR, Day DE. Structural model for nitrogen incorporation in phosphate glasses. *J Mater Res*. 1991;6(8):1757-1762.

214. Reidmeyer MR, Day DE. Phosphorus oxynitride glasses. *J Non Cryst Solids*. 1995;181(3):201-214.

215. Moustafa YM, El-Adawy A. Structural and physical properties of iron oxychloride phosphate glasses. *Phys status solidi*. 2000;179(1):83-93.

216. Matori KA, Sayyed MI, Sidek HAA, Zaid MHM, Singh VP. Comprehensive study on physical, elastic and shielding properties of lead zinc phosphate glasses. *J Non Cryst Solids*. 2017;457:97-103.

217. Shih PY. Properties and FTIR spectra of lead phosphate glasses for nuclear waste immobilization. *Mater Chem Phys*. 2003;80(1):299-304.

218. Carta D, Pickup DM, Knowles JC, Ahmed I, Smith ME, Newport RJ. A structural study of sol–gel and melt-quenched phosphate-based glasses. *J Non Cryst Solids*. 2007;353(18-21):1759-1765.

219. Ahmina W, El Moudane M, Zriouil M, Taibi M. Glass-forming region, structure and some properties of potassium manganese phosphate glasses. *Phase Transitions*. 2016;89(11):1051-1061. doi:10.1080/01411594.2016.1144057

220. Karmakar B. *Functional Glasses and Glass-Ceramics: Processing, Properties and Applications*. Butterworth-Heinemann; 2017.

221. Ahmina W, El Moudane M, Zriouil M, Taibi M. Glass-forming region, structure and some properties of potassium manganese phosphate glasses. *Phase transitions*. 2016;89(11):1051-1061.

222. Aliyu AM, Hussin R, Ahmad NE, Yamusa YA. Samarium doped calcium sulfate ultra-phosphate glasses: Structural, physical and luminescence investigations. *Optik (Stuttg)*. 2018;172:1162-1171.

223. Liu HS, Chin TS, Yung SW. FTIR and XPS studies of low-melting PbO-ZnO-P2O2 glasses. *Mater Chem Phys*. 1997;50(1):1-10.

224. Laengle E, Hackerman N. Electrode Behavior of Iron in 2 M HCl Containing Oximes or Quinuclidine. *J Electrochem Soc*. 1971;118(8):1273.

225. Pillai KC, Narayan R. Anodic dissolution of mild steel in HCl solutions containing thio-ureas. *Corros Sci*. 1983;23(2):151-166.

226. Brow RK, Tallant DR, Myers ST, Phifer CC. The short-range structure of zinc polyphosphate glass. *J Non Cryst Solids*. 1995;191(1-2):45-55.

227. Montagne L, Palavit G, Mairesse G. 31P MAS NMR and FT IR analysis of (50-x/2) Na2O. xBi2O3.(50-x/2) P2O5 glasses. *Phys Chem Glas*. 1996;37(5):206-211.

228. Corbridge DEC, Lowe EJ. The infra-red spectra of some inorganic phosphorus compounds. *J Chem Soc*. Published online 1954:493-502.

229. Bartholomew RF. Structure and properties of silver phosphate glasses—Infrared and visible spectra. *J Non Cryst Solids*. 1972;7(3):221-235.

230. Lee S, Nagata F, Kato K, Nakano T, Kasuga T. Structures and Dissolution Behaviors of Quaternary CaO-SrO-P2O5-TiO2 Glasses. *Mater 2021, Vol 14, Page 1736*. 2021;14(7):1736. doi:10.3390/MA14071736

231. Liu H, Lu Y, Qu Y, Lu H, Yue Y. Effect of the content of Al2O3 on structure and properties of calcium-phosphate glasses: Two experimental case studies. *J Non Cryst Solids*. 2016;450:95-102. doi:10.1016/j.jnoncrysol.2016.07.043

232. Donald IW, Metcalfe BL, Fong SK, Gerrard LA. The influence of Fe2O3 and B2O3 additions on the thermal properties, crystallization kinetics and durability of a sodium aluminum phosphate glass. *J Non Cryst Solids*. 2006;352(28-29):2993-3001. doi:10.1016/J.JNONCRYSOL.2006.04.007

233. Lee ETY, Taylor ERM. Compositional effects on the optical and thermal properties of potassium aluminophosphate glasses. *Opt Mater (Amst)*. 2004;27(2):323-330. doi:10.1016/J.OPTMAT.2004.02.029

234. Shelby JE. *Introduction to Glass Science and Technology*. Royal Society of Chemistry; 2007. doi:10.1039/9781847551160

235. Schneider J, Oliveira SL, Nunes LAO, Bonk F, Panepucci H. Short-range structure and cation bonding in calcium-aluminum metaphosphate glasses. *Inorg Chem*. 2005;44(2):423-430. doi:10.1021/IC0499704/ASSET/IMAGES/IC0499704.SOCIAL.JPEG_V03

236. Omrani RO, Krimi S, Videau JJ, Khattech I, El Jazouli A, Jemal M. Structural investigations and calorimetric dissolution of manganese phosphate glasses. *J Non Cryst Solids*. 2014;389:66-71. doi:10.1016/J.JNONCRYSOL.2014.02.006

237. Zotov N, Schlenz H, Brendebach B, et al. Effects of MnO-Doping on the Structure of Sodium Metaphosphate Glasses. *Zeitschrift fur Naturforsch - Sect A J Phys Sci*. 2003;58(7-8):419-428. doi:10.1515/ZNA-2003-7-806

238. Gongyi G. 31P and 27Al MAS NMR investigations of some lead phosphate glasses. *Mater Res Bull*. 1999;34(4):621-626. doi:10.1016/S0025-5408(99)00038-0

239. Prasad SVGVA, Srinivasa Reddy M, Veeraiah N. Nickel ion—A structural probe in BaO–Al2O3–P2O5 glass system by means of dielectric, spectroscopic and magnetic studies. *J Phys Chem Solids*. 2006;67(12):2478-2488. doi:10.1016/J.JPCS.2006.07.002

240. Hwa LG, Hwang SL, Liu LC. Infrared and Raman spectra of calcium alumino–silicate glasses. *J Non Cryst Solids*. 1998;238(3):193-197. doi:10.1016/S0022-3093(98)00688-7

241. Satyanarayana T, Kalpana T, Ravi Kumar V, Veeraiah N. Role of Al coordination in barium phosphate glasses on the emission features of Ho3+ ion in the visible and IR spectral ranges. *J Lumin*. 2010;130(3):498-506. doi:10.1016/J.JLUMIN.2009.10.021

242. Higazy AA, Bridge B. Elastic constants and structure of the vitreous system Co3O4 P2O5. *J Non Cryst Solids*. 1985;72(1):81-108. doi:10.1016/0022-3093(85)90167-X

243. Gaafar MS, Marzouk SY. Structural Investigation of Na2O–B2O3–SiO2 Glasses Doped with NdF3. *Int J Mater Metall Eng*. 2016;9(10):1249-1257.

244. Macfarlane A, Martin G. *Glass: A World History*. University of Chicago Press; 2002.

245. Filho JC, Zilio SC, Messias DN, et al. Effects of aluminum substitution by potassium in the P2O5–Al2O3–Na2O–K2O phosphate glasses. *J Alloys Compd*. 2020;815:152359. doi:10.1016/J.JALLCOM.2019.152359

246. Bingham PA, Hand RJ, Hannant OM, Forder SD, Kilcoyne SH. Effects of modifier additions on the thermal properties, chemical durability, oxidation state and structure of iron phosphate glasses. *J Non Cryst Solids*. 2009;355(28-30):1526-1538. doi:10.1016/J.JNONCRYSOL.2009.03.008

247. MINAMF T, MACKENZIE JD. Thermal Expansion and Chemical Durability of Phosphate Glasses. *J Am Ceram Soc*. 1977;60(5-6):232-235. doi:10.1111/J.1151-2916.1977.TB14113.X

248. Abou Neel EA, Chrzanowski W, Pickup DM, et al. Structure and properties of strontium-doped phosphate-based glasses. *J R Soc Interface*. 2009;6(34):435-446. doi:10.1098/rsif.2008.0348

249. Laourayed M, El Moudane M, Khachani M, et al. Thermal, structural and corrosion inhibition performances of a new phosphate glasses on mild steel in HCl medium. *Chem Data Collect*. 2019;24:100305. doi:10.1016/j.cdc.2019.100305

250. Snellings R. Surface Chemistry of Calcium Aluminosilicate Glasses. *J Am Ceram Soc*. 2015;98(1):303-314. doi:10.1111/JACE.13263

251. Tauc J. Chap. 5 of “Optical Properties of Solids” ed. By F. Abeles. Published online 1972.

252. Majjane A, Rair D, Chahine A, science ME-C, 2012 undefined. Preparation and characterization of a new glass system inhibitor for mild steel corrosion in hydrochloric solution. *Elsevier*. Accessed June 8, 2023. https://www.sciencedirect.com/science/article/pii/S0010938X12001734?casa_token=YAmJ3t-BCi4AAAAA:HRzOQJ8BinEhrQCAFFOLg1TZIcdZcUmSamu1wBavZZyystUwjHuAlfNqgGbzOatpf7oeJstiUYI

253. Garverick L. *Corrosion in Teh Petrochemical Industry*.; 1994. Accessed June 8, 2023. https://books.google.com/books?hl=en&lr=&id=qTfNZZRO758C&oi=fnd&pg=PP11&dq=L.+Gaverick,+Forms+corrosion+in+the+petrochemical+industry,+ASM.+Int.+2+(1994)+2.&ots=81rLm5tUQV&sig=SOO5Jylb9heWoRExD8CGDiixbGw

254. Iravani D, Arefinia R. Effectiveness of one-to-one phosphate to chloride molar ratio at different chloride and hydroxide concentrations for corrosion inhibition of carbon steel. *Constr Build Mater*. 2020;233:117200. doi:10.1016/J.CONBUILDMAT.2019.117200

255. Hsissou R, Abbout S, Seghiri R, et al. Evaluation of corrosion inhibition performance of phosphorus polymer for carbon steel in [1 M] HCl: Computational studies (DFT, MC and MD simulations). *J Mater Res Technol*. 2020;9(3):2691-2703. doi:10.1016/J.JMRT.2020.01.002

256. Hsissou R, Benhiba F, Abbout S, et al. Trifunctional epoxy polymer as corrosion inhibition material for carbon steel in 1.0 M HCl: MD simulations, DFT and complexation computations. *Inorg Chem Commun*. 2020;115:107858. doi:10.1016/J.INOCHE.2020.107858

257. Hsissou R, Benhiba F, Dagdag O, et al. Development and potential performance of prepolymer in corrosion inhibition for carbon steel in 1.0 M HCl: Outlooks from experimental and computational investigations. *J Colloid Interface Sci*. 2020;574:43-60. doi:10.1016/J.JCIS.2020.04.022

258. Dagdag O, Hsissou R, El Harfi A, et al. Epoxy resins and their zinc composites as novel anti-corrosive materials for copper in 3% sodium chloride solution: Experimental and computational studies. *J Mol Liq*. 2020;315:113757. doi:10.1016/J.MOLLIQ.2020.113757

259. Satapathy AK, Gunasekaran G, Sahoo SC, Amit K, Rodrigues P V. Corrosion inhibition by Justicia gendarussa plant extract in hydrochloric acid solution. *Corros Sci*. 2009;51(12):2848-2856. doi:10.1016/J.CORSCI.2009.08.016

260. Hussin MH, Kassim MJ. The corrosion inhibition and adsorption behavior of Uncaria gambir extract on mild steel in 1 M HCl. *Mater Chem Phys*. 2011;125(3):461-468. doi:10.1016/J.MATCHEMPHYS.2010.10.032

261. Quraishi MA, Singh A, Singh VK, Yadav DK, Singh AK. Green approach to corrosion inhibition of mild steel in hydrochloric acid and sulphuric acid solutions by the extract of Murraya koenigii leaves. *Mater Chem Phys*. 2010;122(1):114-122.

262. Kurniawan F, Madurani KA. Electrochemical and optical microscopy study of red pepper seed oil corrosion inhibition by self-assembled monolayers (SAM) on 304 SS. *Prog Org Coatings*. 2015;88:256-262.

263. Chen Y, Hong T. M-Gopal, WP Jepson. *Corros Sci*. 2000;42:979-990.

264. Jüttner K. Electrochemical impedance spectroscopy (EIS) of corrosion processes on inhomogeneous surfaces. *Electrochim Acta*. 1990;35(10):1501-1508.

265. El Hattabi L. Valorisation de carum carvi, thymus vulgaris et thymus satureioides, trois plantes marocaines aux activités antimicrobiennes et antioxydants et aux propriétés anticorrosives. Published online 2017.

266. El-Etre AY, Abdallah M. Natural honey as corrosion inhibitor for metals and alloys. II. C-steel in high saline water. *Corros Sci*. 2000;42(4):731-738. doi:10.1016/S0010-938X(99)00106-7

267. Stoynov ZB, Grafov BM, Savova-Stoynova B, Elkin V V. Electrochemical impedance. Published online 1991.

268. Growcock FB, Jasinski RJ. Time-resolved impedance spectroscopy of mild steel in concentrated hydrochloric acid. *J Electrochem Soc*. 1989;136(8):2310.

269. Hermas AA, Morad MS, Wahdan MH. Effect of PgTPhPBr on the electrochemical and corrosion behaviour of 304 stainless steel in H 2 SO 4 solution. *J Appl Electrochem*. 2004;34(1).

270. Popova A, Raicheva S, Sokolova E, Christov M. Frequency dispersion of the interfacial impedance at mild steel corrosion in acid media in the presence of benzimidazole derivatives. *Langmuir*. 1996;12(8):2083-2089.

271. Lopez DA, Simison SN, De Sanchez SR. The influence of steel microstructure on CO2 corrosion. EIS studies on the inhibition efficiency of benzimidazole. *Electrochim Acta*. 2003;48(7):845-854.

272. Reick W, Pohl M, Padilha AF. Recrystallization–transformation combined reactions during annealing of a cold rolled ferritic–austenitic duplex stainless steel. *ISIJ Int*. 1998;38(6):567-571.

273. Deyab MA, Essehli R, El Bali B. Inhibition of copper corrosion in cooling seawater under flowing conditions by novel pyrophosphate. *RSC Adv*. 2015;5(79):64326-64334.

274. Herrag L, El Bali B, Lachkar M, Hammouti B. Investigation of adsorption and inhibitive effect of phosphite on corrosion of mild steel in hydrochloric acid media. *Orient J Chem*. 2009;25(2):265.

275. Lebrini M, Lagrenée M, Traisnel M, Gengembre L, Vezin H, Bentiss F. Enhanced corrosion resistance of mild steel in normal sulfuric acid medium by 2, 5-bis (n-thienyl)-1, 3, 4-thiadiazoles: electrochemical, X-ray photoelectron spectroscopy and theoretical studies. *Appl*

Surf Sci. 2007;253(23):9267-9276.

276. Ait Addi B, Mouaamoun S, Ait Addi A, Shaban A, Ait Addi E-H. Electrochemical and surface analytical characterization study of the inhibition effect of boiled red onion extract on tin corrosion in 0.2 M Maleic acid medium. *Moroccan J Chem*. 2020;8(3):700-717.

277. Xie Y, Qiao ZY, Mikula A. The Sn-In-Zn system-application of calphad technique to phase diagram measurement. *Calphad*. 2001;25(1):3-10. doi:10.1016/S0364-5916(01)00024-4

278. CHEN F, LI Y, YANG J, TANG X, LI Y. Corrosion Behavior of X80 Steel Welded Joint in Simulated Natural Gas Condensate Solutions. *Acta Met Sin*. 2019;56(2):137-147.

279. Zhou H, Fu F, Dai Z, Qiao Y, Chen J, Liu W. Effect of laser power on microstructure and micro-galvanic corrosion behavior of a 6061-T6 aluminum alloy welding joints. *Metals (Basel)*. 2020;11(1):3.

280. Hong S, Lin J, Wu Y, et al. Cavitation erosion characteristics at various flow velocities in NaCl medium of carbide-based cermet coatings prepared by HVOF spraying. *Ceram Int*. 2021;47(2):1929-1939. doi:10.1016/J.CERAMINT.2020.09.022

281. Zhou D, Wang J, Gao Y, Zhang L. Corrosion behavior of tinplate in NaCl solution under different temperature. *Int J Electrochem Sci*. 2017;12:192-205. doi:10.20964/2017.01.28

282. Djama M, Benhaddad L, Idir B, Achoui N, Daifallah H. Synergistic corrosion inhibition effect of copolymer and an amphoteric surfactant on carbon steel in 3.5 NaCl solution: experimental and theoretical research. *J Solid State Electrochem*. Published online 2023:1-24.

283. Bommersbach P, Alemany-Dumont C, Millet J-P, Normand B. Hydrodynamic effect on the behaviour of a corrosion inhibitor film: characterization by electrochemical impedance spectroscopy. *Electrochim Acta*. 2006;51(19):4011-4018.

284. Putilova IN, Balezin SA, Barannik VP. *Metallic Corrosion Inhibitors*. Pergamon Press; 1960.

285. Yadav DK, Chauhan DS, Ahamad I, Quraishi MA. Electrochemical behavior of steel/acid interface: adsorption and inhibition effect of oligomeric aniline. *RSC Adv*. 2012;3(2):632-646. doi:10.1039/C2RA21697C

286. El bribri A, El attari H, Siniti M, Tabyaoui M. Temperature effects on the corrosion inhibition of carbon steel in 1N H 3 PO 4 solution by methanolic extract of Euphorbia Falcata . L . *Mor J Chem*. 2015;2:286-297.

287. Boumhara K, Bentiss F, Tabyaoui M, et al. Use of Artemisia mesatlantica essential oil as green corrosion inhibitor for mild steel in 1 M hydrochloric acid solution. *Int J Electrochem Sci*. 2014;9:1187-1206.

288. Laidler KJ. *Reaction Kinetics: Homogeneous Gas Reactions*. Vol 1. Elsevier; 2013.

289. Martinez S, Stern I. Thermodynamic characterization of metal dissolution and inhibitor adsorption processes in the low carbon steel/mimosa tannin/sulfuric acid system. *Appl Surf Sci*.

2002;199(1-4):83-89. doi:10.1016/S0169-4332(02)00546-9

290. Bouklah M, Hammouti B, Lagrenée M, Bentiss F. Thermodynamic properties of 2,5-bis(4-methoxyphenyl)-1,3,4-oxadiazole as a corrosion inhibitor for mild steel in normal sulfuric acid medium. *Corros Sci*. 2006;48(9):2831-2842. doi:10.1016/J.CORSCI.2005.08.019

291. Foo KY, Hameed BH. Insights into modelling of isotherm adsorption systems. *Chem Eng J*. 2010;156(1):2-10.

292. Ivanov IB, Ananthapadmanabhan KP, Lips A. Adsorption and structure of the adsorbed layer of ionic surfactants. *Adv Colloid Interface Sci*. 2006;123-126(SPEC. ISS.):189-212. doi:10.1016/J.CIS.2006.05.020

293. Dražić DM, Vračar L, Dražić VJ. The kinetics of inhibitor adsorption on iron. *Electrochim Acta*. 1994;39(8-9):1165-1170. doi:10.1016/0013-4686(94)E0032-U

294. Döner A, Solmaz R, Özcan M, Kardaş G. Experimental and theoretical studies of thiazoles as corrosion inhibitors for mild steel in sulphuric acid solution. *Corros Sci*. 2011;53(9):2902-2913. doi:10.1016/J.CORSCI.2011.05.027